Novel Polymeric Magnetic Resonance Imaging (MRI) Contrast Agents

A thesis submitted to The University of Strathclyde

by

Steven MacLellan

in fulfilment of the requirements for the degree of

Doctor of Engineering (EngD)

2009

Doctoral Training Centre

Department of Bioengineering

Wolfson Building

106 Rottenrow

Glasgow

G4 ONW

‘This theiss is the result of the author’s original research. It has been composed by the author and has not previously been submitted for examination which has led to the award of a degree’

Acknowledgements

Firstly my supervisors Andreas and Ijeoma, thanks so much for your guidance, encouragement and invaluable support throughout this experience. I really appreciate the numerous opportunities with which I was presented. You have taught me to think in new ways and challenge myself.

Thanks to all at the 7T MR facility; William, Jim, Chris, Lindsay and Barrie. All repeatedly went far above the call of duty without a second thought. Similarly my enormous gratitude to Christine who was always generous with her time and support.

Thanks to Dave McCarthy for all his help with the SEM imaging.

Thanks to Mazen for all his help and encouragement at the start of my research, your advice throughout my research was invaluable.

To all my lab-mates over the years thanks for you help and laughter. Katy and Pui Ee thanks for welcoming me at the Beatson and helping me when I was lost. Kar Wai, Katerina and Hang thanks for all your help, understanding and support and in particular thanks to Adeline.

Mum, Dad and Gillian a massive thanks for all your encouragement and support. This would definitely not have happened without you. I really appreciate all the times you listened and understood, it really helped.

Dougie, thanks for listening (a lot!). Ian, thanks for everything in London.

Above all else, thanks Beth. I would never have been able to get through this without you. London was at times a struggle but you made it so much better, thesis writing was tough but much easier knowing I was coming home to you.

I would also like to thanks the following funding bodies: EPSRC, Tenovus Scotland and Cancer Research UK.

Table of Contents

List of Figures

List of Tables

List of Abbreviations

GC	Glycol Chitosan
GC2	Glycol Chitosan sample obtained with a 2 hour acid degradation
GC48	Glycol Chitosan sample obtained with a 48 hour acid degradation
HA	Hyaluronic Acid
MRI	Magnetic Resonance Imaging
DCE-MRI	Dynamic Contrast Enhanced Magnetic Resonance Imaging
DTPA	Diethylene Triamine Pentaacetic Acid
GPC-MALLS	Gel Permeation Chromatography with Multi Angle Laser Light Scattering
NMR	Nuclear Magnetic Resonance (Spectroscopy)
ICP-AES	Inductively Coupled Plasma Atomic Emission Spectroscopy
DAB-16	Polypropylenimine (PPI) Hexadecaamine Dendrimer Generation 3.0
Gd	Gadolinium
TNBS	2,4,6-Trinitrobenzenesulfonic Acid
RF	Radiofrequency
MRA	Magnetic Resonance Angiography
DMT-MM	4-(4,6-Dimethoxy-1,3,5-triazin-2-yl)-4-methyl-morpholinium Chloride
p-SCN-Bn-DTPA	2-(4-Isothiocyanatobenzyl)-DTPA
D_2O	Deuterium Oxide
NaOH	Sodium Hydroxide

T_r	Repetition Time
T_e	Echo Time
A	Flip Angle
MIP	Maximum Intensity Projection
SEM	Scanning Electron Microscope/Microscopy
MVD	Microvessel Density

Abstract

Three novel magnetic resonance imaging (MRI) contrast agents were synthesised; two with glycol chitosan (GC) backbones and one with a hyaluronic acid (HA) backbone.

The aim of the GC based agents was to produce so-called blood pool agents: those with sufficient plasma residence time allow detailed vascular imaging. Synthesis proceeded as follows: acid degradation of high molecular weight GC, attachment of the chelating agent diethylene triamine pentaacetic acid (DTPA) and finally gadolinium incorporation. The molecular weights of the fragments produced by acid degradation were confirmed using gel permeation chromatography with multi angle laser light scattering (GPC-MALLS) and two samples (12 and 38 kDa) were chosen with which to proceed. DTPA attachment was confirmed using NMR and the composition of the GC-DTPA conjugates was determined using elemental analysis and an arsenazo based colorimetric assay. Subsequent gadolinium inclusion was confirmed using inductively coupled plasma atomic emission spectroscopy (ICP-AES). The agents were tested in-vivo to evaluate their potential for use as blood pool agents by imaging of the mouse head. Both agents showed increased vascular specificity compared with the low molecular weight agent Magnevist (Gd-DTPA). In particular the higher molecular weight GC agent offered very clear vascular enhancement which allowed identification of the larger blood vessels of the head.

The rational behind the synthesis of the HA based agent was to produce an agent that could potentially target tumours. Synthesis proceeded as follows: attachment of the generation 3 polypropylenimine dendrimer DAB-16 to the HA backbone, attachment of DTPA to some of the remaining free amine groups of DAB and finally gadolinium incorporation. Firstly the molecular weight of a purchased HA sample was determined using GPC-MALLS (43 kDa). DAB attachment was confirmed using

NMR and the composition of the HA-DAB conjugate determined using elemental analysis and a 2,4,6-trinitrobenzenesulfonic acid (TNBS) based colorimetric assay. The molecular weight of the conjugate was determined using GPP-MALLS (65 kDa). The level of DTPA attachment was assayed using NMR and elemental analysis. Subsequent gadolinium inclusion was confirmed using ICP-AES.

Alongside these synthesis and characterisation works a number of MRI studies were performed to test a novel solenoid radiofrequency (RF) micro-coil set-up for the imaging of mouse flank tumours. The coil was used to image the tumour vasculature using magnetic resonance angiography (MRA) and to investigate tumoural transport processes using 3D volume imaging. Studies were performed using both Magnevist and the lower molecular weight GC agent to gain an appreciation of the effect of molecular weight on the tumoural delivery of materials and their subsequent transport. On a technical level the studies showed that the coil offered a 10 fold improvement in resolution compared to published studies for angiography and a 15 fold improvement for 3D volume imaging. Experimentally the results indicated that the initial delivery of the contrast agents was well correlated with blood supply and that the subsequent transport of these materials was primarily by diffusion and was limited by molecular weight.

Following imaging studies vascular corrosion casting was performed and novel MRI techniques were developed to analyse the resultant casts. These involved imaging the cast ‘in-situ’ in the tumour prior to tissue maceration and imaging the cast mounted in agarose gel following tissue maceration. The former technique appeared to show that it is possible to image the cast in this manner without loss of 3D structure and the latter gave a method to quickly and absolutely determine the tumour vascular volume.

Chapter One: Background

1.1 Cancer

1.1.1 Introduction

What follows is a brief overview of the biology of cancer, an outline of current and emerging cancer treatment strategies and a review of the present understanding of the tumoural barriers to the interstitial transport of macromolecules. These topics are included to set the scene for the subsequent discussion of the role of magnetic resonance imaging (MRI) in both the clinical and experiment settings of cancer diagnosis, treatment monitoring and novel therapy evaluation. Finally the relevance of the current work is explained in terms of commercially available MRI contrast agents and the state of the art in novel pre-clinical contrast agents.

1.1.2 Biology

Cancer is the general term for a class of more than 100 diseases that are characterised by uncontrolled, abnormal growth of cells. Normally cell division, proliferation and differentiation are strictly controlled and a balance exists between new cell formation and natural cell death. Cancer can be considered to be the result of a breakdown in this balance that leads to uncontrolled cell division (Argyle et al. 2008). Two categories of genes are acutely associated with cancer: oncogenes and tumour suppressor genes (Rang HP et al. 2003). Oncogenes are genes that when mutated or over-expressed contribute to the transition from normal to cancer cells. Cancer cells are engaged in uncontrolled mitosis (or division) and oncogenes are implicated in the over-production of proteins that signal for the cell to enter mitosis. Conversely mutations in tumour suppressor genes that reduce or destroy their function allow for cancer progression. Tumour suppressor genes would normally respond to DNA damage within a cell by signalling for the cell to arrest division and repair the DNA or

enter apoptosis (Kumar et al. 1998). This uncontrolled cell proliferation forms a collection of cells that are characterised by a loss of function and differentiation known as a primary tumour or neoplasm (Fukumura et al. 2007). For this collection of cells to grow beyond 100 μm in diameter the tumour requires its own vascular supply which is generated by a process known as angiogenesis (Padhani et al. 2001). Cancer cells can escape this primary tumour via the lymphatic system or blood supply and travel to another site where they form a secondary tumour or metastasis (Harrington 2008). Jain et al have described a solid tumour as an organ-like structure that consists of neoplastic cells and host stromal cells imbedded in an extracellular matrix and nourished by a blood supply (Fukumura et al. 2007).

1.1.3 Current Treatment Strategies

Statistically one in three people in the EU will develop cancer at one point in their life and one in four deaths in the EU are attributable to cancer (Albreht et al. 2008). Prognosis is dependant on the type of cancer and its level of progression; early detection and treatment offer the best clinical outcome with the ideal situation being identification of the primary tumour prior to metastasis and its removal by surgery (Kumar et al. 1998). Treatment of cancer following metastasis is significantly more difficult and associated with a poorer prognosis (Peake 2008). Surgery, in which the tumour mass and an amount of the surrounding healthy tissue are removed remains the first choice treatment in a number of cancers irrespective of stage. Surgery is now commonly given with an adjuvant therapy which may take the form of radiotherapy or chemotherapy (Parmar 2008). Radiotherapy involves delivering ionising radiation to tumour cells to cause DNA damage and ultimately cell death. Radiotherapy relies on the fact that the undifferentiated cancer cells divide more rapidly and do not have the same capacity for DNA repair as healthy differentiated cells (Robinson 2008).

The side-effects associated with radiotherapy depend on the dose and duration of the treatment, typically they include damage to epithelial surfaces (skin, mouth and bowel mucosa), fatigue and hair loss as well as making the patient more likely to suffer secondary cancers due to the exposure to ionising radiation (Robinson 2008; Warde 2008). Chemotherapy is the name given to the use of cytotoxic agents to kill cancer cells and can be used alone or as an adjuvant therapy to surgery or radiotherapy. Chemotherapy agents generally fall into one of the following categories; alkylating agents, platinum compounds (e.g. cisplatin), antimetabolities, anthracyclines (e.g. doxorubicin), topoisomerase inhibitors, tubulin binding drugs (e.g. paclitaxel) and tyrosine kinase inhibitors (Lind 2008). As with radiotherapy patients suffer as a result of the lack of specificity of chemotherapy drugs, which rely on having a greater effect on rapidly dividing cells. Side effects include bone marrow toxicity, immunosupression, hair loss, nausea and vomiting (Corrie 2008). More recent advances include biotherapy treatments such as hormone therapy and the use of immunological agents. Hormone therapy has been shown to be an effective and relatively side-effect free treatment for breast and prostrate cancers whose progression are linked with increased levels of oestrogen and testosterone and their receptors (Kumar et al. 1998). A number of treatments that aim to either reduce serum hormone levels or interfere with the hormone-receptor interaction are clinically available (Abraham et al. 2008). Unfortunately a number of these hormone treatments are associated with relapse (Abraham et al. 2008). Immunological agents aim to stimulate the body's own immune response to kill the cancer cells, for example monoclonal antibodies for antigens only found on cancer cells are delivered with the aim of alerting the immune system to the presence of the cancer cells (Rescigno et al. 2007). An antibody given alone is classed as naked, but it can also be conjugated to a

chemotherapy drug or radiation source to improve efficacy (Finn 2008). A clinically approved example of a naked monoclonal antibody therapy is rituximab which has a molecular weight of 145 kDa and is used in the treatment of lymphomas (Boyiadzis et al. 2008). Side-effects with these treatments are generally relatively mild such as rashes, fever and weakness (Finn 2008).

1.1.4 Emerging Therapies

An emerging class of cancer treatments are the DNA based biotherapeutics. They aim to modify the disease state by induction and/or inhibition of genes and include plasmids, oligonucleotides, aptomers, ribozymes, DNAzymes and small interfering RNAs (Patil et al. 2005). A biotherapy subset is gene therapy in which a gene is inserted into the cancer cell to replace one that has lost functionality. Naked DNA has a short plasma half life and so a number of methods have emerged that aim to protect the DNA and deliver it to the cancer cells following intravenous administration (Patil et al. 2005). These methods can be split into viral or non-viral delivery vectors. Non-viral systems include using cationic polymers and dendrimers conjugated to the DNA, giving an overall complex with a molecular weight of the order of kilo Daltons (Dufes et al. 2005).

1.1.5 Tumour Transport Barriers

Anti-cancer therapies that have appeared successful in-vitro frequently show far less success when they progress to human trials. It is commonly accepted that the complexity of the tumour itself plays a significant role in these failures (Cassidy et al. 2004). Intravenously delivered therapies have to travel in the blood stream to the site of the cancer cells, leave the blood vessels, negotiate the tumour interstitium to make contact with all the cancer cells. In addition to reaching the cancer cells the tumoural environmental conditions such as pH and oxygen level can play an

important role in the efficacy of the therapeutic. Furthermore the duration of the cellular exposure can be significant if the drug only acts in a certain phase of the cell cycle (el-Kareh et al. 1997). The tumour biology offers a number of barriers to the successful completion of these objectives, barriers which are particularly significant for macromolecular therapies such as gene and monoclonal antibody therapies (Dufes et al. 2005). However, a number of therapeutics rely on passively targeting tumours via the enhanced permeability and retention (EPR) effect, tumour blood vessels are known to be 'leaky' in comparison to normal vessels and this leakiness allows larger molecules to extravasate and collect in tumour tissue (Cassidy et al. 2004). It is thought that defective endothelial monolayers and openings between defective endothelial cells are the cause of this leakiness (Hashizume et al. 2000). Despite this advantage the most significant barrier to tumour treatment is the abnormal organisation, structure and function of the tumour vasculature (Cassidy et al. 2004). Blood supply is heterogeneous and often compromised making it difficult to deliver a therapeutic to the whole tumour, in addition the resultant regions of hypoxia and acidosis can limit efficacy of successfully delivered drug (el-Kareh et al. 1997). Furthermore enhanced vessel permeability coupled with the absence of a functional lymphatic system result in increased interstitial pressure in solid tumours (Fukumura et al. 2007), which compromises the delivery of therapeutics both across the vessel wall and in the interstitium. This effect has been shown to be particularly pronounced for macromolecules such as monoclonal antibodies (Jain et al. 1988).

1.2 Magnetic Resonance Imaging (MRI) and Cancer

1.2.1 Background

A more detailed description of the principles that underpin MRI are given in chapter four, for this section it suffices to say that MRI uses signals emitted from the hydrogen nuclei of the water in the body to generate images. The contrast in these MR images results from the difference in proton density and the longitudinal (T_1) and transverse (T_2) proton relaxation rates within the tissue of interest. MR images are described as being either proton density, T_1 or T_2 weighted depending on which of these differences dominates the image. Contrast agents are compounds that are used to improve image contrast and/or diagnose diseases, they are classified as either T_1 or T_2 agents depending on their primary effect. Contrast agents can then be further classified as extracellular, blood pool or tissue/organ specific. Generally T_1 positive contrast agents will be based on the paramagnetic ion gadolinium (further details of which can be found in chapter two) for this chapter it is sufficient to know that gadolinium alone is toxic and so it must be administered entrapped in a chelating agent. MRI scanners are generally referred to in terms of the strength of the magnetic field that they employ i.e 1.5T denotes a 1.5 Tesla magnetic field.

1.2.2 Clinical Use

MRI is used extensively in diagnosis and staging of diseases of the central nervous system (CNS) such as multiple sclerosis (Coles et al. 2004). In addition MRI and in particular dynamic contrast enhanced MRI (DCE-MRI) have revolutionised cancer investigation (Marcus et al. 2008). DCE-MRI comprises serial imaging in conjunction with the administration of a contrast agent, the subsequent analysis of the contrast agent ‘wash-in’ and ‘wash out’ characteristics allow tumour delineation and staging (Marcus et al. 2008). DCE-MRI use is commonplace in analysis of breast,

head and neck, prostrate and adrenal gland tumours (Padhani et al. 2001). Generally DCE-MRI uses T_1 weighted imaging with a low molecular weight T_1 positive contrast agent (a number of these contrast agents are licensed and details can be found 1.3) (Padhani 2002). Numerous new MRI applications are currently being investigated as a result of the increased clinical availability of 3T scanners. The higher field strength (traditional scanners are 1.5T) offers a higher signal to noise ratio allowing for more complex scanning and shorter acquisition times for existing sequences (Alvarez-Linera 2008). The majority of these emerging imaging techniques are for brain imaging and include diffusion and perfusion MRI, functional (fMRI) and magnetic resonance spectroscopy (MRS) (Alvarez-Linera 2008). Diffusion and perfusion MRI are used in stroke imaging to determine the levels of viable tissue that remain following a stroke (Blondin et al. 2008). fMRI is used to give an indirect indication of neural activity and so can be used to investigate diseases with neuro-degeneration or abnormality. Blood oxygen level dependent (BOLD) imaging is a type of fMRI that is based on the fact that haemoglobin has different magnetic properties depending on its oxygenation. Patients are serially scanned whilst hearing sounds, viewing images or performing simple tasks. Subsequent analysis of the data allows the areas of the brain involved in responding to the stimulus to be determined (Dickerson 2007). Magnetic resonance spectroscopy (MRS) is unique in that an image is not the output of the scanning. Like nuclear magnetic resonance (NMR) spectroscopy in chemistry, MRS generates a spectrum of chemical shifts for various substances such as water, choline, creatine, *N*-acetylaspartate (NAA) and lactate. The relative levels of these substances can be used to investigate various diseases such as cancer, epilepsy, Parkinson's disease and Huntington's disease (Rosen et al. 2007).

1.2.3 Experimental Use

1.2.3.1 General

MRI is used extensively in animal models to investigate the pathogenesis of various conditions and to support the pre-clinical development of novel therapies. The diversity of the type of imaging that is possible has made MRI particularly popular in cancer research: T_2 weighted imaging has been used for volumetric measurement of mouse models of prostrate cancer (Nastiuk et al. 2007), magnetic resonance angiography (MRA) has been used to investigate the vascular characteristics of spontaneous brain tumours in rats (Brubaker et al. 2005), T_1 weighted DCE-MRI has been used to investigate the interstitial fluid pressure distribution in tumours (Hassid et al. 2006) and diffusion imaging has been used to predict the outcome of various treatment protocols in mouse tumour models (Seierstad et al. 2007).

In addition there are a number of methods by which DCE-MRI data sets are analysed to yield descriptive information, such as the gadolinium uptake curves: the initial slope of the contrast uptake has been shown to be a measure of the response to anti-angiogenic treatment in mice (Muruganandham et al. 2006), and the area under the gadolinium concentration-time curve has been shown to be a useful biomarker for necrosis in a rat tumour model (Bradley et al. 2007).

1.2.3.2 Dynamic Contrast Enhanced Magnetic Resonance Imaging (DCE-MRI)

DCE-MRI has been widely investigated clinically in the detection and staging of diseases characterised by the prevalence of abnormal vasculature such as multiple sclerosis (Tofts et al. 1991) and cancer [particularly brain (Pauliah et al. 2007) and breast (Liney et al. 1999; Brown et al. 2000)]. DCE-MRI involves serial imaging of the tissue(s) of interest before and after the injection of a contrast agent, most commonly the low molecular weight substance Gd-DTPA (Magnevist). The first

such studies were performed in Japan in 1989 (Yoshida). In the following years a number of pharmacokinetic/physiological models emerged that were intended to elucidate biologically relevant parameters from the data. The models of Tofts and Kermode (1991) and Larsson et al (1990) were developed to analyse multiple sclerosis lesions in the brain and the model of Brix et al (1991) was developed to analyse data obtained for glioblastoma. The models were developed independently but are very similar having their theoretical basis in the work of Seymour Kety (1951; Kety 1960), an American neuroscientist who worked extensively in the field of schizophrenia including studies on the exchange of an inert gas within tissue to describe local blood flow. Kety (1951) indicated that the rate of transfer of an inert gas from the blood to tissue was directly proportional to the concentration difference between the blood and tissue (equation 1), based on Fick's law of diffusion. This principle was adapted to an MRI context by Tofts and Kermode (1991), and their approach is the most commonly used and is generally referred to as the Tofts model.

$$v_e \frac{dC_t(t)}{dt} = k^{trans}\left[C_p(t) - C_t(t)\right] \qquad \textbf{Equation One}$$

Equation one states that the rate of change of tissue contrast agent concentration is proportional to the concentration difference between the tissue (C_t) and plasma (C_p) (see appendix for further explanation) An attempt was made to harmonise the names and symbols used in kinetic analysis by Tofts et al (1999) and it was decided that the exact biological definition of the parameter k^{trans} depends on the conditions that are assumed in the tissue of interest. The transfer can either be assumed as flow (Kety) or permeability (Tofts) limited. In the permeability limited case the rate of extraction of tracer is small compared with the rate of replenishment via perfusion and k^{trans} is defined as the product of capillary wall permeability (P) and capillary wall surface area (S) per unit volume, $k^{trans}=PS\rho$ where ρ is the tissue density (g/ml). In the flow

limited case delivery of the tracer is insufficient and k^{trans} is defined as k^{trans}=Fρ(1-Hct) where F is the perfusion (ml blood per gram tissue per minute) and Hct is the hematocrit. To simplify this situation a generalised mixed perfusion and permeability limited regime was proposed (Tofts et al. 1999) in which:

$$k^{trans} = EF\rho(1-Hct) \qquad \text{where } E = 1 - e^{-\frac{PS}{F(1-Hct)}} \qquad \textbf{Equation Two}$$

where E is the tracer extraction fraction- the fraction of the tracer that is extracted from plasma to extra-vascular extra-cellular space (EES) in a single capillary bed transit.

This analysis returns the values k^{trans} and v_e (extravascular extracellular volume fraction), interpretation of the biological relevance of these parameters in the context of the experimental set-up is at the discretion of the user. Equations one and two show that k^{trans} is sensitive to changes in both the tissue perfusion and vessel permeability therefore care has to be taken assessing the significance of a change in k^{trans} to monitor the effect of drug treatment. It has been shown (Su 1994; Degani et al. 1997) that confounding results can be obtained for necrotic regions of tumours using this procedure as areas of necrosis have low blood flow and so give low k^{trans} values despite high intrinsic vessel permeability.

For this approach to hold two fundamental assumptions must be satisfied: compartment homogeneity and low tissue blood fraction. As the analysis is performed on a voxel by voxel (MRI volume element the 3D analogue of a pixel) basis the first of these assumptions is only valid if the spatial resolution is such that the tissue within each voxel is homogeneous. The second assumption would appear to exclude the use of this approach in those tumour studies in which vasularisation will be high. It has been shown (Buckley 2002) that increased tissue blood volume fraction has significant impact on the accuracy of the predicted parameters when

using the mixed model and only tissues with low blood volume return accurate values. Furthermore the quality of the results obtained from these approaches is determined by the quality of the input data. The plasma tracer concentration with time [$C_p(t)$, Arterial Input Function (A.I.F)] is an input to the model and is generally found in a separate study ignoring intra-animal variation which has been shown to be significant (Evelhoch 1999; Pickup et al. 2003).

A number of refinements have been made in attempts to improve the models' ability to cope with the pathology unique to tumours, these are discussed in the following section.

In order to counter the problems of high tissue blood fraction the model is refined to include an intravascular component [equation three (Tofts 2003)]. The equation now states that the overall tissue contrast comprises intravascular contrast plus the cumulative contrast that has leaked into the extravascular extracellular space over the time period t'.

$$C_t(t) = v_p C_p(t) + k_{trans} \int C_p(t') e^{-\left[\frac{k^{trans}(t-t')}{v_e}\right]} dt' \qquad \textbf{Equation Three}$$

This model returns values for k^{trans}, v_e and the plasma volume fraction v_p. Obviously the significance of the arterial input function is greatly increased in this adaptation with the associated problems mentioned previously.

A model that incorporates tracer diffusion between neighbouring regions has been developed (Pellerin et al. 2007). Each voxel exchanges tracer with the plasma following the Tofts approach but each voxel can also exchange with its immediate neighbours. Promising results have been obtained using this model for simulated data.

Another approach is to model the 'first pass' of the tracer in the capillary bed (Li et al. 2000). The first pass is described as the first couple of minutes of imaging post

contrast administration. The model (equation four) has the advantage of being simpler and only requiring 1-2 minutes of imaging but sacrifices estimation of v_e. Again the quality of the results obtained from this model have been shown to be limited by the pathology under investigation (Li et al. 2003) the values obtained are expected to be less relevant in highly permeable areas in which the extraction fraction is larger.

$$C_t(t) = v_p C_p(t) + K^{trans} \int C_P(t' dt') \qquad \textbf{Equation Four}$$

Finally a recent study (Lopata et al. 2007) has shown that this approach to DCE-MRI data analysis is not only limited by the pathology of tumour in which it is used but also by the experimental conditions. Using simulated data it was found that temporal resolution, signal to noise ratio and contrast injection rate had significant impact on the quality of the results obtained using the modified Tofts model (equation three).

Pathak (Pathak et al. 2005) developed a three compartment model specifically to analyse the transport of macromolecular blood pool tracers.

Analysis is split into two stages (early and late phase) and the model consists of the following three compartments:

(1) Intravascular Space

(2) Perivascular Space

(3) A more distance space in which slow macromolecular events occur

Tissue uptake of tracer is modelled as a linear function of time.

Early Phase (1)-(2) (0-30 minutes) tissue concentration [$C_{tissue}(t)$] found using equation five.

$$\frac{C_{tissue}(t)}{C_{blood}(t)} = \frac{\Delta R_{1tissue}(t)}{\Delta R_{1blood}(t)} = V_v + (PS)t \qquad \textbf{Equation Five}$$

Late Phase (2)-(3) (90-140 minutes) tissue concentration is found using equation six

$$\frac{C_{tissue}(t)}{C_{blood}(t)} = \frac{\Delta R_{1tissue}(t)}{\Delta R_{1blood}(t)} = \beta_2 + (FR)t \qquad \textbf{Equation Six}$$

where ΔR is the change in relaxation rate (an MRI property). The parameters returned are V_v the vascular volume fraction, *PS* the permeability surface area product and *FR* the flux rate (used to determine whether a voxel is draining or pooling contrast agent). This mathematical derivation of the model assumes that the removal of contrast agent from the vasculature to the tissue is insignificant and so the vascular tracer concentration can be taken as constant, however a study has shown (Pathak et al. 2004) that this may not be the case. Furthermore the long imaging duration required is technically challenging.

Examination of these approaches indicates that a balance exists between accurately representing the processes that occur within a tumour and the complexity of the model that emerges. Furthermore consideration must be given to the exact biological relevance of the parameters that emerge. However, these models are very useful as a means by which to reduce the huge volume of data that is obtained in a DCE-MRI experiment and allow for some comparison between tumours and before and after treatment.

1.3 Magnetic Resonance Imaging (MRI) Contrast Agents

1.3.1 Low Molecular Weight Extracellular Contrast Agents

For the purpose of this discussion extracellular contrast agents are taken as low molecular weight gadolinium chelates. They can be classified in terms of the nature of the chelating agent used: either cyclic or linear and in terms of the nature of the complex formed: either ionic or non-ionic. A number of extracellular agents are licensed for clinical use (Table 1.1, Figure 1.1); they are used in a variety of examinations such as multiple sclerosis diagnosis, breast cancer diagnosis and staging in diseases of the central nervous system (Coles et al. 2004). The first licensed, and still by far the most commonly used contrast agent is gadopentate dimeglumine which is marketed as Magnevist (Yan et al. 2007). It is commonly referred to as Gd-DTPA as it uses the chelating agent diethylene triamine pentaacetic acid (abbreviated to DTPA). In Gd-DTPA, Gd is coordinated with five carboxyl groups and three amino nitrogen groups leaving one coordination site for water. Three of the carboxyl groups are neutralised by the positive charges of Gd and the remaining two by meglumine cations (Morcos 2008). Two similar non-ionic derivates are commercially available, in these agents two of the DTPA carboxyl groups have been substituted giving diethylenetriamine pentaacetate-bis(methylamide) (generic name: Gadodiamine commercial name: Omniscan) and diethylenetriamine pentaacetic acid dimethoxyethylamide (generic name: gadoversetamide commercial name: Optimark) (Morcos 2008). The reduction in number of carboxyl groups reduces the stability of the chelate formed. Two other ionic linear contrast agents are marketed for use in liver imaging. Both are based on DTPA derivates with increased lipophilicity to promote weak, transient protein binding to increase plasma residence time and encourage hepatocyte uptake. They are gadobenate dimeglumine (Multihance) and

gadoxetate sodium (Primovist) (Yan et al. 2007). Three contrast agents based on the marcocyclic chelating agent tetraazacyclododecance tetraacetic acid (DOTA) are available. Macrocylic chelating agents form more stable complexes with gadolinium than linear chelates (table 1.1): for the complex to fail five coordination sites must be broken simultaneously whereas this can occur sequentially for linear chelating agents (Morcos 2008). The most straightforward of the DOTA complexes is Gd-DOTA which is marketed as Dotarem, the other DOTA based agents are Prohance (Gd-HP-DO3A) and Gadovist (Gd-BT-DO3A) in which one of the carboxyl groups of DOTA has been substituted by a hydroxypropyl and a dihydroxypropyl group respectively (Spinazzi et al. 1999).

Generic name	Brand name	Chelating agent	Chemistry	Dissociation half life (at pH 1.0)
Gadobenate dimeglumine	Multihance	BOPTA	Ionic linear	Not available
Gadobutrol	Gadovist	BT-DO3A	Non-ionic cyclic	24 hours
Gadodiamide	Omniscan	DTPA-BMA	Non-ionic linear	35 seconds
Gadopentetate dimeglumine	Magnevist	DTPA	Ionic linear	10 minutes
Gadoterate meglumine	Dotarem	DOTA	Ionic cyclic	>1 month
Gadoteridol	Prohance	HP-DO3A	Non-ionic cyclic	3 hours
Gadoversetamide	Optimark	DTPA-BMEA	Non-ionic linear	Not available

Table 1.1: Gadolinium based low molecular weight contrast agent summary(Morcos 2008)

The stability of gadolinium complexes has become more significant since the first reports of the link between gadolinium based contrast administration and the potentially fatal condition nephrogenic systemic fibrosis (NSF) in patients with severe renal insufficiency (Martin 2008). NSF is characterised by thickening and hardening of the skin which can progress to fibrosis of the organs resulting in severe disability and ultimately death (Martin 2008). The majority of the 190 reported cases of NSF can be attributed to the contrast agent Omniscan (>85%) with the other cases

attributed to Optimark (3-7%) and Magnevist (>1%) (Thomsen et al. 2008). As a result guidelines now state that the administration of these agents in patients with glomerular filtration rate <30 ml/min, those on dialysis and those who have had or are awaiting a liver transplant is contraindicated (Thomsen et al. 2008). It should be noted that the three contrast agents mentioned have the shortest dissociation times (table 1.1), this would appear to favour the use of the more stable macrocyclic chelating agents such as DOTA.

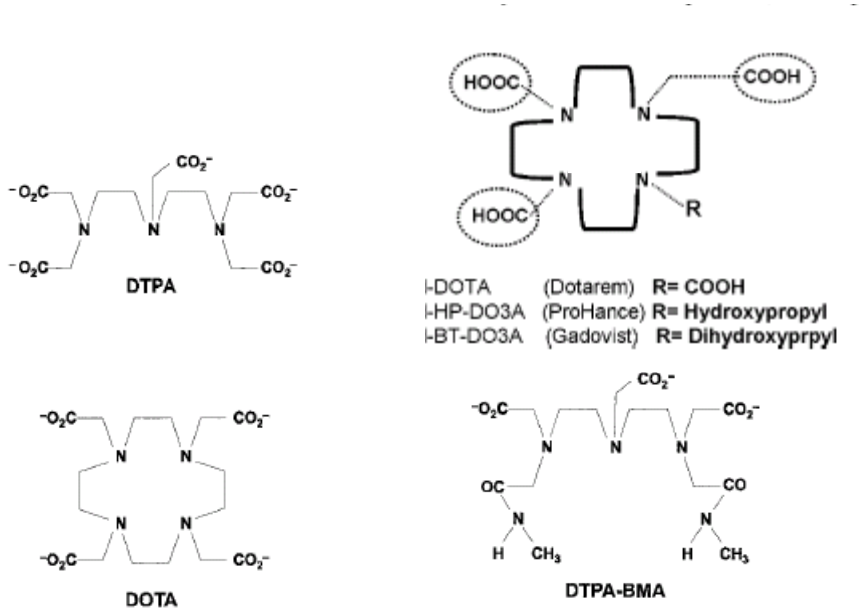

Figure 1.1: Chemical structures of various chelating agents (Morcos 2008)

1.3.2 Blood Pool Contrast Agents

The term blood pool contrast agent was coined in 2003 to describe albumin-(Gd-DTPA) a number of years after it was first synthesised (Daldrup-Link et al. 2003). Generally blood pool contrast agents are those which are designed to have increased plasma residence time compared with low molecular weight gadolinium chelates such as Gd-DTPA. The first blood pool agent was formed by the covalent attachment of albumin to Gd-DTPA and was created in response to the observation that Gd-DTPA alone was cleared too rapidly to provide information about blood volume and perfusion (Schmiedl et al. 1986). Subsequent studies showed that attachemnet of Gd-DTPA to human serum albumin resulted in a contrast agent with an average molecular weight of 92 kDa with an increased relativity and longer vascular enhancement that Gd-DTPA alone (Ogan et al. 1987). Relativity is defined as the reduction in T_1 time that a contrast agent provides per unit concentration of gadolinium. Early results indicated that the increased residence time of albumin-(Gd-DTPA) allowed grading of breast (Daldrup et al. 1998) and prostrate cancer models (Gossmann et al. 1999), characterisation of microvessels in breast cancer models (Turetschek et al. 2001) and facilitated the investigation of the use of vasodilators to improve cancer therapy outcome (Wang et al. 2001). However further development into human studies has been limited by biological problems; the poor clearance profile of the agent and the immunogenicity of albumin. It has been shown that the propensity of albumin to form aggregates can result in the compound remaining in the circulation for several weeks after administration which can lead to gadolinium accumulation in the liver and bone (Zhang et al. 2005). Contrast agent accumulation is to be avoided as over time there is the possibility of gadolinium liberation with the associated toxicity (Morcos 2008). However this agent is still used in experimental

models such as in the investigation of anti-angiogenic treatments (Daldrup-Link et al. 2004; Li et al. 2005; Wilmes et al. 2007) and in studies to model the transport of macromolecules in the tumour interstitium (Pathak et al. 2005).

To counter these problems Gd chelates with the capacity for reversible albumin binding were devised. MS-325 binds non-covalently to serum albumin via a lipophilic group (diphenylcyclohexyl) and is attached to Gd-DTPA via a phosphodiester linkage giving gadofosveset trisodium. MS-325 is administered in a free, low molecular weight (957 Da) state, subsequent serum albumin binding increases the molecular weight to 68 kDa (Barrett et al. 2006). The plasma half-life of MS-325 varies between species according to the affinity for albumin and is significantly shorter (25mins) in rats than rabbits (2-3hrs) (Parmelee et al. 1997). MS-325 was the first blood pool agent to be tested in humans (Grist et al. 1998) and progressed to phase two trials in 2001 (Bluemke et al. 2001). In both trials the agent was well tolerated and proved useful in carotid MR angiography. A large scale phase three study of 174 patients showed that MS-325 offered significant improvement in sensitivity, specificity and accuracy for the diagnosis of clinically significant stenosis compared with unenhanced imaging with no adverse effects reported (Goyen et al. 2005) and it has subsequently been licensed for use in cardiac imaging in the U.S.A., Canada and EU under the name Vasovist (Chiribiri et al. 2008). MS-325 has proved less useful in tumour imaging: it has been hypothesised that during the early phase prior to serum albumin binding extravastion of the low molecular weight precursor makes the derivation of functional parameters and tumour grading inaccurate. Studies have shown that there was no correlation between histology and MRI findings using MS-325 whereas significant correlation between histology and MR derived parameters was obtained using albumin-Gd-DTPA in a rodent breast cancer model

(Turetschek et al. 2001). The inaccuracies may have been due to the short plasma half-life in the animal model employed or the extravasation problem mentioned above. This also highlights how the investigation of the potential applications of this agent is limited by the intra-species variation in pharmacokinetics.

Following the discovery of the problems associated with clearance of albumin-(Gd-DTPA) dextran was proposed as a suitable backbone to which Gd-DTPA could be attached (Wang et al. 1990). To overcome the problems of clearance Gd-DTPA can be attached to the dextran with readily hydrolysable bonds, allowing breakdown in-vivo and elimination of the low molecular weight Gd-DTPA. The linkage can be tuned to give a balance between the desired plasma residence time for imaging whilst maintaining a relatively rapid clearance (Rongved et al. 1996). Additionally dextran has found more widespread use as a coating for iron oxide particles to mediate cellular uptake for use as T_2 contrast agents. Feridex is a dextran coated iron oxide nanoparticle formulation that has FDA approval for MRI of hepatic tumours, the particles are taken up by Kupffer cells found in healthy portions of liver but not in tumour tissue (Gandhi et al. 2006). Other agents based on the use of cleavable linkers to attach the imaging moiety to the macromolecular backbone are poly(L-glutamic acid) linked to gadolinium chelates via a biodegradable cystine linker in which the molecular weight of the PGA backbone can be used to give contrast agents with different pharmacokinetics (Lu et al. 2007). Although this approach improved the clearance relative to contrast agents of a similar molecular weight gadolinium was still detected in the liver, spleen, muscle and kidney 10 days after administration (Ke et al. 2006), however the accumulation in the liver, spleen and kidney was reduced by PEGylation (Mohs et al. 2007). A similar type of agent was synthesised by PEGylation of poly(L-Lysine) conjugated to Gd-DTPA giving a final product with a

molecular weight of 430 kDa. Excellent images of the vasculature of the rat brain were obtained but the long plasma half life (88 hours) and poor elimination profile (15% injected gadolinium dose remaining 12 days after injection) would appear prohibitive to human studies (Bogdanov et al. 1993). This agent has however been used in animal studies to visualise the effects of vascular disrupting agents in mice (Seshadri et al. 2007).

Liposomes have found use as liver imaging contrast agents. Liposomes are vesicles that consist of a lipid bilayer membrane with a hydrophilic interior, they have been investigated extensively in the drug delivery field as they can be used to encapsulate both hydrophobic drugs in the membrane and hydrophilic drugs in the core (Kim 2007). In MRI liposomes were initially investigated as a means of reducing the toxicity of manganese ions which had been conjugated to serum proteins (Navon et al. 1986). They were subsequently investigated as a means to target contrast material to the liver and spleen due to their reticulendothelial system (RES) uptake (Kabalka et al. 1987). More recent studies have focused on protecting the liposomes from RES uptake and modifying the membrane components to produce contrast agents with specific properties. Examples include using low density lipoproteins to target tumours for cellular uptake (Corbin et al. 2006), PEGylation to give a blood pool contrast agent (Weissig et al. 2000) or PEGylation of niosomes to avoid RES uptake and inclusion of surface glucose conjugates to target tumours via over-expressed receptors (Luciani et al. 2004). In these studies the chelated gadolinium was hydrophobically modified to allow encapsulation in the membrane. Similarly polymeric micelles have been developed that are passively targeted to tumours. These contrast agents are designed to have an initially low relaxivity (the contrast material is encapsulated in the hydrophobic core) which increases as the micelles

extravasate and are broken down in the tumour tissue. The breakdown of the micelle gives the contrast material greater access to water and so increases the relaxivity (Nakamura et al. 2006). These studies are at an early stage.

The well defined structure and consistency with which dendrimers can be produced coupled with their high surface functional group to mass ratio makes them attractive candidates for use in contrast agent synthesis (Barrett et al. 2006). A number of contrast agents based on various generations of polypropylenimine dendrimers (DAB) and polyamidoamine dendrimers (PAMAM) have been synthesised and tested in animal models by Kobayahi and co-workers. The higher generation dendrimer agents showed promise in imaging of tumour vasculature such as PAMAM generation 6 (Kobayashi et al. 2001) generation 7 and generation 8 (Kobayashi et al. 2001). Furthermore PAMAM generation 6 agents were shown to be useful as a predictor of the distribution of the macromolecular anti-caner drug Herceptin (Kobayashi et al. 2002) and PAMAM generation 8 agents were shown to be useful in the detection of the tumour vessel permeability changes in response to radiation treatment (Kobayashi et al. 2004). There has also been interest in the use of dendrimer based agents in kidney imaging with generation 3 DAB agents showing efficacy in diagnosing acute renal failure (Kobayashi et al. 2004) and generation 4 PAMAM agents used to detect renal tubular damage (Kobayashi et al. 2002). It is thought that the polyamine structure of these dendrimers facilitates their accumulation in the proximal straight tubules making detailed kidney imaging possible. The limiting factor in the use of dendrimer based agents is their poor total body clearance: 8% of the injected dose of DAB-16 agents and 80% of generation 4 PAMAM agents were retained in the body 48 hours after administration compared with >2% for Gd-DTPA (Kobayashi et al. 2003). Similar results have been obtained using generation 9 PAMAM dendrimers

conjugated to Gd-DOTA for which >60% of the injected dose was detected in the rat liver and spleen four days after injection (Bryant et al. 2002). However it has been shown that the covalent bonding of PEG to the remaining free surface amine groups of PAMAM dendrimers carrying Gd-DOTA significantly reduces the liver uptake of the agent (Margerum et al. 1997). There are concerns that the long-term accumulation of chelates could allow liberation of free gadolinium with the associated toxicity problems (Morcos 2008).

Another dendritic contrast agent that has been developed is Gadomer-17 (Schering AG, Germany). The central core is an aromatic ring, the first generation consists of three diethylenetriamine building blocks followed by two generations of 6 and 12 lysine residues respectively giving a final molecular weight of 17 kDa. The 24 amino groups of the 12 third generation residues are bonded to a macrocyclic gadolinium complex. Tested in rabbits, rats, dogs and monkeys Gadomer-17 was shown to remain intravascular with very low extravasation whilst maintaining a good elimination profile (>95% in 24 hours) (Misselwitz et al. 2001). Gadomer has found use in experimental determination of microvessel density (MVD) in breast cancer models (Orth et al. 2007) and measurement of various vascular parameters in spontaneous canine mammary tumours (Henderson et al. 2000). In addition studies have shown the efficacy of Gadomer in imaging of the coronary arteries in pigs (Li et al. 2001). Gadomer has now progressed to phase II clinical studies in humans where it has been used to evaluate the status of coronary arteries (Chiribiri et al. 2008).

Another approach is to use an intermediate molecular weight contrast agent to improve the plasma half-life whilst promoting rapid renal excretion, these are termed rapid clearance blood pool agents (RCBPA). Guerbet produce such an agent called P792 (Vistarem, Gadomeritol), which comprises Gd-DOTA substituted with four

hydrophilic arms to increase the molecular weight to 6.7 kDa. The structure of P792 means that is has an apparent hydrodynamic volume that is 125 times higher than Gd-DOTA (Port et al. 2001). P792 has found use in a number of applications such as coronary angiography in pigs (Dirksen et al. 2003), tumour characterisation in breast cancer models (Weidensteiner et al. 2006) and in the monitoring of radiotherapy-induced microvascular changes (Ceelen et al. 2006). Initial human trials showed that P792 was well tolerated (Gaillard et al. 2002) and it has progressed to phase II trials but no results have been reported as yet. Another intermediate molecular weight agent is based on a chitosan trimer derivativised with three Gd-DTPA pendant groups, giving a final molecular weight of 2158Da. The compound is named NMS60 and is manufactured by Nihon Medi-Physics Copmany, Japan. NMS60 has a higher relaxivity than Magnevist and has been shown to be of use in tumour imaging in rabbits (de Crespigny et al. 1999), the study of vascular stenosis in pigs (D'Arceuil et al. 2004), contrast enhanced angiography in dogs (Bammer et al. 2004), perfusion imaging of cerebral ischemia in non-human primates (Liu et al. 2005) and evaluation of acute myocardial ischemia in pigs (D'Arceuil et al. 2005). NMS60 has progressed to phase II clinical trials in humans in which it was well tolerated and efficacy in detection of brain tumours was shown (Ito et al. 2006).

Another approach at the early stages of research involves incorporating the chelating group within a copolymer rather than as pendant groups. These include poly-(Gd-DTPA)-co-(1,6-diaminohexane) a 19 kDa linear molecule named NC22181 that has been used to investigate barriers to tumoural transport of macromolecules (Bjornaes et al. 2001). A tartaric acid unit conjugated to DTPA forms the repeat unit of a copolymer (Lucas et al. 2008) that offers increased relaxivity compared with Magnevist but no in-vivo testing has been performed.

Plant extracts have been investigated as a means by which to target the liver for imaging including the use of arabinogalactan derivatives (Li et al. 2008) and panax quinquefolium derivates (Sun et al. 2003).

Other more radical approaches include the use of gadolinium complexes with polyoxometalates (POM) as targeted contrast materials. POMs are anionic clusters with frameworks built from transition metal anions with shared oxide ions that are used instead of traditional chelating agents. Increased relaxivities compared with Magnevist and evidence of liver and kidney specificity have been reported but investigations are at an early stage (Li et al. 2007).

Hyaluronan derivitised with DTPA has been synthesised and patented for use as a contrast agent (Winnik 1999; Gouin et al. 2001). High molecular weight hyaluronan was first coupled to ethylenediamine via an amide bond; one of the carboxyl groups on DTPA is then attached to the free amine group on the ethylenediamine, both steps use the carboxyl activating agent EDC. No reports of the use of this contrast agent in-vivo have been found. The further development of this agent may have been limited by purification issues associated with the use of EDC (Nakajima et al. 1995; Thompson et al. 2006) and the effect that using one of DTPA's carboxyl groups in bonding may have on the gadolinium chelating capability. This approach has however been used as a means by which to visualise hyaluonidase in vivo in tumour models (Shiftan et al. 2005). Hyaluronan-Gd-DTPA was synthesised as above and then attached to avidin-agarose beads, degradation of the hyaluronan by the enzyme hyaluronidase resulted in lower molecular weight fragments with higher relaxivity and thus the capability to detect hyaluonidase activity using MRI (Shiftan et al. 2005).

1.4 Overall Aims and Objectives

The overall aim of the current study is to synthesise, fully characterise and test in-vivo a number of macromolecular polymeric gadolinium based MRI contrast agents. Two different polymeric backbones will be used to which chelating pendant groups will be attached. The aim of the first group of agents, based on a glycol chitosan backbone, is to develop blood-pool contrast agents. The second type of agent will be based on a hyaluronic acid backbone with the potential to target tumours that over-express the CD44 cell surface receptor.

Glycol chitosan (GC) was chosen as a suitable candidate as it is biocompatible, contains a primary amine group which can be used in conjugation and it is possible to vary its molecular weight via acid degradation (Wang et al. 2001). A derivative of the chelating agent diethylene triamine pentaacetic acid (DTPA) that contains an isothiocyanate group will be attached to the backbone to allow the incorporation of gadolinium. The first step is to acid degrade high molecular weight GC and measure the molecular weight of a number of the resultant samples using gel permeation chromatography with multi angle laser light scattering (GPC-MALLS). Two samples will then be chosen with which to proceed with the DTPA attachment. The level of attachment will then be determined by NMR spectroscopy, elemental analysis and an arsenazo based colorimetric assay. Gadolinium will then be added to the conjugates and its levels determined using inductively coupled plasma atomic emission spectroscopy (ICP-AES).

To evaluate their suitability for use as blood pool contrast agents they will be tested by imaging of the mouse brain. A preliminary investigation into the clearance pattern of these agents will be conducted by imaging of the mouse kidney.

In the other strand of this research a hyaluronic acid (HA) based MRI contrast agent will be synthesised as a potentially tumour targeted agent. Hyaluronic acid was chosen as it is the substrate for the CD44 cell surface receptor which is over-expressed in a number of tumours (Zeng et al. 1998; Gotte et al. 2006; Konety 2006). The molecular weight of a purchased HA sample will be confirmed using GPC-MALLS. The proposed route of synthesis is to use the polypropylenimine hexadecaamine dendrimer generation 3.0 (DAB 16) as a linker between the HA backbone and DTPA functional groups. DAB was chosen as the linker due to its 16 primary amine groups and intrinsic anti-tumour activity (Dufes et al. 2005). Hyaluronic acid and DAB will be conjugated using a carboxylic acid activating agent and the conjugate characterised using elemental analysis, NMR spectroscopy, a TNBS based colorimetric assay and GPC-MALLS. A DTPA derivative containing an isothiocyanate group will then be attached to a proportion of the remaining DAB primary amine groups, and the level of attachment determined using elemental analysis and NMR spectroscopy. Gadolinium will then be added to the conjugates and its levels determined using plasma atomic emission spectroscopy.

Appendix: Tofts and Kermode Compartmental Model

The most commonly used compartmental model is that of Tofts and Kermode, which was developed to aid analysis of brain imaging data-sets. The compartments are as shown in figure A(1): plasma, extracellular space (whole body), the kidneys and a lesion compartment which is connected to the plasma via a leaky membrane. The lesion leakage space is defined as the brain extracellular space to which tracer would not normally have access i.e areas containing defective blood brain barrier.

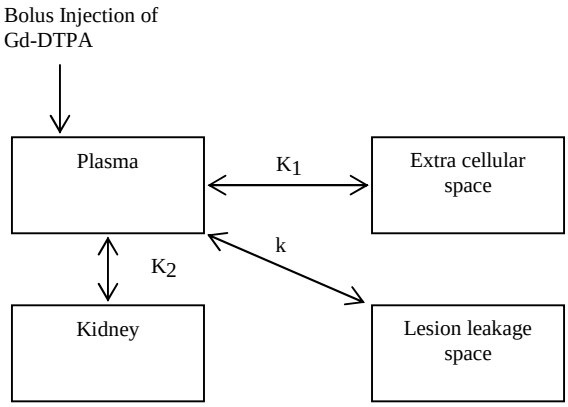

Figure A1: Schematic representation of Tofts model

The following equation relates the tracer concentration in the lesion (C_1) the plasma tracer concentration (C_p), the transfer coefficient (permeability surface area product per unit volume of tissue, k) and the fractional lesion volume (v_1):

$$v_1 \frac{dC_1}{dt} = k\left(C_p - C_1\right)$$

The plasma time concentration of tracer (AIF) is derived as a bi-exponential decay function. The exact function for the experimental set-up is found in a separate study.

Chapter Two: Synthesis and Characterisation Theory, Methods and Results

2.1 Introduction

2.1.1 Overview

Three gadolinium based polymeric T_1 magnetic resonance imaging (MRI) contrast agents were synthesised, two with glycol chitosan (GC) backbones and one with a hyaluronic acid (HA) backbone. As gadolinium ions are toxic they must be chelated for use in-vivo (Caravan et al. 1999), the most commonly used chelating agent is diethylenetriaminepentaacetic acid (DTPA). In these studies an activated DTPA derivative 2-(4-isothiocyanatobenzyl)-DTPA (p-SCN-Bn-DTPA) that contains a benzene ring and an isothiocyante group was used. p-SCN-Bn-DTPA was attached directly to the primary amine of the GC monomers and to HA using the polypropylenimine hexadecaamine dendrimer generation 3.0 (DAB Am-16) as a linker. HA and DAB were conjugated using the carboxylic acid activator 4-(4,6-dimethoxy-1,3,5-triazin-2-yl)-4-methyl-morpholinium chloride (DMT-MM).

2.1.2 Glycol Chitosan

Chitin is a naturally abundant long chain polymer of N-acteylglucosamine that forms the supporting material of invertebrates such as shellfish. Chitin's poor solubility is improved by N-deacetylation which forms chitosan which is soluble at conditions of pH<6.5 (Hyung Park et al. 2006). Chitin and chitosan are biocompatible and biodegradable which presents numerous potential biomedical applications e.g. in wound dressing material, as a drug delivery vehicle and as a candidate for use in tissue engineering (Khor et al. 2003). An aqueous soluble chitosan derivate glycol chitosan (GC) is formed by reacting chitosan with ethylene glycol. GC has found widespread experimental therapeutic use particularly when hydrophobically modified to allow drug encapsulation (Uchegbu et al. 2001; Martin et al. 2002; Qu et al. 2006;

Hwang et al. 2008; Kim et al. 2008; Min et al. 2008). Acid degradation of GC allows lower molecular weights to be generated whilst maintaining the primary amine functional group on the monomer. The degree of depolymerisation and final molecular weight can be controlled by the degradation time (Wang et al. 2001).

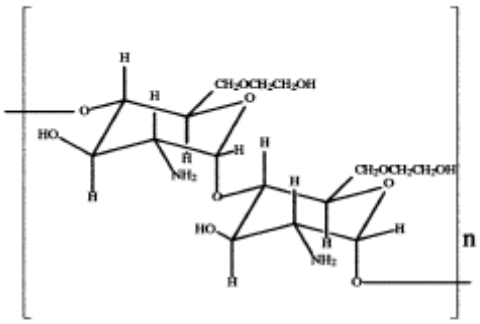

Figure 2.1 Glycol chitosan structure two monomers shown (Uchegbu et al 2001)

2.1.3 Gadolinium

The signal intensity in MRI is dependent on the proton relaxation rate, either the T_1 or T_2 relaxation rate depending on the imaging protocol employed (Merbach et al. 2001). Contrast agents containing gadolinium (III) or iron oxide are used to influence the relaxation rates in T_1 and T_2 imaging respectively (Merbach et al. 2001). Gadolinium (III) is used in this setting as it the most paramagnetic stable metal ion due to its seven unpaired electrons (Caravan et al. 1999). Paramagnetic materials have a magnetic moment that aligns with an externally applied magnetic field making them useful as MRI contrast agents. In solution there is a dipolar magnetic interaction between the electronic magnetic moment of the paramagnetic ion and the much smaller magnetic moment of the protons of nearby water molecules (Caravan et al. 1999). Random fluctuations in this dipolar magnetic interaction as the result of molecular motion reduce the T_1 relaxation time of the water protons. However, gadolinium is toxic as it

has a size similar to calcium (II) but a higher charge allowing it to disrupt critical Ca(II) mediated signalling (Caravan et al. 1999). To counter this problem gadolinium is administered in a chelated form and the most commonly used chelating agent is diethylene triamine pentaacetic acid (DTPA) (Caravan et al. 1999). The process of chelation eliminates the toxicity by both reducing the charge and increasing the molecular weight. The gadolinium ion becomes 'entrapped' in the chelating agent via interactions between the unpaired electrons and the carboxylic acid groups of the DTPA (Morcos 2008).

2.1.4 p-SCN-Bn-DTPA

A DTPA derivative 2-(4-isothiocyanatobenzyl)-DTPA (p-SCN-Bn-DTPA) that contains a benzene ring and an isothiocyante group to allow conjugation to primary amine groups (figure 2.2) is used in these studies.

Figure 2.2: Reaction of a primary amine with an isothiocyanate (Invitrogen)

2.1.5 Hyaluronic Acid

In 1934 Meyer and Palmer isolated a novel glycolsamino glycan (GAG) from the vitreous body of bovine eyes that was composed of a uronic acid and an amino sugar but no sulfoesters (Meyer et al. 1934). They named the compound hyaluronic acid from a combination of hyaloid (vitrous) and uronic acid, over time the material has additionally become known as hyaluronan. Specifically hyaluronic acid (HA) is a negatively charged high molecular weight (millions of Daltons) linear polysaccharide formed from disaccharide units comprising n-acteyl-D-glucosamine and glucoronic acid (figure 2.3). It is found in the connective tissue, vitreous and synovial fluids of

mammals. In clinical medicine it is used as a diagnostic marker for many diseases including cancer, rheumatoid arthritis and liver pathologies as well as for the supplementation of impaired synovial fluid in arthritis sufferers by means of injection (Kogan et al. 2007). It is also used in ophthalmic surgery and cosmetic regeneration (Kogan et al. 2007).

HA is synthesised at the inner face of the plasma membrane in a process catalysed by the enzyme HA synthases (HAS) and is extruded whilst still elongating into the extracellular matrix (ECM) (Yamada et al. 2005). For experimental use HA can be extracted from a number of animal sources such as rooster comb, bovine vitreous and human umbilical cord (Kogan et al. 2007). Bacteria such as streptococci also naturally synthesise HA as an extracellular capsule (Yamada et al. 2005). The HA used in these studies was produced by Lifecore Biomedical U.S.A. using a microbial fermentation process.

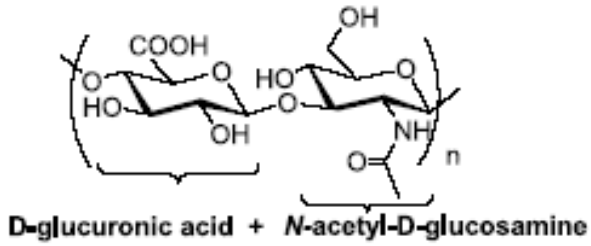

Figure 2.3: Hyaluronic acid structure (Jaracz et al. 2005)

HA has a high turnover rate in vivo with hyaluronidase enzymes catalysing its breakdown (Stern et al. 2007). HA has a number of functions such as in the macrostructure forming the basic unit of cartilage and serving as a lubricant in synovial fluid, on a cellular level it is involved in the promotion of cell proliferation and migration both during embryogenesis and in adult life (Sherman et al. 1994). The

function of HA is molecular weight dependent (Table 2.1) with different molecular weights often having directly opposite effects (Stern et al. 2006). HA interacts with the family of cell surface receptors that include CD44 and RHAMM. For this reason HA is of particular relevance in the field of cancer as the over expression of CD44 and RHAMM and their isoforms have been implicated in tumour growth and metastasis for lymphoma, melanoma and pancreatic cancers (Zeng et al. 1998), breast cancer (Gotte et al. 2006) and bladder cancer (Konety 2006). Normally cells express CD44 in a low affinity state and can only bind HA in response to cellular cues such as from cytokines released in response to environmental factors (Cichy et al. 2003). It is thought that in contrast tumour cells express CD44 isoforms that are permanently in a high affinity state which allows constitutive binding (Cichy et al. 2003). It has been postulated that HA can play a dual molecular weight dependant role in tumour angiogenesis and hence tumour growth (Rooney et al. 1995). High molecular weight HA is thought to attract progenitor cells to sites of differentiation whilst low molecular weight breakdown fragments stimulate angiogenesis. Specifically it has been widely shown that HA oligosaccharides of a specific length (3-10 disaccharide units) simulate vascular endothelial cell proliferation, migration, collagen synthesis, sprout formation and angiogenesis in vitro and in vivo (Slevin et al. 2007). It has also been postulated that high molecular weight HA provides a loose matrix to assist migrating tumour cells and mediate cancer cell adhesion (Fjeldstad et al. 2005).

This seemingly crucial role in cancer progression and the targeting capabilities due to receptor over-expression have seen HA widely investigated as both a targeting moiety and as a target for therapy (Jaracz et al. 2005).

Size (saccharides)	Function
High-molecular-mass HA>1000-5000	Suppression of angiogenesis Immune suppression Inhibition of phagocytosis Suppression of HA synthesis
~1000	Induction of inflammatory chemokines Stimulation of PAI-1 Stimulation of urokinase
10-40	Induction of CD44 cleavage Promotion of tumour cell migration
8-32	Stimulation of angiogenesis Stimulation of tumour neovascularisation
~15	Suppression of smooth muscle proliferation
12	Endothelial cell differentiation Up-regulation of PTEN in tumour cells
10	Displacement of matrix HA on ooctye surface Displacement of proteoglycans from cell surface
6	Suppression of HA cable formation Induction of NO and MMPs in chondrocytes
4-6	Induction of cytokine synthesis in dendritic cells

Table 2.1: Summary of molecular weight dependent function of hyaluronic acid (Sherman et al. 1994)

In these studies it was decided to use HA fragments greater than ten disaccharides in length as to avoid the potential problems of angiogenesis.

2.1.6 Polypropylenimine Hexadecaamine Dendrimer Generation 3.0 (DAB 16)

Dendrimers are monodisperse macromolecules with a regular and highly branched three-dimensional structure (in fact the name dendrimer comes from the Greek dendron which means tree). The well defined architecture and a high ratio of multivalent surface moieties to molecular volume make dendrimers highly interesting as nanomedicine components (Dufes et al. 2005). Dendrimers consist of a central core molecule from which a number of 'arms' emanate in an ordered and symmetrical fashion (figure 2.4). Each layer of arms is designated as a generation with the core as generation zero.

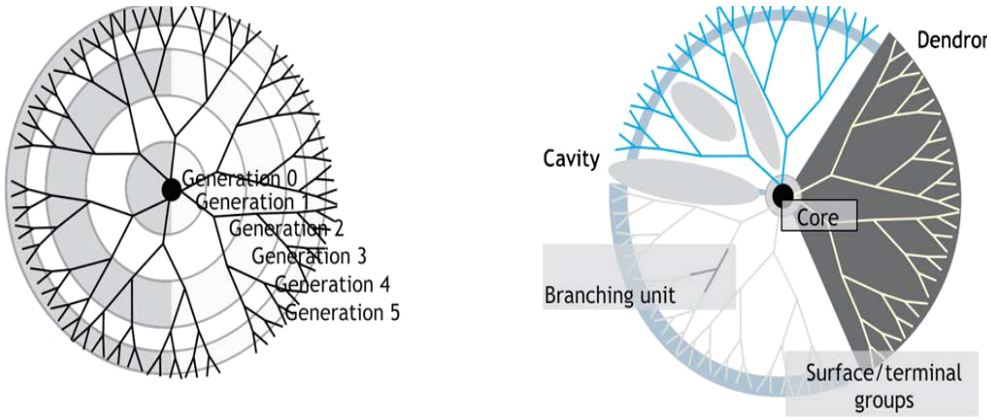

Figure 2.4: Dendrimer architecture (Dufes et al. 2005)

The two most commonly used dendrimers are the polyamidoamine (PAMAM) and polypropylenimine (DAB) dendrimers. PAMAM dendrimers have either an ammonia or ethylenediamine (EDA) core to which methylacrylate is added followed by amidation with ethylenediamine. This synthesis method can give rise to half or full generations, half generations have terminal anionic carboxylate groups and full generations have terminal amine groups (Dufes et al. 2005). DAB dendrimers have a butylenediamine core and poly(propylenime) (PPI) units. The synthesis reaction is based on the Michael addition of acrylnitrile to a primary amino group followed by hyrogenation of nitrile groups to primary amino groups (Klajnert et al. 2001). DAB

dendrimers have terminal primary amine groups and are often described by the number of these groups e.g. DAB-16 has 16 terminal amine groups per molecule. Dendrimers have found widespread biomedical use; in gene therapy non-viral vectors (Dufes et al. 2005), as the basis for MRI contrast agents (Kobayashi et al. 2005) and as carriers in cancer drug delivery (Zamboni 2008). It has also been shown that DAB-16 has intrinsic anti-tumour activity making it an attractive candidate for use in cancer targeted therapies (Dufes et al. 2005). The structure of dendrimers mean that they are useful as components in multifunctional assemblies as the multitude of surface functional groups allow both targeting and active moieties to be attached (Agarwal et al. 2008). It is in such a capacity that DAB-16 is used in these studies as a linker between the tumour targeting moiety hyaluronic acid and an MRI imaging moiety. DAB 16's intrinsic activity as an anti-tumour agent also means that a hyaluronic acid-DAB conjugate with an MR imaging moiety could serve as a targeted theragnostic (combined diagnostic and therapeutic agent).

2.1.7 4-(4,6-dimethoxy-1,3,5-triazin-2-yl)-4-methyl-morpholinium chloride (DMT-MM)

In order to form an amide bond between HA and DAB it is necessary to use a carboxylic acid activating agent and HA dictates that this activator must be water soluble. The most commonly used water soluble amide coupling agents are the carbodiimides such as 1-ethyl-3-(3-dimethylaminopropyl) carbodiimide (EDAC) but they have a number of disadvantages; their optimal conditions are pH 4-5 at which the amine is protonated and unreactive and the activated intermediate has a short half life and is rapidly hydrolysed resulting in unpredictable and low yields (Thompson et al. 2006). To counter these problems EDAC is generally used in a large molar excess, however it has been shown that a very stable and unreactive by-product is formed

between the carboxylic acid group and EDAC under these conditions (Nakajima et al. 1995). The formation of this n-acylurea by-product not only limits the production of the amide but also makes purification and further analysis extremely difficult. A new class of carboxylic acid activator has recently been developed that allows coupling in both aqueous and organic media, 4-(4,6-dimethoxy-1,3,5-triazin-2-yl)-4-methyl-morpholinium chloride (DMT-MM) is formed by the coupling of 2-chloro-4,6-dimethoxy-1,3,5-triazine (CDMT) and n-methylmorpholine (NMM) in THF (Kunishima et al. 1999). DMT-MM has been shown to give high amide yield in a number of different reaction conditions (Kunishima et al. 2001) and specifically with polysaccharides (Farkas et al. 2007). The treatment of a carboxylate anion with DMT-MM forms a 2-ayloxy-4,6-dimethoxy-1,3,5-triazine intermediate which reacts with the amine to form the amide with NMM.HCl and 2-hydroxy-4,6-dimethoxy-1,3,5-triazine as by-products which can be removed by dialysis (Thompson et al. 2006). The reaction scheme is shown in detail in figure 2.5 (Kunishima et al. 1999), the carboxyl (1) and amine (2) are mixed forming ammonium carboxylate (6) which reacts with DMT-MM to form an activated ester (5) which can react with the amine (2) to form the amide (3).

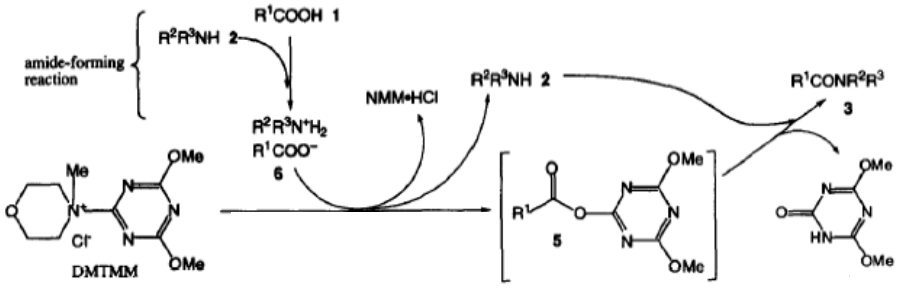

Figure 2.5: Amide formation using DTM-MM (Kunishima et al. 1999)

2.2 Aims and Objectives

2.2.1 GC-DTPA-Gd

The aim of this section of work was to synthesise and fully characterise two polymeric gadolinium-based blood pool T_1 MRI contrast agents. Firstly the molecular weight of glycol chitosan was reduced by acid degradation following the method of Wang et al (2001). The molecular weights of the resultant products were determined by gel permeation chromatography with multi angle laser light scattering (GPC-MALLS). Two different molecular weight degraded GC samples were then conjugated to a reactive DTPA derivative, via a reaction between the primary amine on GC and an isothiocyanate group on the DTPA. DTPA attachment was confirmed by nuclear magnetic resonance (NMR) spectroscopy and its level determined via elemental analysis and a colorimetric assay. The GC-DTPA conjugates were then incubated with gadolinium to produce T_1 contrast agents. Gadolinium content was analysed using inductively coupled plasma atomic emission spectroscopy (ICP-AES).

2.2.2 HA-DAB-DTPA-Gd

The aim of this section of work was to synthesise and fully characterise a tumour targeted T_1 MRI contrast agent. The molecular weight of a purchased hyaluronic acid (HA) sample was confirmed by GPC-MALLS. HA was then conjugated to a polypropylenimine hexadecamine generation 3.0 dendrimer containing 16 terminal primary amine functional groups (DAB 16) using the carboxylic acid activator 4-(4,6-dimethoxy-1,3,5-triazin-2-yl)-4-methylmorpholinium chloride (DMT-MM).

Conjugation was confirmed using NMR spectroscopy and the composition of the conjugate was determined using elemental analysis, a colorimetric assay and GPC-MALLS. DTPA was attached to some of the remaining free primary amine groups and the level of attachment was determined using NMR spectroscopy and elemental

analysis. The HA-DAB-DTPA conjugates were then incubated with gadolinium to produce a T_1 contrast agent. Gadolinium content was analysed using inductively coupled plasma atomic emission spectroscopy (ICP-AES).

2.3 Materials

2.3.1 GC-DTPA-Gd

Item	Abbreviation	Supplier
Glycol Chitosan deacetylated Lot: GC-105K1648	GC	Sigma Aldrich, U.K.
Gadolinium (III) Chloride Hexahydrate	Gd	Sigma Aldrich, U.K.
2-(4-isothiocyanatobenzyl) diethylenetriaminepentaacetic acid	p-SCN-Bn-DTPA	Macrocyclics, U.S.A.
Glacial Acetic Acid		Sigma Aldrich, U.K.
Sodium Acetate		Sigma Aldrich, U.K.
Deuterium Oxide	D_20	Sigma Aldrich, U.K.
Sodium Hydroxide	NaOH	Sigma Aldrich, U.K.
Imidazole		Sigma Aldrich, U.K.
Monosodium phosphate		Sigma Aldrich, U.K.
Disodium phosphate		Sigma Aldrich, U.K.

2.3.2 HA-DAB-DTPA-Gd

Item	Abbreviation	Supplier
Hyaluronic Acid	HA	Lifecore Biomedical, U.S.A.
Polypropylenimine hexadecaamine dendrimer generation 3.0	DAB	Sigma Aldrich, U.K.
4-(4,6-dimethoxy-1,3,5-triazin-2-yl)-4-methylmorpholinium chloride	DMT-MM	Sigma Aldrich, U.K.
Ammonia solution (35 % NH_3 0.88 S.G.)		Fisher Scientific, U.K.
2-(4-isothiocyanatobenzyl)-diethylenetriaminepentaacetic acid	p-SCN-Bn-DTPA	Macrocyclics, U.S.A.
Sodium hydroxide	NaOH	Sigma Aldrich, U.K.
Phosphate buffered saline tablets	PBS	Sigma Aldrich, U.K.
Gadolinium (III) chloride hexahydrate	Gd	Sigma Aldrich, U.K.
Picrylsulfonic acid solution 5% (w/v)	TNBS	Sigma Aldrich, U.K.
Sodium tetraborate		Sigma Aldrich, U.K.

2.4 Synthesis and Characterisation Methods

2.4.1 Synthesis Protocols

2.4.1.1 GC-DTPA-Gd

2.4.1.1.1GC Degradation

Glycol chitosan (2.00g, 9.75mmol) was dissolved in hydrochloric acid (4M, 150ml) with stirring and then placed in a water bath at 50°C with shaking. After incubation for 2 hours (GC2) or 48 hours (GC48) the samples were removed and allowed to cool to room temperature. After cooling the mixture was filtered and the filtrate dialysed against water (MW cut off 12-14 kDa, 5L, 6 changes in 24 hours). The product GC2/GC48 was obtained by freeze-drying.

2.4.1.1.2 GC-DTPA Conjugation

GC2/GC48 (205mg, 1.0mmol) was dissolved in PBS (pH=7.4, 20mls) with stirring. p-SCN-Bn-DTPA (325mg, 0.5mmol) was dissolved in PBS (pH=7.4, 100mls) with stirring. The solutions were mixed and pH adjusted to pH=8 using NaOH (1M) and then stirred overnight at room temperature. The reaction mixture was dialysed against water (MW cut off 3.5kDa, 5L, 6 changes in 24 hours). A white/yellow product (GC2-DTPA/GC48-DTPA) was obtained by freeze-drying.

2.4.1.1.3 GC-DTPA Gd Addition

GC2-DTPA/GC48-DTPA (275mg) was dissolved in imidazole buffer (pH=6.8, 150mls). Gadolinium (200mg, 0.5mmol) dissolved in imidazole buffer (pH=6.8, 200mls). The solutions were mixed and stirred overnight at room temperature, during which time a precipitate (GC-DTPA-Gd) formed. Phosphate buffer (pH=7, 200mls) added to reaction mixture to re-dissolve GC-DTPA-Gd and precipitate excess gadolinium. The solution was filtered (0.45μm) to remove precipitated gadolinium and dialysed against water (MW cut off 3.5kDa, 5L, 6 changes in 24 hours) to remove

buffers. The product (GC2-DTPA-Gd/GC48-DTPA-Gd) was obtained by freeze-drying.

2.4.1.2 HA-DAB-DTPA-Gd

2.4.1.2.1HA-DAB Conjugation

HA (300mg, 0.8mmol) was dissolved in water (50mls), DAB Am-16 (1333.5mg, 0.8mmol) was dissolved in water (200mls) and the solutions mixed and stirred at room temperature for 15 minutes. DMT-MM (586mg, 2.0mmol) was dissolved in water (50mls) and added to the HA, DAB mixture. The solution was stirred overnight at room temperature. The reaction mixture was dialysed against 5% v/v ammonia solution (12-14kDa MW cut off, 18 changes, 72 hours). A white cotton wool like product (HA-DAB) was recovered by freeze-drying.

2.4.1.2.2 HA-DAB-DTPA Conjugation

HA-DAB (120mg) was dissolved in PBS (pH=7.4, 200mls), p-SCN-Bn-DTPA (120mg, 0.19mmol) was dissolved in PBS (pH=7.4,100mls). The solutions were mixed and the pH adjusted to pH=8 with NaOH (1M). The reaction mixture was stirred overnight at room temperature followed by dialysis against 5% v/v ammonia solution (12-14 kDa MW cut off, 18 changes, 72 hours). A white/yellow product (HA-DAB-DTPA) was recovered by freeze-drying.

2.4.1.2.3 HA-DAB-DTPA-Gd Addition

HA-DAB-DTPA (100mg) was dissolved in water (200mls). Gadolinium Chloride (60mg, 0.16 mmol) was dissolved in water (100mls) and the solutions were mixed and stirred overnight at room temperature. The reaction mixture was dialysed against water (12-14 kDa MW cut off, 12 changes, 48 hours). A shiny white product (HA-DAB-DTPA-Gd) was recovered by freeze-drying.

2.4.2 Characterisation Theory

2.4.2.1Nuclear Magnetic Resonance (NMR) Spectroscopy

Nuclear magnetic resonance (NMR) spectroscopy is a non-destructive method used for compound identification and structural determination that is based on the behaviour of atomic nuclei in the presence of an applied magnetic field (Jacobsen 2007). The most useful nuclei for this technique are those with the quantum mechanical property of spin values of ½ such as the isotopes ^{13}C and ^{1}H (Williams et al. 1995). These nuclei can only adopt one of two spin states when placed in a magnetic field: spin up (low energy) or spin down (high energy) (Williams et al. 1995). When placed in a magnetic field slightly more than half will adopt the low energy state at any one time and to move between energy states nuclei must either release or absorb a specific amount of energy equal to the gap between the low and high energy states (Jacobsen 2007). This energy corresponds to a specific frequency of electromagnetic radiation that is proportional to the magnetic field experienced by the nucleus and is known as its resonant frequency. The various nuclei of a compound will have slightly different resonant frequencies as they experience slightly different magnetic fields due to interactions with their neighbours. Samples in solution are placed in a strong magnetic field and a radio frequency pulse which contains a range of frequencies is applied (Jacobsen 2007). Some of the nuclei that resonate at a frequency in the range of the pulse will be temporarily flipped to the high energy state before re-releasing this energy as they relax back to their original state. The system detects this released energy as a free induction decay (FID) signal which contains information from all the nuclei that have relaxed back to the low energy state (Jacobsen 2007). A mathematical operation called a Fourier Transform (FT) is then used to split this signal into peaks at various frequencies. The position of

a peak is given as a shift of a particular p.p.m value (parts per million of the applied field) and its area is proportional to the number of contributing protons (Jacobsen 2007). The position of the peaks can be equated to particular chemical groups using reference tables (Williams et al. 1995). Various types of NMR experiment are possible depending on how the sample is excited and how the data is presented and analysed. The two techniques used here are ^{1}H and Correlation Spectroscopy (COSY). ^{1}H allows the types of hydrogen (methyl, methylene, etc) in the sample and their chemical environment to be determined. COSY is a two dimensional technique that shows the interactions between protons bonded to neighbouring atoms. The solvents used in NMR are deuterated i.e. contain the deuterium (^{2}H) hydrogen isotope. In the experiments in this study deuterium oxide (D_2O) or 'heavy water' was used. Deuterium has similar chemical properties the ^{1}H isotope but has a spin value of 1 meaning that it behaves differently in a magnetic field. This is particularly useful in NMR as it reduces the potential for solvent-sample signal interactions (Williams et al. 1995).

2.4.2.2 Elemental Analysis

Elemental Analysis allows the relative abundance of the major elements present in an organic compound to be determined (Dean 1995). Elemental analysis systems are based on the principle of combustion of the sample in an environment of excess oxygen and catalysts and subsequent analysis of the gases generated. Systems differ in the way in which they separate and analyse the combustion products. The system employed here uses gas chromatography with helium as a carrier for separation and a thermal conductivity detector for quantification. The sample is introduced into a combustion area in tin foil and burned in an oxygen rich environment that also contains substances that aid complete combustion such as quartz wool, electrolytic

copper and copper oxide. The resultant mixture of combustion gases is passed through a gas chromatography column, the constituent gases are impeded to varying degrees by their interactions with the column surface coatings. The output chromatogram has peaks at various time points (figure 2.6) that represent detection of the different gases; carbon dioxide, water, nitrogen and sulphur dioxide. The relative abundance of the elements (carbon, nitrogen, hydrogen and sulphur) is found from the peak areas.

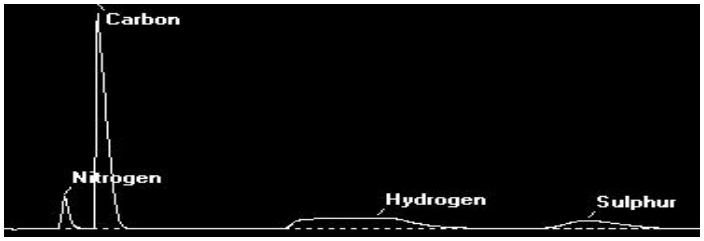

Figure 2.6: Example of chromatogram output of elemental analysis (Dean 1995)

2.4.2.3 2,4,6-trinitrobenzenesulfonic acid (TNBS) Assay

The use of 2,4,6-trinitrobenzenesulfonic acid (TNBS) as a reagent to determine the concentration of amino groups in proteins and peptides was established in 1960 (Satake et al. 1960). The assay procedure was modified to allow the determination of amines, amino acids and proteins in mixtures (Mokrasch 1970) and Snyder and Sobocinski found that the assay could be simplified without loss of sensitivity by removal of the quenching step (Snyder et al. 1975). The assay is based on a trinitrobenzoylation reaction (figure 2.7) in which at pH greater than 7 a highly chromogenic trinitrophenyl derivate is formed following the reaction of primary amines with TNBS, a reaction which proceeds rapidly and is considered complete after 30 minutes. The absorbance at 340 or 420nm is proportional to the amine

concentration in the sample. After calibration using various concentrations of amine the level of amine in an unknown sample can be determined.

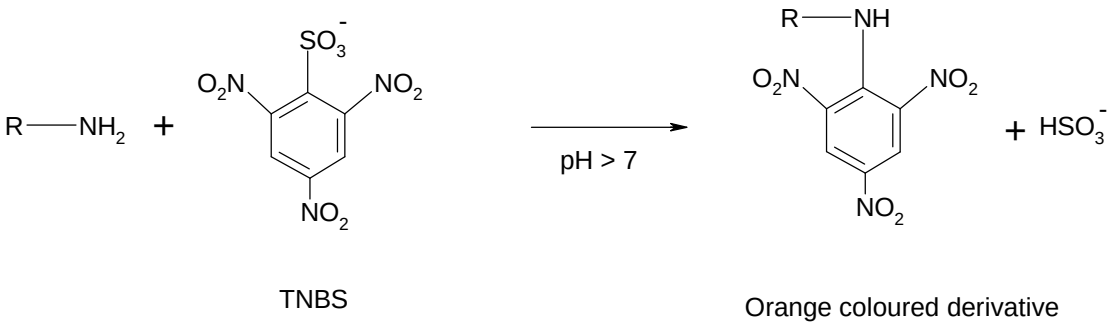

Figure 2.7: TNBS reaction scheme (Work et al. 1976)

2.4.2.4 Gel Permeation Chromatography Multi Angle Laser Light Scattering

Gel permeation chromatography with multi angle laser light scattering (GPC-MALLS) is an analytical technique that can be used to determine absolutely the size and molar mass of macromolecules in solution (Wyatt 1993). The principle of light scattering is that some of a light source that passes through a solution will be scattered by solute particles in a process known as Rayleigh scattering. The intensity of light that is scattered is related to the molar mass and concentration of solute and the angular variation of the scattered light is related to solute molecular size. Experimentally a laser light source is used with a number of detectors placed at various angles to the beam to measure the scattered light. Gel permeation chromatography (GPC) allows characterisation of polydisperse samples, species are separated based on their hydrodynamic size by passing them through a column packed with porous media. The largest molecules leave the column first as they cannot diffuse into the pores of the packing material whereas smaller molecules diffuse in and out of the pores and their transit is delayed. Each eluting fraction can then be

classified by light scattering. Weighted average values of molar mass and size for the polydisperse sample are found using a differential refractive index (DRI) detector to measure the concentration of each fraction. The DRI system contains a cell in which the sample flows in parallel to a reference channel of solvent alone, light is shone through the two columns and its intensity measured. This value can be converted into a concentration using the refractive index increment with concentration (dn/dc) value of the sample that had been determined in an ancillary experiment. A pump is used to constantly elute the system with the mobile phase. The sample is generally injected into the system using an autosampler, the mobile phase then carries the sample through a column where is separated based on hydrodynamic radius, each fraction then passes through the LS and DRI detectors in series before passing to waste (Figure 2.8).

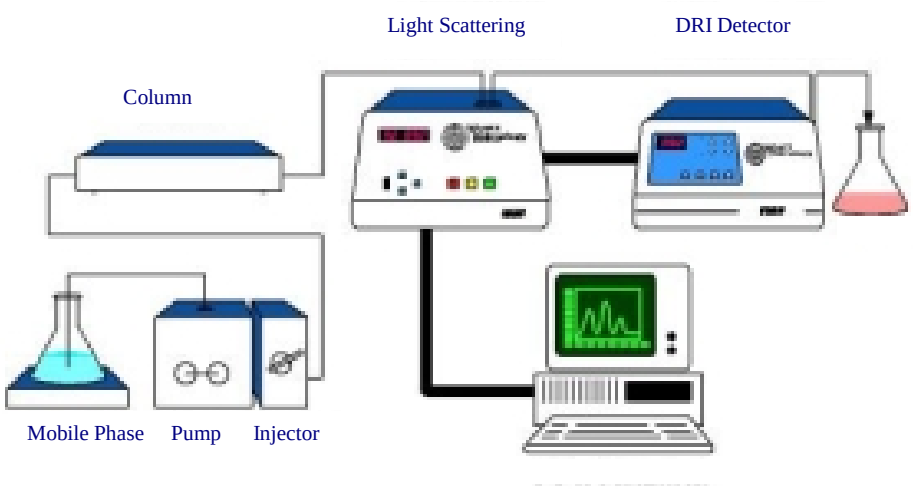

Figure 2.8: GPC-MALLS experimental set-up (www.wyatt.com)

2.4.2.5 Arsenazo Assay

Arsenazo III is a bis-azo derivative of chromotropic acid that is used extensively in spectrophotometric assays, it forms complexes with lanthanides resulting in an absorbance shift from 538nm to 653nm (figure 2.9), and therefore can be used to detect gadolinium ions (Dean 1995). Based on this phenomenon Winnik et al proposed arsenazo III as a suitable reagent to characterise novel MRI contrast agents (Gouin et al. 2001). Two calibration experiments are performed, the first uses variable concentrations of gadolinium to establish a relationship between free gadolinium concentration and absorbance. Subsequently, a fixed amount of gadolinium is added to samples of varying chelating agent (DTPA) concentration, the unchelated gadolinium is measured (using the previous calibration) from which the chelated level of gadolinium can be inferred. Using these calibration relationships DTPA levels in samples of novel contrast agents can be determined by incubation with an excess of gadolinium and the subsequent detection of remaining free gadolinium. This procedure is made possible due to the higher stability of the Gd-DTPA complexes (logK=22.46) (Cacheris et al. 1987) compared to gadolinium arsenazo complexes (logK=15.85) (Gouin et al. 2001).

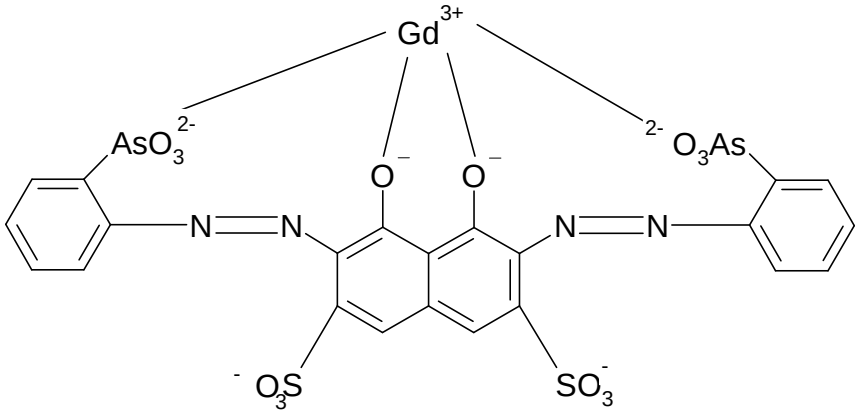

Figure 2.9: Reaction of arsenazo (III) with gadolinium (Dean 1995)

2.4.2.6 Inductively coupled plasma atomic emission spectroscopy (ICP-AES)

Inductively coupled plasma atomic emission spectroscopy (ICP-AES) is a technique used to determine concentrations of trace metals in samples (Manning et al. 1997). ICP-AES consists of three main steps; atom formation, excitation and emission. The first two stages of the process are mediated by inductively coupled plasma (ICP) which is used to generate excited atoms and ions that produce light at a characteristic wavelength. An ICP is an ionised gas generated by electromagnetic induction (time varying magnetic fields) in which a proportion of the electrons are free (unbound to parent atoms). The sample solution is first converted to an aerosol in a nebuliser and then introduced into a flow of support gas (typically Argon) in a quartz tube. A radiofrequency generator produces an oscillating current in an induction coil wrapped round the tube which generates an oscillation magnetic field. This magnetic field induces an oscillating current in the ions and electrons of the support gas. The gas transfers energy to the sample atoms by collisions to create a very high temperature (>7000K) plasma (figure 2.10). As the sample atoms gain energy via these collisions their electrons will temporarily change energy level and as they relax back to their original level the absorbed energy is released in the form of light at a wavelength that is unique to each element (figure 2.11).

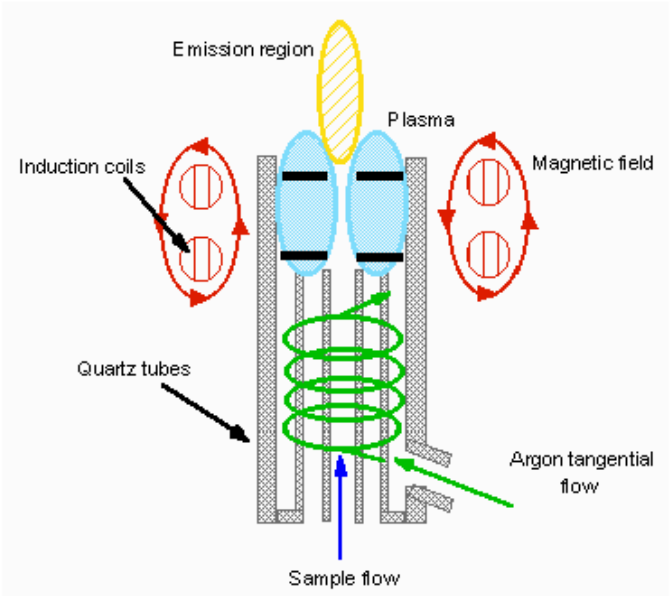

Figure 2.10: ICP schematic

The emitted light is converted to an electrical signal so that it can be measured quantitatively. The light is resolved into its components using a diffraction grating and intensity can be measured at the desired wavelength for the element(s) of interest using a photomultiplier. The intensity value is compared to values obtained using calibration to obtain the unknown concentration. The advantages of this technique are that several elements can be measured simultaneously and a low sample volume (<10ml) is required.

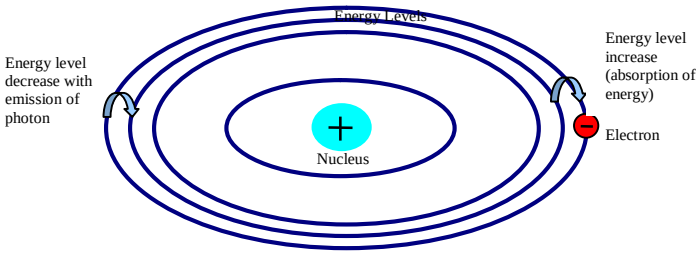

Figure 2.11: Scheme of electron relaxation with emission of light

2.4.3 Characterisation Protocols

2.4.3.1 NMR

^{1}H and COSY NMR analyses were performed on a Bruker AMX 400MHz (Bruker Instruments, U.K.) spectrometer. All samples were prepared at a concentration of 10 mg ml^{-1} using deuterated water (D_2O) as a solvent.

2.4.3.2 Elemental Analysis

Samples (10mg) were wrapped in tin foil and then introduced directly into the combustion chamber of the instrument (Thermo Finnigan EA1112, Thermo Scientific, U.K.). Following combustion, purification and separation of gases the relative abundances of carbon, hydrogen, nitrogen and sulphur were given.

2.4.3.3 GPC-MALLS

A summary of the buffers used as solvents and mobile phases for the various dn/dc and GPC analyses is shown in table 2.2.

Compound	Mobile Phase
GC	Acetate buffer, pH=4.4 0.3M sodium acetate, 0.2M acetic acid
HA	Phosphate buffered saline, pH=7.4, 0.01M phosphate buffer, 0.0027M potassium chloride, 0.137M sodium chloride
HA-DAB	Sodium carbonate-sodium bicarbonate buffer pH=10.5, 0.1 M

Table 2.2: Summary of GPC mobile phases

For dn/dc measurements samples were dissolved in the appropriate mobile phase to produce stock solutions of 1 mg ml^{-1} from which 0.8, 0.6, 0.4, 0.2, and 0.1 mg ml^{-1} (2ml) solutions were prepared and filtered using 0.22µm nylon filters. Samples were loaded into the system individually using a Rheodyne 7725 sample injector and analysed using a refractive index detector OPTILAB DSP (Wyatt Technology, U.S.A., λ=690nm). The data were processed using DNDC for Windows 5.10 software (Wyatt Technology, U.S.A.).

For GPC analyses samples (5mg) were dissolved in the appropriate buffer (1ml) and filtered using 0.22µm nylon filters. Samples (200µl) were loaded into the system using a Waters 717 autosampler. GC fractionation was performed on a PSS HEMA-Bio 300 column (Polymer Standards Services, Germany, dimensions= 300 x 8mm, particle size= 10µm, exclusion limit for dextran= 500,000 Da) and a PSS HEMA-Bio 40 column (Polymer Standards Services, Germany, dimensions= 300 x 8mm, particle size= 10µm, exclusion limit for dextran= 3,000,000 Da). HA and HA-DAB fractionation was performed on a POLYSEP-GFC-P 4000 column (Phenomenex, U.K., 300 x 7.8 mm, exclusion limit for PEG 200,000Da). The system comprised a Dawn EOS detector (Wyatt technology, U.S.A.) equipped with a 30mV linearly polarised GaAs laser (λ=690nm) and a refractive index detector OPTILAB DSP (Wyatt Technology, U.S.A., λ=690nm). Data were processed using Astra for Windows 4.73 software (Wyatt Technology, U.S.A.).

2.4.3.4 TNBS Assay

A DAB stock solution 20 µg/ml in sodium tetraborate buffer (pH=10.5, 0.1M) was prepared from which a range of DAB concentrations (0-20µg/ml) were produced (table 2.3)

Concentration (µg/ml)	DAB Stock (ml)	Buffer (ml)
0	0.0	1.0
2	0.1	0.9
4	0.2	0.8
8	0.4	0.6
12	0.6	0.4
16	0.8	0.2
20	1.0	0.0

Table 2.3: TNBS Assay- DAB calibration concentrations

TNBS (25µL, O.03M in water) solution was added to each concentration. After a 30 minute period of incubation the absorbance was read (350nm) using a UV-2401PC

spectrometer (Shimadzu, Japan). HA-DAB (40μg/ml) samples were prepared and analysed in a similar fashion.

2.4.3.5 Arsenazo Assay

Two aqueous stock solutions were prepared; gadolinium (0.1mM) and arsenazo (0.6mM). A number of calibration standards were prepared (0.0-0.6 ml Gd stock solution) to which a fixed amount of arsenazo stock solution was added (0.3ml) the solutions were mixed and made up to a final volume of 3ml using acetate buffer (0.3M sodium acetate, 0.2M acetic acid, pH=4.4). Following a 30 minute incubation period the absorbances (653nm) were read (UV-2401PC spectrometer Shimadzu, Japan).

A 50ug/ml aqueous p-SCN-Bn-DTPA stock solution was prepared. Gd stock solution (0.5ml) was then added to various amounts of this DTPA solution (0.0-0.6ml) and the solutions mixed and incubated for 15 minutes. Arsenazo stock solution was added (0.3ml) and the sample made up to a final volume of 3 ml using acetate buffer. Following a 30 minute incubation period absorbances (653nm) were read (UV-2401PC spectrometer Shimadzu, Japan). Finally aqueous GC-DTPA solutions (50ug/ml) were prepared and tested (0.5, 0.7, 0.9 ml) as with the DTPA samples.

2.4.3.6 ICP-AES

A number of gadolinium calibration standards were prepared (0-40 ml L^{-1}) and the emission at 310nm was measured using a Varian Vista Pro Inductively Coupled Plasma Atomic Emission Spectrometer (Varian Inc, U.S.A.). A range of concentrations of aqueous GC-DTPA-Gd and HA-DAB-DTPA-Gd samples were then tested (0-250 mg L^{-1}).

2.5 GC-DTPA-Gd Characterisation Results

2.5.1 GC Degradation Yields

High molecular weight glycol chitosan was acid degraded for 2 (GC2) or 48 hours (GC48) giving a white cotton like substance following freeze-drying. The yield of this degradation reaction ranged from 62-75% and was inversely proportional to the degradation time (table 2.4). The yields are as expected as the longer degradation would generate a larger number of very small fragments which are lost in dialysis.

Sample	Starting mass (g)	Mass after degradation (g)	%Yield
GC48	2.00	1.24	62
GC2	2.00	1.50	75

Table 2.4: GC degradation reaction yields

2.5.2 GC Molecular Weight Determination

2.5.2.1 dn/dc

The dn/dc values for the GC2 and GC48 polymers were found to be 0.129 ± 0.003 ml g^{-1} and 0.156 ± 0.007 ml g^{-1} respectively. Representative plots are shown in figure 2.12 (GC2) and 2.13 (GC48).

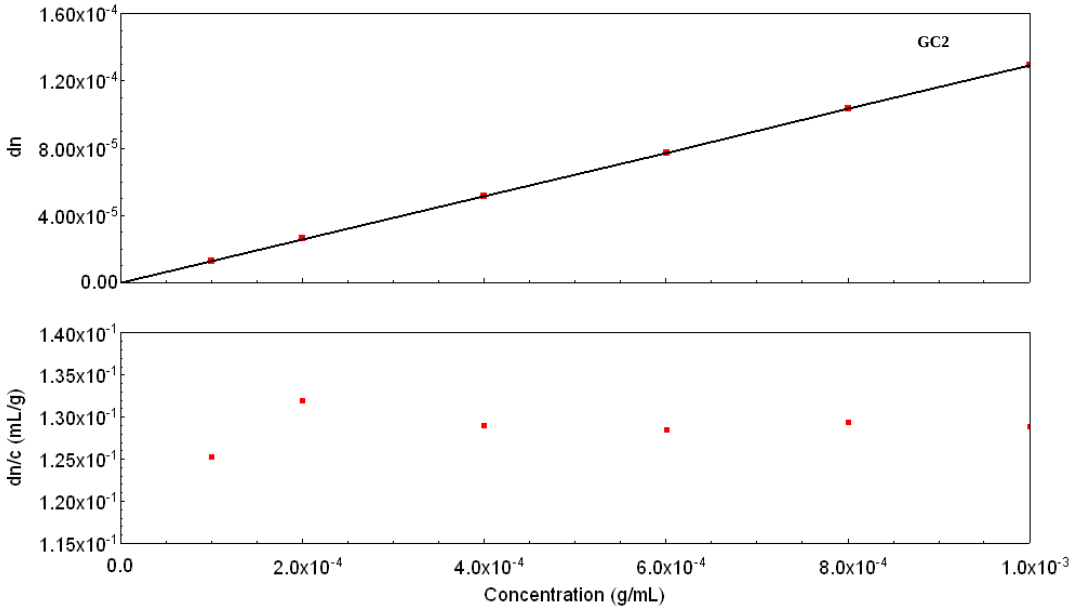

Figure 2.12: Representative dn/dc plot GC2 polymer

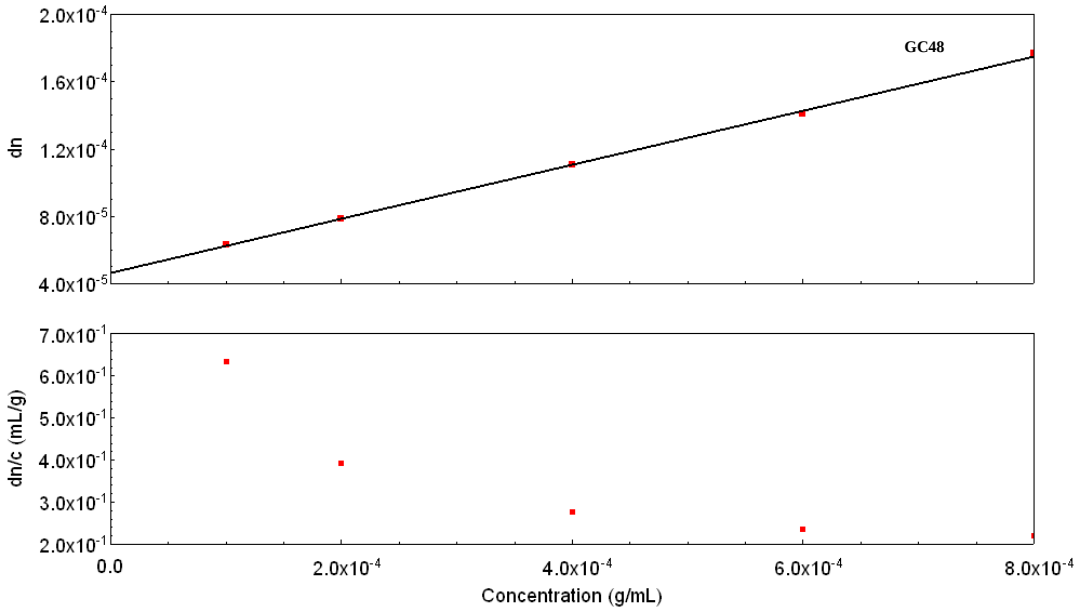

Figure 2.13: Representative dn/dc plot GC48 polymer

2.5.2.2 GPC-MALLS

The weight average molecular weights (M_w) values for the GC2 and GC48 polymers were found to be 37,823 ± 1427 Daltons and 12,335 ± 191 Daltons respectively. Representative chromatograms are shown in figures 2.14 (GC2) and 2.15 (GC48) for 5 mg/ml samples.

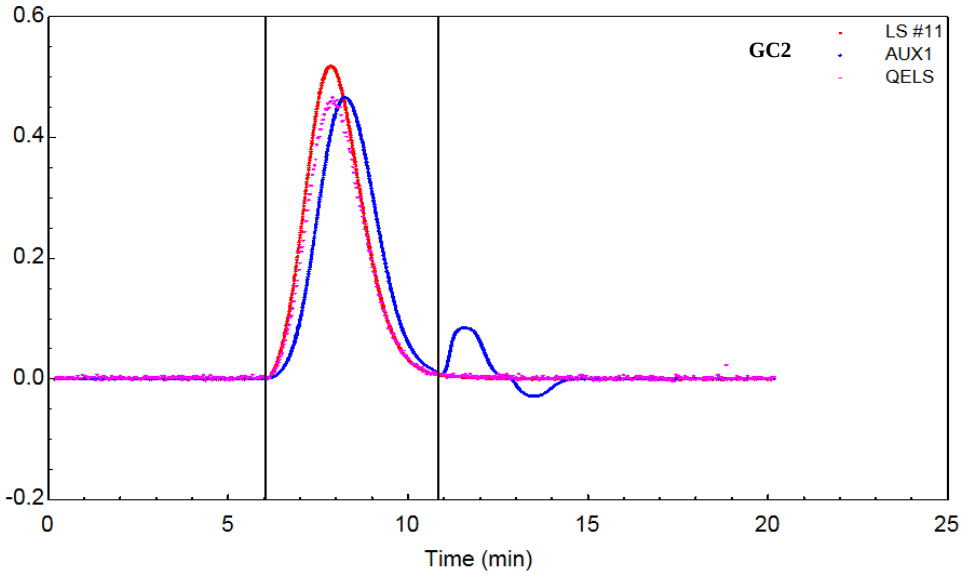

Figure 2.14: Representative GPC chromatogram GC2 polymer

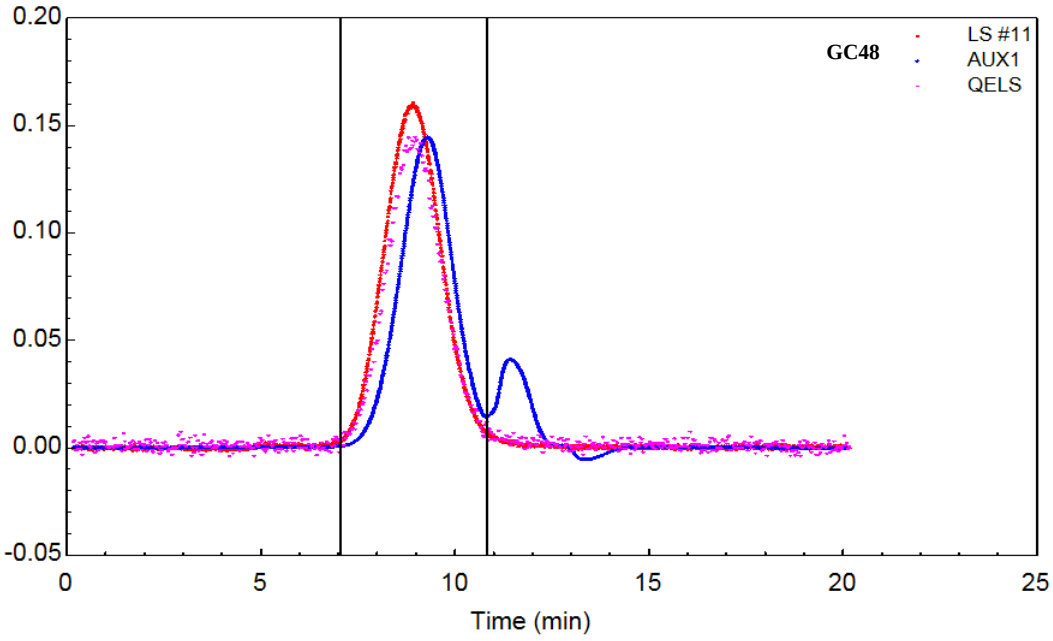

Figure 2.15: Representative GPC chromatogram GC48 polymer

The results of the GPC-MALLS experiments are as expected: the polymers with shorter degradation times have higher molecular weights. This is reflected in the shorter elution time for the GC2 polymer (6 minutes v 7.5 minutes) and greater peak height. The chromatograms show only one elution peak with good overlap of the RI (blue) and light scattering (red) peaks. The two additional peaks in the RI trace represent the exclusion limit of the column (negative peak at 13.5 ml) and the injection peak (positive peak at 12 ml) which results from the difference between the sample and reference solvents.

2.5.3 GC-DTPA Conjugation reaction yields

A white/yellow cotton like product (GC-DTPA) was obtained after freeze-drying. Yields were similar for both molecular weight starting materials at approximately 60% (table 2.5).

Sample	Total starting mass (mg)	Mass after conjugation (mg)	%Yield
GC48-DTPA	(325 + 205) = 530	325	61.32
GC2-DTPA	(325 + 205) = 530	332	62.64

Table 2.5: GC-DTPA conjugation reaction yields

2.5.4 NMR

NMR was used to confirm the presence of both GC and DTPA in the conjugate. Both the starting materials (GC and DTPA) and the final compounds (GC2-DTPA and GC48-DTPA) were analysed.

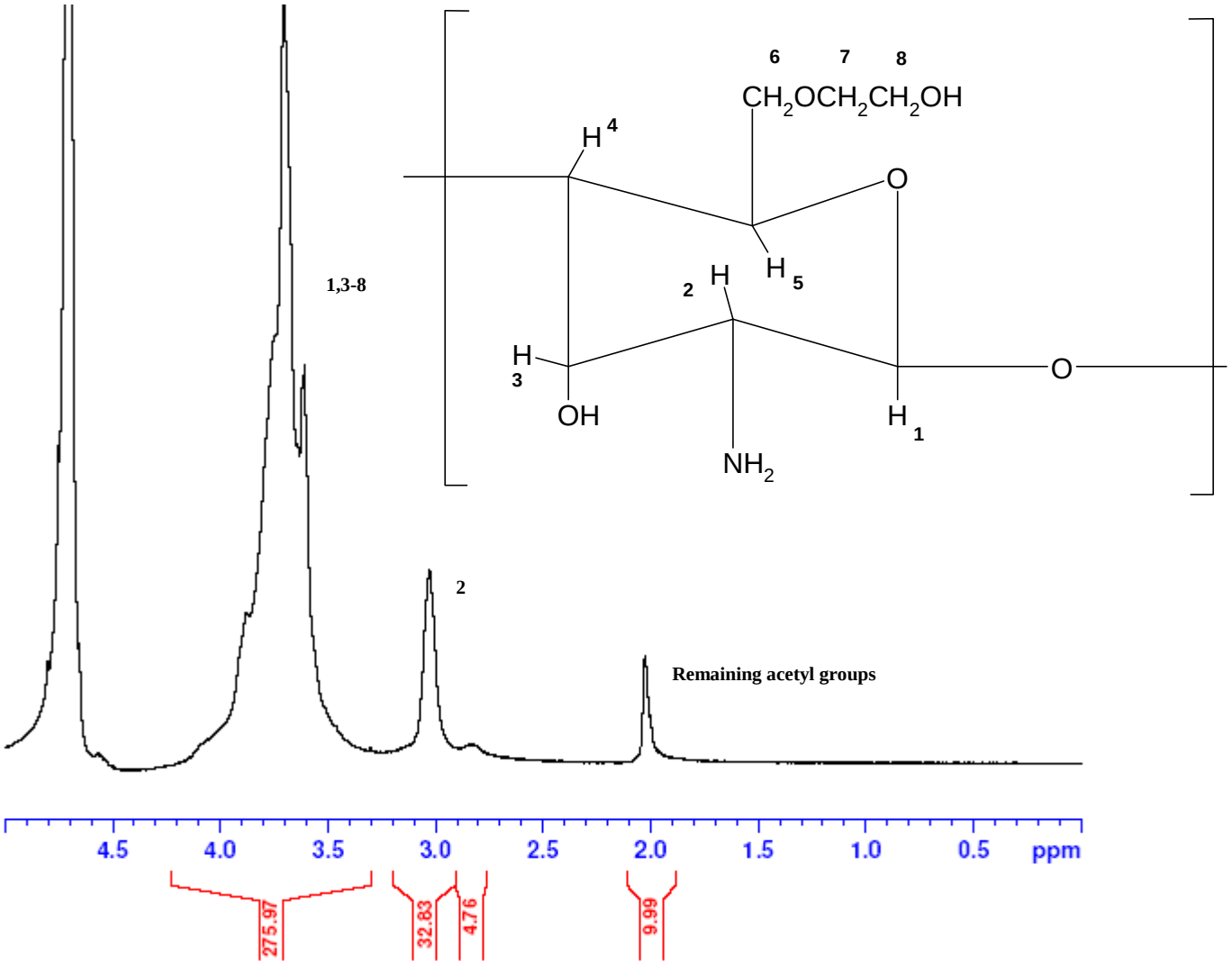

Figure 2.16: GC2 ^{1}H NMR Spectrum

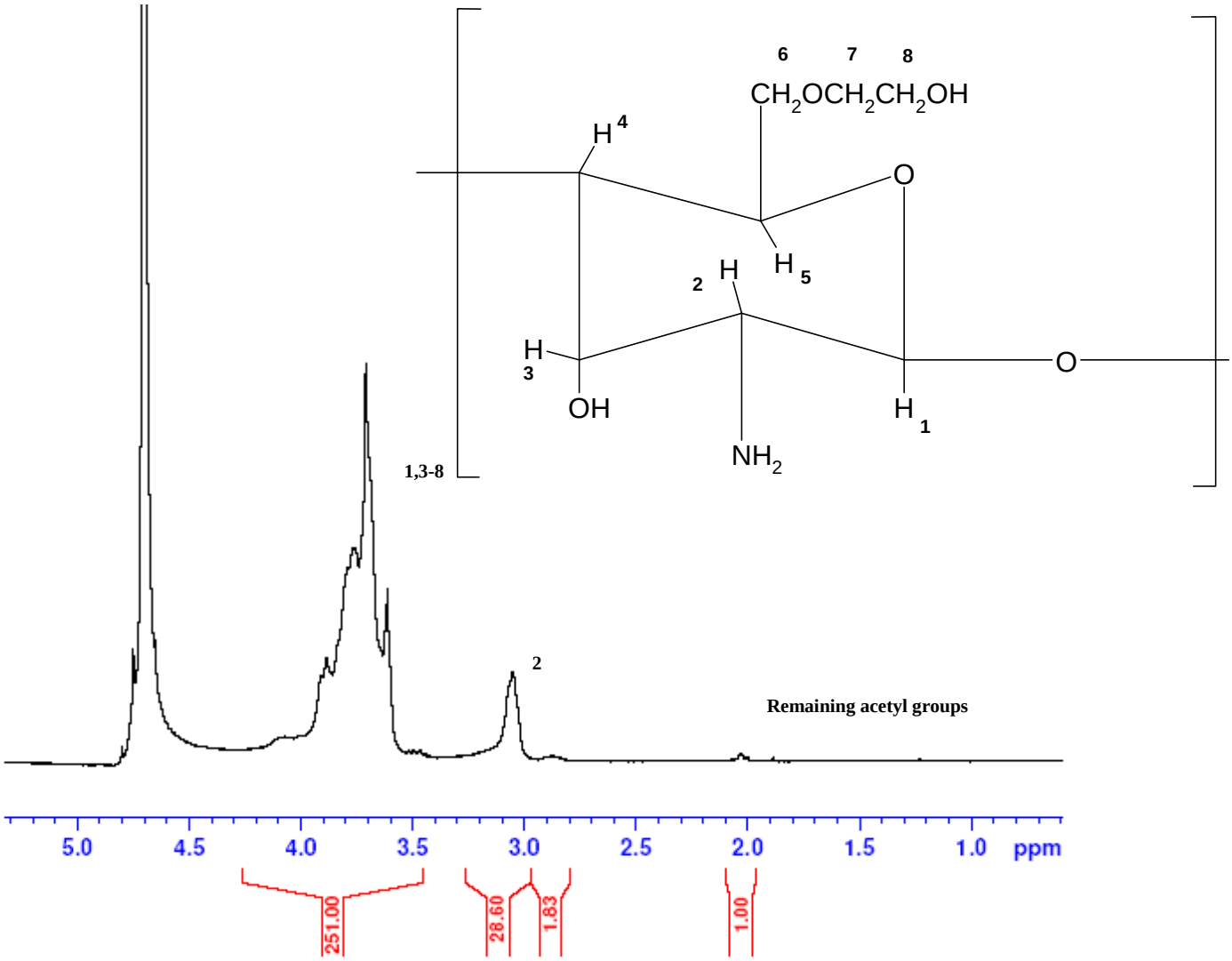

Figure 2.17: GC48 ^{1}H NMR Spectrum

The GC starting material is described as de-acetylated but up to 5% acetylation can remain which gives the distinctive peak at 2.0 p.p.m. It would appear that acid degradation reduces this remaining acetylation as the acetyl peak is clear on the GC2 (figure 2.16) spectrum but has almost disappeared on the GC48 spectrum (figure 2.17). Only the proton at C2 can be uniquely identified (3.1 p.p.m.) as the signals for all the other protons overlap (3.5-4.2 p.p.m). No additional information was provided by the COSY spectra.

There are two distinctive peaks in the 1H NMR for the DTPA compound (figure 2.18) that correspond to the protons in the ring structure at 7.2 and 7.3 p.p.m. The remaining signals appear further upfield in the range of 2.5-3.6p.p.m.

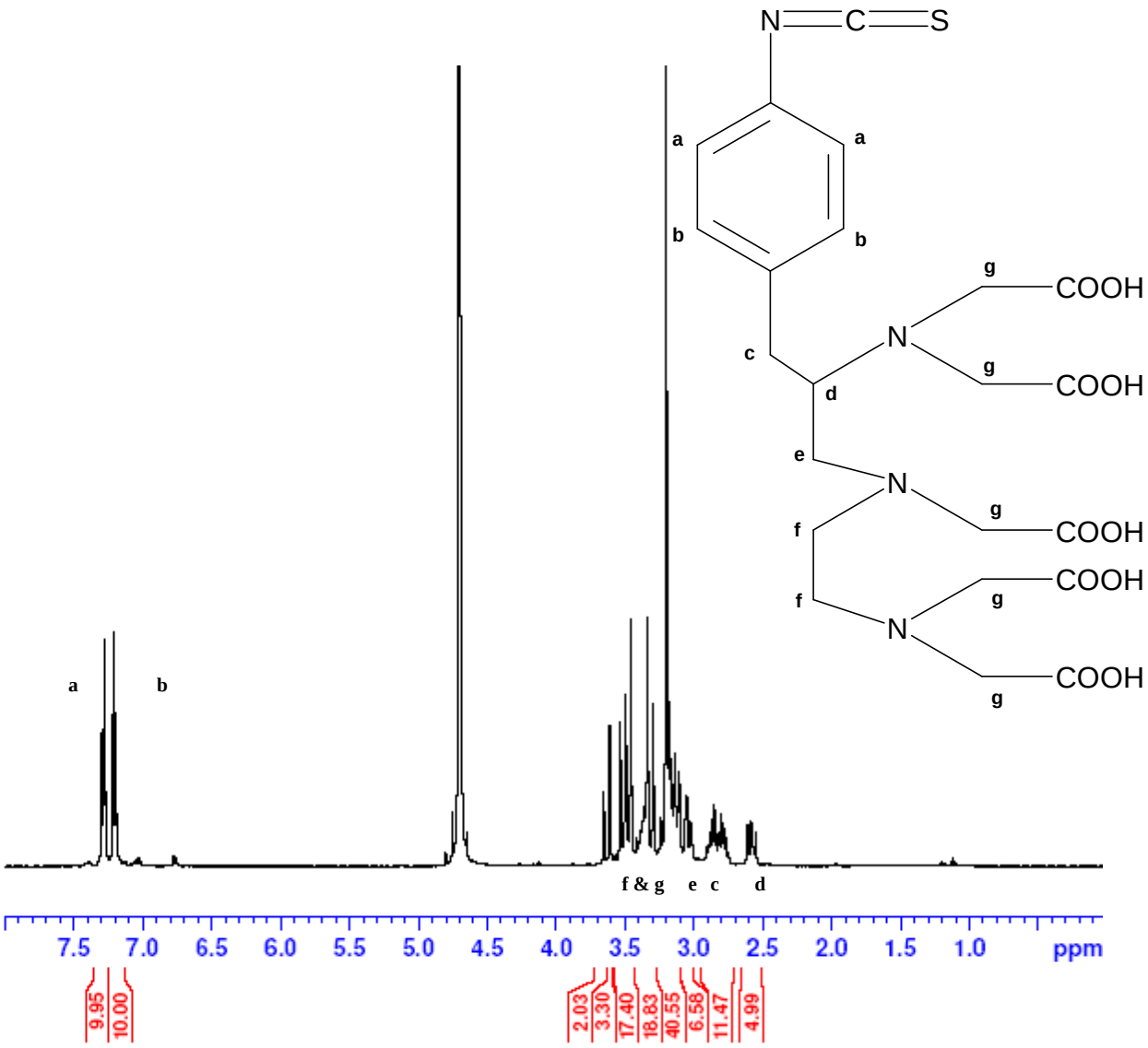

Figure 2.18: p-SCN-Bn-DTPA ^{1}H NMR Spectrum

The peaks at approximately 7.3 p.p.m. in figures 2.19 and 2.20 confirm the presence of the benzylisothiocyanate group of DTPA in the final product. The other DTPA and GC peaks overlap in the 2.5-4.0 p.p.m. range and cannot be uniquely identified. There is a new peak at 4.4 p.p.m. in both the GC2-DTPA and GC48-DTPA spectra

which could be from the GC anomeric proton as this position at which this signal would be expected. The reason that this is now apparent but was not observed in the GC spectra could be as a result of conformational changes due to DTPA conjugation.

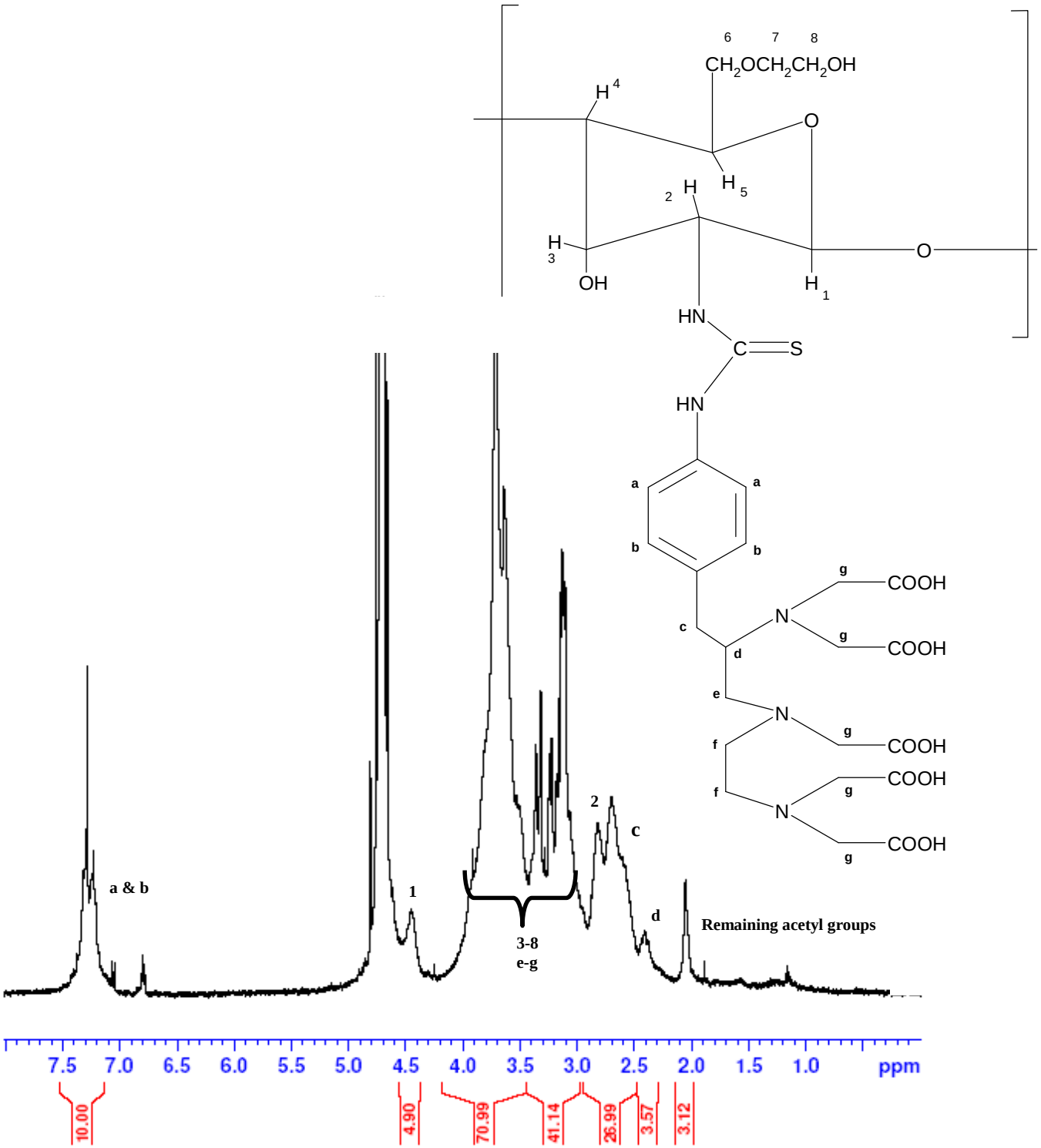

Figure 2.19: GC2-DTPA ^{1}H Spectrum

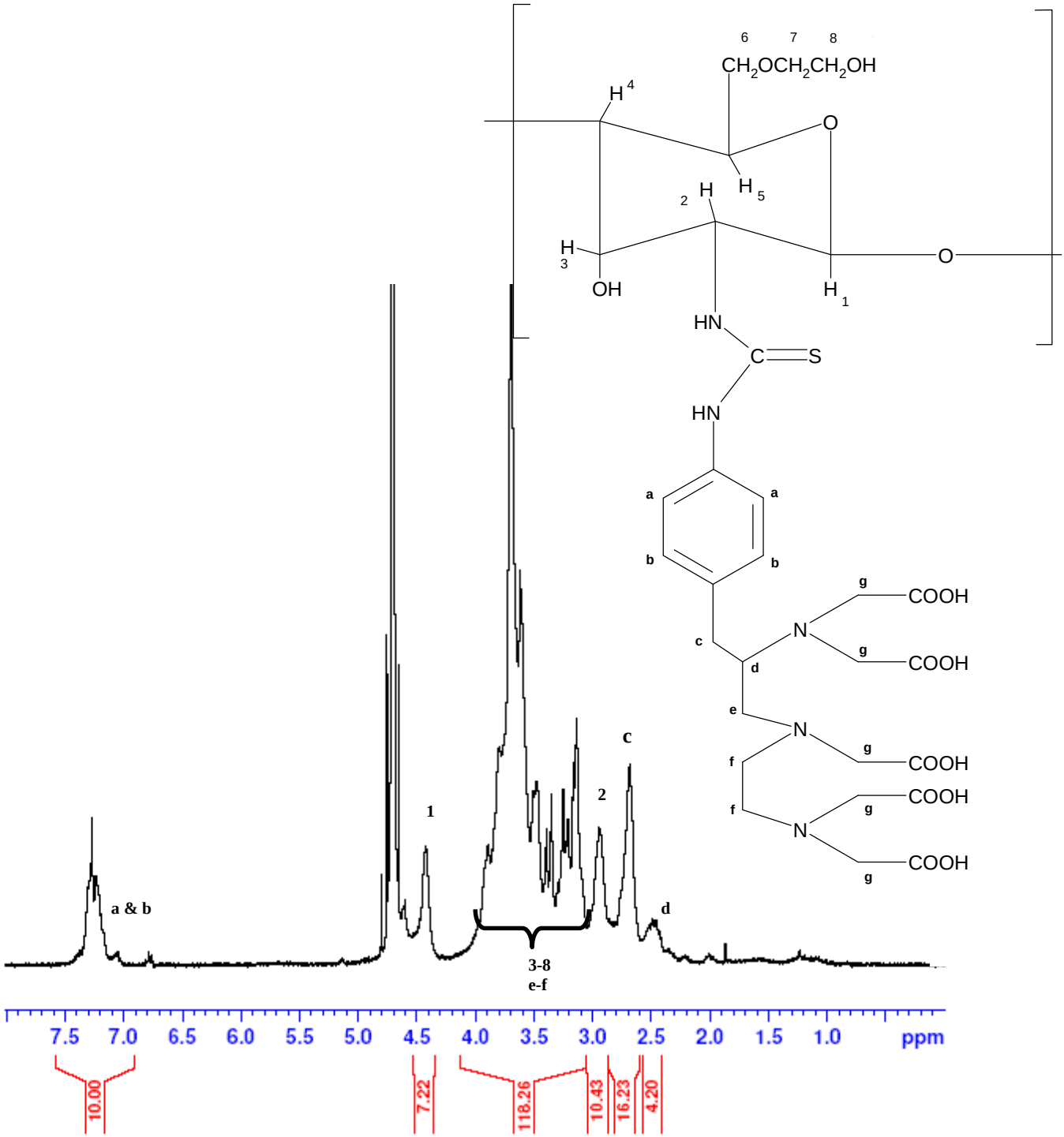

Figure 2.20: GC48-DTPA ^{1}H Spectrum

2.5.5 Elemental Analysis

C, H, N, S elemental analysis was performed to determine the GC-DTPA conjugate composition. The starting materials (GC2 [table 2.6], GC48 [table 2.7] and p-SCN-Bn-DTPA [table 2.8]) and conjugated products (GC2-DTPA [table 2.9] and GC48-DTPA [table 2.10]) were analysed. Firstly the results for are normalised by the sulphur level. DTPA is the only source of sulphur in the conjugate hence subtracting the results for DTPA returns the C, H and N contribution of GC. These values can then converted to a relative number of GC monomers. The conjugate composition is then expressed in terms of number of monomers per pendant group.

GC2	Element		
	C	H	N
% Found Sample 1	36.63	7.18	5.20
% Found Sample 2	36.45	7.34	5.08
% Found Sample 3	36.95	7.06	4.96
Average	**36.68**	**7.19**	**5.08**
Molecular Weight	12.00	1.00	14.00
Moles per 100 g	3.06	7.19	0.36
Moles per Mole N	8.42	19.82	1.00

Table 2.6: Elemental analysis results for GC2 polymer (negligible levels of sulphur were detected).

GC48	Element		
	C	H	N
% Found Sample 1	37.07	7.70	5.41
% Found Sample 2	37.36	7.50	5.42
% Found Sample 3	37.35	8.45	5.49
Average	**37.26**	**7.88**	**5.44**
Molecular Weight	12.00	1.00	14.00
Moles per 100 g	3.11	7.88	0.39
Moles per Mole N	7.99	20.29	1.00

Table 2.7: Elemental analysis results for GC48 polymer

The results are consistent with the molecular formula for the polymer ($C_8H_{15}NO_5$), the slight increase in the C:N ratio for the GC2 polymer compared with the GC48

polymer could be as a result of the increase in the degree of remaining acetylation as seen in the NMR spectra.

p-SCN-Bn-DTPA	Element			
	C	H	N	S
% Found Sample 1	38.46	5.78	8.21	4.20
% Found Sample 2	37.95	5.62	8.05	4.77
% Found Sample 3	38.25	5.55	8.07	4.35
Average	**38.22**	**5.65**	**8.11**	**4.44**
Molecular Weight	12.00	1.00	14.00	32.00
Moles per 100 g	3.19	5.65	0.58	0.14
Moles per Mole S	22.95	40.72	4.18	1.00

Table 2.8: Elemental analysis results for p-SCN-Bn-DTPA

The C:N:S ratio found is as expected from the molecular formula ($C_{22}H_{28}N_4O_{10}S$).

GC2-DTPA	Element			
	C	H	N	S
% Found	37.02	8.83	6.66	1.59
Molecular Weight	12.00	1.00	14.00	32.00
Moles per 100 g	3.09	8.83	0.48	0.05
Moles per Mole S	**62.09**	**177.71**	**9.57**	**1.00**
DTPA Contribution	22.95	40.72	4.18	1.00
GC Contribution	39.14	136.99	5.39	0.00

Table 2.9: Elemental analysis results for GC2TPA conjugate

GC48-DTPA	Element			
	C	H	N	S
% Found	38.51	7.96	6.61	1.64
Molecular Weight	12.00	1.00	14.00	32.00
Moles per 100 g	3.21	7.96	0.47	0.05
Moles per Mole S	**62.73**	**155.60**	**9.23**	**1.00**
DTPA Contribution	22.95	40.72	4.18	1.00
GC Contribution	39.78	114.88	5.05	0.00

Table 2.10: Elemental analysis results for GC48-DTPA conjugate

Only one sample of each conjugate was analysed due to scarcity of material and it was felt that the results for the analyses of the starting materials showed that the technique was consistent

The GC contribution is found by subtracting the elemental values for DTPA from the conjugate results. The remaining carbon and nitrogen represent the polymer backbone and are converted into an equivalent number of monomers by dividing by the ratios for the unmodified starting material (tables 2.6 and 2.7).

GC2-DTPA conjugate:

Using the carbon ratio (39.14÷7.99) = 4.90:1

Using the nitrogen ratio (5.39÷1.00) = 5.39:1

Hence the average ratio of GC monomers to DTPA pendant groups is **5.15:1**

GC48-DTPA conjugate:

Using the carbon ratio (39.78÷8.42) = 4.72:1

Using the nitrogen ratio (5.05÷1.00) = 5.05:1

Hence the average ratio of GC monomers to DTPA pendant groups is **4.89:1**

The close relationship between the ratios calculated using the carbon and nitrogen ratios give confidence that there are no impurities in the final conjugates.

2.5.6 Arsenazo assay

An arsenazo based colorimetric assay was used to confirm the GC-DTPA conjugate composition. The reaction of arsenazo with gadolinium forms a chromophore with maximum absorbance at 653nm. The Beer's law range was found by reacting variable amounts of gadolinium with a fixed amount of arsenazo, a linear relationship was observed for 0-8 mol^{-8} gadolinium (figure 2.21). The experiment was repeated three times and the low errors values indicate the consistency of the technique.

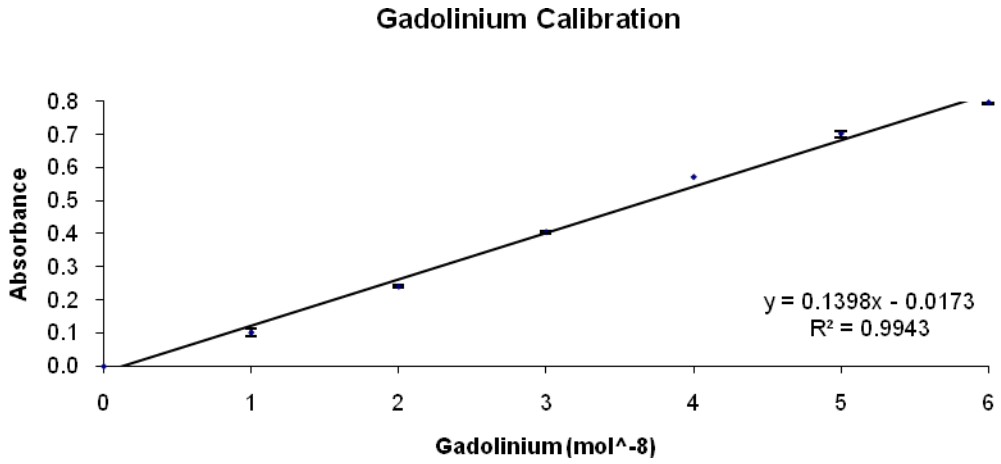

Figure 2.21: Arsenazo assay gadolinium calibration

Subsequently the stoichiometry of the gadolinium chelation reaction was investigated. It is expected that one mole of DTPA would chelate one mole of gadolinium, to confirm this a constant amount of gadolinium was added to four different amounts of DTPA followed by arsenazo addition. The higher stability of the Gd-DTPA complex relative to the arsenazo-Gd complex coupled with the delay before arsenazo administration should ensure that only free (unchelted) gadolinium is detected. The average molar ratio of DTPA to chelated gadolinium was found to be 1.060 (±0.03):1 (table 2.11).

DTPA (mols x 10^{-8})	Av Abs	Std Dev	Free Gd (mols x 10^{-8})	Chelated Gd (mols x 10^{-8})	Ratio (DTPA:Chelated Gd)
0.00	0.675	0.021	4.952	0.048	n/a
1.54	0.484	0.033	3.582	1.418	1.09
2.32	0.376	0.025	2.813	2.187	1.06
3.09	0.277	0.013	2.105	2.895	1.07
3.86	0.156	0.006	1.240	3.760	1.03

Table 2.11: Arsenazo assay molar ratio DTPA:Chelated Gadolinium

A similar approach was employed to assay the level of DTPA in the GC-DTPA conjugate: a fixed amount of gadolinium was incubated with three different amounts of the GC-DTPA conjugate followed by addition of arsenazo to detect the remaining free (unchelated) gadolinium. The amount of chelated gadolinium was then calculated and the equivalent number of moles of DTPA found. The mass of DTPA was then subtracted from that of the conjugate to deduce the GC mass. The final result was expressed as a ratio of GC monomer to DTPA pendant groups. The GC2-DTPA polymer was found to have an average of 4.83±0.14 monomers per pendant group whereas the GC48-DTPA conjugate had an average value of 5.36±0.06 (tables 2.12 and 2.13).

GC2-DTPA (ml)	GC2-DTPA (µg)	Abs	Free Gd	Chelated Gd	DTPA (mols^{-8})	DTPA (µg)	GC (µg)	GC (mols^{-8})	Ratio (GC:DTPA)
0.5	25	0.46	3.45	1.55	1.65	9.06	15.94	7.78	4.72
0.7	35	0.38	2.84	2.16	2.29	12.58	22.42	10.94	4.78
0.9	45	0.30	2.30	2.70	2.86	15.73	29.27	14.28	4.99

Table 2.12: Arsenazo assay GC2-DTPA analysis

GC48-DTPA (ml)	GC48-DTPA (µg)	Abs	Free Gd	Chelated Gd	DTPA (mols^{-8})	DTPA (µg)	GC (µg)	GC (mols^{-8})	Ratio (GC:DTPA)
0.5	25	0.48	3.57	1.43	1.51	8.33	16.67	8.13	5.37
0.7	35	0.40	2.98	2.02	2.14	11.75	23.25	11.34	5.31
0.9	45	0.33	2.45	2.55	2.70	14.88	30.12	14.69	5.43

Table 2.13: Arsenazo assay GC48-DTPA analysis

2.5.7 Summary of GC-DTPA characterisation results

It would appear that the three fold difference between the molecular weights of the starting materials (12 and 40 kDa) has no effect on the level of pendant groups that can be attached (table 2.14 and 2.15). This suggests that within this molecular weight range the level of pendant attachment is limited by the conjugation stoichemistry rather than the flexibility of the backbone.

GC2-DTPA

Analysis Method	Number of GC Monomers per DTPA Pendant Group
Elemental Analysis	5.15
Arseanzo Assay	4.83±0.14
Average	4.99

Table 2.14: Summary of GC2-DTPA characterisation results

GC48-DTPA

Analysis Method	Number of GC Monomers per DTPA Pendant Group
Elemental Analysis	4.89
Arseanzo Assay	5.37±0.06
Average	5.13

Table 2.15: Summary of GC48-DTPA characterisation results

2.5.8 GC-DTPA-Gd Reaction Yields

A white/yellow product (GC2-DTPA-Gd, GC48-DTPA-Gd) was obtained after freeze-drying. The yield of the higher molecular weight (217 mg) compound was considerably greater than that of the lower molecular weight compound (120mg) (Table 2.16). The experiment would have to be repeated to rule out experimental error as the source of this disparity before other explanations could be explored.

Sample	Yield (mg)
GC48-DTPA-Gd	120
GC2-DTPA-Gd	217

Table 2.16: GC-DTPA-Gd reaction yields

2.5.9 ICP-AES

The gadolinium content of the final products was determined directly using ICP-AES. The amount of gadolinium in each sample was used to find an expression for the mass ratio of gadolinium to total contrast agent (table 2.17). The average ratio for the GC-DTPA-Gd contrast agent was 0.079 ± 0.003 mg of gadolinium per mg of contrast agent for GC2-DTPA-Gd and 0.073 ± 0.005 mg of gadolinium per mg of contrast agent for GC48-DTPA-Gd.

Contrast Agent	Gd (mg/L)	Gd (mg/ml)	Gd (mg/20 ml)	GC-DTPA-Gd mg)	Mass Ratio (Gd:Contrast Agent)
GC2-DTPA-Gd	4.21	0.004	0.084	1.050	0.080
	6.03	0.006	0.121	1.480	0.081
	9.40	0.009	0.188	2.460	0.076
				Average (GC2)	**0.079 ± 0.003**
GC48-DTPA-Gd	2.88	0.003	0.058	0.730	0.079
	6.78	0.007	0.136	1.940	0.070
	9.22	0.009	0.184	2.580	0.071
				Average (GC48)	**0.073 ± 0.005**

Table 2.17: ICPAE results

In order to allow validation of these results the masses of the components of each of the final contrast agents were summed assuming the ratios of GC monomers to DTPA pendant groups found previously **(2.5.7)**. From this a mass ratio similar to that expressed in table 2.17 was found.

Component	Unit Mass	Number of Units	Total
GC2	205	4.99	1022.95
p-SCN-Bn-DTPA	540	1.00	540.00
Gd	157	1.00	157.00
		Total Mass	**1719.95**

Table 2.18: Empirical mass GC2-DTPA-Gd

Hence the ratio of gadolinium to the total contrast agent mass is (157/1719.95) = 0.09 mg of gadolinium per mg of contrast agent.

Component	Unit Mass	Number of Units	Total
GC48	205	5.13	1051.65
p-SCN-Bn-DTPA	540	1.00	540.00
Gd	157	1.00	157.00
		Total Mass	**1748.65**

Table 2.19: Empirical mass GC48-DTPA-Gd

Hence the ratio of gadolinium to the total contrast agent mass is (157/1719.95) = 0.09 mg of gadolinium per mg of contrast agent.

2.6 HA-DAB-DTPA-Gd Characterisation Results

2.6.1 HA Molecular Weight Determination

HA samples were purchased with a guide molecular weight of approximately 35 kDa.

The exact molecular weight was determined using GPC-MALLS

2.6.1.1 dn/dc

The dn/dc value was found to be 0.1480 ± 0.005 ml g^{-1} (figure 2.22).

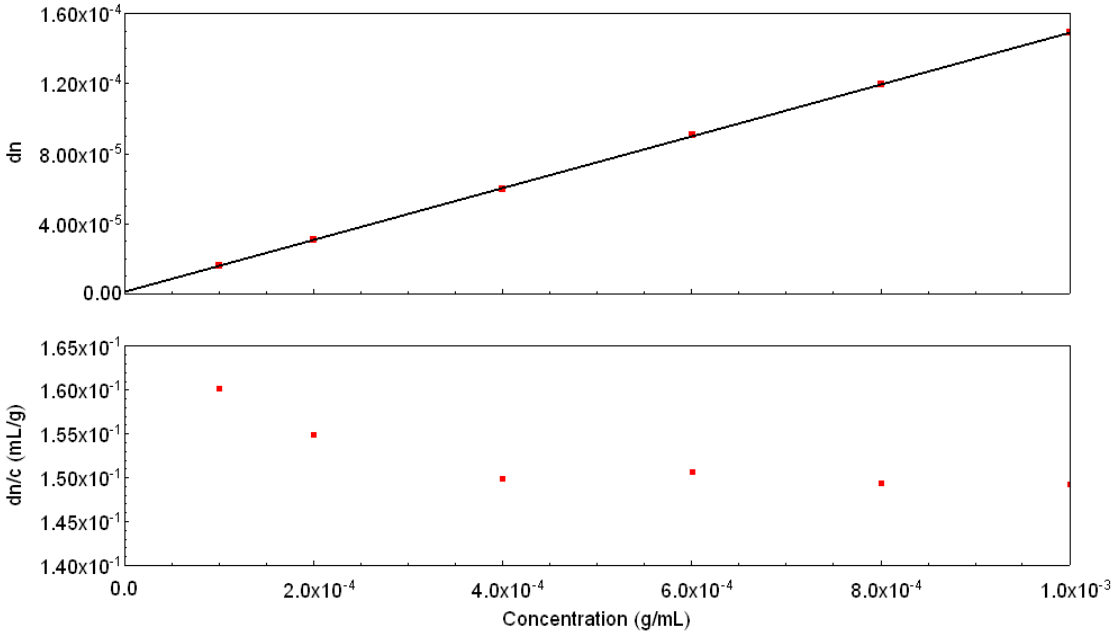

Figure 2.22: Representative dn/dc curve for purchased HA samples

2.6.1.2 GPC-MALLS

The molecular weight of the HA sample was found to be 42894 ± 802.13 Daltons (figure 2.23). There is good overlap of the RI (blue) and light scattering (red) peaks.

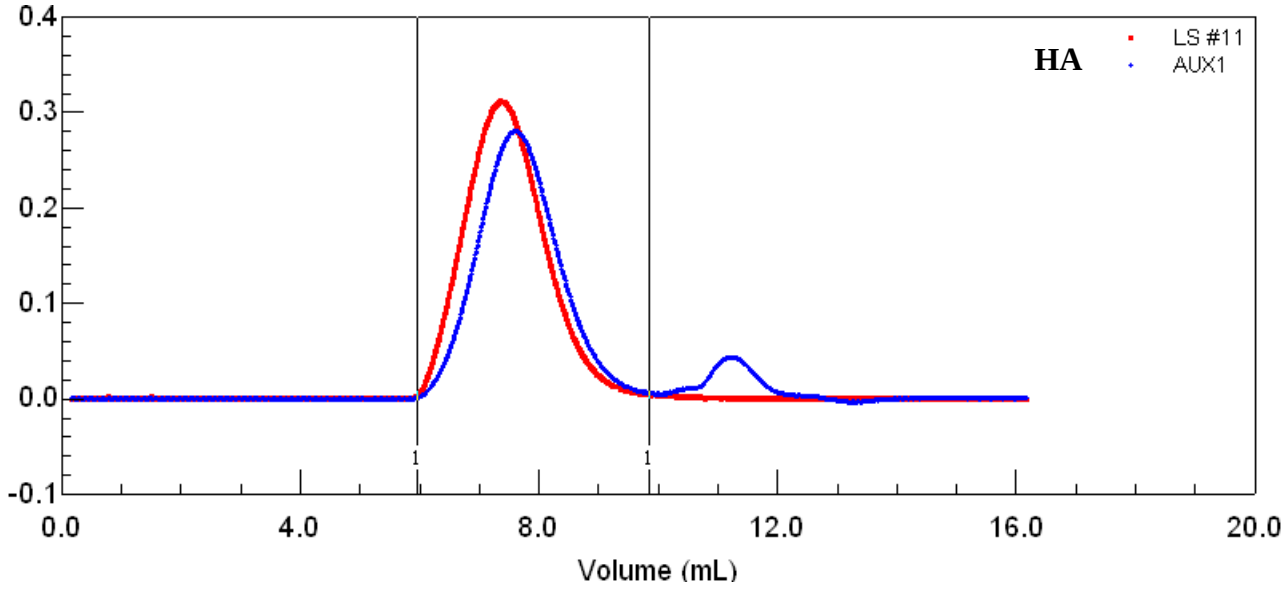

Figure 2.23: Representative GPC chromatogram HA polymer

2.6.2 HA-DAB NMR

NMR was used at each stage of the synthesis to both confirm conjugation and characterise the conjugates. The starting materials (HA and DAB) were analysed: HA has distinctive peaks at 2.0 p.p.m. and 4.4 and 4.5 p.p.m. that represent the signals from the methyl protons on the acetylglucosamine monomer and the anomeric protons respectively (figure 2.24). The COSY spectrum (figure 2.25) indicates that there are correlations between the peaks at 3.3 and 3.8 p.p.m. and the anomeric proton peaks so they can be designated as the C2 protons for each monomer.

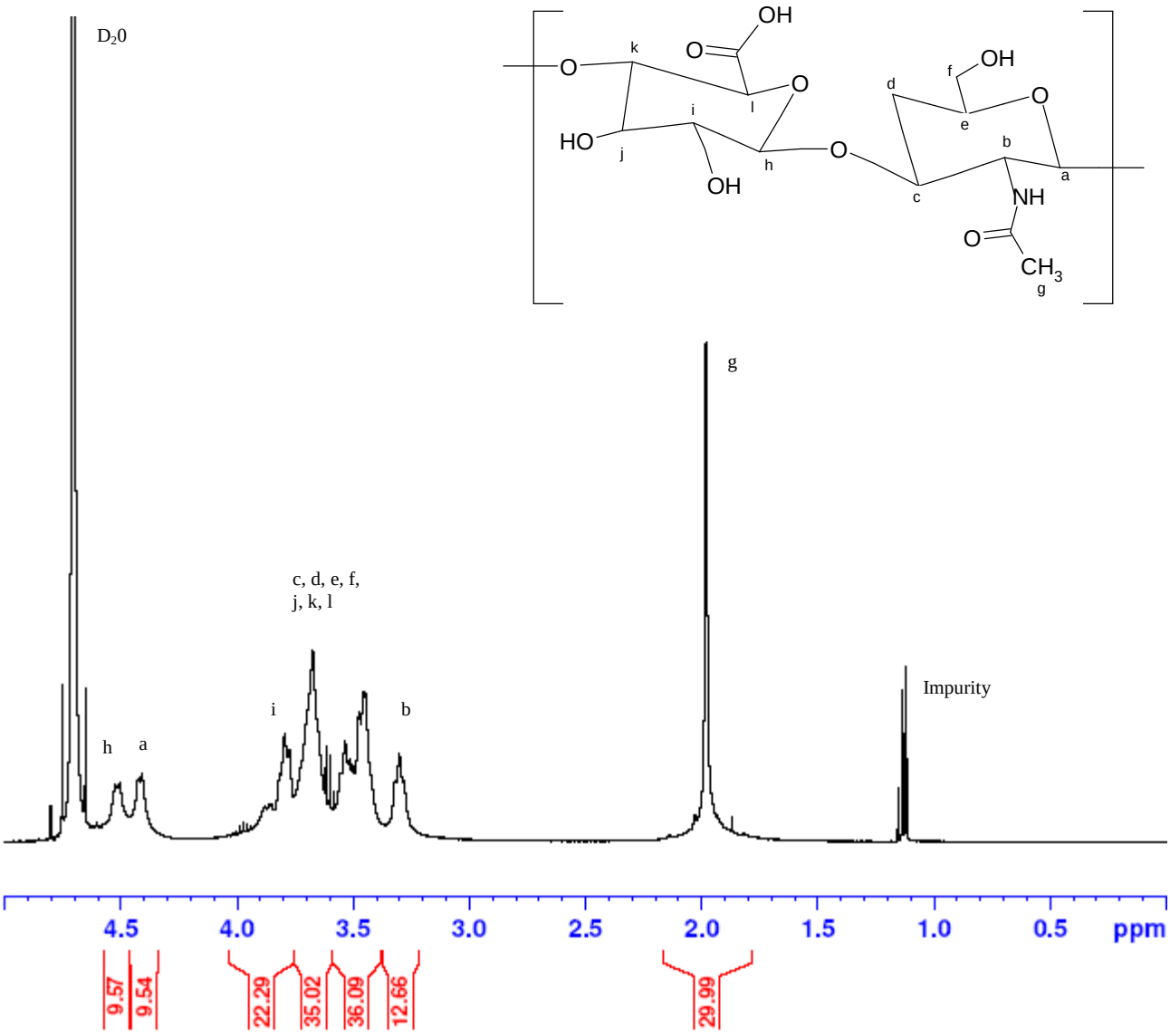

Figure 2.24: HA ^{1}H NMR Spectrum

ppm	Reference	Total Number of Protons	Area (Units)	Units/Proton
2.0	g	3	29.99	10.0
3.3	b	1	12.66	12.7
3.4-3.7	c, d, e, f, j, k, l	7	71.13	10.2
3.8	i	1	12.29	12.3
4.4	a	1	9.54	9.5
4.5	h	1	9.57	9.6

Table 2.20: HA ^{1}H NMR Proton assignment

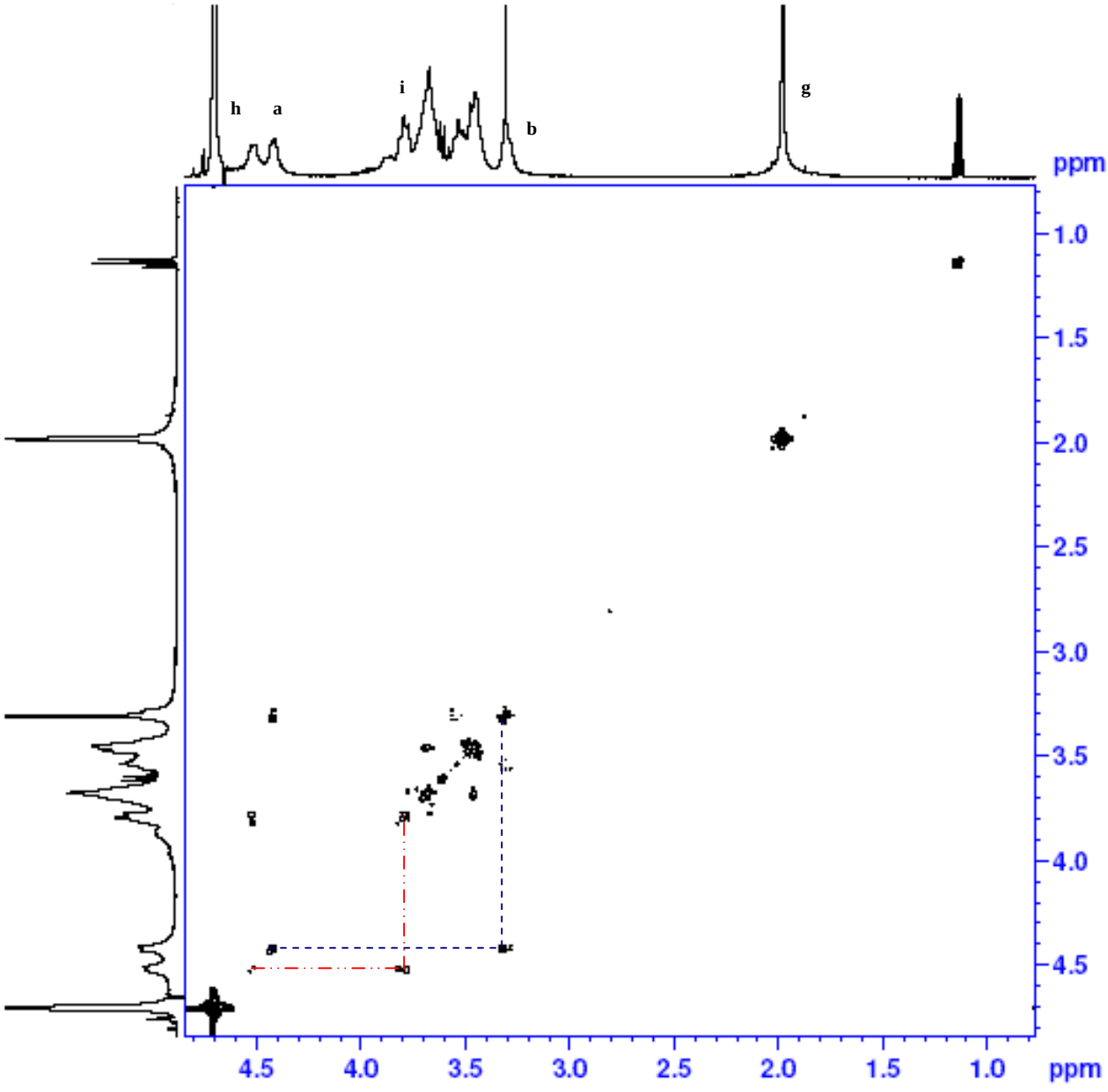

Figure 2.25: HA COSY Spectrum

The regular molecular architecture of DAB gives rise to clearly defined NMR peaks (figure 2.26), which can be easily assigned (table 2.21)

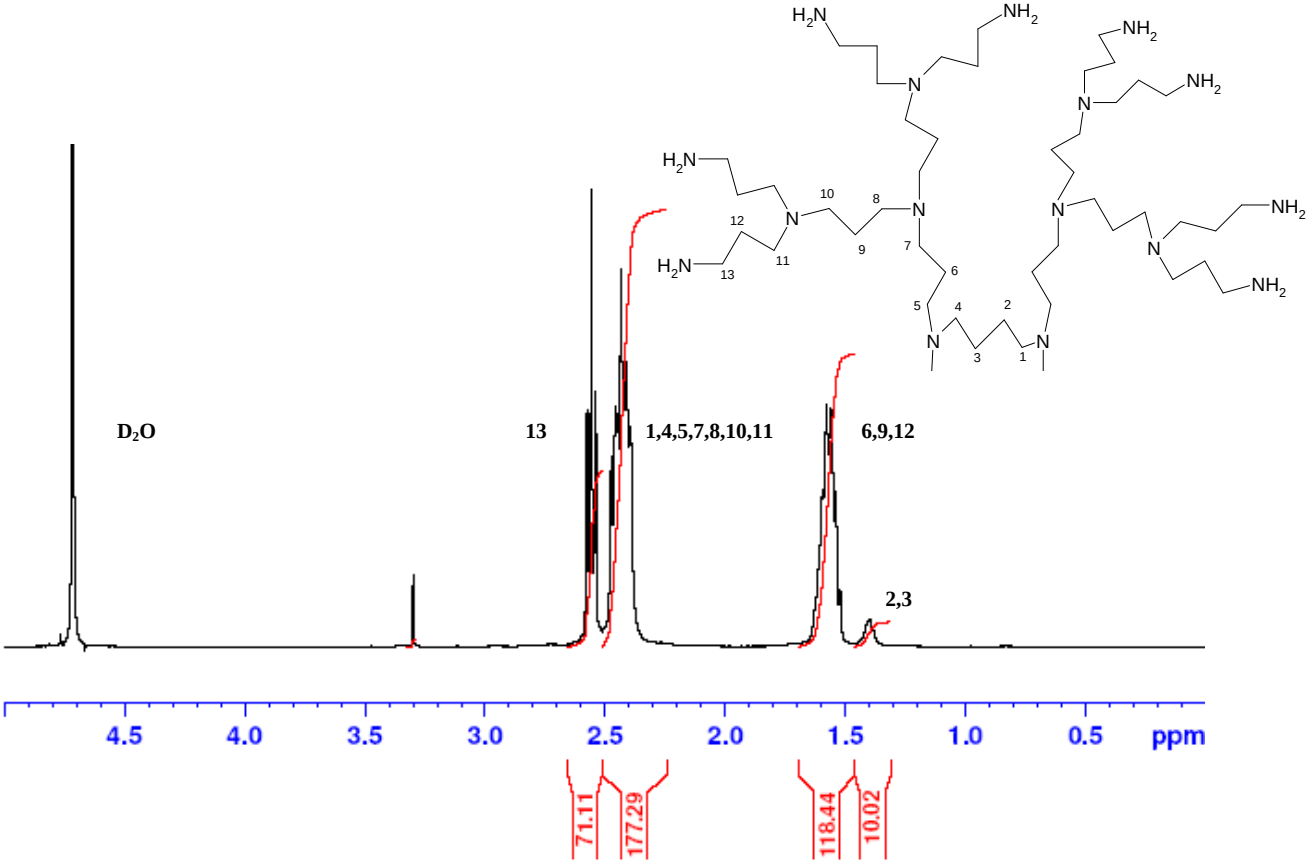

Figure 2.26: DAB ^{1}H NMR Spectrum

ppm	Reference	Number of Protons	Total Number of Protons	Area (Units)	Ratio (Units/Proton)
1.4	2	2			
	3	2	4	10.02	2.5
1.6	6	8			
	9	16			
	12	32	56	118.44	2.1
2.4	1	2			
	4	2			
	5	8			
	7	8			
	8	16			
	10	16			
	11	32	84	177.29	2.1
2.6	13	32	32	71.11	2.2

Table 2.21: DAB ^{1}H NMR Proton Assignment

The cosy spectrum (2.27) shows the interactions between the 4 protons in the core and between the protons on the central carbon in generations 1, 2 and 3 and their neighbours.

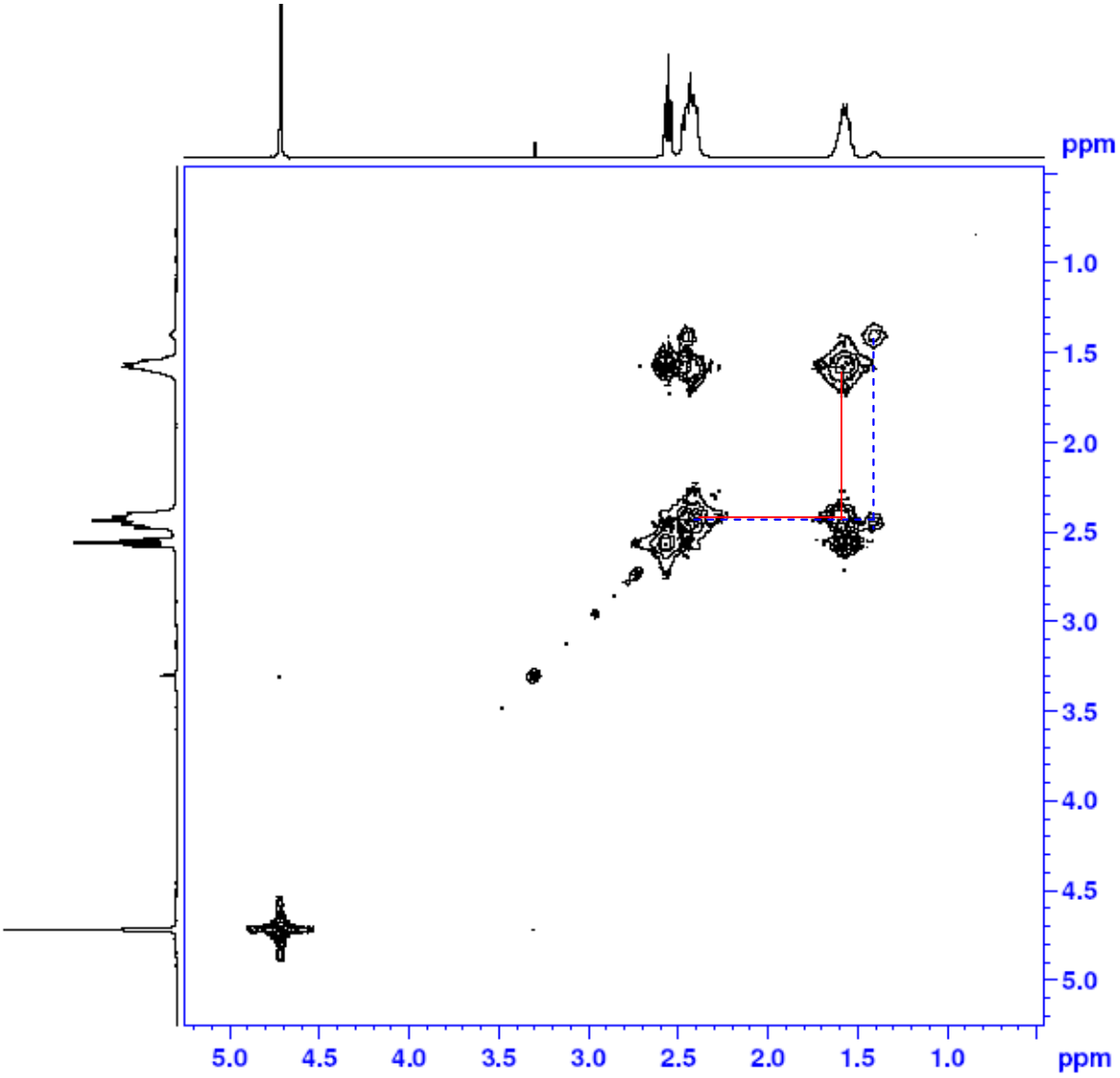

Figure 2.27: DAB COSY NMR Spectrum

The emergence of a new peak at 3.0 p.p.m. in the HA-DAB ^{1}H NMR spectrum (figure 2.28) is indicative of conjugation between HA and DAB. This new peak is a triplet representing the signal from the methylene protons on the carbon bonded to the terminal amine group involved in the amide bond formation. The downfield shift from its original position at 2.6 p.p.m. represents the increase in electronegativiy due to the proximity of the carbonyl group. The similarity of the signal units per proton ratios of this new peak and the original peak (table 2.22) suggest that there is neither free (unconjugated) DAB nor cross linking i.e. DAB molecules attached to more that one HA chain in the conjugate. If there were free DAB the ratio for the original peak would be higher and conversely if there were cross linking it would be expected that the ratio for the new peak would be higher than the original peak. Comparison of the relative areas of the signals attributable to HA (2.0, 4.4 & 4.6 p.p.m.) and DAB (1.4, 1.6 & 2.5 p.p.m.) allows the relative abundances of HA and DAB in the conjugate to be calculated (table 2.23). This analysis shows that there are on average 15.16 HA disaccharides per DAB molecule in the conjugate.

ppm	Area (Units)	Number of Protons	Units/Proton
3.0	3.93	2	1.97
2.6	58.14	30	1.94

Table 2.22: Analysis of HA-DAB ^{1}H NMR conjugation peak

ppm	Area (Units)	Number of Protons	HA/DAB
1.4	10.00	10	DAB
1.6	118.00	56	DAB
2.0	89.72	3	HA
2.5	180.17	84	DAB
4.4	32.40	1	HA
4.6	33.61	1	HA
		DAB Area/Proton (308.17/150)	**2.05**
		HA Area/Proton (155.73/5)	**31.15**
		Ratio HA:DAB	**15.16:1**

Table 2.23: HA-DAB ^{1}H NMR Analysis

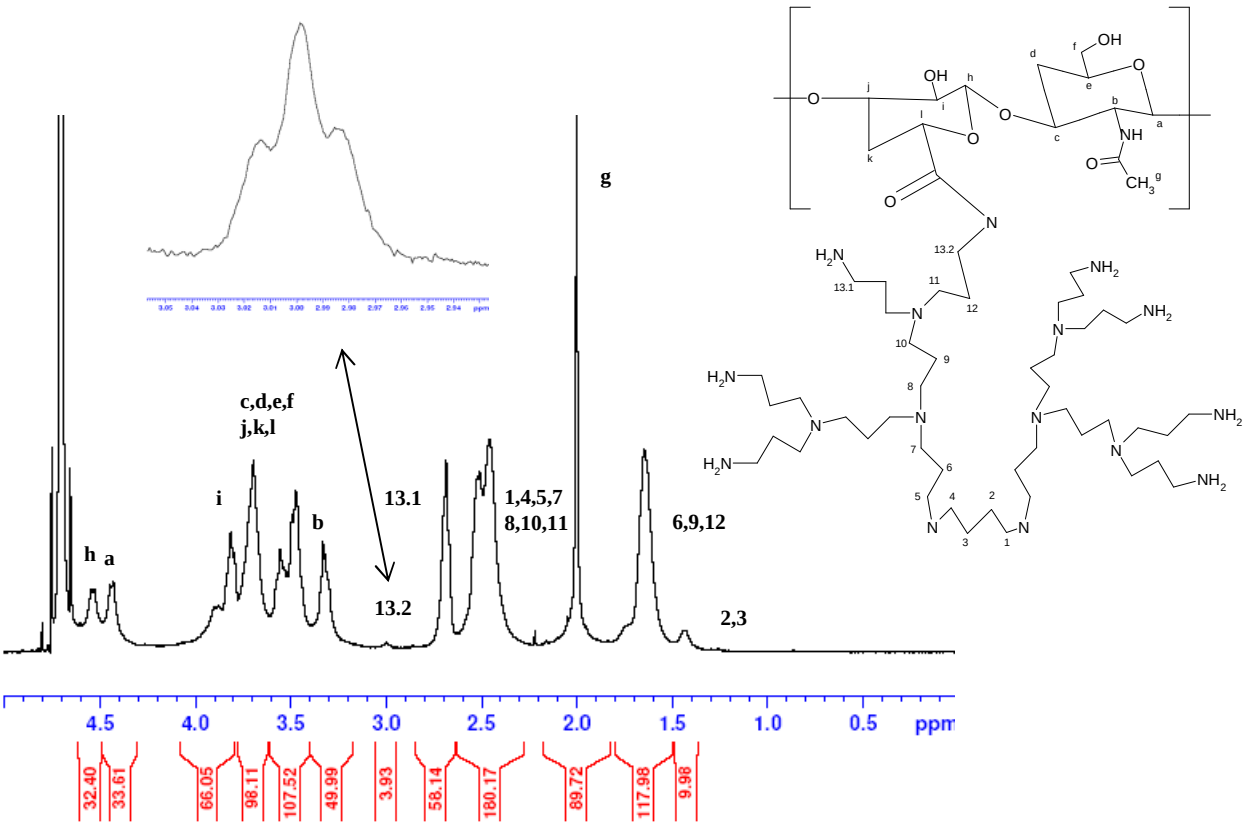

Figure 2.28: HA-DAB ^{1}H NMR Spectrum

The COSY spectrum (figure 2.29) confirms that the new peak at 3.0 p.p.m. emanates from DAB as it interacts with the DAB peak at 1.6 p.p.m.

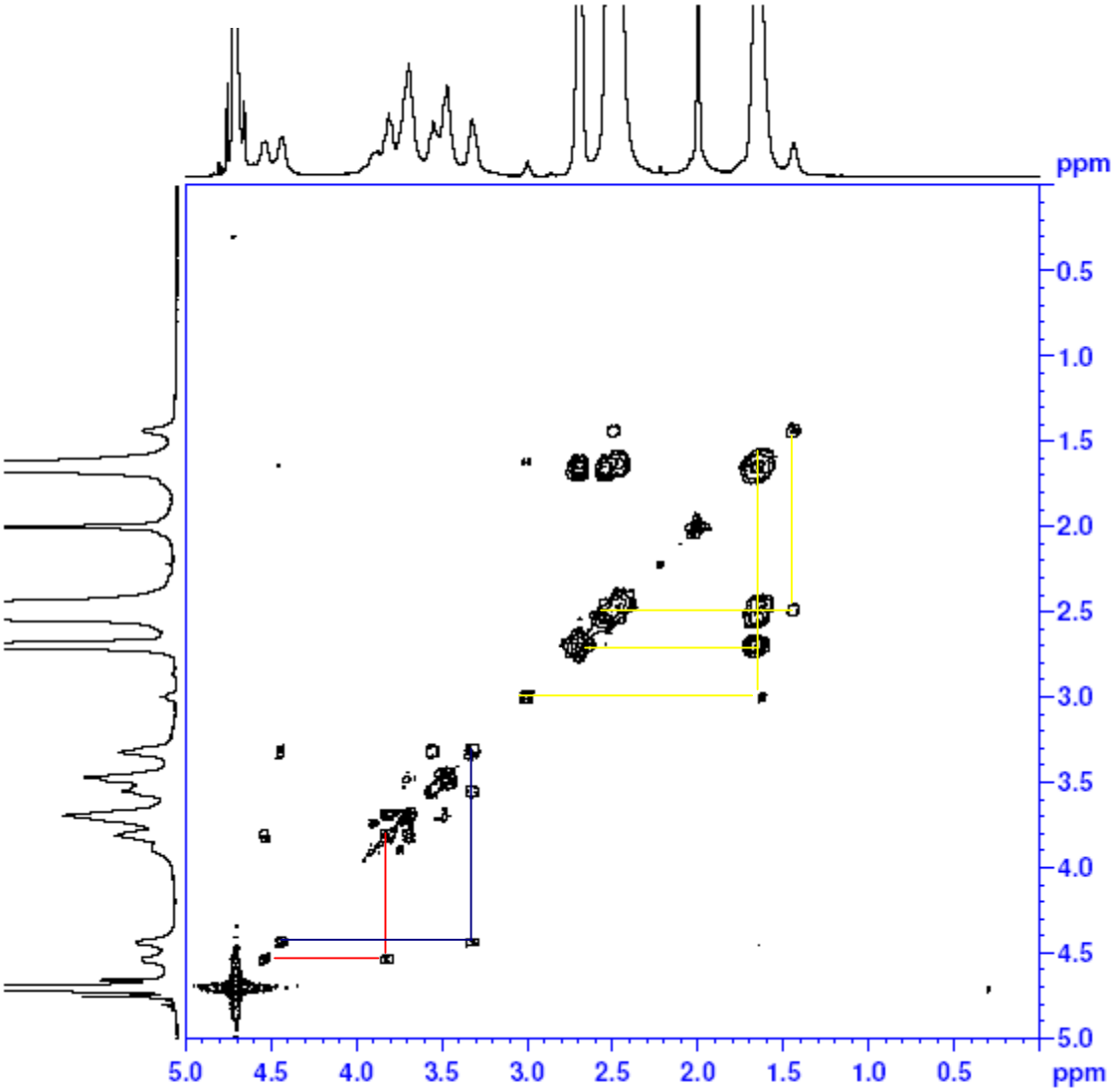

Figure 2.29: HA-DAB COSY Spectrum

2.6.3 TNBS Assay

The TNBS assay was used to determine the level of DAB in the HA-DAB conjugate by detecting terminal amine groups. A calibration was performed to determine the range in which Beer's Law was observed and to establish a relationship between amine concentration and absorbance. A fixed amount of TNBS was added to varying amounts of DAB and the absorbance read at 325nm, a linear relationship was found in the DAB range of 0-200 mol^{-9} (figure 2.30). The amount of DAB was converted to amine by multiplication by 16 to simplify subsequent analysis.

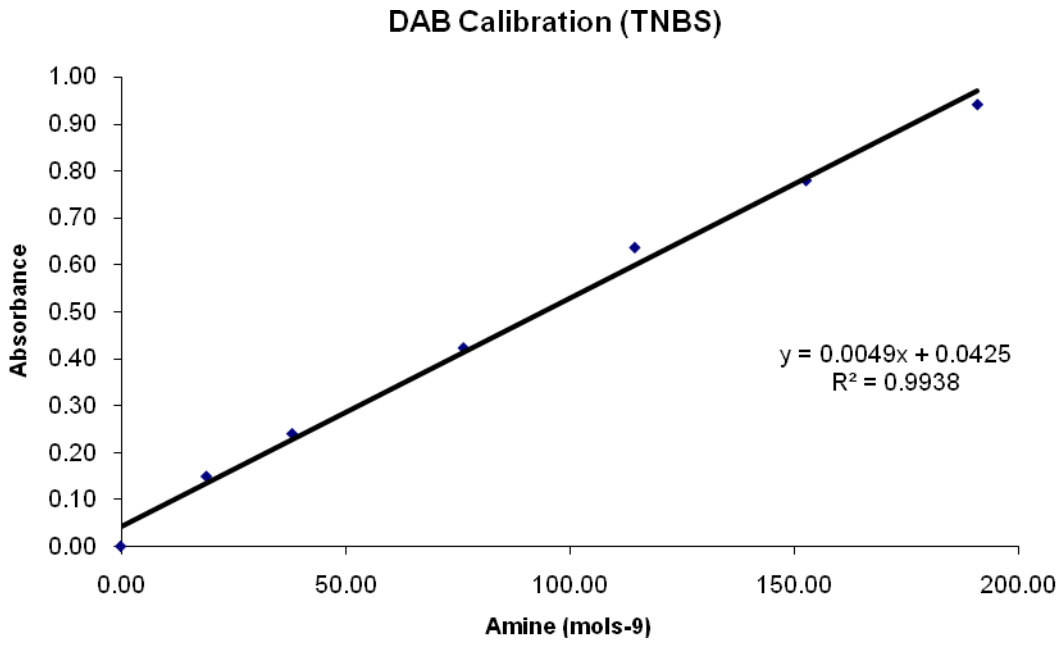

Figure 2.30: TNBS assay DAB calibration

Subsequently a 40 μg/ml HA-DAB sample was analysed and gave an absorbance of 0.44 units. Using the calibration curve this absorbance value was converted to an equivalent primary amine concentration. This value was divided by 15 (assuming that each conjugated DAB will have only 15 free primary amine as one has been used in the conjugation). From this value the mass of DAB in the HA-DAB sample was

found and subtracted from the total to give the mass of HA in the conjugate (table 2.24). The analysis showed that there are on average 15.13 HA disaccharides per DAB molecule in the conjugate.

HA35-DAB (µg)	Absorbance	Amine (mols^{-9})	DAB (mols^{-9})	DAB (µg)
40.00	0.44	81.12	5.41	9.07

HA (µg)	HA (mols^{-9})	Ratio (moles HA:DAB)
30.93	81.81	15.13

Table 2.24: TNBS assay HA-DAB sample analysis

The process (calibration and sample analysis) was repeated three times so that a standard deviation could be found. The average number of HA disaccharides per DAB molecule was found to be 14.70±0.39.

2.6.4 HA-DAB Elemental Analysis

C, H, N elemental analysis was performed to determine the composition of the HA-DAB conjugate. The starting materials (HA and DAB) were analysed and the results were found to be in good agreement with values expected from their molecular formulas (tables 2.25 and 2.26).

Element	C	H	N
% Found	35.62	6.16	3.08
Molecular Weight	12.01	1.01	14.01
Moles per 100g	2.97	6.10	0.22
Moles per Mole N	13.49	27.74	1.00

Ratio expected from molecular formula: **C:H:N 14:20:1**

Table 2.25: Elemental analysis results for HA

Element	C	H	N
% Found	52.78	11.67	21.22
Molecular Weight	12.01	1.01	14.01
Moles per 100g	4.39	11.55	1.51
Moles per Mole N	2.90	7.63	1.00

Ratio expected from molecular formula **C:H:N 2.93:6.93:1**

Table 2.26: Elemental analysis results for DAB

The conjugate was analysed by normalising the levels of the constituent elements to the level of nitrogen (table 2.27).

Element	C	H	N
% Found	41.32	7.52	7.48
Molecular Weight	12.01	1.01	14.01
Moles per 100g	3.44	7.45	0.53
Moles per Mole N	6.44	13.95	1.00

Table 2.27: Elemental analysis results for HA-DAB

The conjugate contains:

- 6.44 moles of carbon for every 1 mole of nitrogen
- or 19.33 moles of carbon for every 3 moles of nitrogen

As HA has been shown to be the backbone of the conjugate the carbon to nitrogen ratio for HA (13.49:1.00) was subtracted from that found for the conjugate (19.33:3.00). This gave a remaining ratio of 5.84:2.00 that is attributable to DAB.

- (19.33-13.49) 5.84 moles of carbon due to the presence of DAB
- (3.00-1.00) 2.00 moles of nitrogen due to the presence of DAB

As each mole of DAB contains 88.00 moles of carbon and 30.00 moles of nitrogen

- Using the carbon ratio for each mole of hyaluronic acid the conjugate contains (5.84/88.00) 0.066 moles of DAB
- Using the nitrogen ratio for each mole of hyaluronic acid the conjugate contains (2.00/30.00) 0.067 moles of DAB

In summary:

	Moles C	Moles N
HA-DAB Conjugate	**6.44**	**1.00**
HA-DAB Conjugate	**19.32**	**3.00**
Hyaluronic Acid Contribution	**13.49**	**1.00**
Per HA Disaccharide	13.49	1.00
Equivalent Moles HA Disaccharide	1.00	1.00
DAB Contribution	**5.83**	**2.00**
Per DAB Molecule	88.00	30.00
Equivalent Moles DAB molecule	0.066	0.067
Ratio (HA Disaccharide: DAB molecule) by carbon	**1.00**	**0.066**
Ratio (HA Disaccharide: DAB molecule) by nitrogen	**1.00**	**0.067**
Ratio (HA Disaccharide: DAB molecule) by carbon	**15.09**	**1.00**
Ratio (HA Disaccharide: DAB molecule) by nitrogen	**15.00**	**1.00**

Thus the average number of HA disaccharides per DAB molecule found using this analysis was 15.05.

2.6.5 Summary of HA-DAB Characterisation Results

The results obtained from the various analysis methods are in good agreement (table 2.28): it was found that on average there are 14.97±0.24 HA disaccharides per DAB molecule in the HA-DAB conjugate.

Analysis Method	Number of HA disaccharides per DAB molecule
NMR	15.05
TNBS	14.70±0.39
Elemental Analysis	15.16

Table 2.28: Summary of HA-DAB Characterisation Results

2.6.6 HA-DAB Molecular Weight Determination

2.6.6.1 dn/dc

The molecular weight of the conjugate was determined to confirm the results presented in section 2.6.5 and to confirm that only one HA-DAB species was present. The dn/dc for the HA-DAB conjugate was found to be 0.151 ml g^{-1} (figure 2.31).

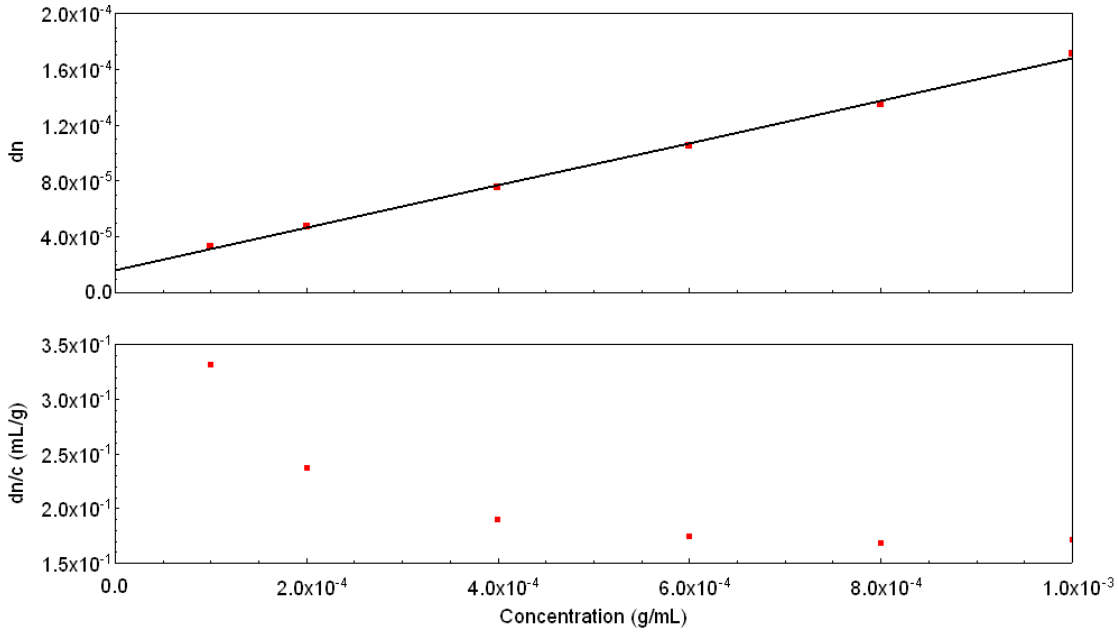

Figure 2.31: HA-DAB dn/dc curve

2.6.6.2 GPC-MALLS

The weight average molecular weight of the HA-DAB conjugate was found to be 65070 Daltons (figure 2.32).

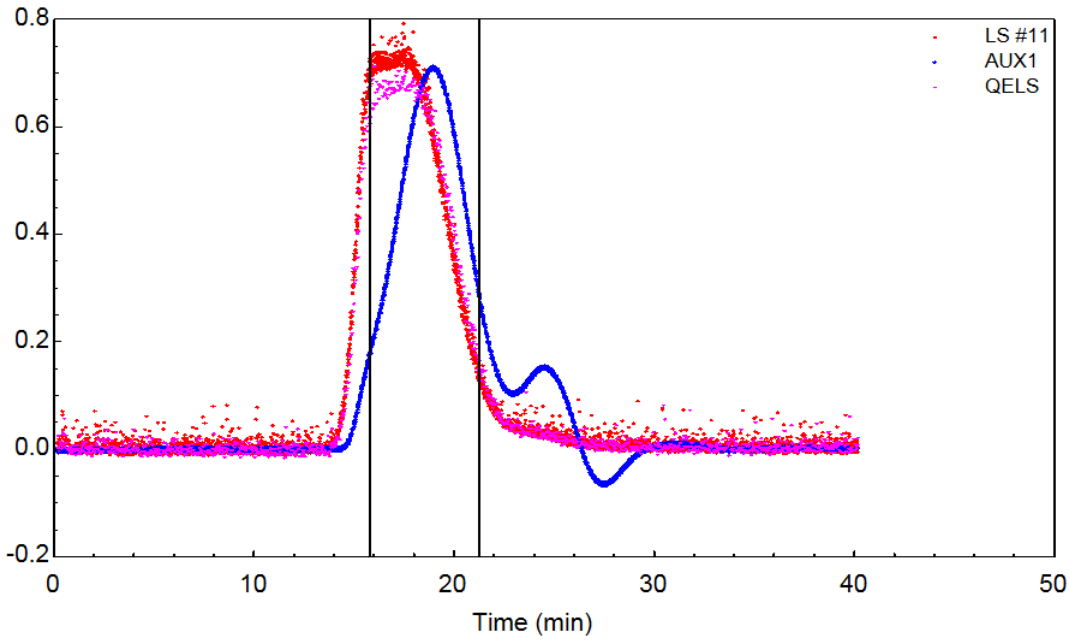

Figure 2.32: HA-DAB GPC-MALLS chromatogram

For comparison the expected molecular weight of the conjugate was calculated using the following method:

Number of disaccharides per HA chain: (42894/378) = 113.48

(Based on the previously determined MW of the parent material)

Number of DAB molecules per HA chain: (113.48/14.97) = 7.58

(Based on the previously determined HA:DAB ratio)

Total molecular weight: 42894 + (7.58x1678) = 55613.64 Daltons

The molecular weight found using GPC is approximately 15% higher than expected, this could be due to inaccuracies in the molecular weight assumed for DAB as this was not confirmed by GPC-MALLS.

2.6.7 HA-DAB-DTPA NMR

^{1}H NMR was used to determine the level of DTPA attachment to the HA-DAB conjugate. The average of the values for the anomeric hyaluronic acid protons (4.3 and 4.4 p.p.m., 22.25 and 22.38 units respectively) were taken to give the HA-DAB contribution to the HA-DAB-DTPA conjugate and the value for the benzyl protons (7.3 and 7.4 p.p.m., 39.99 units) was taken to give the DTPA contribution (figure 2.33).

- Average value for HA [(22.25 + 22.38)/2.00] = 22.32 units per proton
- DTPA value (39.99/4.00) = 10.00 units per proton

This suggests that there are (22.32/10.00) = 2.23 hyaluronic acid disaccharides per DTPA molecule.

- On average there are 14.97 HA disaccharides per 1.00 DAB molecules.

(From previously calculated HA:DAB ratio)

- Therefore proportionally there are 2.23 HA disaccharides are associated with 0.15 DAB molecules.

It follows that the ratio of the final conjugate is

- 2.23:0.15:1.00 (HA disaccharides: DAB molecules: DTPA molecules),
- alternatively 14.97:1.00:6.70 (HA disaccharides: DAB molecules: DTPA molecules).

No further information was provided by the COSY spectrum.

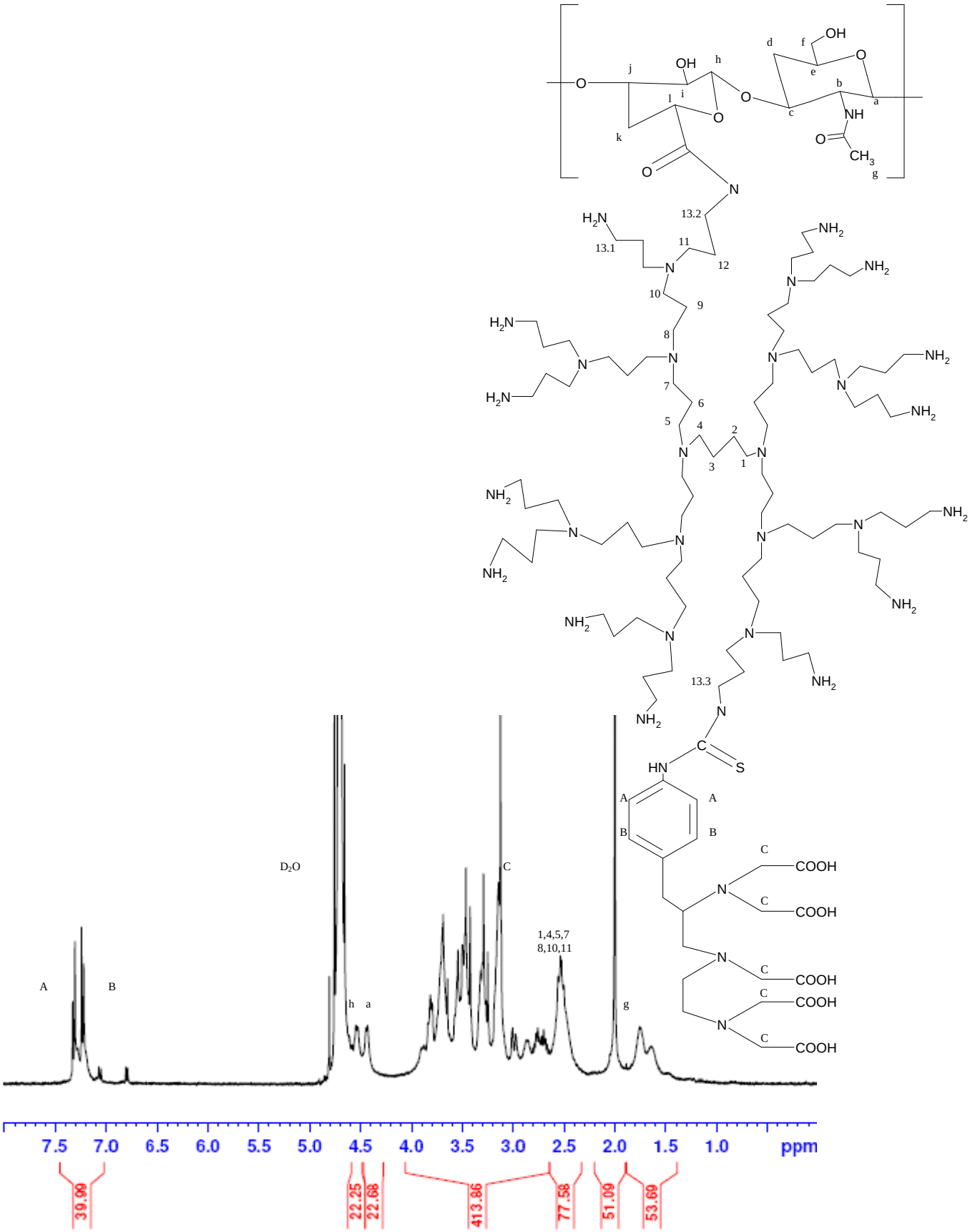

Figure 2.33: ^{1}H NMR HA-DAB-DTPA

2.6.8 HA-DAB-DTPA Elemental Analysis

Elemental analysis was also used to determine the level of DTPA attachment to the HA-DAB conjugate. The results for the HA-DAB-DTPA conjugate were normalised to the sulphur content (table 2.29) to allow the DTPA contribution to be removed (table 2.30).

HA-DAB-DTPA	Element			
	C	H	N	S
% Found	47.30	6.74	10.20	2.10
Molecular weight	12	1	14	32
Moles	3.94	6.74	0.73	0.07
Moles per mole S	60.06	102.70	11.10	1.00

Table 2.29: Elemental analysis results for HA-DAB-DTPA

	Element			
	C	H	N	S
HA-DAB-DTPA	60.06	102.70	11.10	1.00
DTPA	22.00	40.72	4.00	1.00
HA-DAB Contribution	38.06	61.98	7.10	0.00

Table 2.30: Elemental analysis calculation HA-DAB-DTPA

- The HA-DAB conjugate comprises 14.97 HA disaccharides for every DAB molecule (*from previously calculated HA:DAB ratio)*
- Therefore there are (14.97 x 14) + (88 x 1) = 297.58 moles of carbon per mole of DAB in the conjugate
- and (14.97 x 1) + (30 x 1) = 44.97 moles of nitrogen per mole of DAB in the conjugate.
- Therefore, for each DTPA molecule there are (38.06/297.58) = 0.13 HA-DAB units using the carbon contribution
- and (7.10/44.97) = 0.16 HA-DAB units using the nitrogen ratio.

Taking the average of these gives 0.15 HA-DAB units per DTPA group. This converts to a ratio of HA disaccharides to DAB molecules to DTPA molecules of 14.97:1.00:6.8 (HA:DAB:DTPA).

2.6.9 Summary of HA-DAB-DTPA Characterisation Methods

There was excellent agreement between the two different analysis methods for determining the level of DTPA attachment to the HA-DAB conjugate (table 2.31). The average ratio of DTPA groups attached to each DAB molecule is 6.75.

Analysis Method	DTPA:DAB Ratio
NMR	6.7:1.0
Elemental Analysis	6.8:1.0

Table 2.31: Summary of HA-DAB-DTPA conjugate characterisation results

2.6.10 ICP-AES

ICP-AES was used to determine the level of gadolinium in the HA-DAB-DTPA-Gd contrast agent. The values are expressed as a ratio of gadolinium mass to total contrast agent mass (table 2.32).

Gd (mg/L)	Gd (mg/ml)	Gd (mg/20 ml)	HA-DAB-DTPA-Gd (mg)	Mass Ratio (Gd:Contrast Agent)
6.44	0.006	0.129	1.41	0.091
11.20	0.011	0.224	2.20	0.102
18.40	0.018	0.368	3.88	0.095

Table 2.32: ICP-AES results for HA-DAB-DTPA-Gd

The gives an average value for the mass ratio of gadolinium to total contrast agent is 0.096 ± 0.005.

To validate this result the HA:DAB:DTPA ratio given in 4.2.3.3 is converted to an equivalent mass ratio (table 2.33).

Component	Unit Mass	Number of Units	Total
HA	378	14.97	5658.66
DAB	1678	1.00	1678.00
DTPA	540	6.75	3645.00
Gd	157	6.75	1059.75
		Total Mass	12041.41

Table 2.33: Empirical mass HA-DAB-DTPA-Gd

Hence the ratio of mass of gadolinium to the total contrast agent mass is (1059.75/12041.41) = 0.088 mg gadolinium per mg contrast agent, which is in excellent agreement with the value found by ICP-AES.

2.7 Discussion and Conclusions

Three polymeric gadolinium based MRI contrast agents were synthesised and fully characterised: two agents with glycol chitosan backbones and one with a hyaluronic acid backbone.

2.7.1 GC-DTPA-Gd: Discussion of Synthesis Results

The GC agents were synthesised in a step wise manner by first attaching DTPA to GC and then incorporating gadolinium. Two different molecular weight GC backbones were generated by varying the duration of acid degradation (2 and 48 hours) of the starting high molecular weight GC. The molecular weights of the resultant fragments were confirmed as 37,823 ± 1427 Daltons and 12,335 ± 191 Daltons in accordance with degradation time. Other degradation times were investigated (8 and 24 hours) but it was felt that the molecular weights generated were too similar to the 48 hour product hence the choice to use a 2 hour degradation. These findings were consistent with those of Wang et al (Wang 2001) who found the degradation reaction proceeded in an exponential fashion. The GC was not used in its undegraded form as degradation seemed to improve solubility.

The process to attach DTPA to the GC backbone via a reaction between the primary amine on GC and the isothiocyanate group on DTPA required iterative modification. The DTPA compound is poorly soluble in water and the reactive group is readily hydrolysed which gave the problem of solubilising the compound whilst maintaining its reactivity. It was found that both GC and DTPA dissolved readily in PBS (pH=7.4) which also provided a favourable pH for the bonding reaction. This process highlights the usefulness of acid degraded GC in this application as it is soluble in a variety of environments of pH and salt concentration. Yields were fairly high (>60%)

for both compounds with losses expected to be the result of DTPA hydrolysis or steric hindrance limiting the proportion of GC monomers that could be derivativised.

The GC-DTPA products were analysed using NMR, elemental analysis and an arsenazo based colorimetric assay. NMR confirmed the presence of both GC and DTPA in the compounds and elemental analysis and the arsenazo assay determined the ratio of GC monomers to DTPA pendant groups in the conjugate. The results of these two methods were similar with both conjugates having approximately one in five GC monomers derivativised with DTPA. Further confidence in the results of these assays is given by analysis of the yields:

- assuming no loss of GC and that one in every five GC monomers has a DTPA molecule attached a theoretical yield can be calculated:
    - GC2-DTPA: 1 mmol GC + 0.2 mmol DTPA = 205.00 mg + 108.21 mg = 313.21 mg
    - GC48-DTPA: 1 mmol GC + 0.19 mmol DTPA = 205.00 mg + 105.26 = 310.26 mg

These theoretical values compare well with the actual values obtained (332 and 325 mg respectively).

There were a number of factors to consider when determining the optimum conditions for the addition of gadolinium to the GC-DTPA conjugate. As with DTPA the GC-DTPA conjugate was poorly soluble in water but readily soluble when buffered close to neutral pH. PBS was used in the earlier conjugation step but was unsuitable at this stage as gadolinium forms precipitates with phosphate ions. A number of buffers were investigated and the most suitable was found to be an imidazole-hydrochloric acid system which provided pH control without precipitating gadolinium. It subsequently transpired that whilst GC-DTPA was soluble in this buffer GC-DTPA-

Gd was not. This meant that following chelation GC-DTPA-Gd would precipitate out of solution, however, it could be re-solubilised and excess gadolinium precipitated by the addition of phosphate buffer (pH 7). The excess gadolinium was removed by filtration and the remaining phosphate by dialysis. The system offered a good yield (~70%) for the GC2-DTPA-Gd agent but considerably less for the GC48-DTPA-Gd system (~40%). It is difficult to identify the source of this disparity without first repeating the reaction to eliminate experimental error as the potential source. Comparison of the final gadolinium level using the DTPA level in the conjugate and the ICP-AES results would appear to suggest that not all DTPA took up gadolinium. The ICP-AES results show between 10 and 20% less gadolinium than had been predicted (0.073 and 0.079 mg gadolinium per mg contrast agent for GC48 and GC2 respectively compared with the predicted level of 0.09 mg gadolinium per mg contrast agent). It is also possible that this disparity is a result of differences in sensitivities between the assays.

In summary two polymeric contrast agents were synthesised and fully and consistently characterised. One particularly interesting feature of these contrast agents was that despite a four fold difference in molecular weight the level of DTPA attachment was very similar. This consistency removes degree of substitution as a variable between the contrast agents and allows for more rigorous comparison of the molecular weight effect on the in-vivo behaviour.

2.7.2 HA-DAB-DTPA-Gd: Discussion of Synthesis Results

The HA based agent was also synthesised in a step-wise fashion by first conjugating HA and DAB then attaching DTPA and finally the incorporation of gadolinium. HA was purchased with a guide molecular weight of 35 kDa, the exact molecular weight found by GPC-MALLS was 42894 ± 802 Daltons

HA and DAB were attached using the recently commercially available carboxylic acid activating agent DMT-MM. HA is totally insoluble in organic solvents so only water soluble carboxylic acid activating agents could be used. Purification problems had been encountered when using EDAC, the most commonly used water soluble agent, hence the decision to use DMT-MM. DMT-MM proved to give good conjugation efficiency (DAB attachment to approximately 1 in 15 HA disaccharides) with no evidence (NMR and elemental analysis) of fragments remaining in the product. The ratio of starting materials (HA, DAB and DMT-MM) was expected to be crucial to the composition of the final product and it was felt that it was important to avoid cross-linking (i.e. a DAB molecule attaching to more than one HA fragment) as this would hinder characterisation and DTPA attachment. Trial and error proved that equimolar amounts of HA and DAB (which actually represents a 16 fold excess of amine to carboxylic acid groups) coupled with an excess of DMT-MM gave the best balance of level of DAB attachment and avoidance cross linking. Larger amounts of DAB proved to be difficult to remove and lower amounts of either DAB or DMT-MM gave very sparse attachment. A number of purification methods were investigated such as gel columns, ultracentrifugation and precipitation of the HA-DAB product using organic solvents with the former two methods unsuccessful in removing all unreacted DAB and the latter giving very low yields. Finally exhaustive dialysis against an ammonia solution proved to be effective in removing all unreacted DAB whilst offering reasonable yields. It was felt that the difficulty in removing excess DAB stemmed from the fact that it was possible for HA and DAB to form stable non-covalent aggregates. Further investigation proved that these complexes did form in the pH range of 3-10 (the pKas of carboxylic acid and amine groups respectively). DAB itself in sufficient quantities hinders complex formation as it has

a very alkaline pH in aqueous solution. It would appear that as unreacted DAB is removed from the reaction mixture the pH drops below 10 allowing complex formation which hinders the removal of any further non-covalently attached DAB. Ammonia is used to keep the pH above 10 and facilitate removal of all unreacted DAB. NMR was used to confirm that unreacted DAB had been removed from the final product and the GPC-MALLS results appear to confirm this as only one high molecular weight species was detected.

NMR, elemental analysis and the TNBS assay were used to determine the level of DAB attachment to the HA backbone. There was good agreement between the different techniques with the average level of attachment found to be one DAB molecule per 14.97 ± 0.24 HA disaccharides. GPC-MALLS gave a molecular weight approximately 15% higher than would be predicted but confirmed that there were no large aggregates or small species (free DAB) in the final product. The reason for the disparity in the expected and measured molecular weights could be that the conjugate's structure gives it a higher effective molecular weight. In addition, the fact that the molecular weight of DAB used in calculations was assumed from its molecular formula and not confirmed experimentally could be a source of error.

Following this characterisation DTPA was attached to the conjugate and the level of attachment determined by NMR and elemental analysis. Further analysis using the arsenazo assay was not possible as the conjugate was not soluble in the acidic conditions the assay requires. There was excellent agreement between the results of these two techniques with NMR and elemental analysis indicating that there were 6.7 and 6.8 DTPA groups attached to each DAB molecule respectively. The level of attachment is high, assuming each DAB molecule has 15 amines available for attachment just less than half of these have reacted with DTPA. These analyses do

not differentiate between free and conjugated DTPA but it would appear unlikely that free DTPA would remain in the product as the molecular weight of DTPA (550 Da) is considerably less than the cut off of the dialysis tubing that was used (12-14 kDa).

ICP-AES confirmed both the presence of gadolinium in the final HA-DAB-DTPA-Gd product and that its levels were as expected from previous characterisation. From the DTPA levels detected in the HA-DAB-DTPA conjugate it would be expected that there would be 0.088 mg of gadolinium per mg of contrast agent and the level detected by ICPAE was 0.096 mg of gadolinium per mg of contrast agent.

2.7.3 GC-DTPA-Gd Synthesis Conclusions

As far as we are aware this is the first report of a precipitation type approach being used in the synthesis of diethylene triamine pentaacetic acid (DTPA) based MRI contrast agents. Generally these agents are produced using an excess of gadolinium which is removed using dialysis (Shiftan et al. 2005) or difiltration (Kobayashi et al. 2001). The advantage of this approach for this synthesis protocol was the minimisation of material losses compared with the traditional dialysis approach.

A number of polymeric backbones have been proposed for MRI contrast agents details of which are given in chapter one. The most similar to the agents produced here in terms of structure and intended use is NMS60 which comprises a tri-chitosan backbone with 3 Gd-DTPA units attached giving an overall molecular weight of 2158 Daltons (de Crespigny et al. 1999). It has been shown that, as expected, this compound has a longer plasma residence time and greater relaxivity than Magnevist. However, the published results of the imaging studies make direct evaluation of NMS60 as a blood pool agent difficult as magnetic resonance angiography (MRA) studies were used. These studies would be expected to highlight blood vessels even

in the absence of contrast material and so compromise the ability to evaluate the vascular specificity of the NMS60 agent (Bammer et al. 2004; D'Arceuil et al. 2004).

The main advantage of the agents reported here over those in the literature is the range of molecular weights that can be produced using a glycol chitosan backbone. Varying the degree of acid degradation generates fragments with molecular weights in the range of 8-250 kilo-Daltons (Wang et al. 2001) and other degradation techniques can be used to give molecular weights as low as 4 kilo-Daltons (Qu et al. 2006). This is advantageous as it should allow an optimum molecular weight for the balance between plasma residence time and whole body clearance to be found. Furthermore it affords the potential to produce contrast agents with a variety of molecular weights which can be used as surrogates for a number of different types of drugs in transport studies (discussed further in the next chapter).

2.7.3 HA-DAB-DTPA-Gd: Synthesis Conclusions

Dendrimers have been used extensively in the synthesis of MRI contrast agents (Kobayashi et al. 2005) due to the repeatability with which they can be produced and their large number of surface functional groups (Dufes et al. 2005). Contrast agents have been produced based on various generations of both the PAMAM and DAB dendrimers using an activated DTPA (2-(isothiocyanatobenzyl)-6-methyl-diethylenetriaminepentaacetic acid) (Kobayashi et al. 2005). Hyaluronic acid has also found use in MRI contrast agents as a probe for hyaluronidase activity (Shiftan et al. 2005). Gd-DTPA was attached to high molecular weight hyaluronic acid using an ethylenediamine linker and the coupling agent N-(3-dimethylaminopropyl)-N-ethylcarbodiimide hydrochloride (EDC), the conjugate was then attached to agarose beads (Shiftan et al. 2005). The premise being that hyaluronidase activity is elevated in Ovarian carcinoma and that preferential degradation of the hyaluronuic acid in the

tumour would ‘activate’ the contrast agent hence imaging the tumour (Shiftan et al. 2005).

Few contrast agents have been reported which attempt to directly target tumours via over-expressed receptors. One which does and is of particular relevance to this study involved the attachment of a folic acid targeting moiety to a PAMAM generation 5 dendrimer derivitised with Gd-DOTA (Swanson et al. 2008). This study is particularly good as the targeting efficacy is confirmed by comparison with the results of a folic acid free version of the dendrimer Gd-DOTA conjugate, it also gives some confidence in the principle of an HA-DAB-DTPA-Gd conjugate to target tumours over-expressing the CD44 receptor.

We believe that this is the first MRI contrast agent that has been designed to have potentially tumour targeting and therapeutic capabilities. Furthermore, it is worth noting that this is the first report of the synthesis and exhaustive characterisation of the HA-DAB conjugate. This conjugate alone would be expected to have targeted anti-tumour activity due to the intrinsic anti-tumour activity of DAB (Dufes et al. 2005) and the HA affinity for tumours over-expressing the CD44 receptor (Sherman et al. 1994).

Chapter Three MRI Theory, Methods and Results

3.1 Introduction

3.1.1 Background

This chapter contains a brief overview of the physics underpinning magnetic resonance imaging (MRI). The basis of MRI is the theory of nuclear magnetic resonance (NMR): the absorption and emission of energy by atomic nuclei in the presence of an externally applied magnetic field. It is generally believed that MRI was adopted as the name due to the negative connotations of the word nuclear. This discussion covers the history of the technique, the concepts of nuclear spin, excitation and relaxation, signal localisation, the different types of MRI sequence, the mathematics of MRI and the mechanism of action of contrast agents.

Specific details of the imaging protocols, hardware and data analysis methods used in these studies are given.

3.2 Aims and Objectives

The overall aims of the MRI section of this work can be split into three categories; imaging, data analysis and image presentation. The major objectives in imaging terms were to investigate the suitability of two different molecular weights of a novel polymeric MRI contrast agent for use as blood pool agents and to explore their kidney clearance pattern. The first objective was achieved by the 3D imaging of the contrast agents in the mouse head and the second by 2D imaging of a number of slices through the mouse kidney. Separate studies on mice bearing flank tumours were performed to explore the capabilities of an in-house produced solenoid radio-frequency (RF) coil set-up. These studies involved both dynamic contrast enhanced (DCE)-MRI and magnetic resonance angiography (MRA). Techniques were developed in parallel to

process the raw data produced in a manner that facilitated effective image presentation.

3.3 MRI Theory

3.3.1 Background

The 1952 Nobel Prize in Physics was jointly awarded to Felix Bloch and Edward Mills Purcell who worked independently in the "development of new methods for nuclear magnetic precision measurements" (Nobel-Foundation 2008). The basis of their discoveries which were the first steps in the development of clinical magnetic resonance imaging (MRI) were:

- atomic nuclei in a strong magnetic field rotate at a frequency that is dependent on the strength of the magnetic field
- the energy state of atomic nuclei can be increased if they absorb resonant radio waves i.e. those with the same frequency
- the nuclei release radio waves as they return to their original energy level

The first observation is based on the Larmor relationship which states that the angular frequency or precession of nuclear spins is proportional to the strength of the applied magnetic field (Nobel-Foundation 2008). A number of subsequent discoveries and technological advances led to the publishing of the first human image obtained using MRI in 1977 (Mansfield et al. 1977). The image was a cross section of a human finger showing considerable anatomic detail. Paul Lauterbur and Peter Mansfield were jointly awarded the Nobel Prize in Physiology or Medicine in 2003 for their work in developing the principles of modern MRI that facilitated its breakthrough in medical diagnostics and research (Mansfield et al. 1977).

3.3.2 MRI Physics

3.3.2.1 Spin

Only an overview of the fundamental principles of MRI is given as a more detailed discussion would involve theories based in the field of quantum mechanics which are beyond the scope of this thesis. However, the concept of nuclear spin is important in any discussion of the theory of MRI, spin is like charge or mass in that it is an intrinsic property of elementary particles. Specifically it is a quantum mechanical property and as such it is incorrect to think of it in the purely classical sense of rotation (Merbach et al. 2001) that its name would suggest. Hydrogen atoms are the most abundant in the human body and the ^{1}H isotope which contains one unpaired proton has a spin number of ½. In simple terms the spin of the hydrogen nuclei can be thought of as a magnetic moment vector that makes them behave like a compass needle when placed in a magnetic field (McRobbie 2002). The spin number (I) of a nuclei determines the number of possible discrete orientations that it may adopt when placed in a magnetic field as predicted by the equation 2I+1, hence a hydrogen nuclei has two possible orientations (Merbach et al. 2001). These two orientations represent either the high energy (anti-parallel) or low energy (parallel) state. At equilibrium in a magnetic field a small majority of the nuclei will be in the low energy state with their magnetic dipoles in the direction of the applied field giving a net magnetization vector in the direction of the field (figure 3.1) (Merbach et al. 2001). It can also be seen that out with the influence of a magnetic field these magnetic moments are randomly orientated giving a net magnetisation of zero

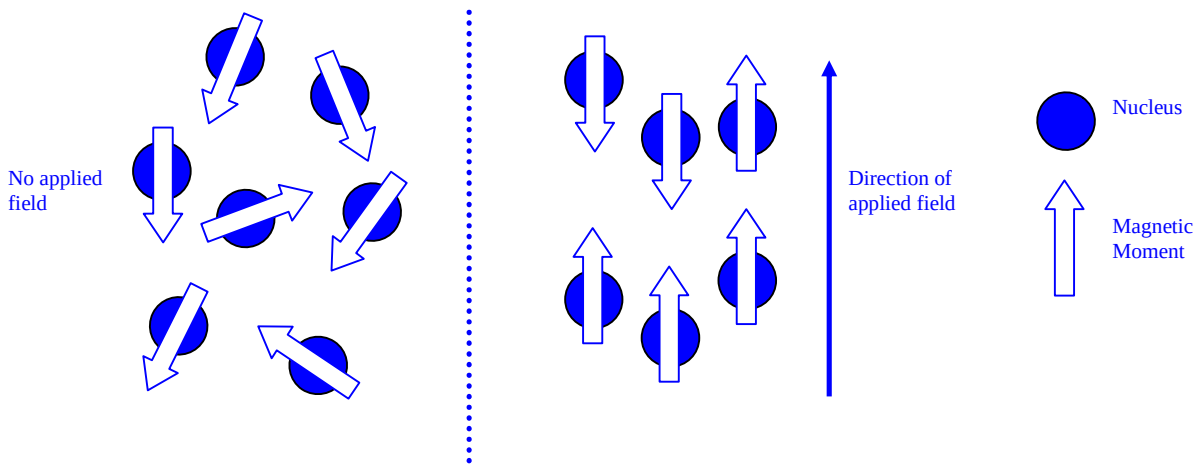

Figure 3.1: Representation of spin orientation with and without an applied magnetic field (Merbach et al. 2001)

The nuclei not only align with the field (either parallel or anti-parallel) they also precess around it at a frequency proportional to the magnitude of the applied field known as the resonant or Larmor frequency (figure 3.2) (Merbach et al. 2001). Spins can move between high and low energy states either by absorbing or releasing energy at the resonant frequency (Merbach et al. 2001).

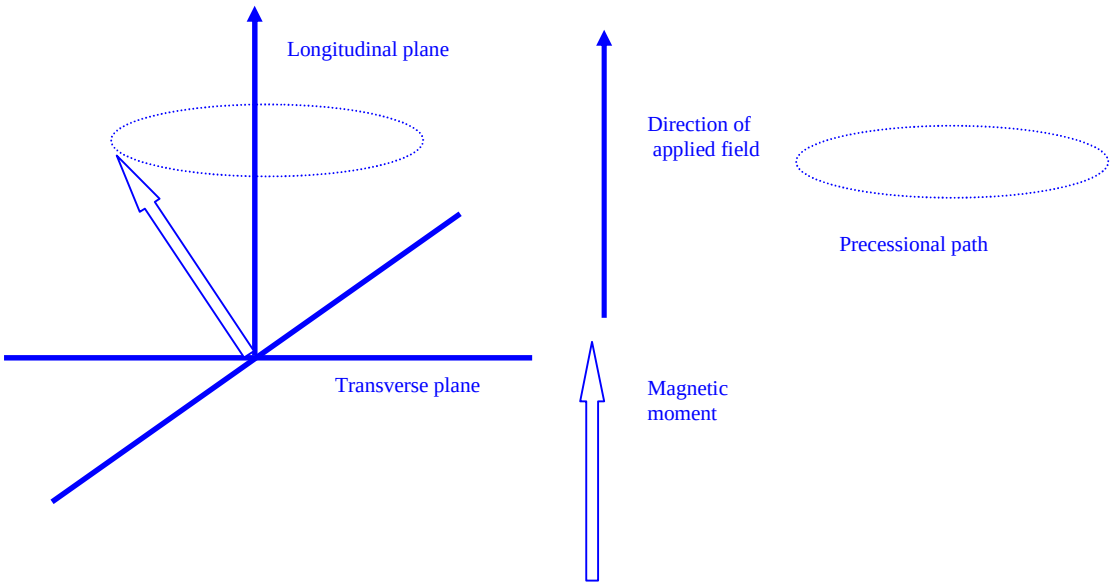

Figure 3.2: Precession of net magnetisation in applied magnetic field (Merbach et al. 2001)

3.3.2.2 Excitation and Relaxation

As mentioned above when a body is placed in a magnetic field the magnetic moments of the hydrogen nuclei will form a net magnetisation vector in the direction of the applied field, this vector is described as longitudinal magnetisation (Merbach et al. 2001). The vector must be 'flipped' into the transverse plane to allow it to be detected and this is achieved using a radiofrequency (RF) pulse at the resonant frequency applied at 90° to the static magnetic field (figure 3.3). Following this pulse an RF receiver can be used to detect the transverse magnetisation (Merbach et al. 2001). The pulse is said to have 'excited' the spins and they will transiently 'relax' back to their original equilibrium position. The spins continue to precess but now around the transverse plane and the net magnetisation vector induces a current in the

detector coil each time it passes into alignment, this time varying signal is known as a free induction decay (FID) (McRobbie 2002).

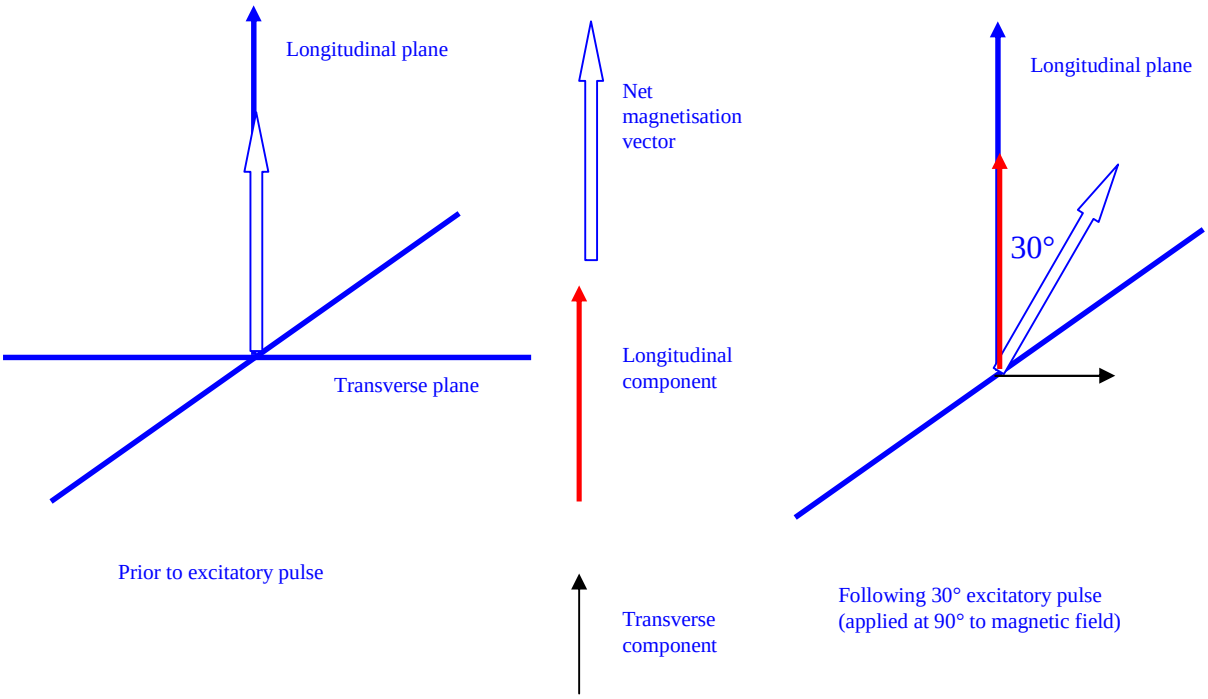

Figure 3.3: Representation of the effect of an excitatory pulse on the net magnetisation vector (McRobbie 2002)

Two processes occur after the RF pulse: longitudinal magnetisation recovery and transverse magnetisation decay. The former occurs as the result of the loss of energy of the nuclei in the high energy state by a process known as spin-lattice relaxation (Merbach et al. 2001). The fluctuating magnetic field generated by the random motion of molecules in the surrounding medium stimulates the nuclei to release energy. This process is characterised by the spin lattice relaxation time or T_1 time constant (defined as the time taken for 63% of the longitudinal magnetisation to recover) (Merbach et al. 2001). The T_1 value depends on the tissue in which the nucleus is located (McKie et al. 2005):

- fatty tissues have short T_1 values

- water based tissues have intermediate values
- fluids have the longest T_1 values

The transverse (measured) magnetisation decays as a result of spin-spin relaxation characterised by the time constant T_2 (Merbach et al. 2001). Immediately after a 90° RF pulse the spins precess coherently in the transverse plane at the Larmor frequency. Over time the spins de-phase as a result of the influence of the magnetic field of neighbouring spins (spin-spin interactions) (Merbach et al. 2001). The T_2 time constant is defined as the time taken for a 63% reduction in transverse magnetisation (Merbach et al. 2001) (figure 3.4). Another time constant exists, T_2^* that takes into account both the effect of spin-spin interactions and of inhomogeneities in the applied field, as a result the T_2^* time will be shorter than the T_2 time (Merbach et al. 2001). Fluids have the longest T_2 times and fat the shortest (McKie et al. 2005).

Next Page Figure 3.4: Representation of the MRI relaxation processes

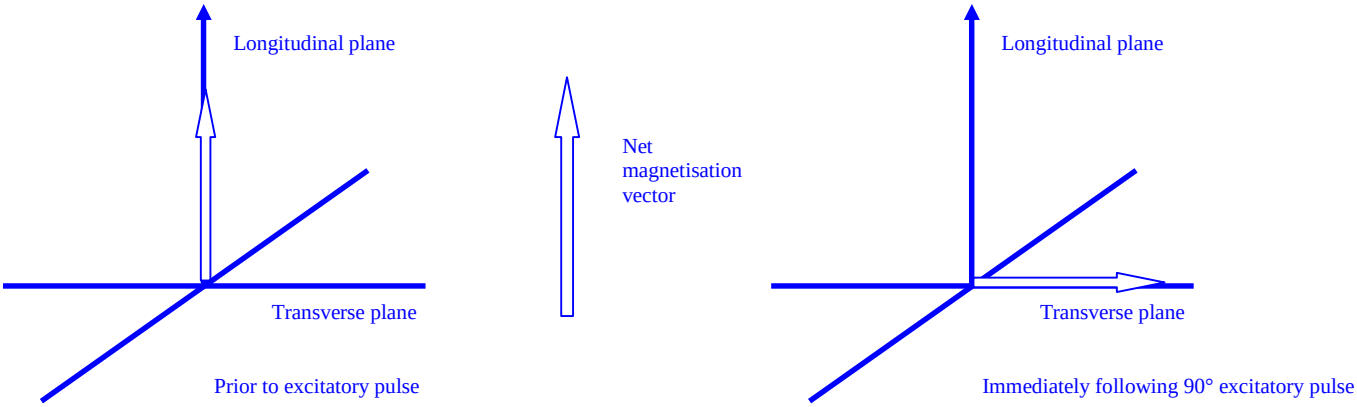

T_1 recovery (left) occurs simultaneously but independently from T_2 decay (right)

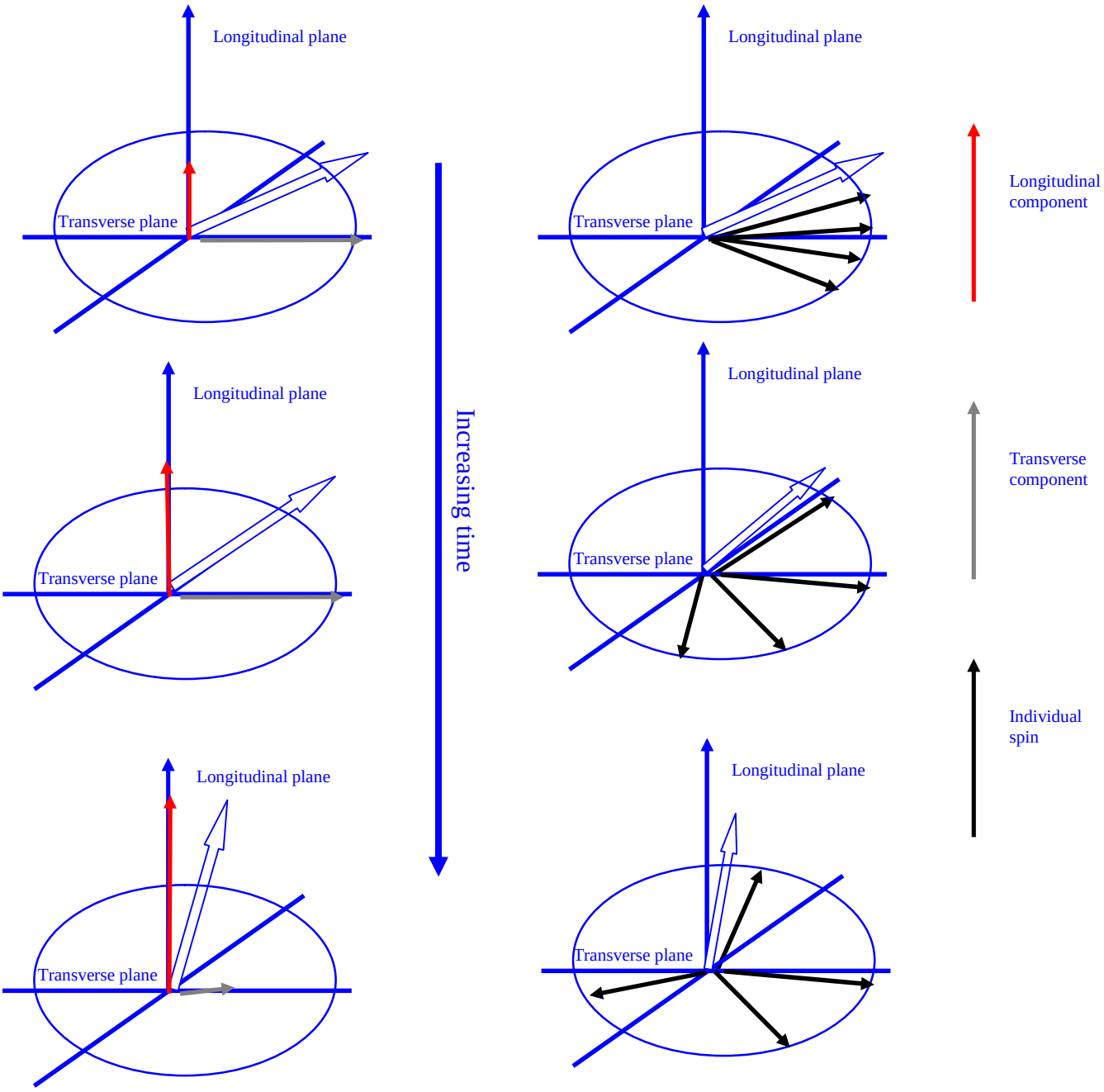

3.3.2.3 Signal Localisation

The applied magnetic field can be varied in three directions to allow localisation of the origin of a detected signal (McRobbie 2002). The variations are achieved using three sets of gradients which allow three dimensional localisation via the processes of slice selection and frequency and phase encoding. The slice selection process uses a set of gradients to modify the local magnetic field experienced by a small tissue subsection thus changing the resonant frequency of the spins in that region (resonant frequency is proportional to applied field) (McRobbie 2002). These spins can then be selectively excited by subsequent pulses at this specific frequency. The remaining two gradient sets are used to influence the frequency and phase of the spins in this sub-section. This information is then contained in the FID from which the 3D origin of the signal is found via the Fourier Transform mathematic operation (McRobbie 2002).

3.3.2.4 Proton Density, T_1 and T_2 Weighted Sequences

In practise the region of interest (ROI) will be repeatedly excited and a number of FIDs measured, the chain of events is known as a pulse sequence (McRobbie 2002). Pulse sequences are tailored to highlight features specific to the condition under investigation. The parameters T_r (repetition time), T_e (echo time) and α (flip angle) are used to describe the pulse sequence and their relative values determine whether the resultant image will be weighted by proton density or T_1 or T_2 effects (McRobbie 2002). For example T_1 imaging pulse sequences have shorter repetition times which means that tissues with short T_1 times have the highest signal. The signal from tissues with long T_1 times are diminished as there is insufficient time between pulses to allow full relaxation of longitudinal magnetisation (McRobbie 2002). This means that with each pulse the signal from these tissues reduces as the magnitude of the starting vector

has been reduced. This type of imaging is useful for anatomical investigations. T_2 imaging uses longer echo times allowing the decay of tissues with short T_2 times (McRobbie 2002). Thus high signal (bright) regions are identified as having a high fluid content and so is useful in the imaging of oedema and inflammation. If a short echo time and long repetition time are selected the T_1 and T_2 effects will be minimised and the resultant image is described as being weighted by proton density (McRobbie 2002).

3.3.2.5 Gradient and Spin Echo Sequences

The signal that emanates from coherent spins following excitation is known as an echo (Merbach et al. 2001). Generally echoes are produced by one of two methods: spin echo or gradient echo. A spin echo (SE) pulse sequence uses a 180° refocusing pulse to flip the spins in the transverse plane at a specific time following the initial excitatory pulse (Merbach et al. 2001). This 180° pulse can be thought of as re-phasing the spins: those that had a higher frequency of precession will now be 'behind' those with a lower frequency. The faster spins will again 'catch-up' forming a coherent signal after a specific time (T_e) forming a spin echo. The SE sequence known as the multi-slice multi echo (MSME) sequence is used in the kidney imaging studies in this work. In a gradient echo (GE) sequence there is no 180° pulse, instead two opposite gradients are applied sequentially following the excitatory pulse to generate the echo by reversing the direction of the spins (Merbach et al. 2001). Generally GE sequences use lower flip angles in conjunction with shorter Tr and Te which allows more rapid imaging (McRobbie 2002), however they are more influenced by the quality of the applied magnetic field. Two commonly used pulse sequences based on the GE principle are known as FLASH (Fast Low Angle Shot) [used in these studies] and SPGR (Spoiled Gradient) sequences (McRobbie 2002).

3.3.2.6 Magnetic Resonance Angiography (MRA)

Magnetic Resonance Angiography (MRA) is a technique that provides images in which flowing blood is prominent (Muhs et al. 2007). Gradient echo sequences form the basis for the most commonly used types of MRA: time of flight (TOF) angiography and phase contrast angiography. The principle of the TOF technique is to use multiple pulses with a short T_r to saturate the signal from the spins in a particular tissue slice. Thus the echo for this slice will only contain signal from blood which has flowed into the slice during the pulse sequence and so not been fully saturated. Images are built up using this approach on a slice by slice basis and the slices can be 'joined' in post processing. Phase contrast angiography relies on the fact that flowing blood induces a shift in phase of the MR signal. Pairs of images with different sensitivities to this flow effect are obtained and subtraction removes the background signal leaving only the signal that results from the flowing blood. Phase contrast MRA can be used to measure velocity as the phase shift is proportional to velocity. MRA has found clinical relevance particularly in brain imaging but it has a number of limitations such as the achievable spatial resolution and the fact that images are influenced by the direction and speed of blood flow.

3.3.2.7 Radiofrequency Source and Detection

The radiofrequency (RF) transmitter provides the pulses of energy that excite the protons. The RF system consists of a frequency synthesiser, a power amplifier and a transmitter coil (McRobbie 2002). The transmitter coil can also be used to detect the resultant signals generated by the tissue. Ideally the coil should be as close as possible to the tissue of interest to reduce losses, in practice this is achieved using coils with different geometries which include birdcage head coils and surface coils which can be placed directly on the skin.

3.3.2.8 k-Space and the Fourier Transform

The signals detected from the body are stored in an array known as k-space (McRobbie 2002). k-space is related to the final image by the Fourier transform mathematical operation. The radiofrequency signal that is detected can be thought of as an oscillating wave, this wave is converted into a series of complex numbers that represent the amplitude, frequency and phase of the wave at a given point by a digitaliser. Each point in k-space represents a different spatial frequency in the final image and the value at that point determines the brightness of that spatial frequency in the final image. This concept becomes clearer by examining the effects on the final image of filtering the k-space data (figure 3.5). The size of the k-space array and the image array will be identical but values at the same point in each array do not correspond to each other geometrically. k-space data is sometimes referred to as raw data and the final image data as the reconstruction.

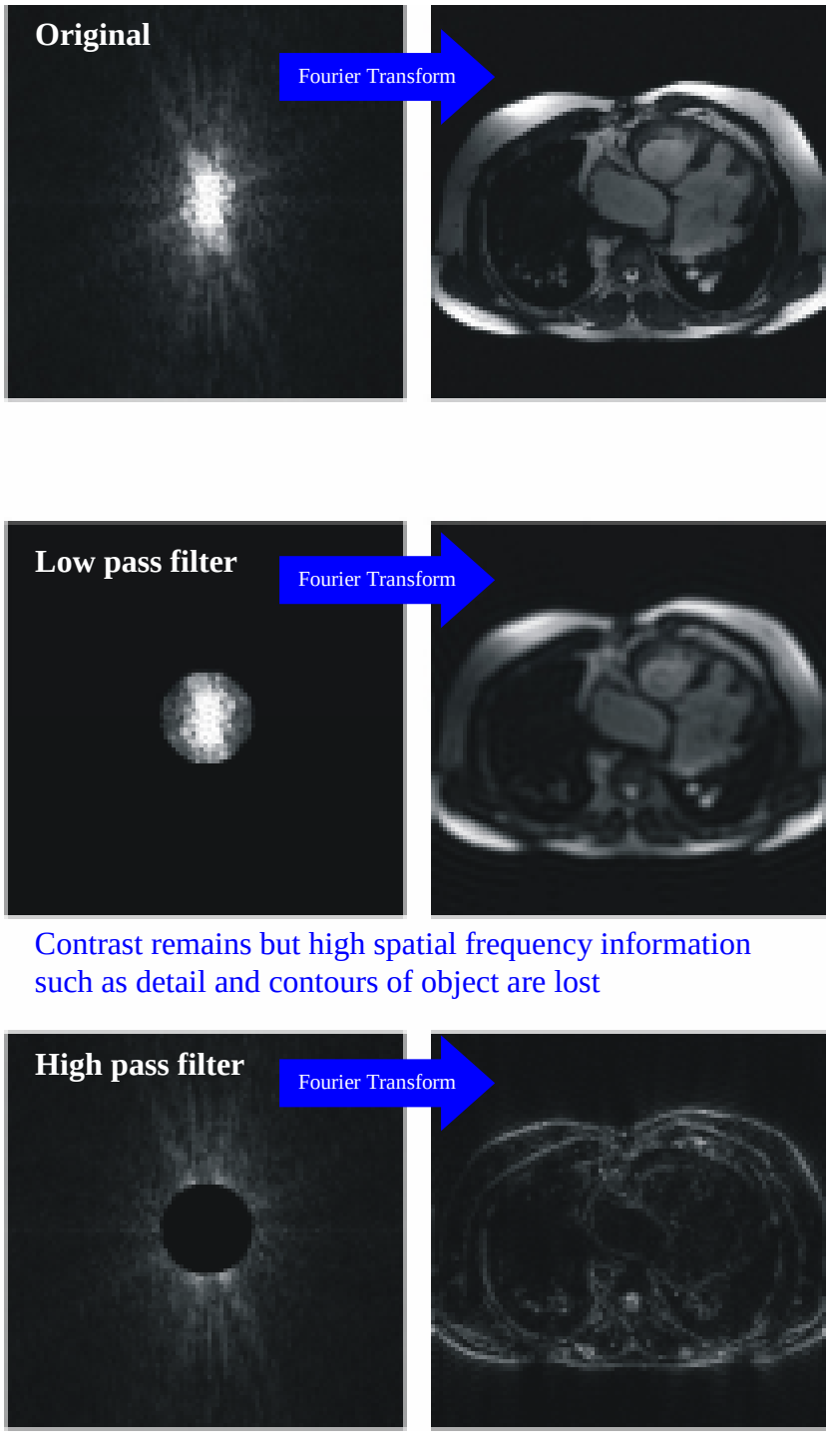

Figure 3.5: Relationship between k-space (left) and MR image (right) showing effect of low and high pass filtering (Moratal et al. 2008)

3.3.2.9 Mechanism of Action of Contrast Agents

Contrast agents are compounds that are used to improve image contrast and/or aid in the diagnosis of diseases, they are classified as either T_1 or T_2 agents depending on their primary effect (Caravan et al. 1999). In T_1 imaging a T_1 contrast agent will cause a brightening of the tissues in which it is present as a result of a reduction in the T_1 time (Caravan et al. 1999). Conversely T_2 contrast agents in T_2 weighted imaging will darken the regions in which they are present as a result of the reduction in T_2 time (loss of transverse magnetisation) (Caravan et al. 1999). The majority of contrast agents used clinically are based on either paramagnetic (T_1) or ferromagnetic (T_2) materials (Raymond et al. 2005). This work is concerned with T_1 contrast agents and so they will be discussed in more detail. Paramagnetic materials are those that align with a magnetic field but exhibit no properties of magnetism out with an applied field. Paramagnetic materials exhibit a T_1 shortening effect by creating local fluctuations in magnetic field which stimulates spins to release energy and hence 'relax' back to the longitudinal plane (Caravan et al. 1999). These materials have an effect directly on co-ordinated water molecules (inner sphere) and indirectly on the surrounding water molecules linked via hydrogen bonding (outer sphere) (Raymond et al. 2005). The T_1 shortening effect of a contrast agent depends on the total number of inner and outer sphere water molecules, the water exchange rate and the rate of molecular tumbling of the contrast agent (Raymond et al. 2005). An optimal contrast agent will have a greater number of inner sphere water molecules, a short residence time and the slow tumbling rates associated with larger molecules (Raymond et al. 2005).

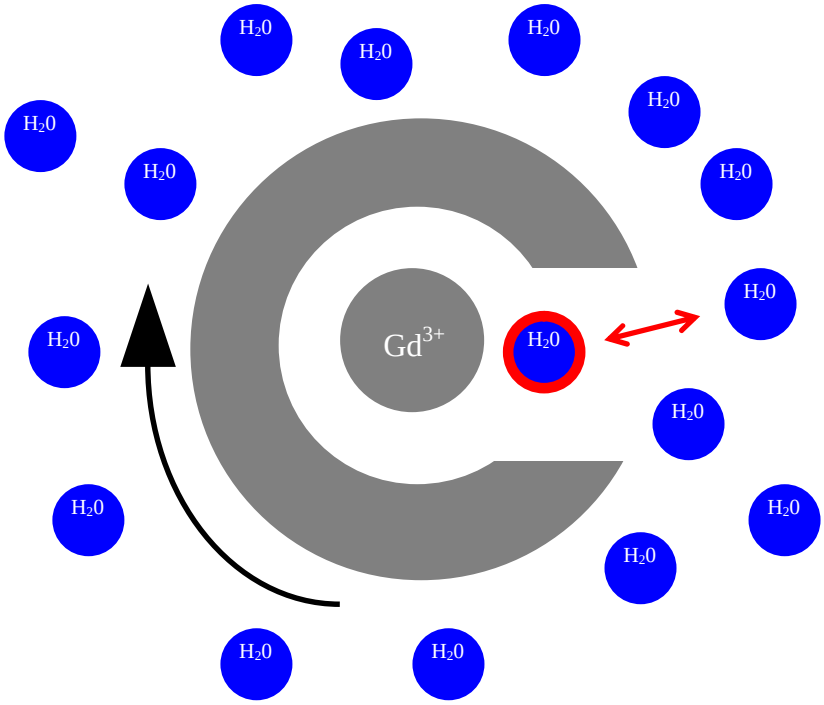

Figure 3.6: Representation of features of contrast agent relaxation; inner sphere water molecule (red), bulk water (blue), water exchange rate (red arrow) and molecular tumbling rate (black arrow)

3.4 Methods

3.4.1 General Information

All MR imaging was performed on a Bruker Biospin Advance system using a 7T horizontal 30cm bore magnet (figure 3.7). A Bruker micro-imaging gradient insert (BG-6) inner diameter 60mm was used with a 100A amplifier giving a maximum gradient of 1000 mTm^{-1} with a rise time of 50µs. The scanner was operated using Paravision software version 3.0.

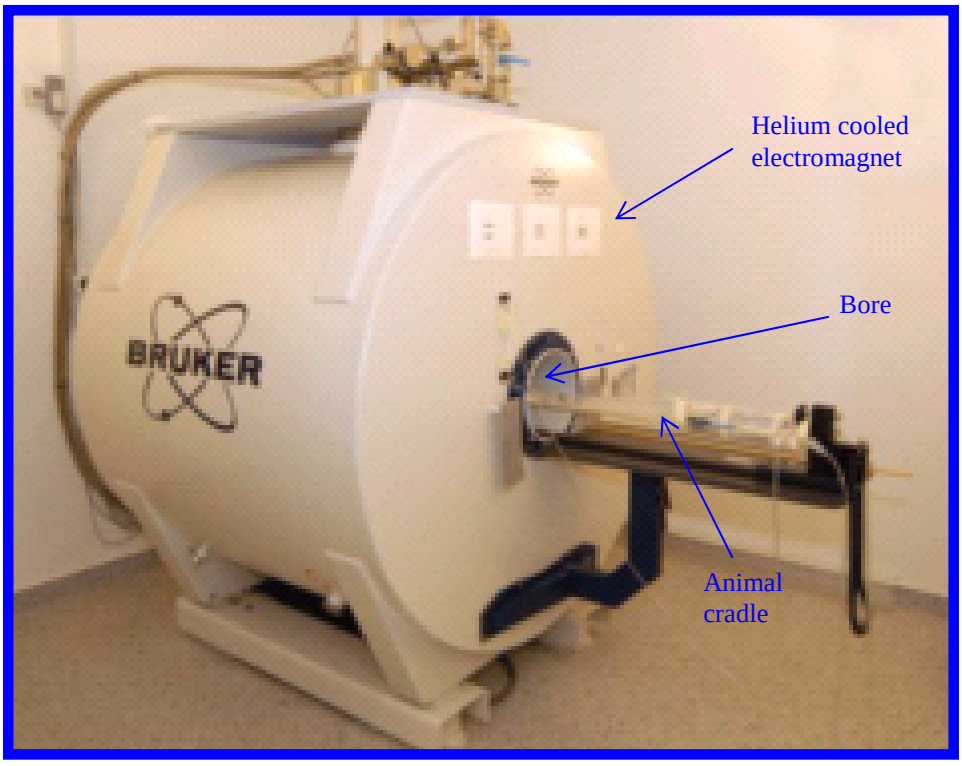

Figure 3.7: Bruker Biospin Advance 7T MRI scanner

3.4.2 Animal Preparation and Maintenance

All studies used female nude mice (CD1-nu, mean weight 20 g). Mice were anaesthetized using 2–3% isofluorane, in a 70/30 mixture of nitrous and oxygen, applied via a face mask. The body temperature was maintained at 37°C, using a water jacket. Temperature, respiration and ECG were monitored using a BIOPAC system (Goleta, CA, U.S.A.).

3.4.3 Tumour Cell Lines

All tumour studies were performed on nude mice bearing established A431 epidermoid carcinoma flank xenografts of approximately 5 mm in diameter.

3.4.4 Animal Cradle and Solenoid RF Coil

In all cases mice were introduced into the bore of the magnetic using a plastic cradle (figure 3.8-3.12). For brain and kidney studies a cylindrical RF resonator coil (Bruker, Germany) was used. For tumour studies a custom built solenoid RF micro-coil that slots into the animal cradle was used (Holmes et al. 2008). The flank tumours were placed directly within the plastic cylinder round which the coil was wrapped.

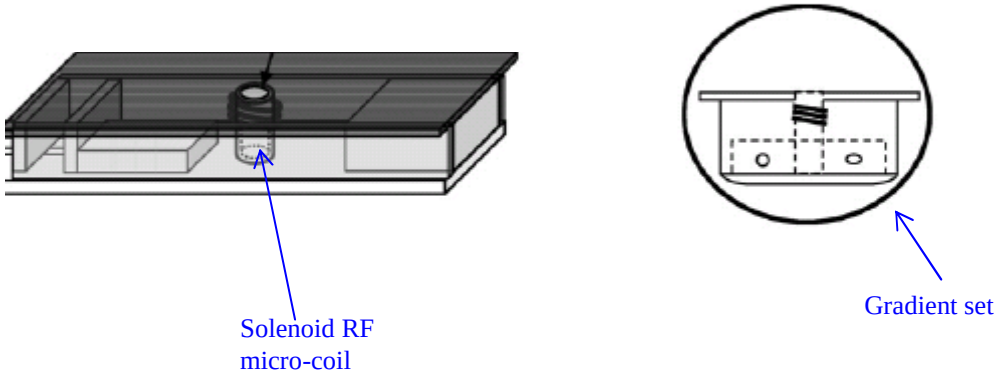

Figure 3.8: Schematic of tumour RF micro-coil set-up, perspective (left) and cross-sectional (right) views

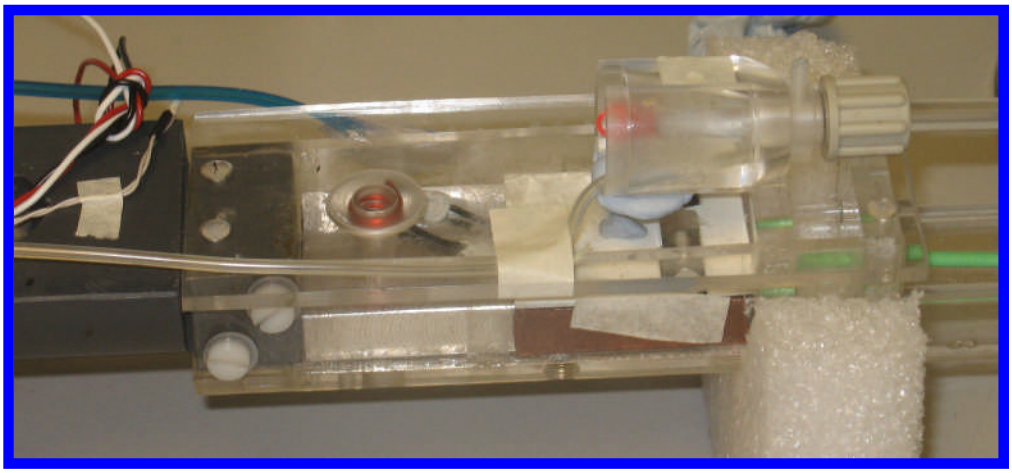

Figure 3.9: Photograph of RF micro-coil set-up

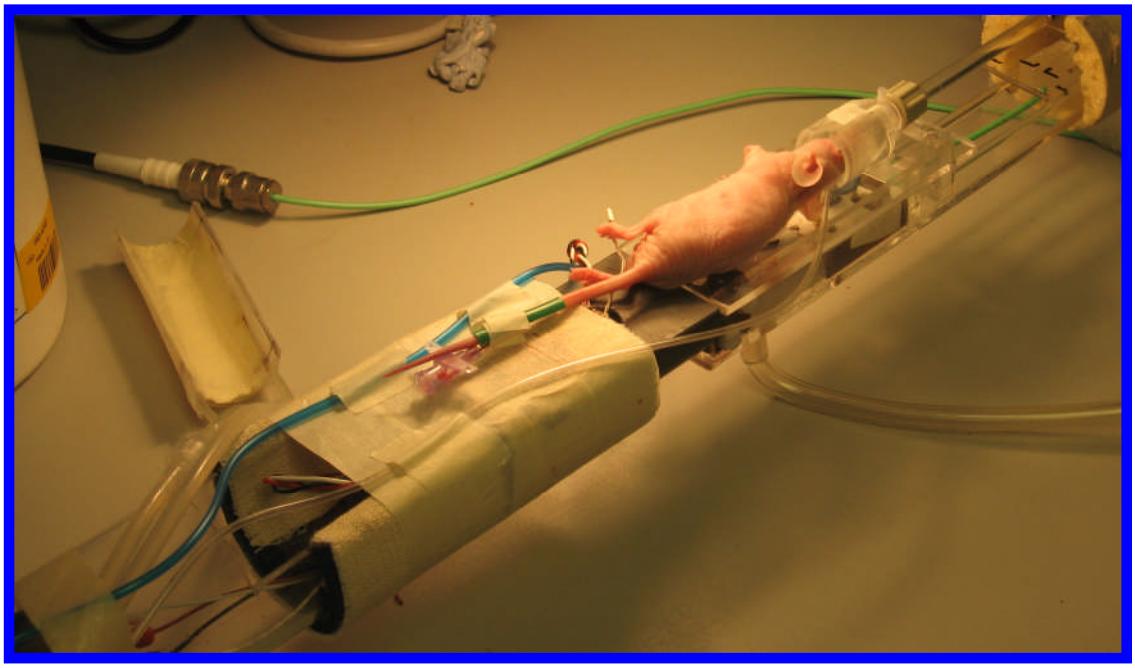

Figure 3.10: Photograph of mouse in position on cradle

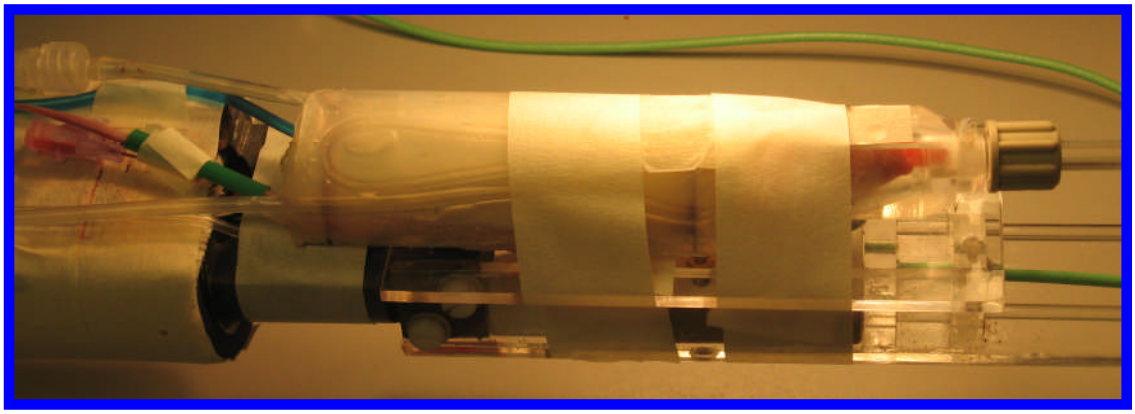

Figure 3.11: Photograph of mouse on cradle with water jacket in place immediately prior to transfer to MRI scanner

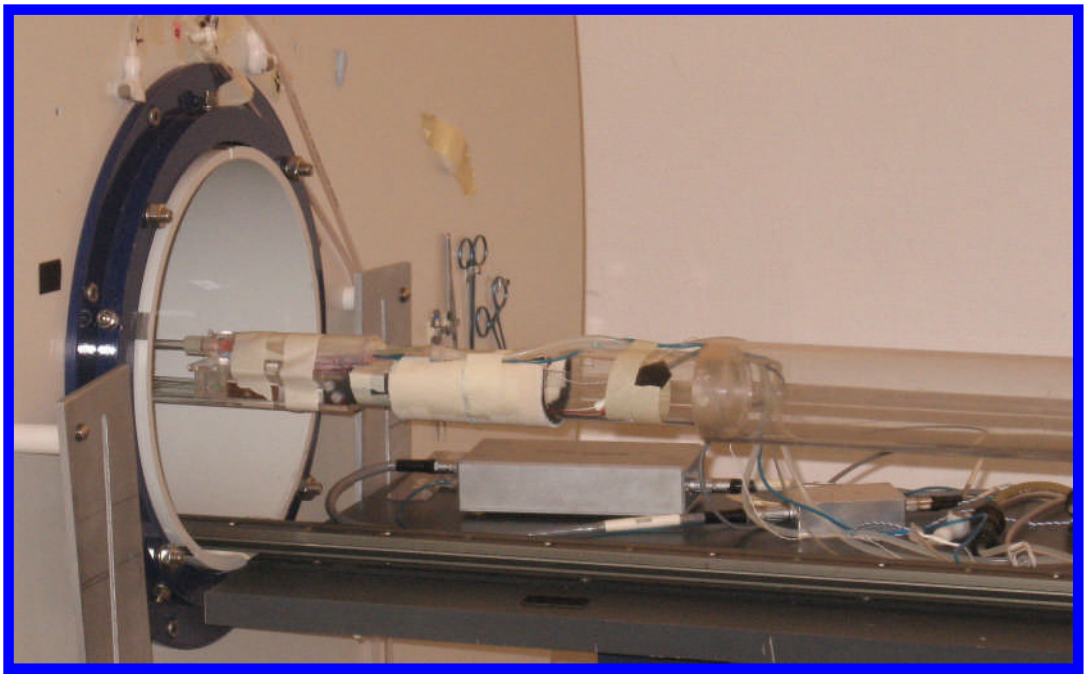

Figure 3.12: Photograph of animal cradle in MRI scanner prior to entering the bore of the magnet

3.4.5 Imaging Protocols

3.4.4.1 Kidney Studies

Kidney studies were performed using a multi slice multi echo (MSME) 2D sequence, with four slices. The scans had the following parameters: in-plane isotropic voxels 150 × 150 μm^2 with a slice thickness of 2 mm and an in-plane field of view 60 × 34 mm. The sequence used an echo time of 10.5 ms, a repetition time of 75 ms, a flip angle of 90° with a 180° re-focusing pulse and four averages. Total scan time for the four slice package was 1 minute 7 seconds.

3.4.4.2 Brain Studies

Brain studies were performed using a 3D FLASH sequence with the following parameters: isotropic voxels 160 × 160 × 160 μm^3 and a field of view 20 × 16 × 16 mm^3. This sequence used an echo time of 3.7 ms, a repetition time of 20 ms, a flip angle of 30° and one average. The total scan time was 3 minutes 20 seconds.

3.4.4.3 Tumour Studies

(a) Early tumour studies were performed using a 3D FLASH sequence with the following parameters: isotropic voxels 100 × 100 × 100 μm^3 in a field of view 80 × 80 × 80 mm^3. This sequence used an echo time of 3.5 ms and a repetition time of 25.0 ms, a flip angle of 30° and four averages. Total scan time was 10 minutes 40 seconds.

(b) Subsequent tumour studies were performed using the same sequence with only two averages to reduce the scan time to 5 minutes 20 seconds. The echo time was altered slightly to 3 ms and all other parameter remained the same.

3.4.4.4 Tumour Angiography Studies

Tumour angiography studies used a multi-slice 2D time of flight (TOF) gradient echo sequence. Slicing was perpendicular to the axis of the coil or sagittal in anatomical terms. Isotropic voxels were acquired with 100 × 100 μm^2 in-plane resolution and 60 sequential slices of 100 μm thickness. The echo time used was 5 ms and the recovery time was 40 ms with 8 averages. The total scan time was 22 min.

3.4.6 Data Analysis

3.4.6.1 General Information

Raw data was exported (the free induction decay [FID] file) and then processed using in-house generated routines written in Interactive Data Language (IDL, RSI, Boulder, Colorado, U.S.A.). In all cases the FID was imported into IDL as a binary file then manipulated and the Fourier transform performed. The raw data was processed rather than using the reconstructed images generated by Paravision to give total freedom in the ways in which the data could subsequently be viewed and analysed. Furthermore it allowed for direct comparison between successive images in a time series without any problems that may have been encountered with the automatic scaling of images in Paravision.

The raw data files contain a continuous string of 32 bit numbers in the little endian format. These numbers represent the values stored in k-space but have lost their array structure. Prior to performing the Fourier transform to obtain the image, the data must be put back into an array with the same dimensions as the acquisition file.

The first step is to use the import binary macro (figure 3.13) to import the raw data into IDL. Prior to importing the size of the raw data file is determined as illustrated by the following example for a 2D acquisition matrix of size 780 × 226:

- the first dimension (frequency encoding) is doubled: 780 × 2 = 1560, as this will contain a pair of complex numbers
- the first dimension is then rounded to the nearest even multiple of 128, in this case 1792 (these ‘new’ points contain zeros, this ‘zero-filling’ simplifies storage and subsequent analysis for the computer)
- the number of 32 bit numbers contained in the raw data file size can now be calculated as 1792 × 226 = 404992 data points per slice

For a 2D data set this number is multiplied by the number of slices and for a 3D data set by the size of the acquisition matrix in the third dimension.

The raw data is now manipulated into either the 2D or 3D structure of the acquisition matrix and then Fourier transformed to give the image. Sections 3.4.6.2 and 3.4.6.2 give details of this is done for the kidney, tumour and brain studies.

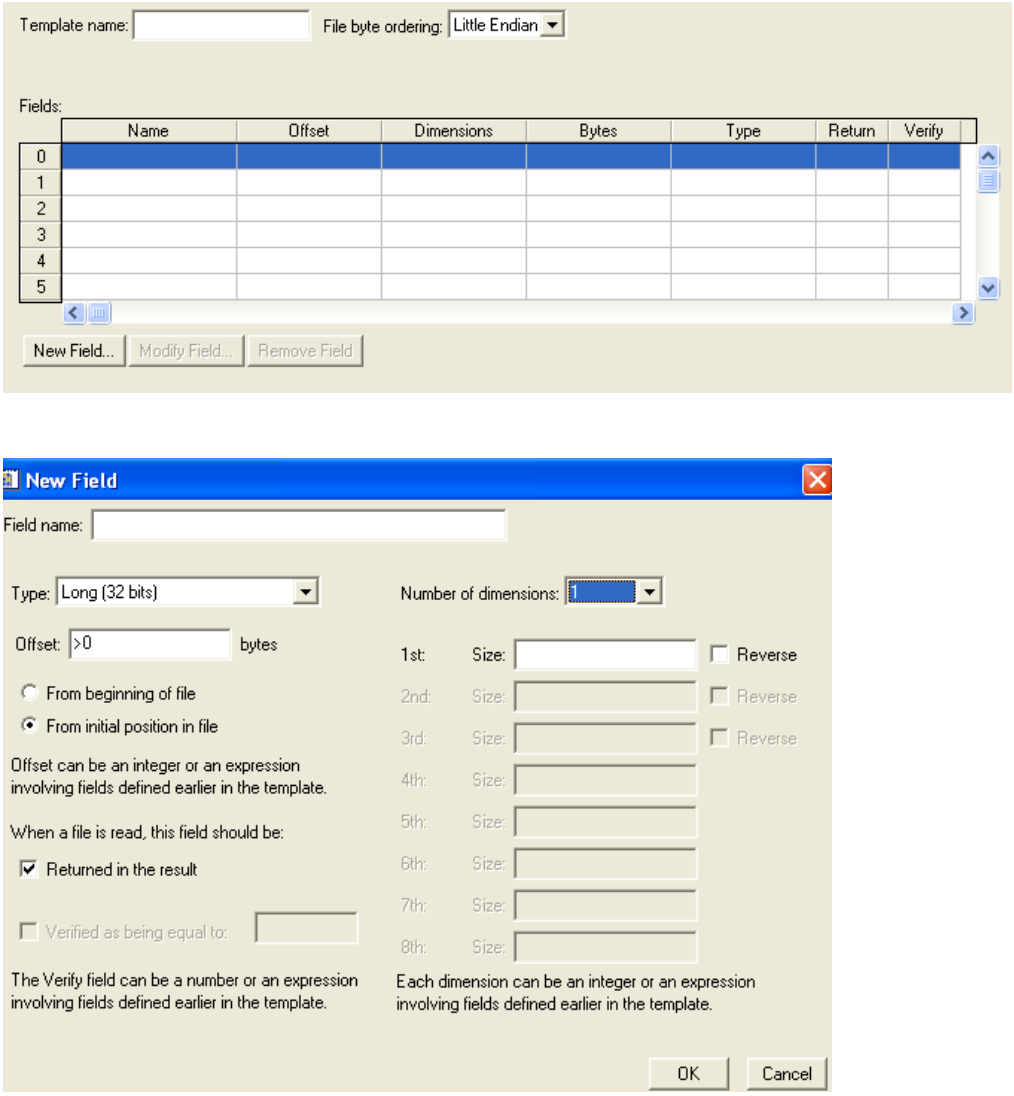

Figure 3.13: Screen captures of the IDL import binary macro

3.4.6.2 Kidney Studies (2D)

As mentioned previously the data is held in the raw data file as a continuous string and it is written to this string in the order in which it is read. To reduce scan time the sequence used for whole body studies uses an interleaving method in which the first line of k-space for the first slice is read followed by the first line of k-space for the second slice and so on. Before the data can be Fourier transformed it must be collected into blocks for each slice using the following IDL commands:

```
nlen = 1792
n = n_elements(scan_name)
r = reform(scan4, nlen, n / nlen)
slice1 = reform(r[*, 0:*:4], n / 4)
slice2 = reform(r[*, 1:*:4], n / 4)
slice3 = reform(r[*, 2:*:4], n / 4)
slice4 = reform(r[*, 3:*:4], n / 4)
```

An IDL function (figure 3.14) can now be used to perform the Fourier transform slice by slice. Zero-filling is removed in the subsequent image processing.

```
Function convert5,data,dim0,dim1

Nrows= 167552

real=fltarr(Nrows)
imag=fltarr(Nrows)

twocolumndata=reform(data,2,Nrows)
real=twocolumndata(0,*)
imag=twocolumndata(1,*)

Cdata=complex(real,imag)

Carray=reform(Cdata,dim0,dim1)
a=complexarr(dim0,dim1)
a=Carray(0:895,0:186)

b=shift(abs(fft(a)),460,-100)

return,b
end
```

This section re-orders the data and forms two arrays containing the real and imaginary complex numbers that represent each data point

This section forms a array of complex numbers with the geometry of the acquisition slice

This line performs the Fourier transform

Figure 3.14: IDL function used to perform Fourier transform of data from whole body studies

3.4.6.3 Brain and Tumour Studies (3D)

Both brain and tumour imaging studies used 'true' 3D imaging. This means that k-space is acquired as a three dimensional block rather than a series of 2D slices which are reconstructed into a 3D volume in post-processing. The raw data string must be manipulated into a three dimensional array prior to Fourier transform. Again the raw data was imported using the import binary macro and analysed using similar IDL routines (figures 3.15 and 3.16). In these studies to simplify subsequent analysis the functions first remove the zero-filling, reconstruct the remaining data into the 3D array format of the acquisition matrix and then perform the Fourier transform.

```
Function convertbrain,data,dim0,dim1,dim2

data=reform(data,512,10000,/overwrite)
data=data(0:499,*)
data=reform(data,n_elements(data),/overwrite)

nrows=long(1)*dim0*dim1*dim2

real=fltarr(Nrows)
imag=fltarr(Nrows)

twocolumndata=reform(data,2,Nrows)
real=twocolumndata(0,*)
imag=twocolumndata(1,*)

Cdata=complex(real,imag)

Carray=reform(Cdata,dim0,dim1,dim2)
a=complexarr(dim0,dim1,dim2)
a=Carray(0:249,0:99,0:99)

b=shift(abs(fft(a)),126,54,24)

return,b
end
```

This section removes the zero filling

This section re-orders the data into the format of the original acquisition matrix

This section performs the Fourier transform

Figure 3.15: IDL function used to perform Fourier transform of data from brain studies

```
Function convert,data,dim0,dim1,dim2

data=reform(data,512,6400,/overwrite)
data=data(0:319,*)
data=reform(data,n_elements(data),/overwrite)

nrows=long(1)*dim0*dim1*dim2

real=fltarr(Nrows)
imag=fltarr(Nrows)

twocolumndata=reform(data,2,Nrows)
real=twocolumndata(0,*)
imag=twocolumndata(1,*)

Cdata=complex(real,imag)

Carray=reform(Cdata,dim0,dim1,dim2)
a=complexarr(dim0,dim1,dim2)
a=Carray(0:159,0:79,0:79)

b=shift(abs(fft(a)),40,50,-15)

return,b
end
```

This section removes the zero filling

This section re-orders the data into the format of the original acquisition matrix

This section performs the Fourier transform

Figure 3.16: IDL function used to perform Fourier transform of data from tumour studies

3.4.6.4 Angiography Studies

Data from angiography experiments was analysed using ImageJ which is a public domain java based image processing program developed at the National Institutes of Health (NIH, USA). This program can be used to open the reconstructed images directly, eliminating the need for data processing and Fourier transform. ImageJ was used for analysis as no quantification or comparison between successive images was required and so the issue of scaling was not important.

3.4.7 Image Presentation

Images were presented using either ImageJ or the iimage or ivolume tools in IDL.

3.5 MRI Results

3.5.1 Head Imaging

3.5.1.1 Introduction

The suitability of the glycol chitosan (GC) based agents for use as blood pool agents was tested by imaging of the mouse head. The head was imaged as it is highly vascularised and can be firmly constrained to minimise movement artefacts. Separate studies were performed for the GC2-DTPA-Gd and GC48-DTPA-Gd agents with Magnevist used as a control. The resultant data is presented in a number of formats including maximum intensity projections, slices at various time points, volume projections and graphs of signal profile time courses. Finally the GC2-DTPA-Gd agent is used to identify some of the larger vessels in the head. The diagrams [figures3.17(a and b)] that follow are included as a reference to aid orientation in future images.

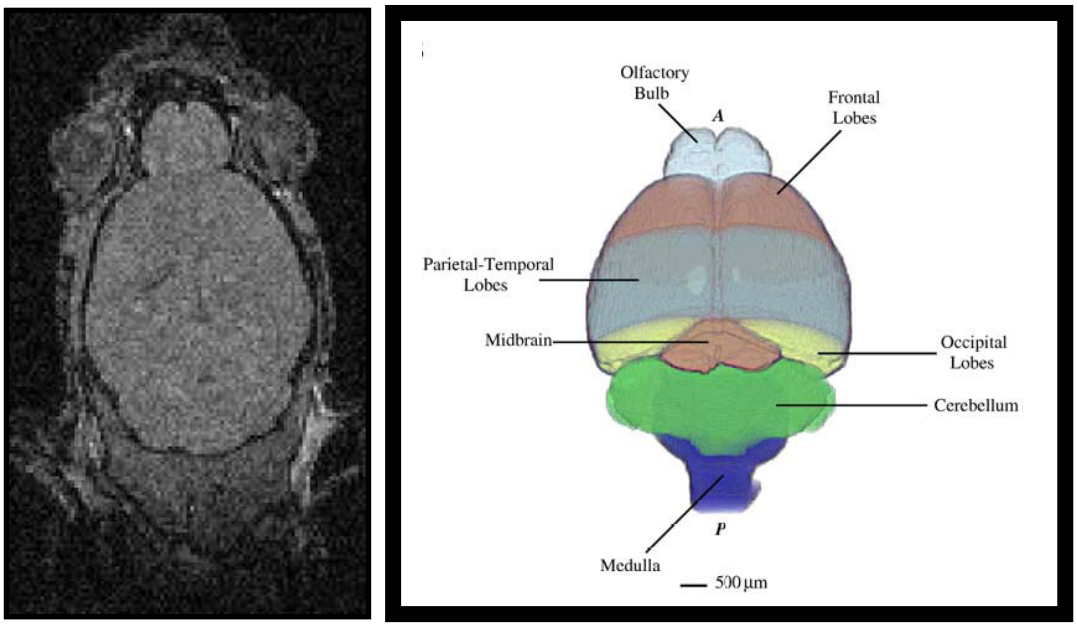

Figure 3.17(a): Coronal orientation for head imaging. Image from MRI scanning (left) and diagramatically (right) (Dorr et al. 2007)

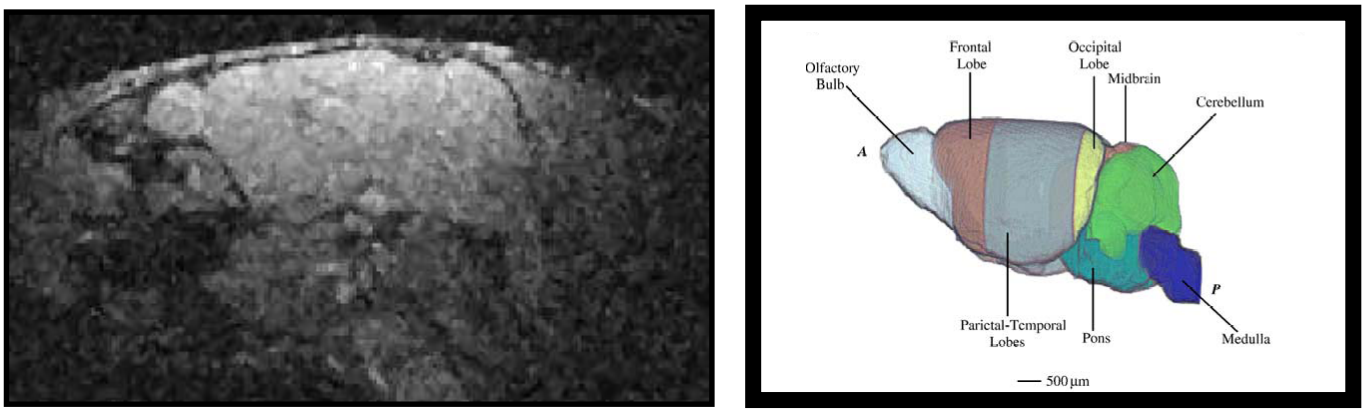

Figure 3.17(b): Saggital orientation for head imaging. Image from MRI scanning (left) and diagramatically (right) (Dorr et al. 2007)

3.5.1.2 Comparison between Magnevist, GC2-DTPA-Gd and GC48-DTPA-Gd

Firstly, images made from maximum intensity projections (MIPs) in three directions before and after (3 minutes 20 seconds) the administration of the different contrast agents were used to compare their specificity [figures 3.18 (a, b and c)]. MIPs are an effective way in which to visualise 3D data sets on paper, the technique involves constructing a 2D (x,y) image in which each pixel contains the maximum value at that (x,y) location in the third dimension (z).

The diffuse enhancement of figure 3.18 (a) shows the lack of specificity of Magnevist and is the result of leakage of contrast material into the tissues that surround the brain. Conversely GC2-DTPA-Gd [3.18 (b)] appears to have remained confined to the blood pool giving clear enhancement of the brain vasculature. An intermediate effect is seen with the GC48-DTPA-Gd contrast agent [3.18 (c)].

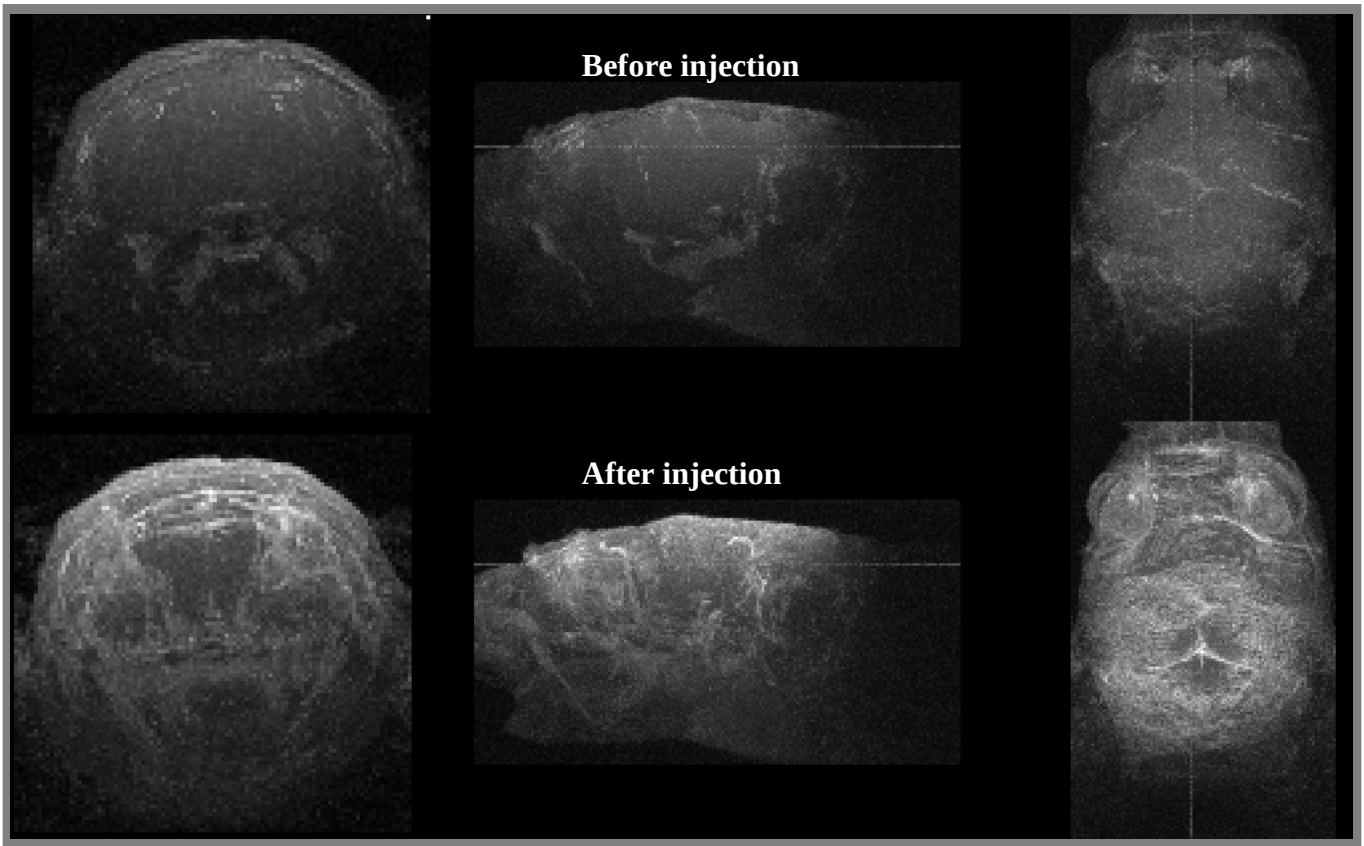

Figure 3.18 (a) **Magnevist**

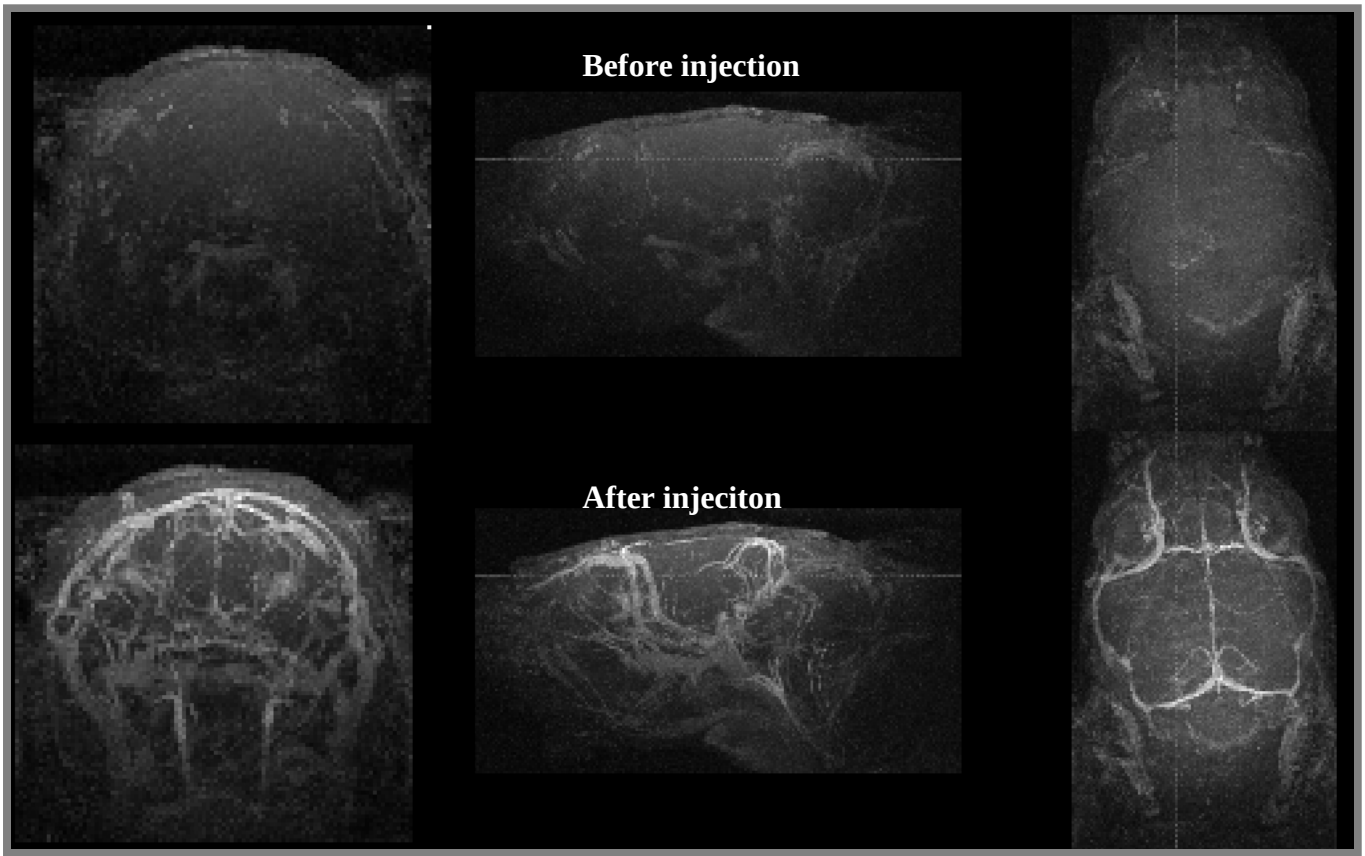

Figure 3.18(b) **GC2-DTPA-Gd**

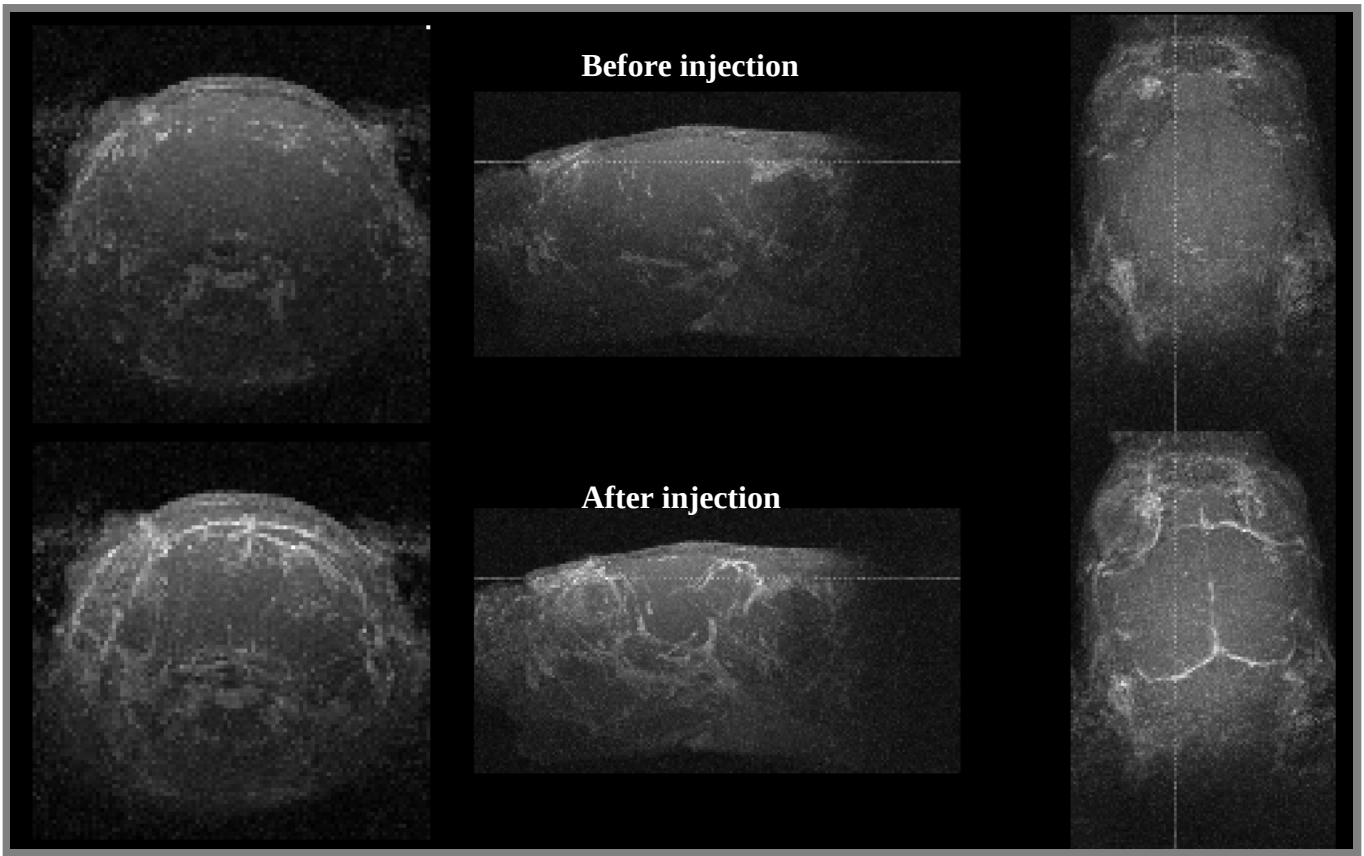

Figure 3.18 (a-c): Maximum intensity projections of head imaging before and after administration of Magnevist (a), GC2-DTPA-Gd (b) and GC48-DTPA-Gd (c).

Individual central coronal slices from each data set at various time points are displayed to further investigate the enhancement pattern. The diffuse enhancement of Magnevist can again be clearly seen [figure 3.19 (a)] and in particular the strong enhancement of the tissue of the scalp. In contrast the GC2-DTPA-Gd agent appears to have remained entirely contained in the vascular space [figure 3.19 (b)]. Some minor tissue enhancement is seen for the GC48-DTPA agent [figure 3.19 (c)]. Difference maps constructed by subtracting the data obtained before injection from the data obtained 3 and 30 minutes post injection further reinforce these points [figure 3.20 (a-c)].

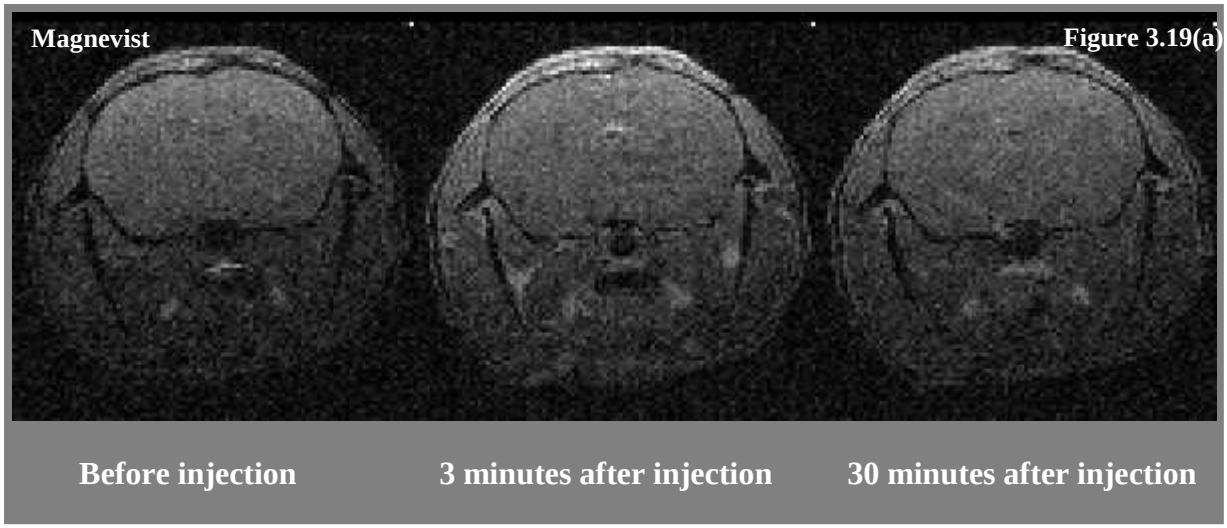

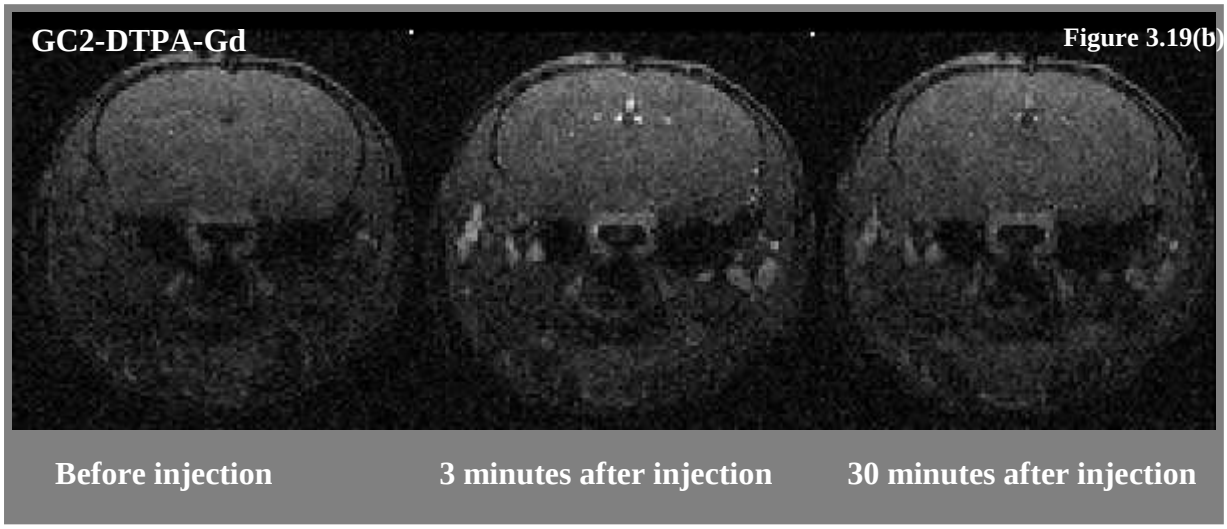

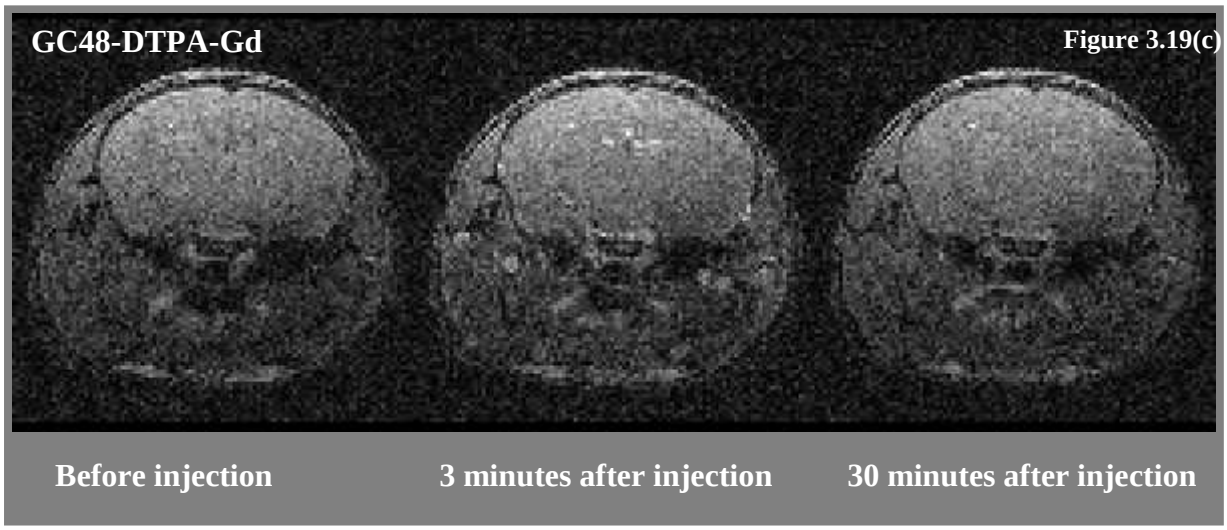

Figure 3.19 (a-c): Central coronal slice from head imaging data sets at various time points before and after administration of Magnevist (a), GC2-DTPA-Gd (b) and GC48-DTPA-Gd (c).

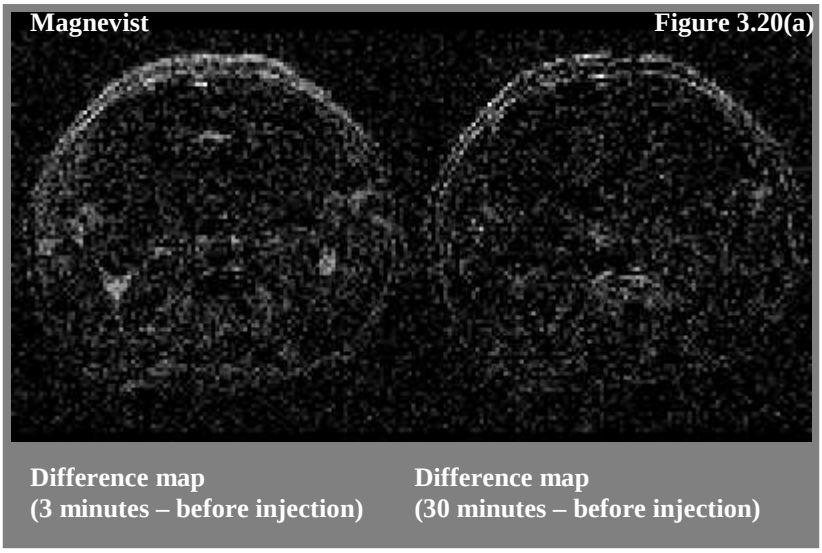

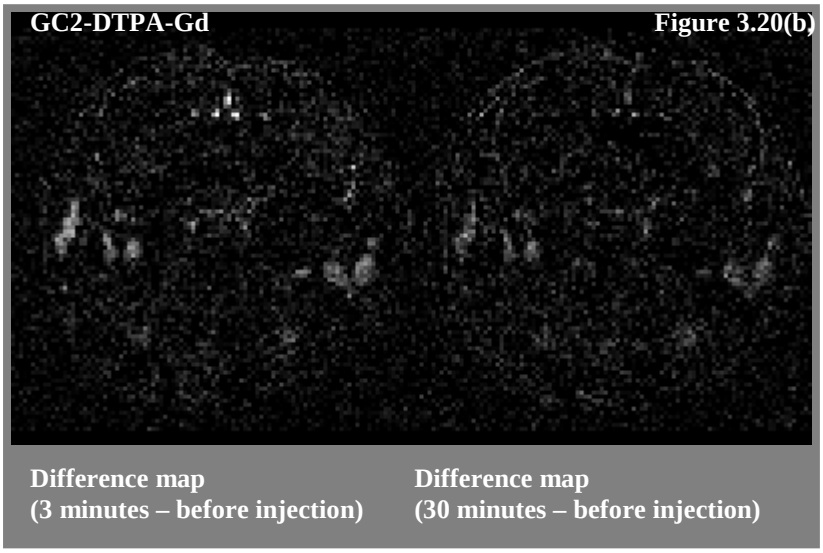

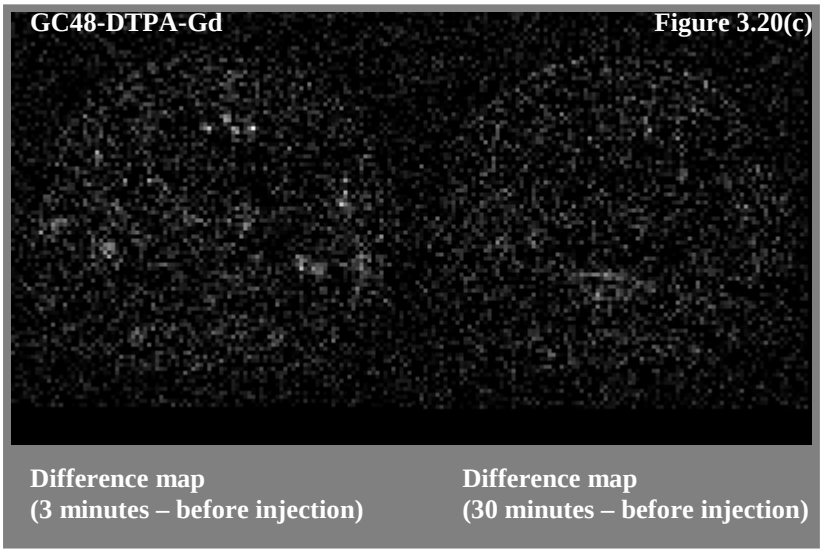

Figure 3.20(a-c): Difference maps from central coronal slice for Magnevist (a), GC2-DTPA-Gd (b) and GC48-DTPA-Gd (c).

Although maximum intensity projections are a useful way in which to present volume data, the depth of the data set is obviously lost. A volume projection is used here in an attempt to give an impression of the depth of the data sets. These images are constructed by subtracting the data obtained before injection from the data obtained immediately after injection (3 minutes 20 seconds later). Regions with a level of enhancement greater than 20% are then displayed in red [figure 3.21(a-c)]. These images enforce the differences in biodistribution observed using the previous techniques.

Figure 3.21(a) Magnevist

Figure 3.21(b) GC2-DTPA-Gd

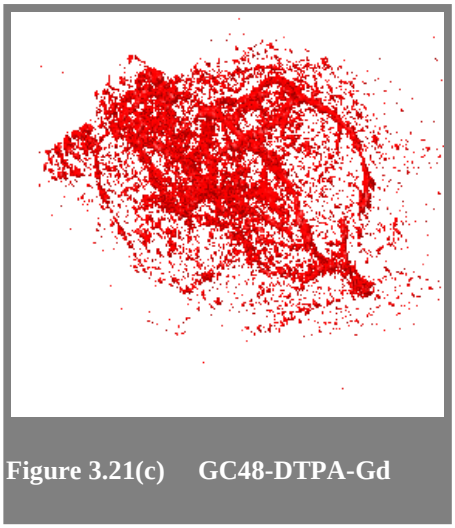

Figure 3.21(c) GC48-DTPA-Gd

Figure 3.21(a-c): Volume projections showing areas of greater than 20% enhancement following the administration of Magnevist (a), GC2-DTPA-Gd (b) and GC48-DTPA-Gd (c).

Graphs of the signal profile [figure 3.22(a-c)] for various regions over the course of the experiment were constructed to semi-quantify the findings of the images in figure 3.18-3.21.

Regions of interest (ROI) were placed in:

- the brain as this would not be expected to enhance with any of the agents due to the blood-brain barrier (red)
- what was presumed to be blood supply (blue)
- an area of tissue surrounding the brain (green/torquoise)

For both the GC2-DTPA-Gd and GC48-DTPA-Gd agents the ROIs in the scalp showed a lack of enhancement similar to the control regions in the brain. Conversely the same region in the Magnevist data set showed the greatest enhancement and longest time to peak suggestive of accumulation via diffusion. In all cases the ROI in the blood supply showed a sharp initial enhancement, and whereas this initial

enhancement peak was brief for both Magnevist and GC48-DTPA-Gd the rate of reduction was far lower for the GC2-DTPA-Gd agent. These results suggest that GC2-DTPA-Gd has a longer plasma half-life than Magnevist and GC48-DTPA-Gd.

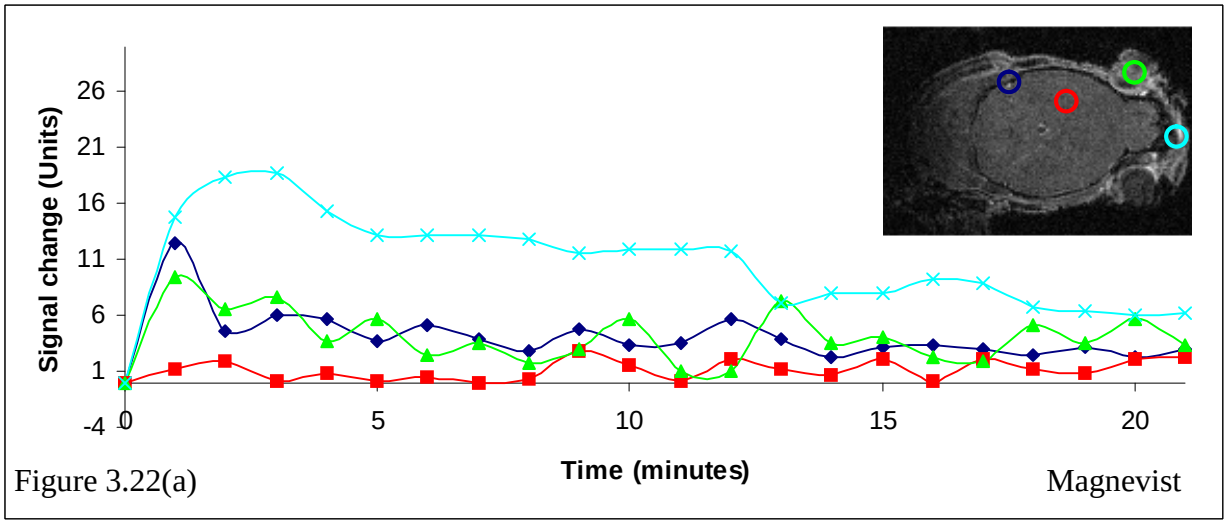

Figure 3.22(a) Magnevist

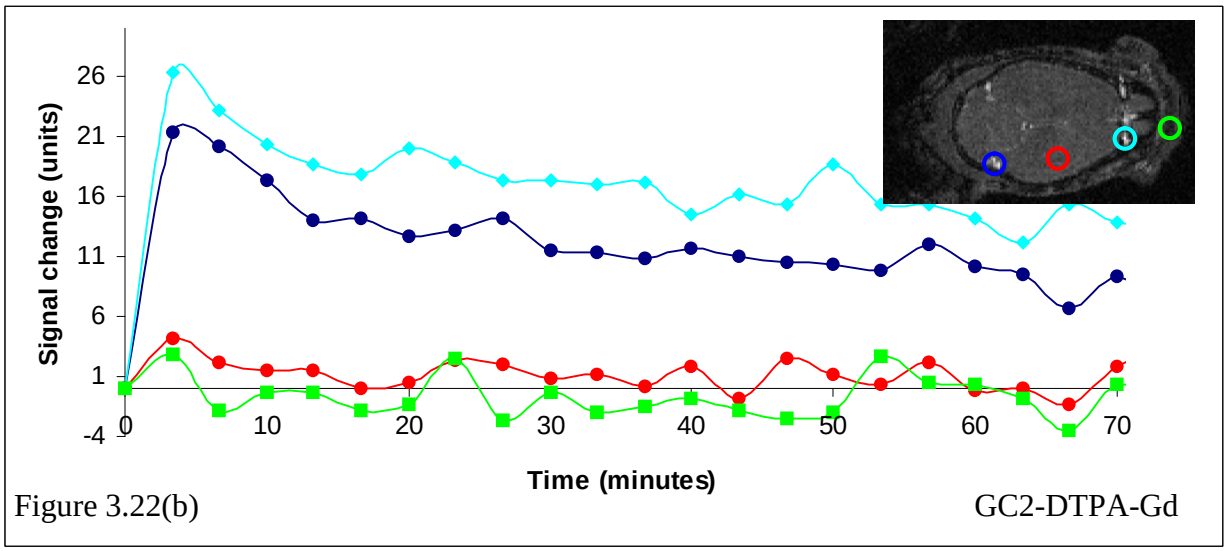

Figure 3.22(b) GC2-DTPA-Gd

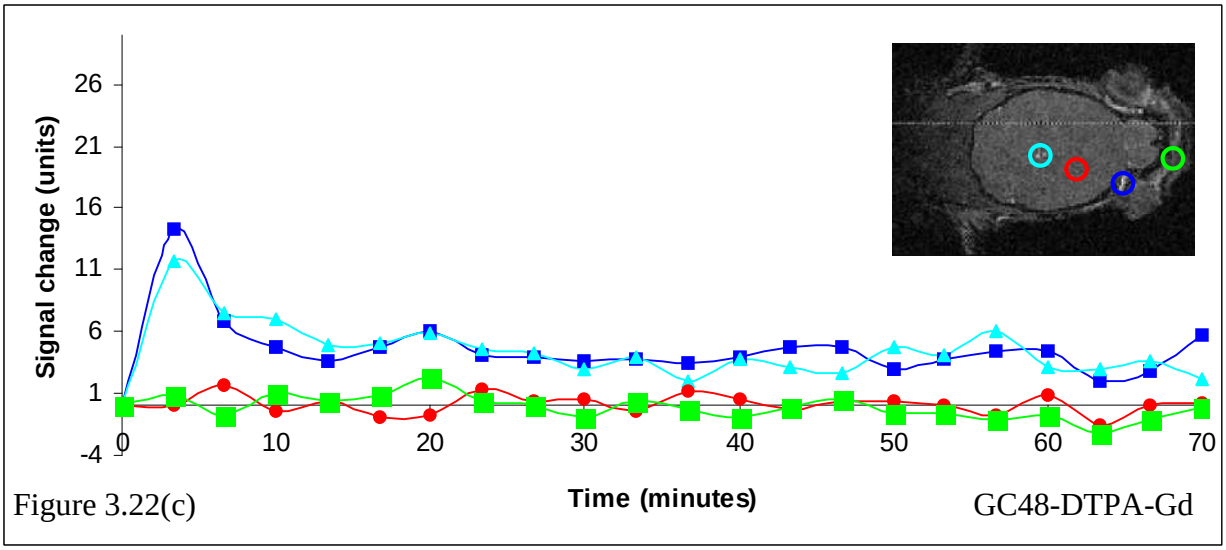

Figure 3.22(c) GC48-DTPA-Gd

Figure 3.22(a-c): Signal profile graphs for a number of regions of interest for Magnevist (a), GC2-DTPA-Gd (b) and GC48-DTPA-Gd (c).

In summary both the GC2-DTPA-Gd and GC48-DTPA-Gd agents proved their worth as potential blood pool agents. The GC2 agent in particular provided very clear specific enhancement of the vasculature. Furthermore the signal profile graphs obtained would suggest that neither of the agents would have excessively large plasma half-lives. Despite the GC2-DTPA-Gd agent having a longer half-life considerable reduction in the signal in a blood vessel has occurred over an hour and if this pattern continued the level would be expected to return to its starting value within another hour. This is a significant advantage as excessively long plasma residence times are associated with an increase in the potential for the liberation of toxic gadolinium (as mentioned in chapter one).

3.5.1.3 Blood Vessel Identification using GC2-DTPA-Gd (Cook 1965; DeArmond et al. 1989; Hanaway et al. 1998; Bullitt et al. 2007; Dorr et al. 2007)

As the images obtained using the GC2-DTPA-Gd agents showed the vasculature of the head so clearly it was decided to attempt to identify a number of the larger vessels [figures 3.23(a & b), 3.24(a & b) and 3.25]. Maximum intensity projections were constructed for smaller regions of the head to simplify the analysis.

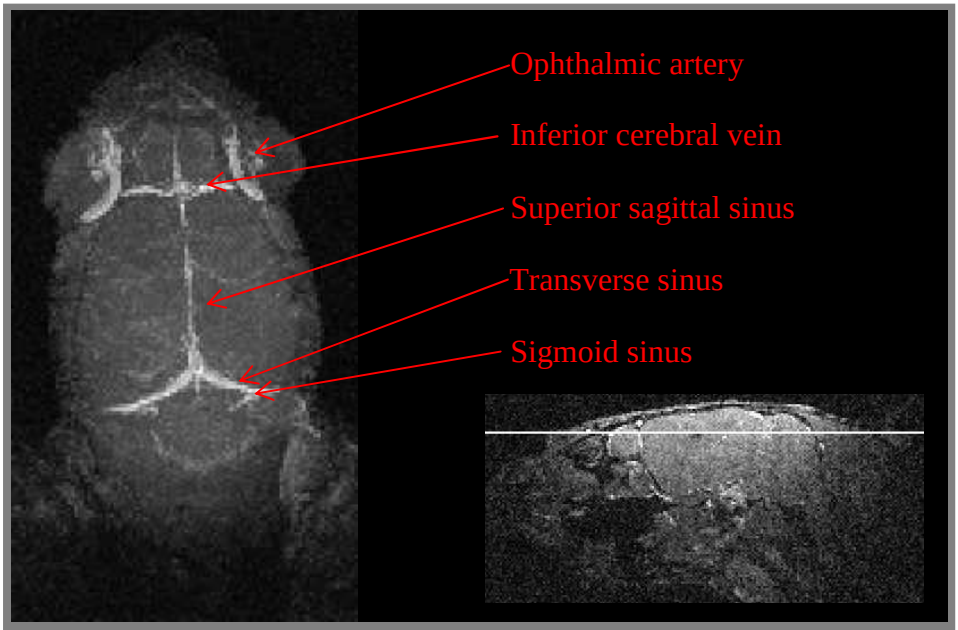

Figure 3.23(a)

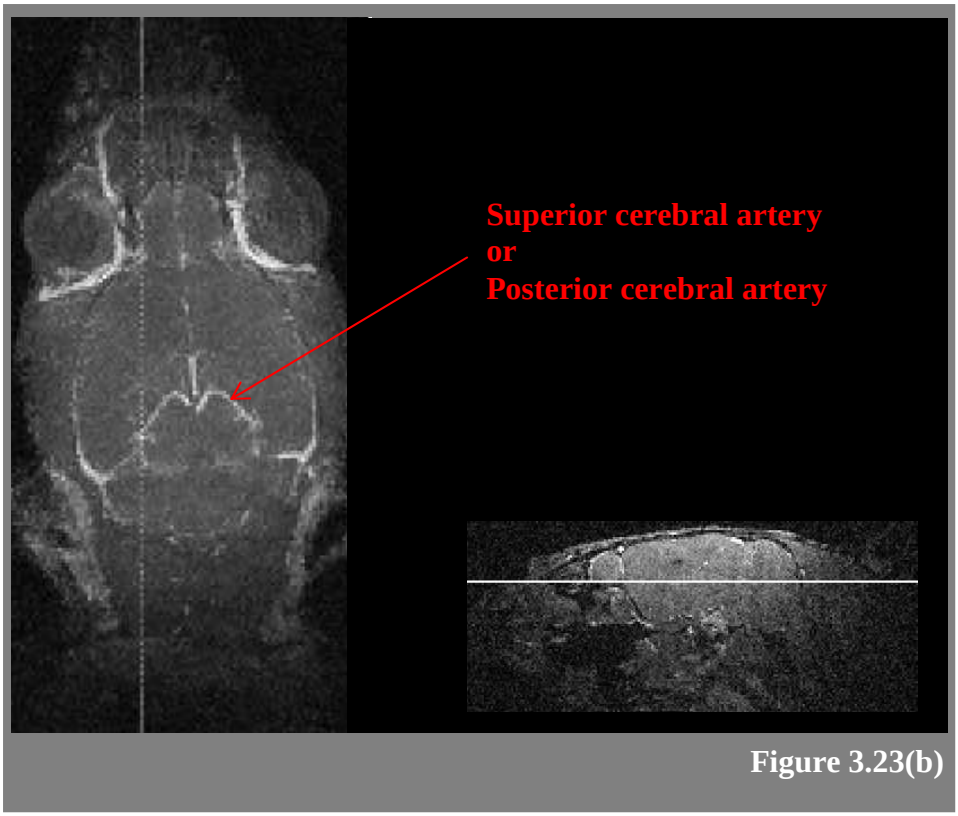

Figure 3.23 (a & b): Maximum intensity projections in the transverse plane with major vessels annotated

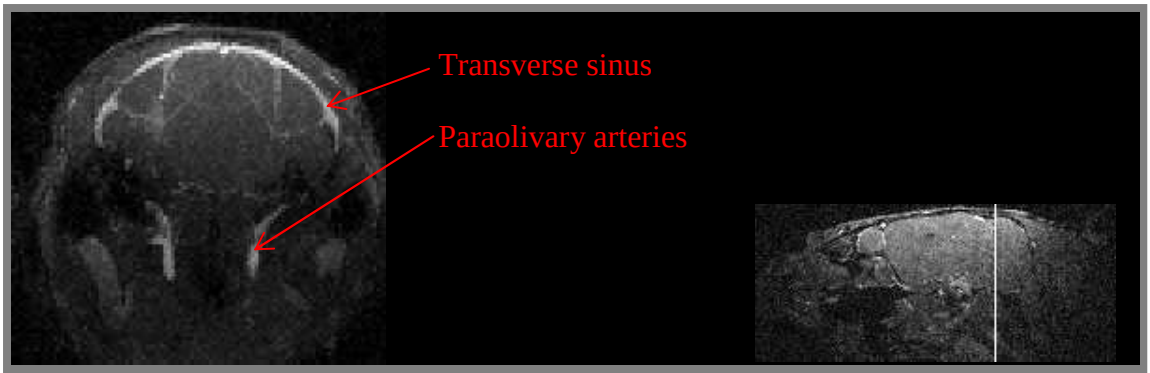

Figure 3.24(a)

Figure 3.24(b)

Figure 3.24 (a & b): Maximum intensity projections in the coronal plane with major vessels annotated

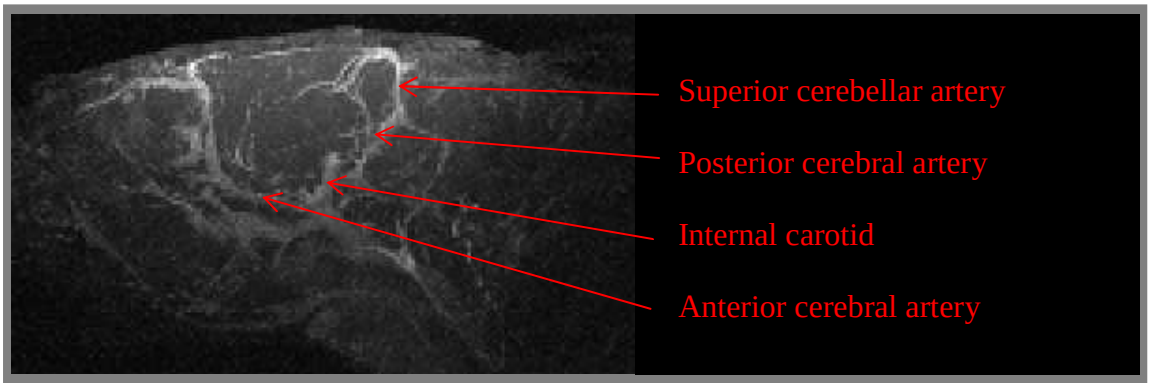

Figure 3.25

Figure 3.25: Maximum intensity projections in the sagittal plane with major vessels annotated

3.5.2 Kidney Imaging

It was mentioned in chapter one that a number of the novel blood pool contrast agents have been associated with poor whole body clearance (Caravan et al. 1999). It is generally thought that this is the result of reticuloendothelial system uptake and in particular preferential hepatic uptake (Caravan et al. 1999). As an introductory study into the clearance patterns of GC2-DTPA-Gd and GC48-DTPA-Gd a slice through the kidneys was serially imaged. The kidney was chosen to image in preference to the liver for reasons of technical simplicity. It can be seen (figure 3.26 and 3.27) that the contrast agents are both present in the kidneys immediately after injection followed by rapid passage to the ureter. Images are displayed at higher time points for the GC2-DTPA-Gd contrast agent as the evidence of the brain imaging (figure 3.22) would suggest that it has a longer plasma residence time. These experiments give some confidence that the agents are filtered by the kidneys over a significant time period and passed in the urine.

Obviously these studies only give limited information, however, there are reports in the literature of renal enhancement being taken as indicative of contrast agent removal from the blood and elimination by the kidneys (Li et al. 2007), further studies would be required to elucidate more concrete conclusions (see future work-chapter five).

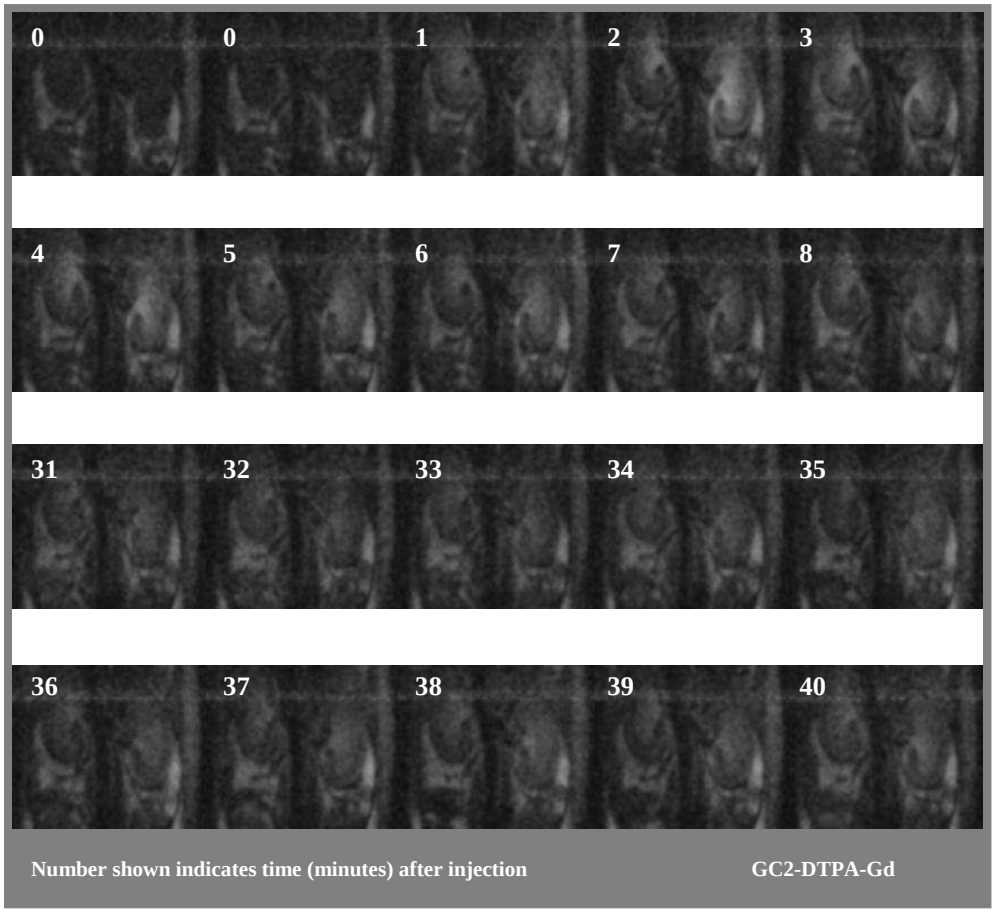

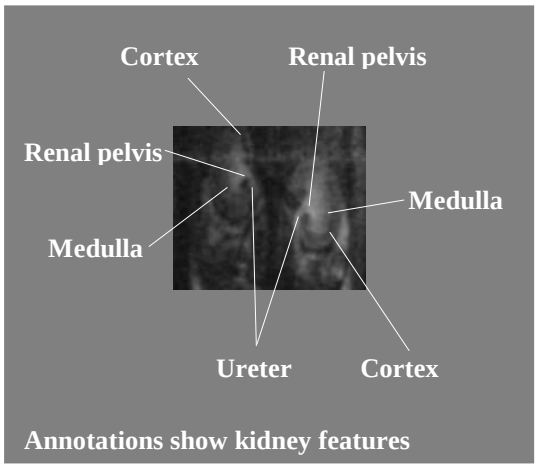

Figure 3.26: Kidney slice showing clearance of GC2-DTPA-Gd agent

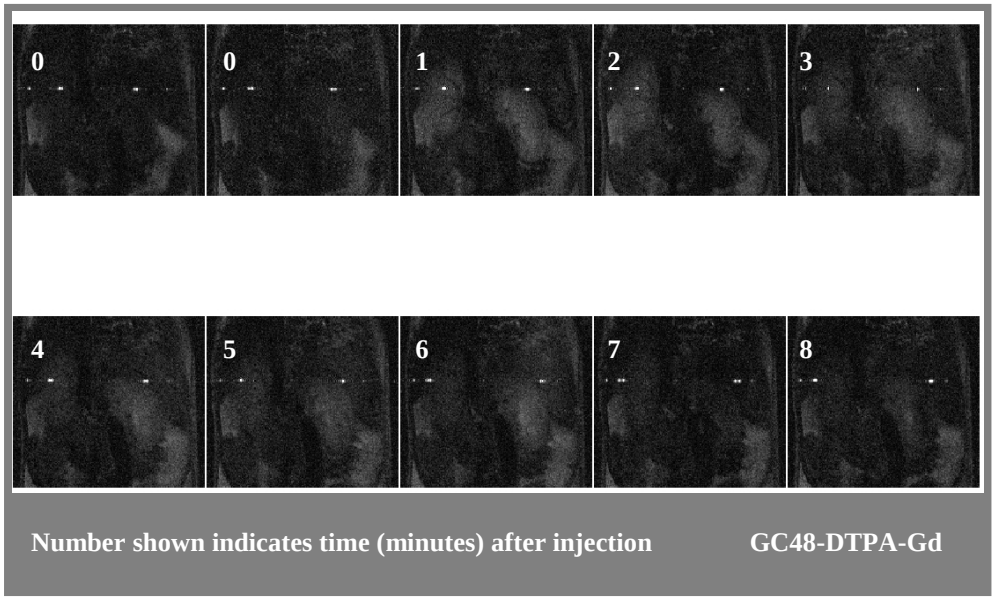

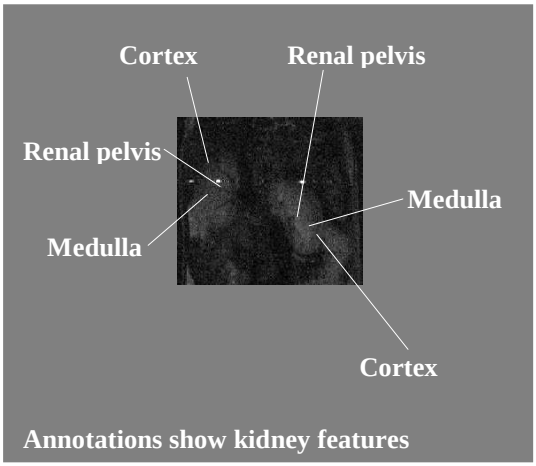

Figure 3.27: Kidney slice showing clearance of GC48-DTPA-Gd agent

3.5.3 Tumour Imaging

3.5.3.1 Introduction

The multitude of barriers that exist to the successful drug treatment of solid tumours were introduced in chapter one. Studies were performed to show how MRI and in particular DCE-MRI can be used to investigate these barriers. The investigation was conducted in two stages: firstly studies to gain a general appreciation of the delivery and transport of a low molecular weight material in solid tumours and secondly to explore the effect of molecular weight on delivery and transport. Experiments were performed using Magnevist as a surrogate for the delivery of a low molecular weight drug and the GC48-DTPA-Gd agent as a high molecular weight surrogate.

It was also mentioned in chapter one that there is a significant body of work involved in the mathematical modelling of DCE-MRI data and how these studies are sensitive to the quality and resolution of the input data. The experiments performed here also served as a means by which to test the capabilities of a new RF solenoid micro-coil set-up for tumour imaging to provide high quality, high resolution data (Holmes et al. 2008) (Full text can be found in Appendix A).

3.5.3.2 Low Molecular Weight Material Delivery and Transport

It is widely held that the vasculature of solid tumours is irregular in structure and function and that the resultant blood flow has both temporal and spatial heterogeneity (Jain 2001). Magnetic resonance angiography (MRA, figure 3.28) studies appear to confirm this theory as a wide disparity between highly vascularised regions assumed to be growing (generally at the tumour periphery) and potentially dormant poorly vascularised areas (generally in the tumour interior) were found. Blood vessels with stagnant or slow moving blood may not be detected by this technique

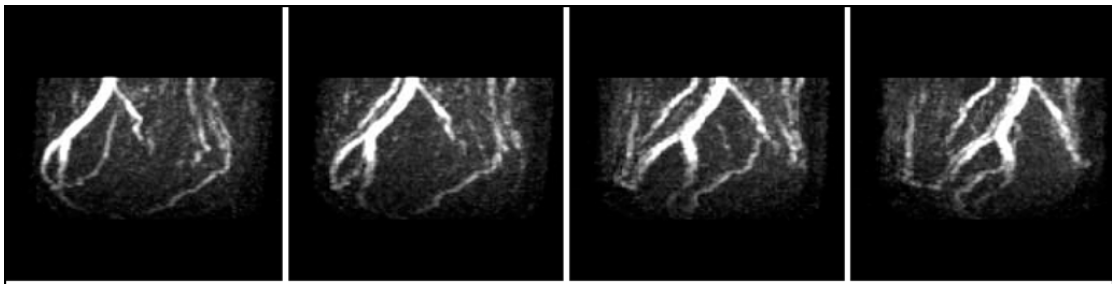

Figure 3.28: Maximum intensity projection from tumour angiography study viewed from a number of angles

The images show how a very clear snapshot of the vasculature can be obtained relatively quickly (22 minutes) using the novel coil set-up. There are only a very few reports of mouse tumour angiography studies in the literature (Kobayashi et al. 2001; Fink et al. 2003) and the resolutions achieved here are significantly better than those reported (10 fold difference in voxel volume).

The effect of this apparently heterogeneous vasculature on delivery and transport of material was investigated using serial 3D T_1 weighted imaging in conjunction with the administration of a contrast agent (Magnevist) a technique known as dynamic contrast enhanced MRI (DCE-MRI). The entire tumour volume was imaged in true 3D which allows the data to be presented in a number of different fashions to elucidate maximum information. It is worth bearing in mind when looking at these images that in this type of T_1 imaging in pre-contrast images bright areas are denser (fatty) tissue and dark areas are fluid based. Small hyperintense regions are assumed to be blood rich due to the inflow of blood during imaging increasing the signal. Following the administration of the contrast agent any change in signal intensity is taken as being due to the presence of contrast material with the change being proportional to the contrast agent concentration. Analysis of a central coronal slice of two different

tumours [figure 3.29 (a & b)] shows that initial delivery of contrast material is well correlated with what is assumed to be the blood supply (identified on the before injection image). Subsequent transport of the contrast material appears to be by diffusion from these initial high signal areas. The images are characterised by the heterogeneous distribution of contrast material and the presence of regions that do not enhance throughout the course of the experiments.

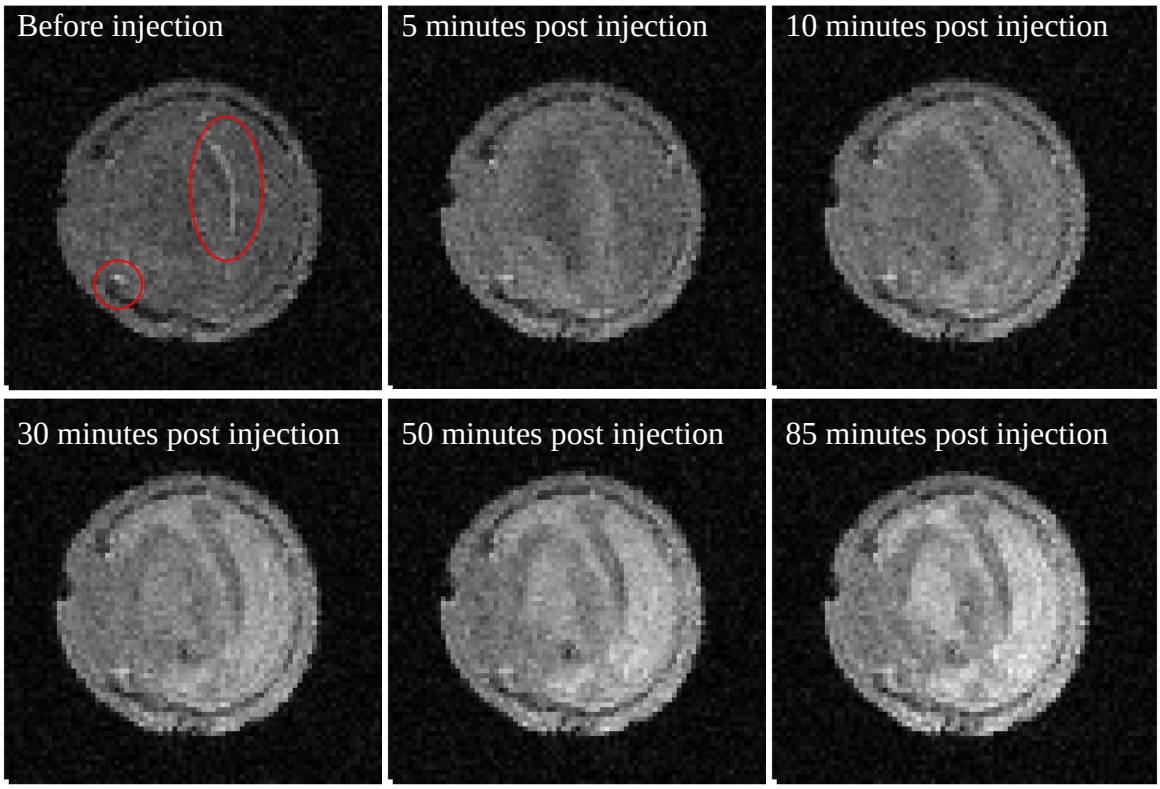

Figure 3.29(a): Central coronal slice tumour (a) from DCE-MRI using Magnevist, regions highlighted in red are assumed to be blood supply

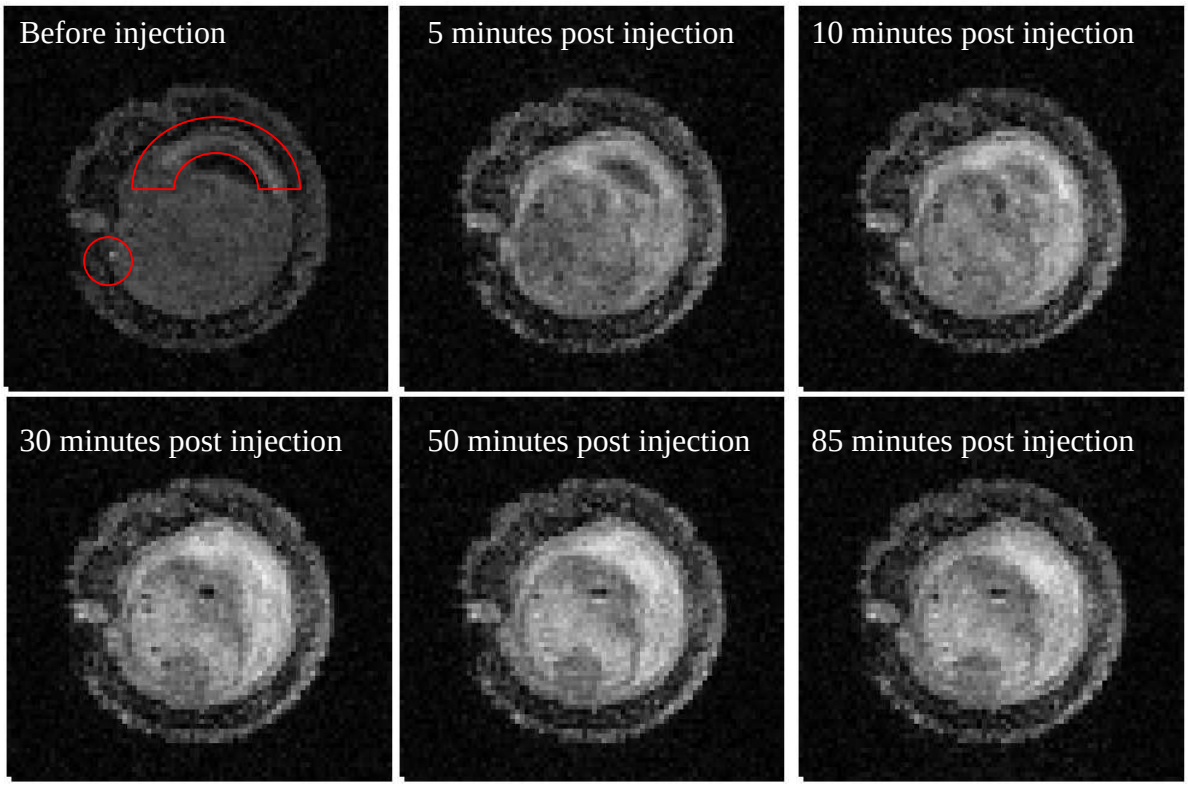

Figure 3.29(b): Central coronal slice tumour (b) from DCE-MRI using Magnevist regions highlighted in red are assumed to be blood supply

Tumour b [figure 3.29(b)] contains a large hypointense region in the pre-contrast image which is likely to be a fluid rich area and could possibly be an area of necrosis. Interestingly this region appears to take up contrast material via diffusion from the surrounding tissues. This has significance in terms of drug treatment as it would be expected that this area would be treated whereas other persistently hypointense regions would not.

An advantage of this 3D imaging of the entire tumour volume is that these transport effects can be visualised across the whole tumour. The tumour is ‘re-sliced’ to give a

central sagittal slice to get an impression of the overall transport issues within the tumour [figure 3.30(a) and (b)].

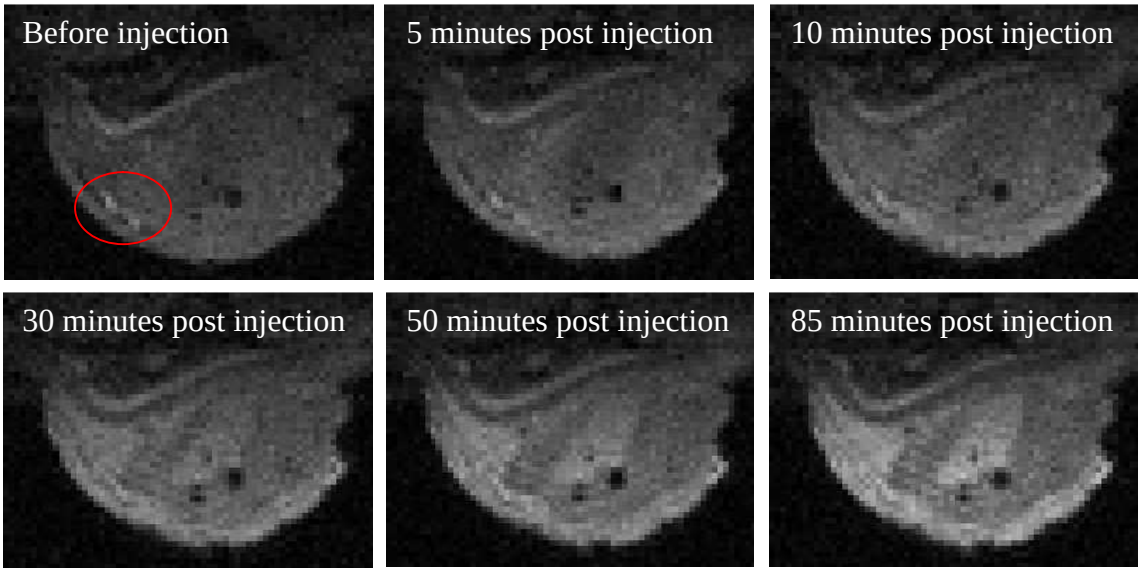

Figure 3.30(a): Central sagittal slice tumour (a) from DCE-MRI using Magnevist

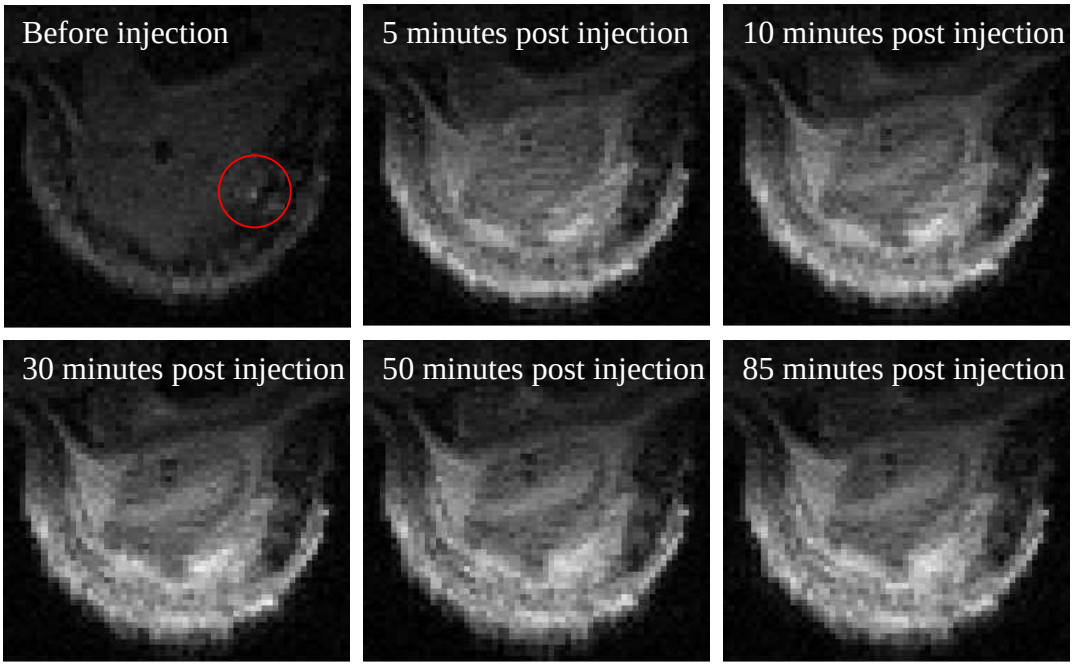

Figure 3.30(b): Central sagittal slice tumour (b) from DCE-MRI using Magnevist

Further analysis of another data set was performed to investigate the apparent phenomenon of contrast agent delivery and subsequent transport from high to low concentration areas by diffusion. It is seen that in this particular tumour delivery of contrast material is radial from the tumour periphery to the interior (figure 3.31).

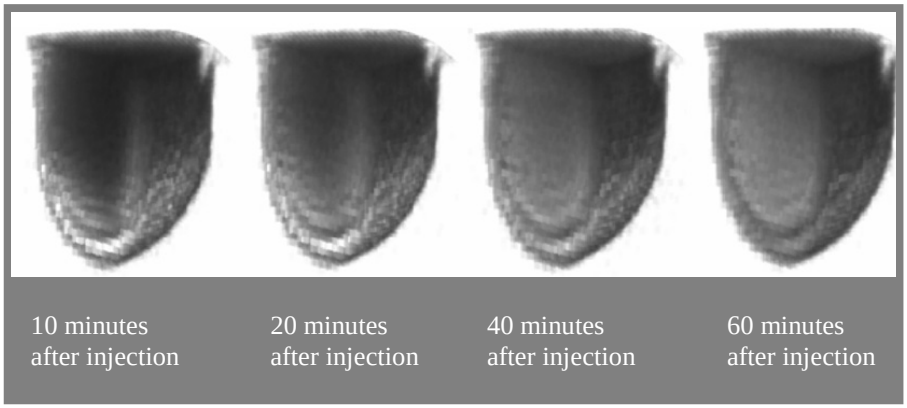

Figure 3.31: Tumour (c) DCE-MRI data set

To simplify the analysis the data is extracted and graphed (figure 3.32), from this it clear to see the regions to which the contrast agent has been transported over a time period of 60 minutes. Fick's law of diffusion is used to give an estimate as to the distance that the contrast agent could be transported by diffusion in 60 minutes. Firstly an approximation for the apparent diffusion co-efficient (ADC) of Magnevist (D_M) in tumour tissue is made as the true value has not been determined experimentally. The approximation is based on the following assumptions:

- diffusion co-efficient of Magnevist in water is 0.4×10^{-9} m^2s^{-1} (Osuga et al. 2004)
- self diffusion co-efficient of water is 2.1×10^{-9} m^2s^{-1}
- diffusion co-efficient of water reduced to 0.6×10^{-9} m^2s^{-1} in tumour tissue (Herneth et al. 2003)

- a similar reduction in the diffusion co-efficient of Magnevist would give a tumour tissue value of 0.1 x 10^{-9} m^2s^{-1}

Applying Fick's Law of Diffusion (Diffusion length = √4Dt) gives approximately 1.4mm as the expected distanced travelled by Magnevist molecules due to diffusion. This concurs with the information provided by the graph (figure 3.32) which shows that regions approximately 1-2mm away from the site of the initial sharp enhancement peak have enhanced in the ensuing 60 minutes.

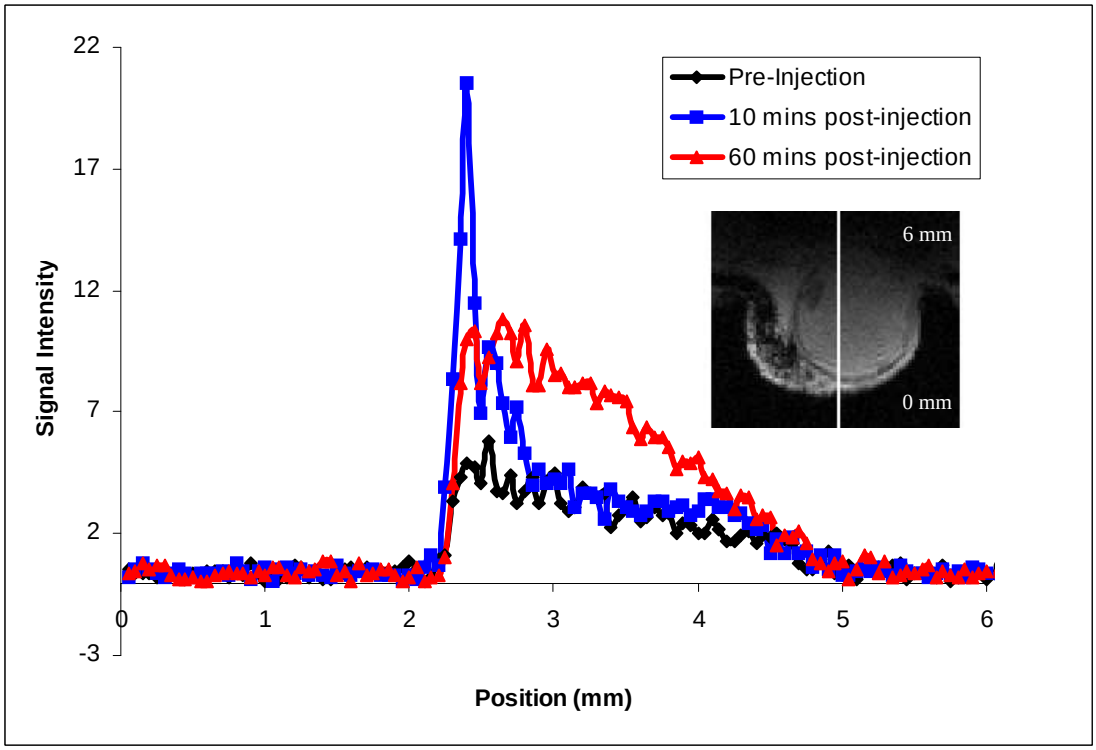

Figure 3.32: Graph showing signal intensity profile variation with time for a central sagittal tumour slice

In summary the coil set-up gave high quality images with resolutions significantly higher that those previously reported (see section 3.6 for full details). These studies appeared to show that the initial delivery of Magnevist was well correlated with the

blood supply identified on pre-contrast images and that diffusion appears to play a significant role in the subsequent transport of the contrast material. These findings are of particular significance in the development and application of the mathematical transport models mentioned in chapter one.

3.5.3.3 Effect of Molecular Weight on Delivery and Transport

A number of emerging cancer therapies such as monoclonal antibodies and targeted gene therapy involve the delivery of molecules of the order of kilo Daltons. DCE-MRI was used to investigate the differences in delivery and transport of low and high molecular weight materials. The contrast agents Magnevist and GC48-DTPA-Gd were administered to the same tumour separated by a washout period. It was found that delivery of both agents was correlated with blood supply (figure 3.33). However, there was a clear difference between the subsequent diffusion of the agents (3.34). As would be expected the lower molecular weight material exhibited greater diffusion and consequently covered a larger area of the tumour. A volume projection is used to give an impression of the overall disparity in tumour coverage of the two agents (figure 3.35).

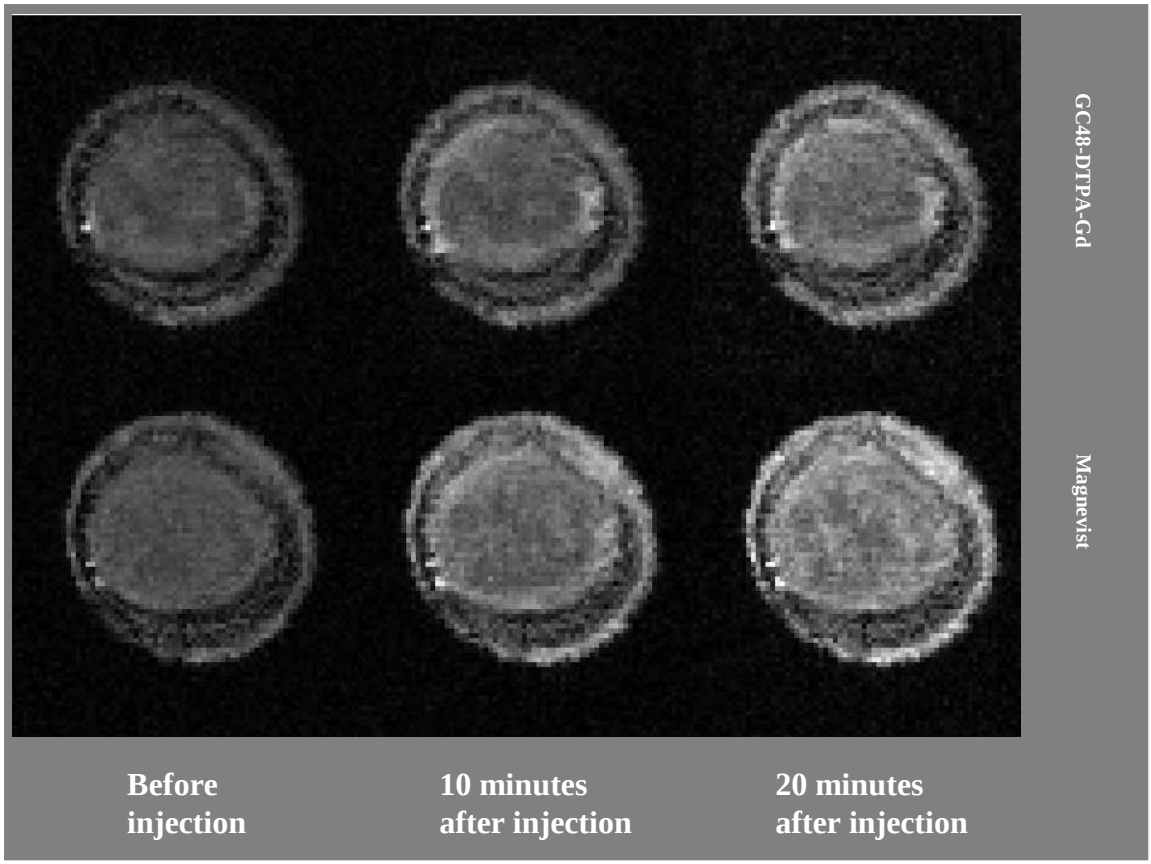

Figure 3.33: Central coronal tumour slice following the administration of GC48-DTPA-Gd (top row) and Magnevist (bottom row).

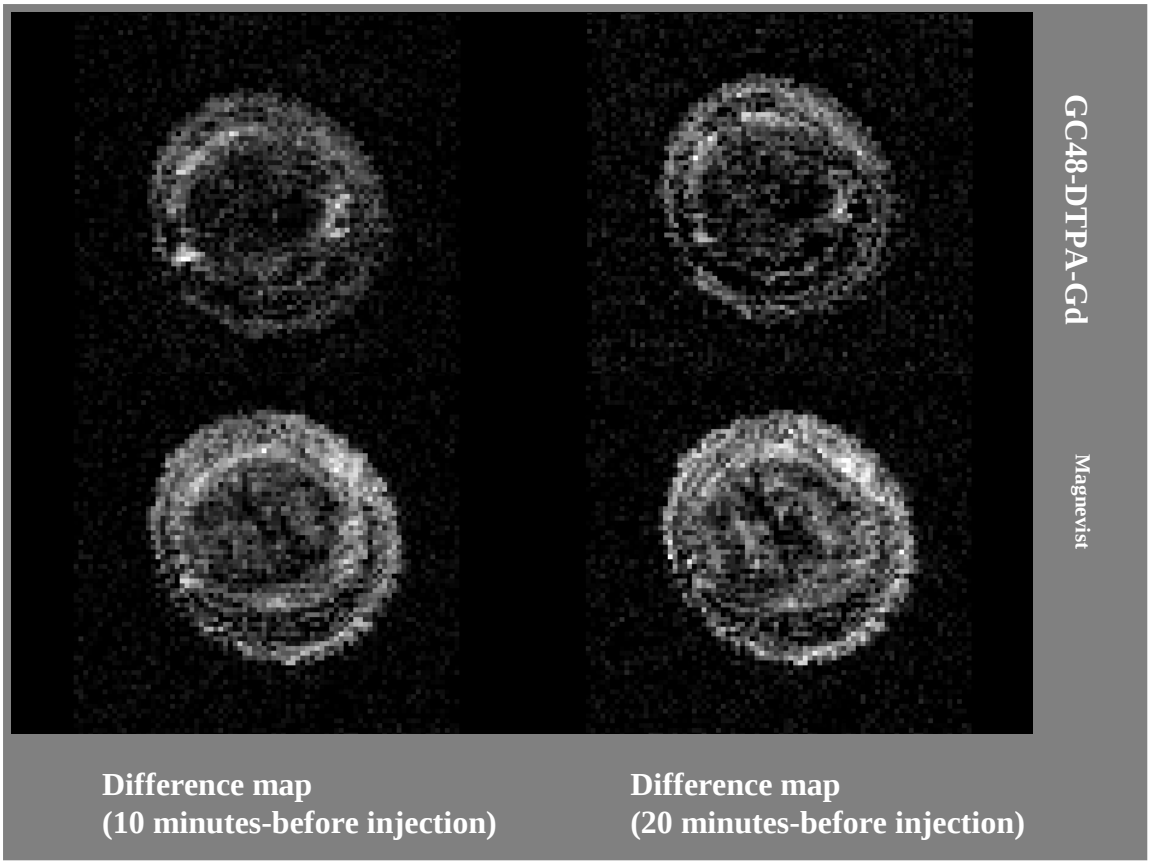

Figure 3.34: Difference maps for central tumour coronal slices following the administration of GC48-DTPA-Gd (top row) and Magnevist (bottom row)

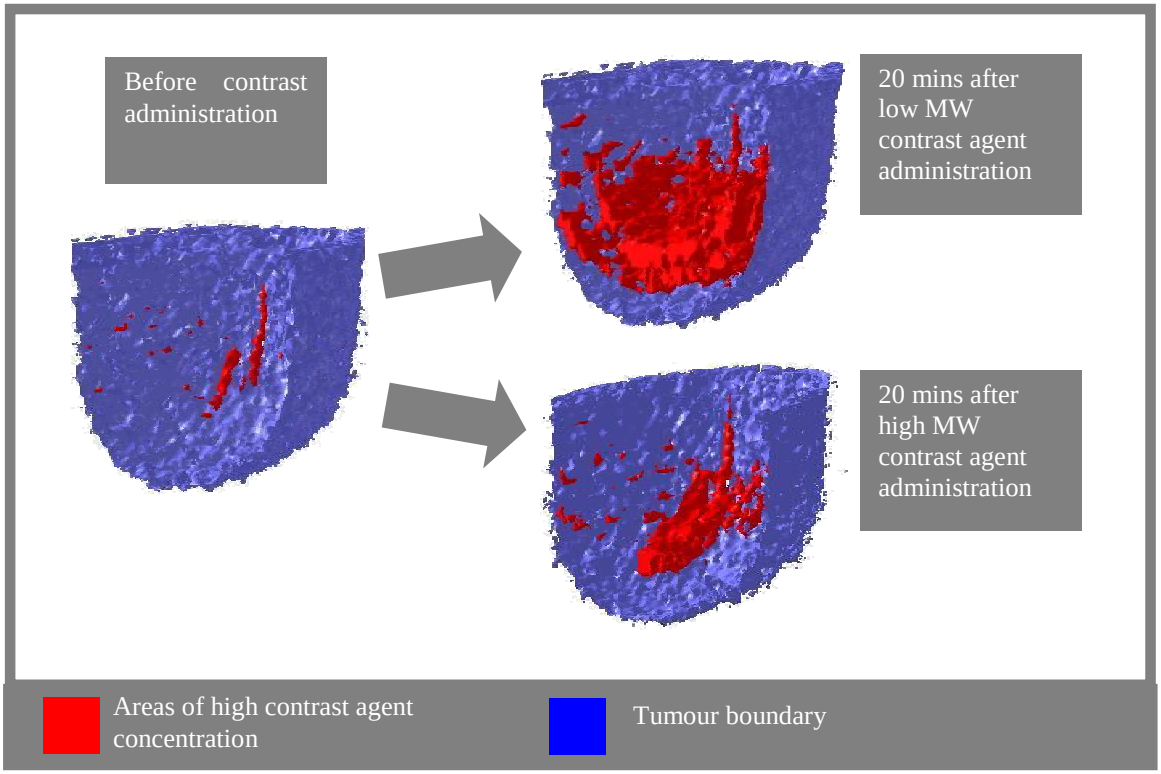

Figure 3.35: Tumour volume projections before and 20 minutes after the administration of GC48-DTPA-Gd and Magnevist.

3.6 Discussion and Conclusions

The aims of this section of work were to explore the potential of new polymeric contrast agents as blood pool agents and evaluate a new solenoid micro-coil set-up for the imaging of flank xenografts whilst elucidating information about the molecular weight effect on tumoural delivery and transport of materials.

Both the novel contrast agents showed increased vascular specificity compared with Magnevist. In particular the GC2-DTPA-Gd agent offered very clear vascular enhancement which allowed the identification of the larger blood vessels of the head. There are reports in the literature of a number of different blood pool contrast agents that are at various stages of development (see chapter one for further details). The main perceived advantage (discussed in chapter two) of using GC as a backbone for MRI contrast agents is that a wide range of molecular weight starting materials can be generated. Ultimately the molecular weight could be tailored to give the optimal combination of plasma residence time and overall clearance.

This flexibility is also relevant in the context of the use of contrast agents as drug surrogates in tumour transport studies. A wide range of molecular weights of contrast agents means that a number of different types of drugs and therapies could be investigated.

Furthermore it would be predicted by considering the components of this polymeric agent that there should be few problems with biocompatibility or immunogenicity to hinder its ultimate clinical development.

A study of the literature was performed to give a technical context to the tumour imaging performed here using the novel coil set-up. It was found that the majority of DCE-MRI studies use 2D imaging with anisotropic voxels in which the in-plane resolution is significantly finer than the slice thickness. The following are some

examples of the voxel dimensions for groups who publish regularly in this area: 0.125 × 0.125 × 1.000 mm^3 (Bhujwalla et al. 2003), 0.400 × 0.500 × 1.000 mm^3 (Li et al. 2005), 0.310 × 0.310 × 2.000 mm^3 (Benjaminsen et al. 2008), and 0.200 × 0.200 × 1.000 mm^3 (Kobayashi et al. 2004). The highest resolution 3D scanning with isotropic voxels found in the literature was 0.275 mm^3 (Shiftan et al. 2005).

The results presented here are for 3D imaging with a resolution of 0.100 mm^3, in volume terms this is 20 fold difference compared to the 3D results reported above and a 16 fold difference compared to the 2D results. We feel that there is a risk that 2D imaging in which the slice thickness represents a large proportional of the overall tumour size will not accurately reflect the heterogeneity of the tumour. Analysis of coronal and sagittal slices from our 3D data shows that the tumour varies in all directions and that there are a number of small features which could be averaged out in a thick slice.

Similarly the resolution achieved (0.100 mm^3) for the magnetic resonance angiography (MRA) of the tumour was a 10 fold improvement on those previously reported (Kobayashi et al. 2001; Fink et al. 2003). The technical challenge of recording sufficient signal is probably the reason why there are so few reports of angiography studies of flank tumours in the literature. Angiography is of particular interest in cancer due to the relationship between blood supply and tumour growth and spread. It is well known that a tumour requires its own blood supply in order to grow beyond 1mm diameter (Padhani et al. 2001). An array of therapeutics exist that aim to treat tumours by targeting the vasculature in order to deprive the cancer cells of oxygen and nutrients (O'Connor et al. 2008). Whilst the vessels detected by MRA are influenced by size and direction and speed of flow (Muhs et al. 2007) the results show how the coil set-up can be used to give a snapshot of the overall vascularisation of the

tumour. This technique may be especially useful when considered in conjunction with the theory of vascular normalisation as proposed by Jain and co-workers. They offer evidence of a time window following angiogenic therapy in which the tumour vasculature gains more of the structural and functional characteristics of normal vasculature allowing for more efficient subsequent drug delivery (Jain 2005). The effects of a particular treatment on the vasculature could be serially monitored by MRA to identify the optimum time period for the subsequent administration of a chemotherapy agent.

In tumour biology terms a myriad of publications were found in the literature in which DCE-MRI and associated mathematical derivation of parameters such as transfer co-efficient, vascular volume fraction and measures of permeability and perfusion were found (see chapter one). These studies apply models based on the unidirectional transfer of contrast material between compartments such as the Tofts two compartment model (Tofts et al. 1991) and the three compartment model (Pathak et al. 2005). We decided to look at the tumour in more elementary fashion and analyse the relationships between blood supply and contrast agent delivery and the modes of the subsequent transport of this material. As far as could be found these were the first studies in which experimental DCE-MRI was used to confirm the link between blood supply and the delivery of contrast material. Furthermore despite it being well established that diffusion plays a major role in the movement of materials in the tumour intersitium (Jain 1987) no published reports of the direct MRI investigation of this phenomenon could be found.

The concept of using MRI contrast agents as surrogates for drugs to investigate tumoural delivery and transport issues is not new. Both low molecular weight contrast materials (Artemov et al. 2001) and macromolecular contrast materials

(Kobayashi et al. 2002) have been used to predict the delivery and transport of drugs of a similar molecular weight. In both cases the delivery of the drug confirmed by histology proved to be well correlated with the prediction by MRI. Furthermore studies have been performed in which contrast agents with different molecular weights have been serially administrated to the same tumour in order to optimise modelling procedures (Turetschek et al. 2004; Orth et al. 2007). The studies reported here would appear to be the first time that these two concepts (the use of contrast agents as drug surrogates and the serial administration of contrast agents with different molecular weights) have been brought together. The imaging showed that the diffusion distances for higher molecular weight materials were lower than for low molecular weight materials. The relevance of this type of experiment could be as a means by which to determine which drug treatments (based on their molecular weight) would be expected to offer good coverage of a specific tumour. In essence, ultimately, a therapeutic molecular weight cut-off below which the successful treatment of a particular tumour would be significantly improved could be found. In drug development terms this may also help in the selection of a suitable tumour model to test a new treatment.

Chapter Four: Vascular Corrosion Casting

4.1 Introduction

Vascular corrosion casting is the process of obtaining a plastic mould of the vascular structure of an organism. Casts are produced by filling the vascular space with liquid plastic following exsanguination, after curing (the liquid plastic contains a hardener) the cast is recovered by dissolving the supporting tissues and bones. Traditionally the cast are subsequently imaged using scanning electron microscopy (SEM) or optical microscopy. The procedure was first reported in 1975 (Shively et al.) and has subsequently been used to characterise various vascular beds such as those in the eye (Mackenzie et al. 2008), liver (Pannarale et al. 2007), placenta (Peker et al. 2006), kidney (Wei et al. 2006), and heart (von Ludinghausen et al. 2001). The technique has also been used to verify the results of magnetic resonance angiography (MRA) in the study of cerebrovascular abnormalities in mouse models of Alzheimer's disease (Beckmann et al. 2003) and in the study of the response to vascular targeted therapies in cancer (Malcontenti-Wilson et al. 2001; Kuruppu et al. 2002; Hafez et al. 2007).

All of these studies used SEM to image the cast, however it is widely recognised that the inherent loss of 3D structure is an important disadvantage of this technique. To address this issue, research has been conducted into the use of confocal microscopy (Wagner et al. 2006), an approach which can also be used to generate information related to the vascular surface area and volume but is time consuming and non-absolute.

4.2 Aims and Objectives

The aim of this section of work was to obtain vascular corrosion casts of mouse flank tumours and investigate new magnetic resonance imaging (MRI) based approaches for their analysis. The first approach involved mounting a cast in gadolinium doped

agarose gel with the aim of developing a simple and accurate method to measure vascular volume. The second approach was to image the cast 'in situ' prior to tissue maceration with the aim of maintaining the 3D vascular structure. Alongside these novel approaches a cast was analysed using the traditional methods of optical and scanning electron microscopy (S.E.M).

4.3 Materials and Methods

4.3.1 Materials

Item	Supplier
PU4ii Resin	VasQtec Zurich, Switzerland
PU4ii Hardener	VasQtec Zurich, Switzerland
PU4ii Blue Dye	VasQtec Zurich, Switzerland
2-Butanon	Sigma Aldrich, U.K.
Sodium Chloride	Sigma Aldrich, U.K.
Sodium Bicarbonate	Sigma Aldrich, U.K.
Glucose	Sigma Aldrich, U.K.
Magnesium Sulphate	Sigma Aldrich, U.K.
Potassium Chloride	Sigma Aldrich, U.K.
Sodium Phosphate	Sigma Aldrich, U.K.
Calcium Chloride	Sigma Aldrich, U.K.
Heparin	Sigma Aldrich, U.K.
4% Formalin	Sigma Aldrich, U.K.
Potassium Hydroxide	Sigma Aldrich, U.K.
Formic Acid	Sigma Aldrich, U.K.
Agarose Gel	Sigma Aldrich, U.K.
Magnevist	Bayer Healthcare

4.3.2 Methods

Firstly the resin, pigment and hardener solutions were prepared: 5g of the resin was weighed in a disposable centrifuge tube, a 1cm length of the blue pigment was applied to the inside of a disposable centrifuge tube and dissolved in 2-butanone (5-10mls) and 0.8g of hardener was weighed in a separate centrifuge tube. The pigment solution was then added to the resin and mixed well using a vortex mixer. Immediately prior to perfusion the resin and pigment mixture was added to the hardener and mixed well

using a vortex mixer. Following MRI sessions the anaesthetic level was increased to 5% isofluorane, in a 70/30 mixture of nitrous and oxygen. Following an incision through the chest the left ventricle of the heart was cannulated and the cannula clamped in place, a three way luer connector was used to connect the cannula to a primed section of tubing attached to a syringe containing the pre-heated (37°C) heparinised rinsing solution (30mls). The syringe had been previously loaded into a syringe pump (NE-1000, New Era Pump Systems) programmed at a flow of 4ml/min. The three way connector was used to ensure no air ingress into the cannula. The right side of the heart was punctured to allow fluid outflow. Following the passage of the rinsing solution the animal was fixed by the perfusion of heparinised 4% formalin solution (30mls) using the syringe pump as above. Finally the animal was perfused with the resin/pigment/hardener mixture. For both the traditional SEM and new agarose gel methods the resin was allowed to set at room temperature for 72 hours followed by soft tissue maceration in 20% potassium hydroxide (24 hours) and decalcification in 5% formic acid (12 hours). The cast was then rinsed thoroughly with water and dried. In the case of the agarose gel method the cast was placed in a small plastic container into which liquid agarose was poured (5-10mls, 3% w/v agarose containing 0.5mM Magnevist). MR imaging was performed after the agarose had set. For the 'in situ' method the tumour was surgically removed following perfusion and curing and then soaked for 72 hours in Magnevist solution (20mls, 0.5mM), neither of the maceration steps were performed. Tumours were removed from the Magnevist solution immediately prior to imaging.

4.3.3 Optical Microscopy: Theory and Experimental Details

Optical microscopes use visible light and a series of lenses to magnify a sample (Bradbury 1984). A modern microscope consists of a light source, stage, objective lenses, eyepiece lenses and a mounting point for a digital camera to record images. The light source is focused through a condenser which gives control over the light intensity and ensures that it strikes the sample uniformly. The sample is generally mounted on a glass slide and then loaded onto the stage. The course and fine focus knobs are used to adjust the height of the stage to bring the object into focus. The objective lens collects light from the sample and provides the majority of the magnification. A number of objective lenses mounted on a carousel are used to give different degrees of magnification typically ranging from 4× to 100×. The lenses in the eyepiece also provide some magnification as well as forcing the light to converge on the retina to allow the user to view the image. The overall magnification is calculated by multiplying the magnification provided by the objective and eyepiece lenses. A Nikon FXA optical microscope (Nikon Corp., Japan) equipped with digital image capture was used in these studies. Casts were simply mounted on a microscope slide and imaged with no further preparation.

4.3.4 Scanning Electron Microscope (S.E.M): Theory and Experimental Details

Whereas an optical microscope uses light to generate an image electron microscopy uses a beam of electrons (Chescoe et al. 1990). The principle of scanning electron microscopy is that a beam of electrons is scanned across the surface of a sample and a detector is used to measure the intensity of a chosen secondary signal. A number of secondary signals can be detected including secondary and backscattered electrons. As the names would suggest backscattered electrons are beam electrons that have been reflected by elastic collisions with the sample whereas secondary electrons

originate in the sample and are released due to inelastic collisions with the beam. The intensity of the particular secondary signal is displayed on a cathode ray tube (CRT). Sample surfaces must both conduct electricity and be grounded to prevent the build up of electrostatic charge, non-metal samples are coated with an ultrathin layer of a conductor such as gold, platinum, tungsten or graphite. A scanning electron microscope comprises an electron source, a vacuum system, a focusing system, deflector coils, an aperture, a detector, and a CRT display. Electrons are generated by either a tungsten filament heated to 2800°C or a lanthanum hexaboride crystal mounted on a heated tungsten filament. The electrons are accelerated towards the sample by a voltage gradient then focused into a beam which is made to sweep across the sample line by line using two sets of deflector coils.

Cast samples were first completely dried under vacuum and then coated with gold again under high vacuum. The instrument used was a Philips XL30 (Philips, U.S.A.) which has a lanthanum hexaboride crystal electron source and is capable of 200,000× magnification with a resolution of 3.5nm. Secondary electrons were the detected signal in all imaging.

4.3.5 MRI: Experimental Details

MRI was performed on both the agarose get mounted cast and the ‘in-situ’ tissue mounted casts. In both cases the zero MR signal plastic was used to give a negative image which could be manipulated in post processing to give a 3D representation of the cast.

4.4 Results

4.4.1 Optical Microscopy

Images of the cast at various resolutions were taken, a discussion of the vascular features observed follows in section 4.4.3.

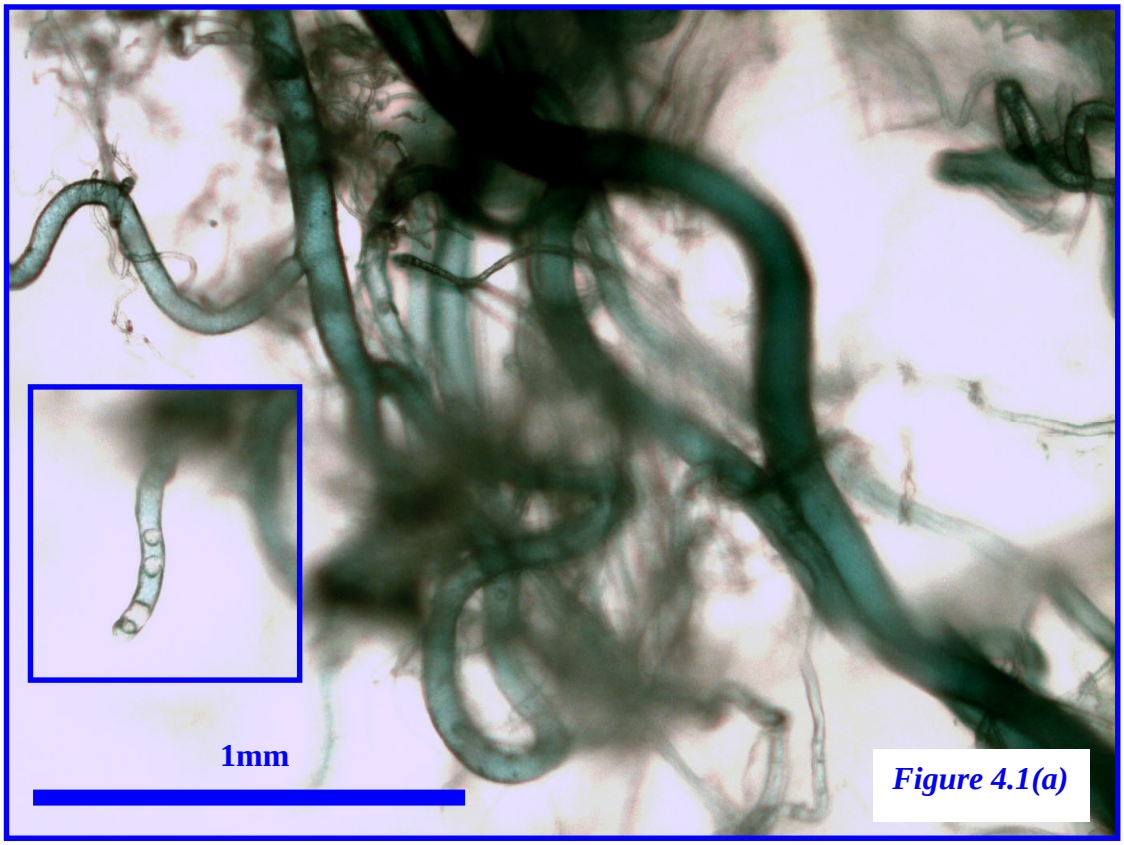

Figure 4.1(a)

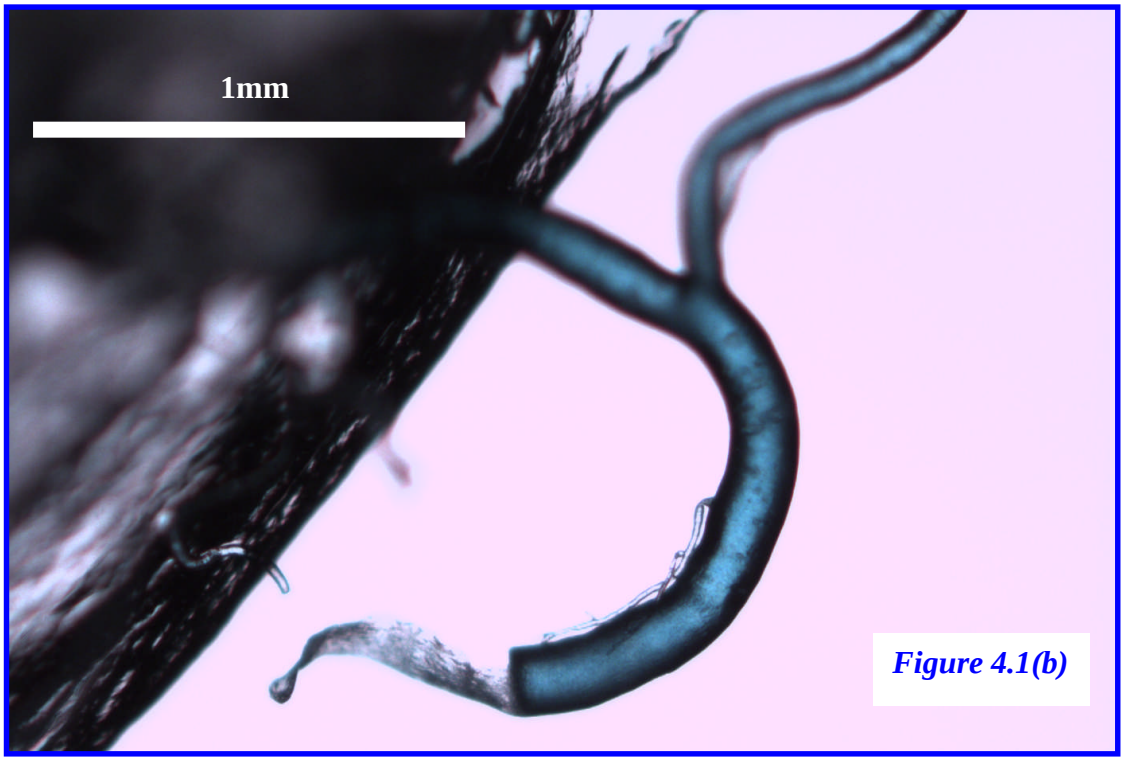

Figure 4.1(b)

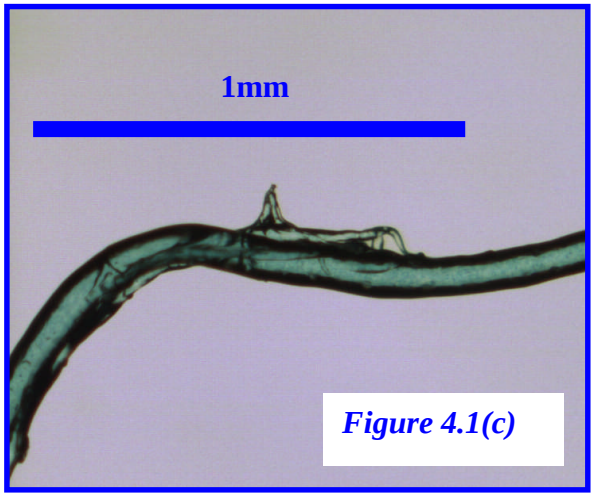

Figure 4.1(c)

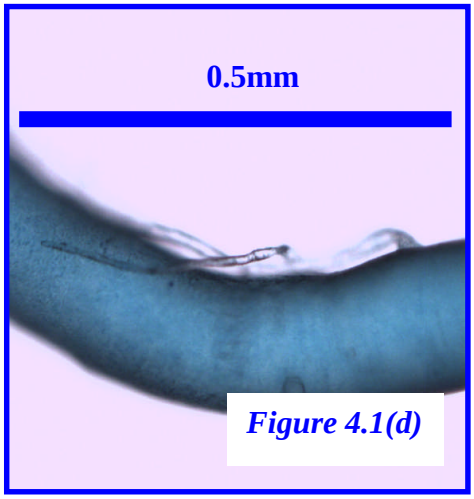

Figure 4.1(d)

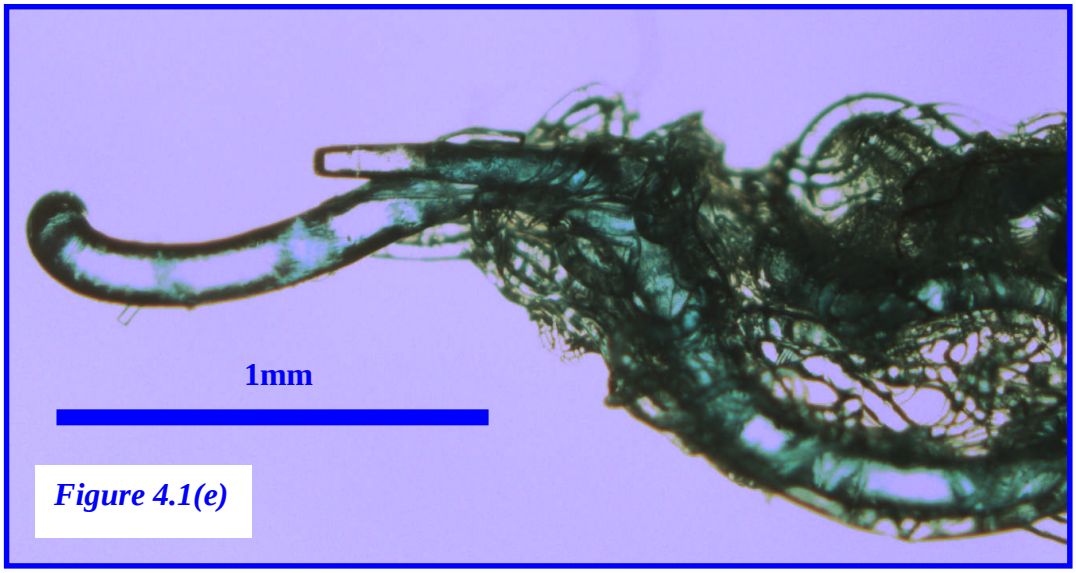

Figure 4.1(e)

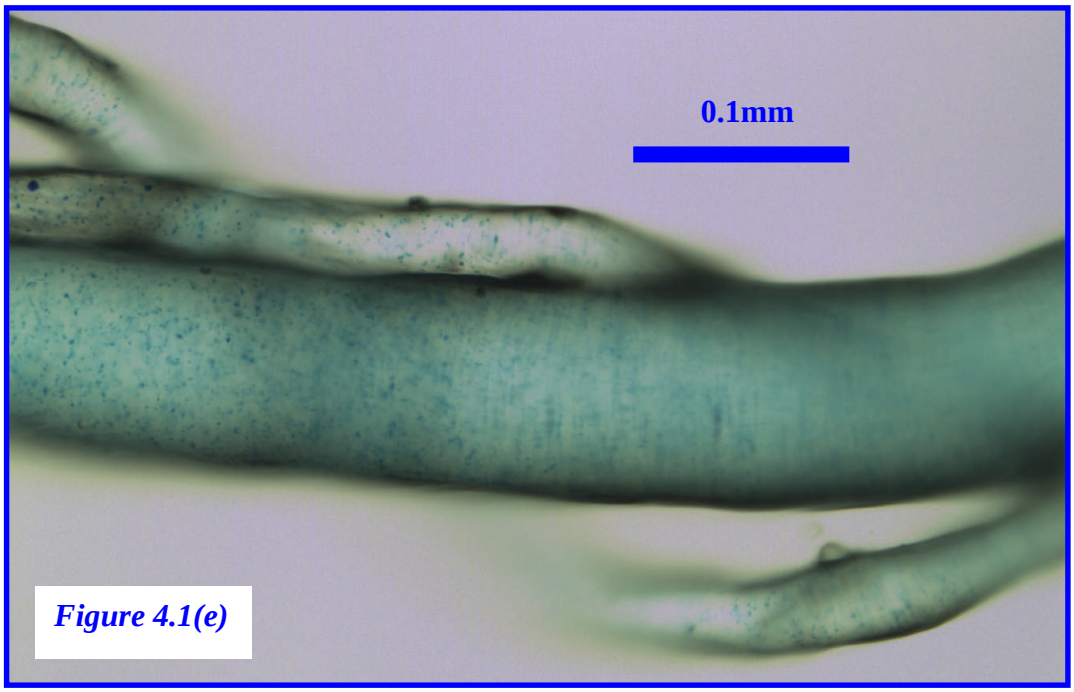

Figure 4.1(e)

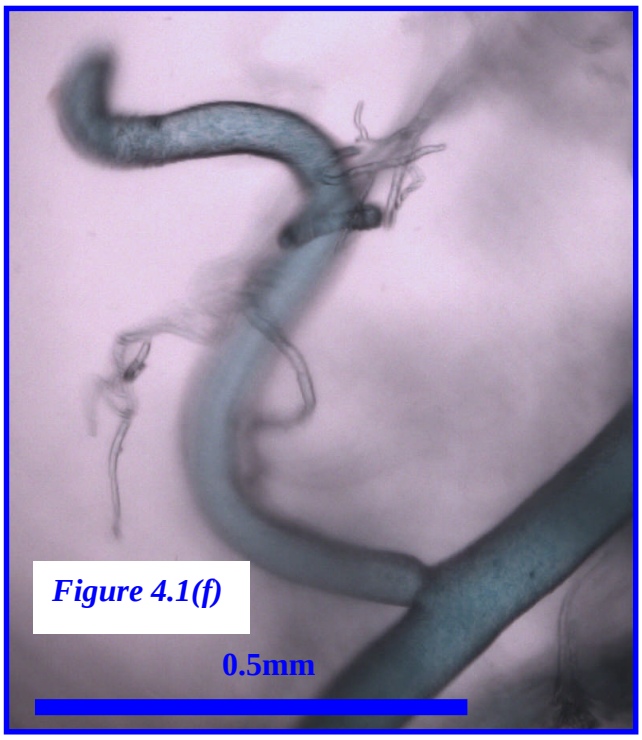

Figure 4.1 (a-f): Optical microscope images of vascular corrosion cast at various resolutions

4.4.2 Scanning Electron Microscope

Again images at various resolutions and orientations were taken, a discussion of the vascular features observed follows in section 4.4.3.

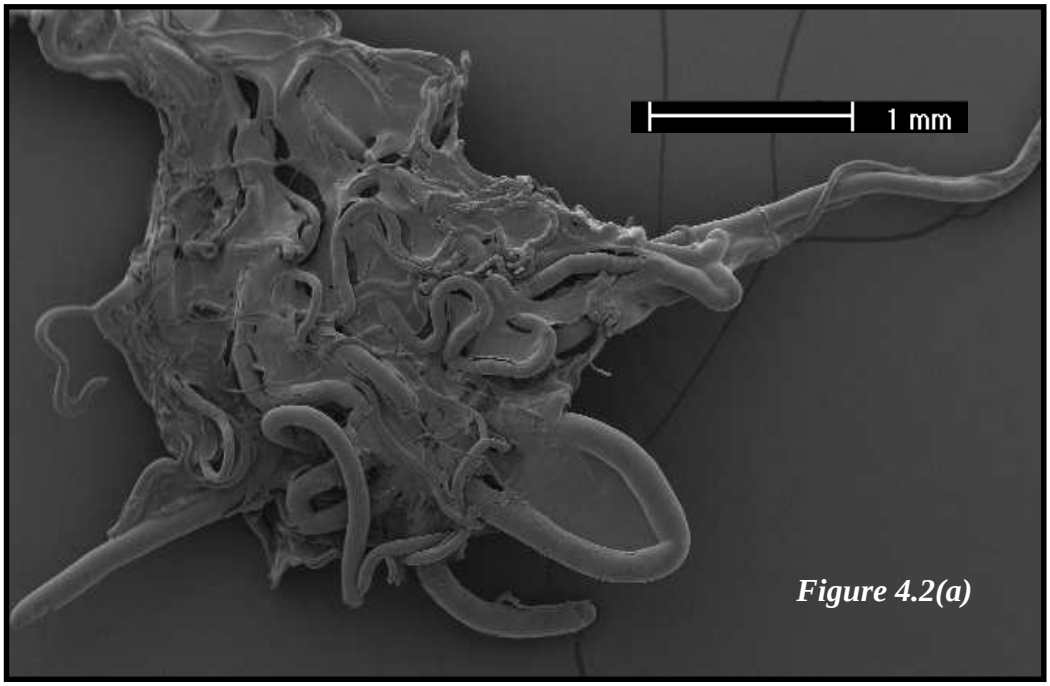

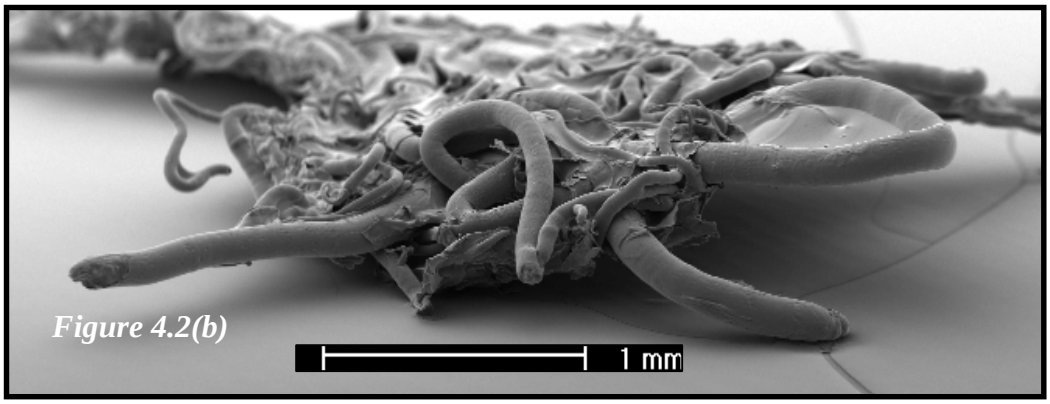

Figure 4.2(b)

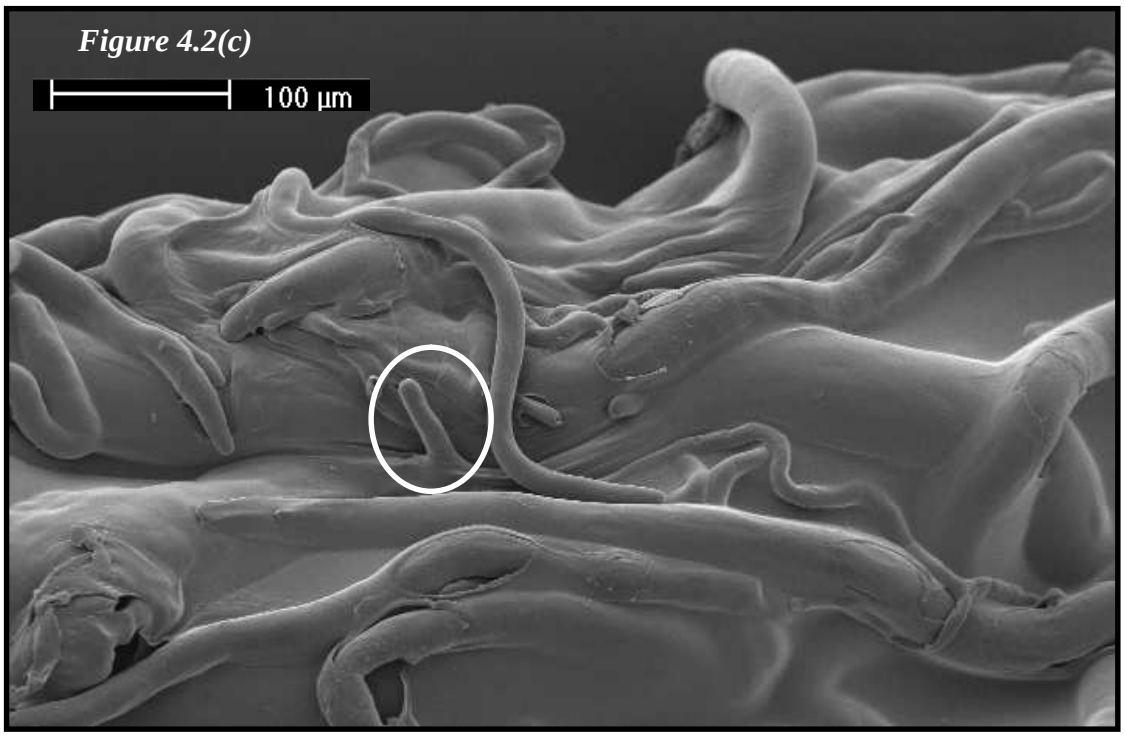

Figure 4.2(c)

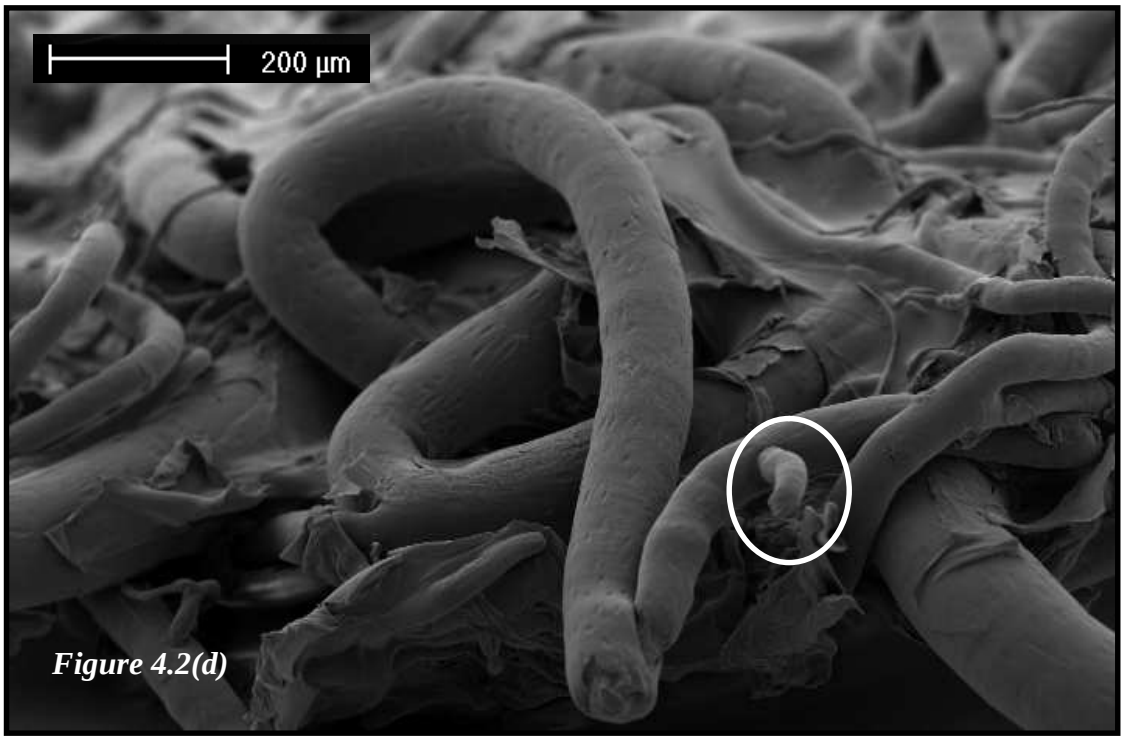

Figure 4.2(d)

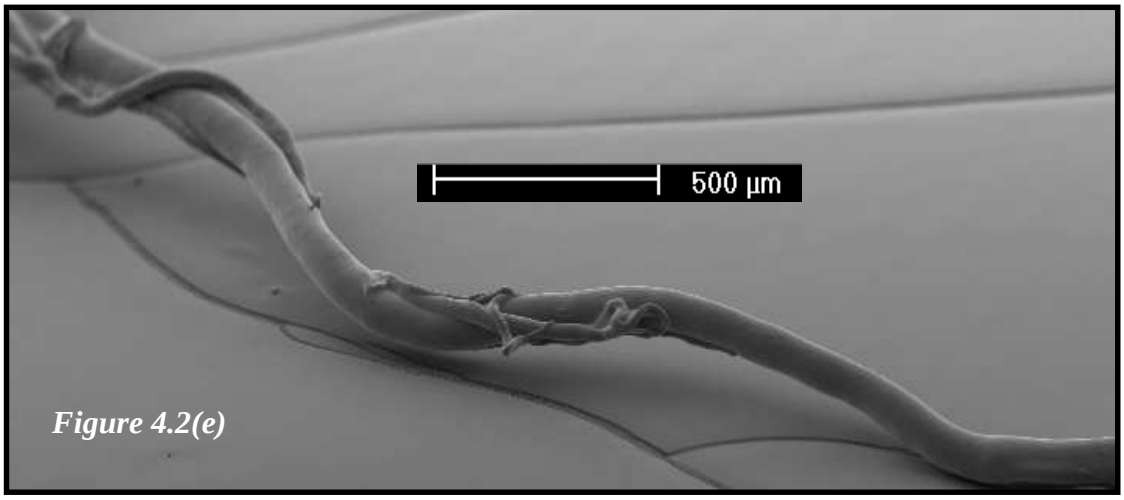

Figure 4.2(e)

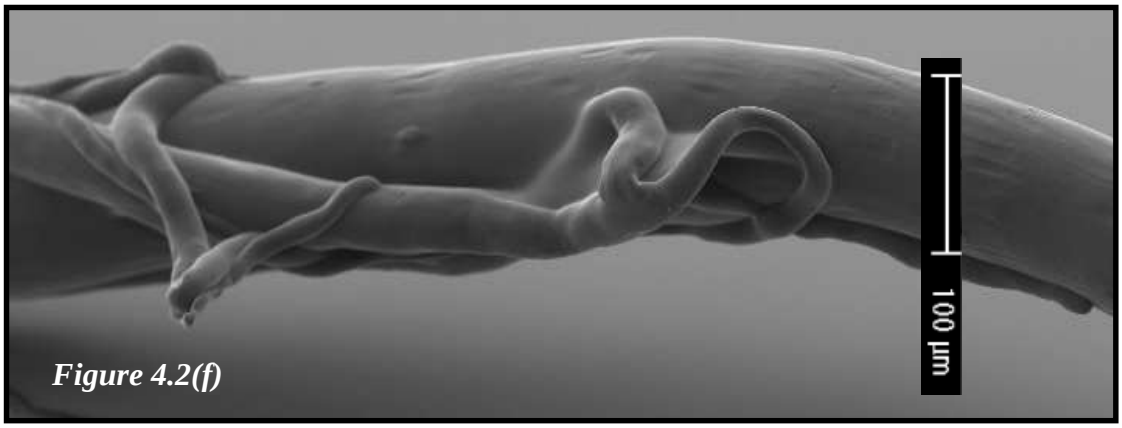

Figure 4.2(f)

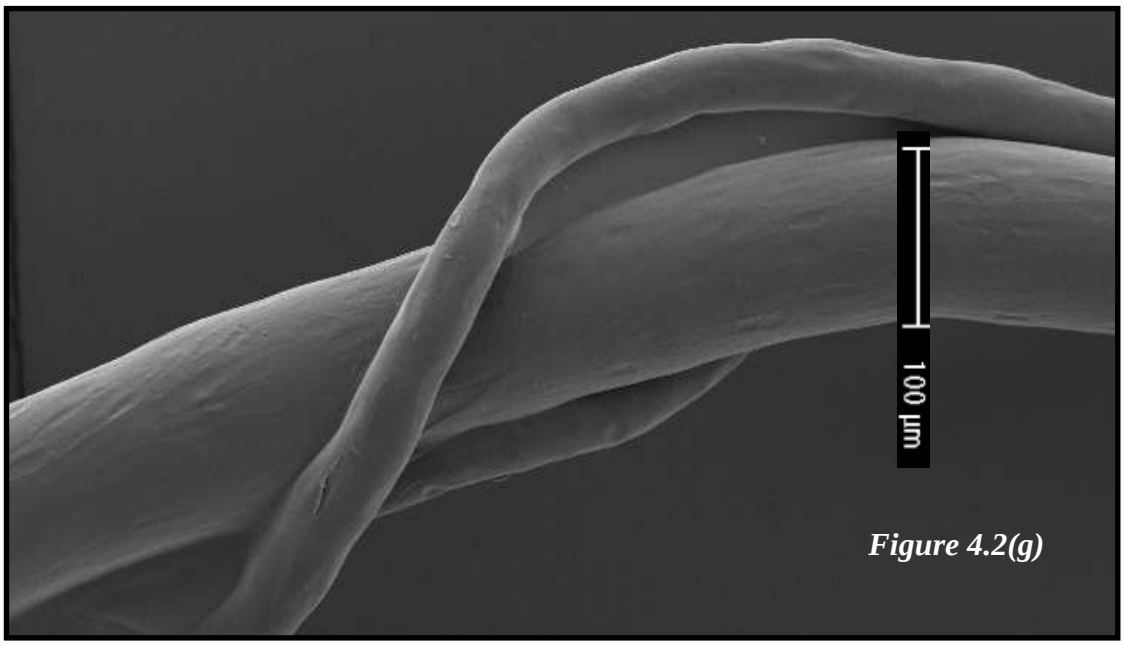

Figure 4.2(g)

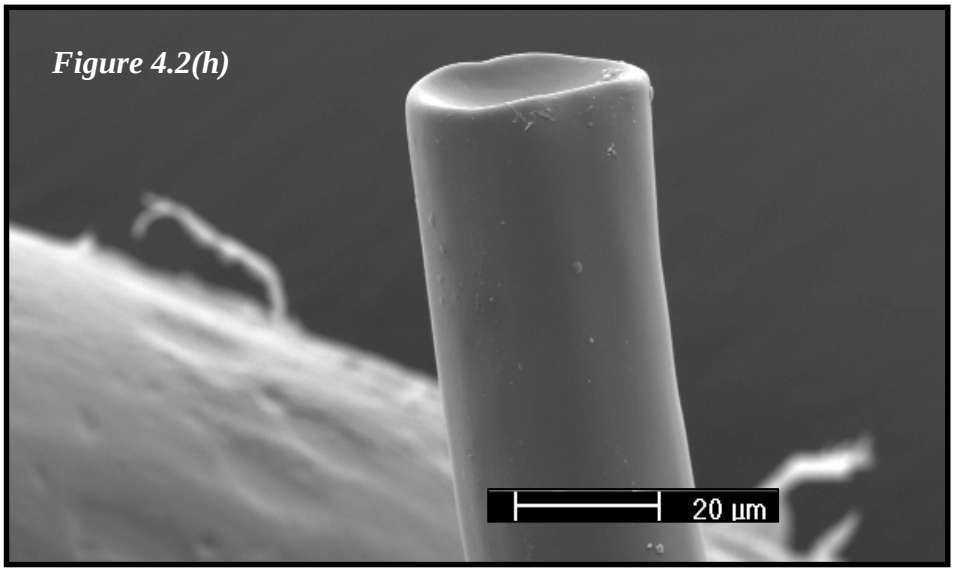

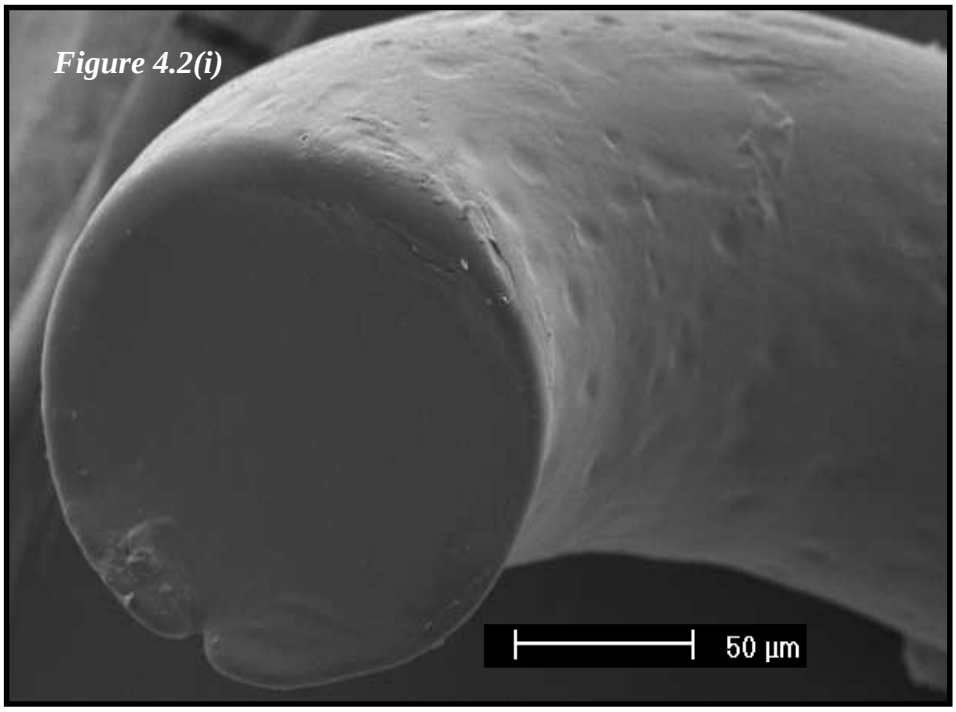

Figure 4.2 (a-i): Scanning electron microscope images of vascular corrosion cast at various resolutions

4.4.3 Discussion of Optical and Scanning Electron Microscopy Results

The vascular structure of normal tissue consists of arterioles, capillaries and venules that form a well organised, regulated and functional system (Martini 1998). Conversely tumour vasculature has high spatial heterogeneity and transient patency with vessels that are characterised as dilated, saccular and tortuous. Furthermore the vessels of normal tissue contain dichotomous branching whilst the tumour vasculature commonly contains trifurcations with uneven vessel diameters and sprout formation (Fukumura et al. 2007).

A number of these features are apparent in the images of figures 4.1 and 4.2. For example the overall tortuosity and complexity of the tumour vasculature is evident in figures 4.1 (a) and 4.2 (a&b), sprout formation is apparent in figure 4.2 (c&d) and the lack of regulation is clear in figure 4.2 (e&f) in which smaller vessels appear to be coiled around larger vessels. These images also allow for the differentiation between arteries and veins. In the higher resolution images the elongated imprint of endothelial cells characteristic of an artery can be seen [figure 4.2 (f&g)] in comparison with the rounded imprint characteristic of veins [figure 4.2 (i)] (Krucker et al. 2006). Furthermore there is evidence of how morphology is maintained by this technique in figure 4.2 (b) in which the constriction at the branch point of two vessels can be seen.

4.4.4 Cast MRI

4.4.4.1 Cast Mounted in Agarose Gel for Vascular Volume Measurement

ImageJ was used to analyse and present the data generated [figure 4.3(a-d)], the plastic cast generates no signal and the doped agarose gel generates a high signal. The images are inverted and a binary mask applied so that the cast shows as bright white against a black background.

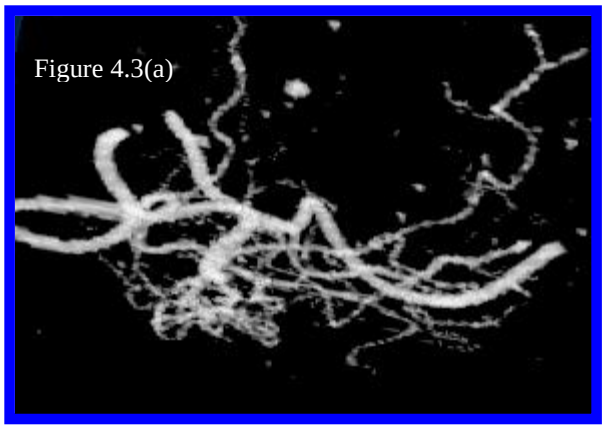

Figure 4.3(a)

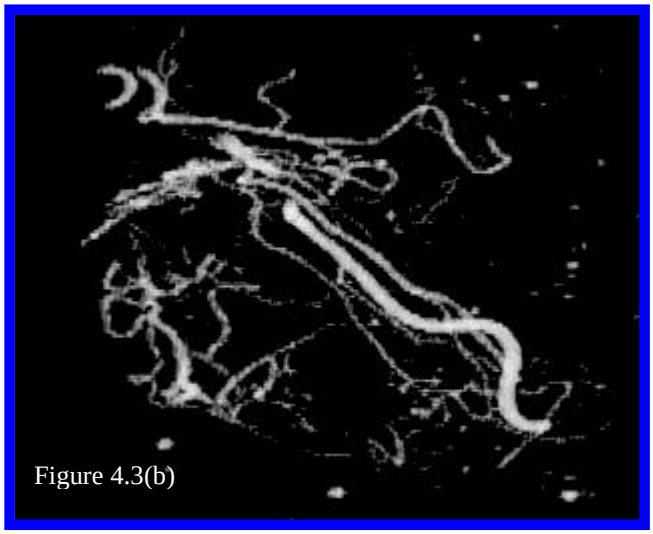

Figure 4.3(b)

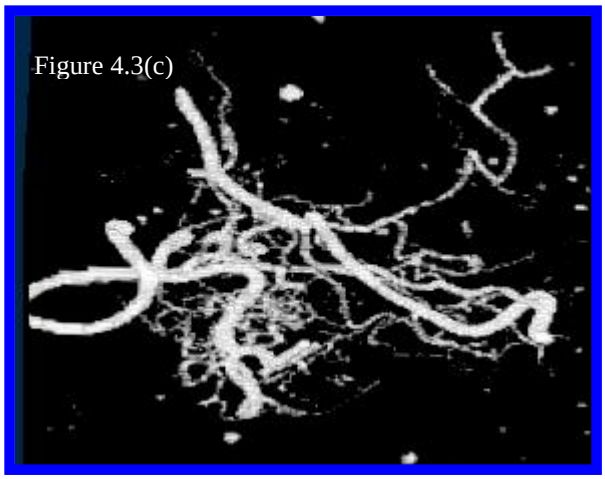

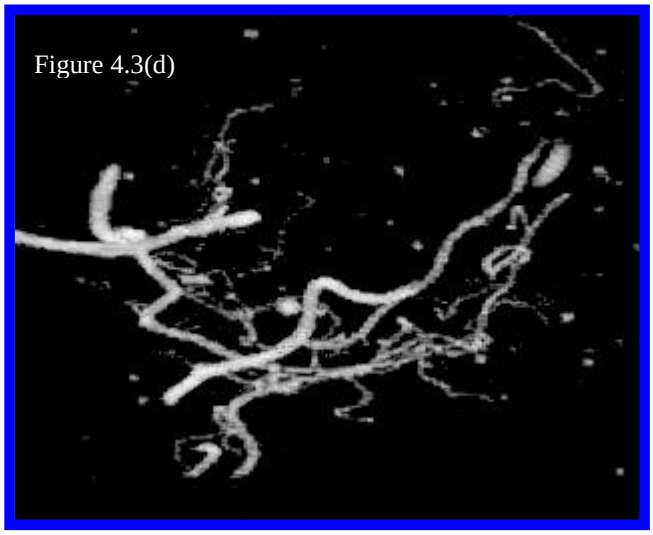

Figure 4.3 (a-d): MR images of cast mounted in agarose gel

The images (figure 4.3) would appear to suggest that there are a fair number of bubbles in the gel, however it is felt that this problem could be easily reduced if the gel was held under vacuum for a longer time. This technique allows high quality 3D representations of the tumour vasculature to be obtained as well as facilitating simple estimation of the absolute vascular volume.

The application of a binary mask means that voxels can only have a value of 1 (contain cast) or 0 (contain gel).

The volume is estimated by the multiplication of the number of voxels with a value of 1 (or white in the image) by the size of the voxel. In this example

- there are 604 voxels which have a value of 1 (contain cast)
- the voxels have a volume of 0.001 mm^3
- giving a vascular volume of 0.604 mm^3.

Unfortunately the volume of this tumour was not determined prior to tissue maceration so an exact vascular volume fraction cannot be given. But to put this value in context the tumours examined in these studies had an average volume of approximately 10.0 mm^3 which would suggest a vascular volume fraction of approximately 6%. No details of the experimental determination of the vascular volume fraction of this cell line could be found in the literature. However, MRI based studies used to estimate the vascular volume fraction of a number of other cell lines were found (Bhujwalla et al. 2001; Bremer et al. 2003; Jordan et al. 2005). The values range from 2-8% which gives some confidence in the result obtained above.

This shows how quickly and easily this technique can yield the absolute vascular volume of a tumour and there is no reason why this approach could not be extended to any other organ/tissue in the body.

4.4.4.2 Cast Imaged Prior to Tissue Maceration

The results of the 'in-situ' cast imaging are compared with the resulted obtained for previous in-vivo imaging of the same tumour. The cast images have been inverted and presented using ImageJ (low signal regions now appear as the brightest areas in the image). In-vivo imaging was performed with a sequence in which flowing blood will appear hyperintense, images were analysed and presented using IDL.

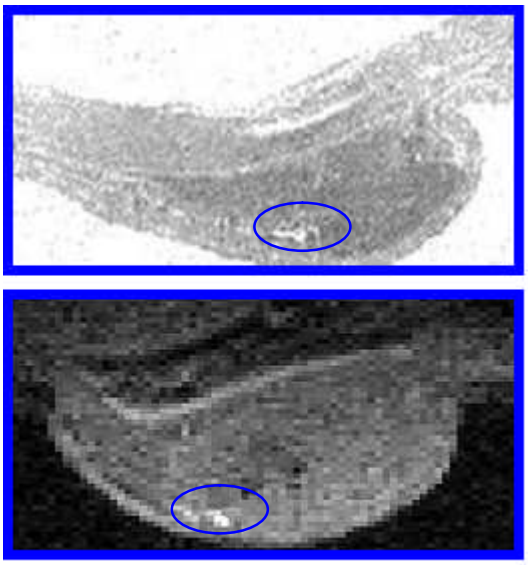

Figure 4.4: Coronal slices from tumour centre comparing imaging of surgically removed cast containing tumour (top) and in-vivo imaging of tumour (bottom)

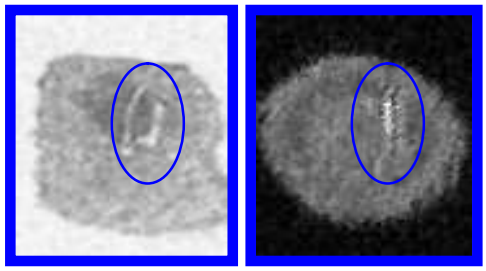

Figure 4.5: Sagittal slices from near tumour tip comparing imaging of surgically removed cast containing tumour(left) and in-vivo imaging of tumour (right)

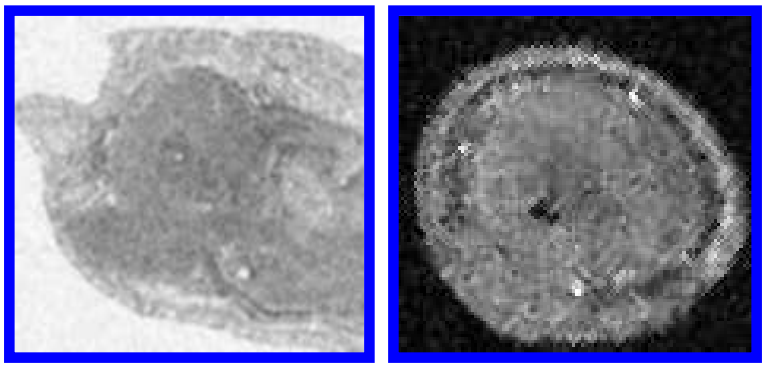

Figure 4.6: Sagittal slices from tumour centre comparing imaging of surgically removed cast containing tumour(left) and in-vivo imaging of tumour (right)

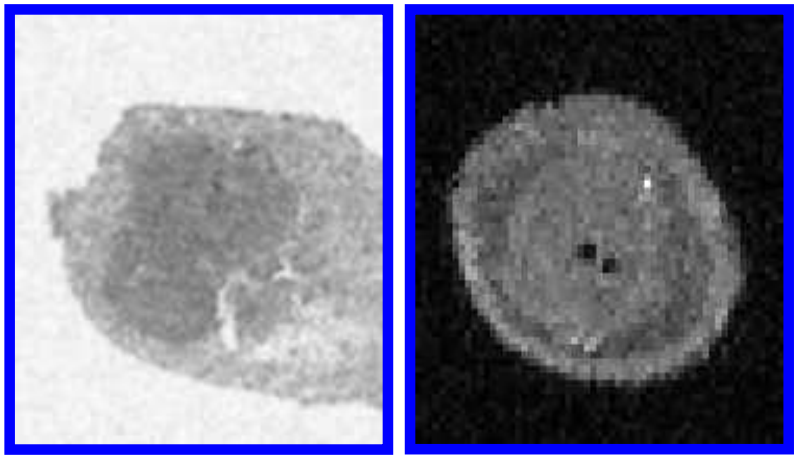

Figure 4.7: Sagittal slices from tumour root comparing imaging of surgically removed cast containing tumour(left) and in-vivo imaging of tumour (right)

Encouragement in the potential of this technique to provide a 3D representation of the cast without loss of structure is given by comparing the images in the four sets of pairs. The cast is clearly visible as hyperintense in the images and seems to have remained in position as it appears in same anatomical locations as the hyperintense blood in the in-vivo imaging. It is felt that this technique requires some optimisation in terms of Magnevist doping concentration, imaging sequence and method of tumour storage after the casting procedure prior to imaging.

4.5 Discussion and Conclusion

Overall it is felt that the traditional SEM approach to vascular cast analysis and the MRI techniques described here are complimentary: SEM gives image resolution and anatomical detail far outwith that of MRI whereas MRI offers the potential to image the cast without the loss of 3D structure and determine absolutely the vascular volume fraction.

As mentioned in the introduction vascular corrosion casting has been employed extensively to characterise the structure of various vascular beds. Furthermore casting has gained increasing use to investigate the disease related changes in gross vascular structure due to conditions such as Alzheimer's (Meyer et al. 2008) and diabetes (Tee et al. 2008). Interest in this technique to investigate cancer has developed due to the intimate relationship between blood supply and the growth and spread of tumours: a tumour requires its own blood supply to grow beyond 1mm in diameter (Padhani et al. 2001). As a result a multitude of cancer therapies are targeted to the vasculature and aim to kill or arrest the development of the tumour by depriving it of oxygen and nutrients (O'Connor et al. 2008). A number of studies have used vascular casting to investigate the morphological effects of these so-called anti-angiogenic treatments (Malcontenti-Wilson et al. 2001; Kuruppu et al. 2002; Hafez et al. 2007). In these circumstances casting was only used in general qualitative terms to compare the vasculature of treatment and control groups. However it would appear that the full potential of corrosion casting to quantitatively characterise vascular beds and in particular tumour vasculature has not yet been fully exploited.

The only evidence of obtaining quantitative information form the cast involved the use of microcomputed tomography (μCT) in the analysis of the differences between a number of regions within the brains of mice genetically engineered to overexpress

VEGF (Heinzer et al. 2008). The cast was prepared in the traditional manner and then small sections were stained with osmium tetroxide to improve absorption contrast. Network analysis was then performed to yield parameters such as vessel volume density and vessel thickness. This technique greatly improves the understanding of the vascular architecture of the brain but is relatively complex, time-consuming and reliant on the availability of high power CT equipment.

No reports of a method for the direct measurement of the vascular volume fraction in solid tumours could be found in the literature. Indirect estimates for this parameter are commonly found by the analysis of dynamic contrast enhanced magnetic resonance imaging (DCE-MRI) or contrast enhanced computed tomography (CE-CT) data sets (O'Connor et al. 2008). The factors that limit the accuracy of these results were discussed in detail in chapter one and include the resolution of the input data and the determination of an arterial input function. There are numerous such DCE-MRI studies in which changes in blood volume derived mathematically are taken as being indicative of response to various treatments such as anti-VEGF therapies (Turetschek et al. 2004; Kim et al. 2005) and transcription factor inhibitors (Jordan et al. 2005). In general such studies are validated using histological techniques in which vessels are stained using a fluorescently labelled substance such as lectin and the number of vessels in a slice are counted manually to give the microvessel density (MVD) (Bremer et al. 2003; Kim et al. 2005) . Although correlation between this measure of MVD and vascular volume assessed by DCE-MRI has been observed (Gillies et al. 2000) this process is time consuming and does not accurately reflect the entire tumour. Another technique that has been used to indirectly evaluate the values obtained by DCE-MRI is the use of a fluorescent label for hypoxia which is visualised

using optical imaging and was shown to correlated with areas of low vascular volume (Raman et al. 2006).

It is felt that corrosion casting with vascular volume measurement could have been added as a final step to a number of these studies to elucidate further useful information. There are also examples of studies in which corrosion casting was performed to look for features of angiogenesis such as sprout formation in which simple measurement of the cast volume prior to SEM analysis would have provided further relevant information (Arkudas et al. 2007).

In summary the greatest relevance of this MRI technique to measure the volume of a vascular corrosion cast is probably in the field of pre-clinical development of novel angiogenesis inhibitors. Studies could be performed either stand alone or in conjunction with DCE-MRI or CE-CT. In a stand alone context the effect of a therapy could be evaluated by comparing the vascular volume fractions of treatment and control groups. Optimal dosing regimes and conditions could also be investigated to maximise drug efficacy. Similarly in dynamic imaging studies the technique could be used to validate the mathematically derived values for vascular volume fraction.

It is felt that further development of the second technique reported here in which the cast was imaged ‘in-situ’ in the tumour could give a useful tool to evaluate the results of magnetic resonance angiography (MRA) studies. It is known that detection of vessels by MRA is susceptible to the speed and direction of blood flow (Muhs et al. 2007). The images obtained show that there was fairly good contrast between cast and tissue and it could be expected that with optimisation it would be possible to obtain co-registered MRA and cast data sets. Comparison of these data sets would then show the over/underestimation of the vasculature by MRA. Again no evidence could be found in the literature of direct methods to validate the results of MRA

experiments. This technique would not be limited to studies of tumour xenografts and could find applications in kidney, liver and brain imaging.

Chapter Five: Overall Summary and Future Work

5.1 Summary

There has been sustained interest in the development of so-called 'blood pool' gadolinium based T_1 positive magnetic resonance imaging (MRI) contrast agents. These agents are designed to remain confined to the vascular space to allow detailed imaging of blood vessels. It has long been realised that whilst increased plasma residence time is obviously a necessary feature of a blood pool agent excessively long residence times are to be avoided due to the risk of the liberation of toxic free gadolinium. This issue has gained further relevance following the discovery of a link between the administration of gadolinium based contrast agents to patients with renal insufficiency and the potentially fatal condition nephrogenic systemic fibrosis (NSF) (Martin 2008).

We have reported here the synthesis, characterisation and in-vivo testing of a new type of polymeric blood pool agent based on a glycol chitosan (GC) backbone. The molecular weights of a number of acid degraded GC samples were determined using gel permeation chromatography with multi angle laser light scattering (GPC-MALLS). Two samples (13 and 38 kDa) were chosen with which to proceed with the synthesis. A functionalised form of the chelating agent diethylene triamine pentaacetic acid (DTPA) was then attached to the GC backbone via a reaction between an isothiocyanatobenzyl group (DTPA) and a primary amine (GC). The level of substitution, determined using elemental analysis and a colorimetric assay, was found to be approximately 5 DTPA pendant groups per GC monomer for both molecular weights of backbone. This result was of some interest as it might have been expected that a four fold difference in length of backbone with the associated difference in flexibility would have resulted in compounds with different degrees of

substitution. This result is seen as advantageous as the similarity of the composition of the two compounds allows for a more rigorous comparison of their in-vivo behaviour. The level of subsequent gadolinium incorporation in the polymers was determined using inductively coupled plasma atomic emission spectroscopy (ICP AES). Approximately 10-20% lower levels of gadolinium were detected than had been predicted from the level of DTPA in the polymers possibly attributable to differences in sensitivities between the assays.

The potential for these conjugates to be used as blood pool contrast agents was tested in-vivo by the imaging of the mouse head. Both agents offered improved vascular specificity when compared with the low molecular weight agent Magnevist. In particular, the larger molecular weight agent gave clear and prolonged enhancement of the vasculature and allowed for the identification of larger blood vessels. Encouragingly preliminary studies also appear to show to show that the agent is cleared from the blood by the kidney and does not have an excessively long plasma residence time.

The next set of experiments focused on the technical examination of a novel solenoid RF micro-coil set-up for the imaging of mouse flank tumours. The resolutions achieved in angiography studies offered a 10 fold improvement on those previously reported and those obtained in 3D volume imaging represented a 15 fold improvement on literature values.

In biological terms; studies performed using the coil set-up in conjunction with Magnevist and the lower molecular weight GC agent showed that the initial delivery of the contrast agents was well correlated with blood supply and that the subsequent transport of these materials was by diffusion as was limited by molecular weight. It was felt that these studies show that the GC-DTPA-Gd agent offered good potential as

drug surrogates that could ultimately be used to predict the delivery, transport and hence expected treatment outcome for therapeutics with similar molecular weights. The strength of this system is that acid degradation of GC allows a myriad of molecular weights from 4-250 kDa to be generated so allowing for comparison with a number of different classes of drug.

Vascular corrosion casting was performed following these imaging sessions and novel MRI techniques were developed to analyse the resultant casts. These involved imaging the cast 'in-situ' in the tumour prior to tissue maceration and imaging the cast mounted in agarose gel following tissue maceration. The former technique appeared to show that it is possible to image the cast in this manner without loss of 3D structure and the latter gave a method to quickly and absolutely determine the tumour vascular volume.

A separate tumour targeted contrast agent was synthesised using a hyaluronic acid (HA) backbone with DTPA attached using the DAB-16 dendrimer as a linker. HA fragments with molecular weight of approximately 40kDa were chosen to maximise targeting potential whilst avoiding the angiogenic properties associated with lower molecular weight fragments. The HA-DAB conjugate was consistently characterised using elemental analysis, NMR, a colorimetric assay and GPC-MALLS. The results showed that approximately one in every 15 disaccharide units had been derivitised with DAB. It is worth noting at this stage that it would be expected that this HA-DAB conjugate would be expected to have anti-tumour activity against CD44 positive tumours due to the intrinsic anti-tumour properties of DAB and the targeting ability of HA. DTPA was attached to some of the remaining primary amine groups of DAB and the level assayed using elemental analysis and NMR. The assays were in good agreement showing approximately 6.8 DTPA molecules attached to each DAB

molecule. Gadolinium was successfully added to the conjugate and its level measured by ICP-AES was found to correlate well with what was predicted by the level of DTPA in the compound. Unfortunately this agent was not tested in-vivo due to pressures of time but a number of suggestions as to how this could be carried out are given in the next section.

5.2 Future Work

For the GC agents the next steps would be to fully investigate their whole body elimination profile. This could be achieved either by harvesting organs following administration and assaying them for gadolinium content or by collecting urine following administration and assaying for gadolinium content. Furthermore it would be worthwhile to determine the relaxivity values for both agents.

In the vascular casting work the agarose gel method should be repeated and refined to remove air bubbles. It would then be very interesting to perform DCE-MRI studies and use existing modelling techniques to obtain an estimate for the vascular volume fraction and compare this with a value obtained using the casting method. Furthermore methods to accurately measure the volume of the cast without using MRI could be investigated (such as volume of water displacement) as could measuring the weight of the cast and using the density of polyurethane to determine the volume.

The next steps for the HA-DAB-DTPA-Gd agent would be to test its tumour targeting capabilities in-vivo. These experiments could take a number of formats including:

- whole body MR imaging in comparison with Magnevist and/or GC-DTPA-Gd agents in a CD44 positive tumour bearing animal
- competition studies in which HA-DAB-DTPA-Gd agent was given alone and then with/immediately after free HA to see if the targeting effect could be reduced with competition.

Abraham, J. and J. Staffurth (2008). "Hormonal therapy for cancer." **36**(1): 29-32.

Agarwal, A., S. Saraf, A. Asthana, U. Gupta, V. Gajbhiye and N. K. Jain (2008). "Ligand based dendritic systems for tumor targeting." Int J Pharm **350**(1-2): 3-13.

Albreht, T., M. McKee, D. M. Alexe, M. P. Coleman and J. M. Martin-Moreno (2008). "Making progress against cancer in Europe in 2008." Eur J Cancer **44**(10): 1451-6.

Alvarez-Linera, J. (2008). "3 T MRI: Advances in brain imaging." European Journal of Radiology **In Press, Corrected Proof**.

Argyle, D. J. and T. Blacking (2008). "From viruses to cancer stem cells: Dissecting the pathways to malignancy." Vet J **177**(3): 311-23.

Arkudas, A., J. Tjiawi, O. Bleiziffer, L. Grabinger, E. Polykandriotis, J. P. Beier, M. Sturzl, R. E. Horch and U. Kneser (2007). "Fibrin gel-immobilized VEGF and bFGF efficiently stimulate angiogenesis in the AV loop model." Mol Med **13**(9-10): 480-7.

Artemov, D., M. Solaiyappan and Z. M. Bhujwalla (2001). "Magnetic resonance pharmacoangiography to detect and predict chemotherapy delivery to solid tumors." Cancer Res **61**(7): 3039-44.

Bammer, R., A. J. de Crespigny, D. Howard, S. Seri, Y. Hashiguchi, A. Nakatani and M. E. Moseley (2004). "A comparative evaluation of CH3-DTPA-Gd (NMS60) for contrast-enhanced magnetic resonance angiography." Magnetic Resonance Imaging **22**(5): 619-624.

Barrett, T., H. Kobayashi, M. Brechbiel and P. L. Choyke (2006). "Macromolecular MRI contrast agents for imaging tumor angiogenesis." European Journal of Radiology **60**(3): 353-366.

Beckmann, N., A. Schuler, T. Mueggler, E. P. Meyer, K. H. Wiederhold, M. Staufenbiel and T. Krucker (2003). "Age-dependent cerebrovascular abnormalities and blood flow disturbances in APP23 mice modeling Alzheimer's disease." J Neurosci **23**(24): 8453-9.

Benjaminsen, I. C., K. G. Brurberg, E. B. Ruud and E. K. Rofstad (2008). "Assessment of extravascular extracellular space fraction in human melanoma xenografts by DCE-MRI and kinetic modeling." Magn Reson Imaging **26**(2): 160-70.

Bhujwalla, Z. M., D. Artemov, K. Natarajan, E. Ackerstaff and M. Solaiyappan (2001). "Vascular differences detected by MRI for metastatic versus nonmetastatic breast and prostate cancer xenografts." Neoplasia **3**(2): 143-53.

Bhujwalla, Z. M., D. Artemov, K. Natarajan, M. Solaiyappan, P. Kollars and P. E. Kristjansen (2003). "Reduction of vascular and permeable regions in solid tumors detected by macromolecular contrast magnetic resonance imaging after treatment with antiangiogenic agent TNP-470." Clin Cancer Res **9**(1): 355-62.

Bjornaes, I. and E. K. Rofstad (2001). "Transvascular and interstitial transport of a 19 kDa linear molecule in human melanoma xenografts measured by contrast-enhanced magnetic resonance imaging." J Magn Reson Imaging **14**(5): 608-16.

Blondin, D., R. J. Seitz, O. Rusch, H. Janssen, K. Andersen, H. J. Wittsack and B. Turowski (2008). "Clinical impact of MRI perfusion disturbances and normal diffusion in acute stroke patients." Eur J Radiol.

Bluemke, D. A., A. E. Stillman, K. G. Bis, T. M. Grist, R. A. Baum, R. D'Agostino, E. S. Malden, J. A. Pierro and E. K. Yucel (2001). "Carotid MR angiography: Phase II study of safety and efficacy for MS-325." Radiology **219**(1): 114-122.

Bogdanov, A. A., Jr., R. Weissleder, H. W. Frank, A. V. Bogdanova, N. Nossif, B. K. Schaffer, E. Tsai, M. I. Papisov and T. J. Brady (1993). "A new macromolecule as a contrast agent for MR angiography: preparation, properties, and animal studies." Radiology **187**(3): 701-6.

Boyiadzis, M. and K. A. Foon (2008). "Approved monoclonal antibodies for cancer therapy." Expert Opin Biol Ther **8**(8): 1151-8.

Bradbury, S. (1984). An Introduction to the Optical Microscope, Oxford University Press.

Bradley, D. P., J. J. Tessier, S. E. Ashton, J. C. Waterton, Z. Wilson, P. L. Worthington and A. J. Ryan (2007). "Correlation of MRI biomarkers with tumor necrosis in Hras5 tumor xenograft in athymic rats." Neoplasia **9**(5): 382-91.

Bremer, C., M. Mustafa, A. Bogdanov, Jr., V. Ntziachristos, A. Petrovsky and R. Weissleder (2003). "Steady-state blood volume measurements in experimental tumors with different angiogenic burdens a study in mice." Radiology **226**(1): 214-20.

Brix, G., W. Semmler, R. Port, L. R. Schad, G. Layer and W. J. Lorenz (1991). "Pharmacokinetic parameters in CNS Gd-DTPA enhanced MR imaging." J Comput Assist Tomogr **15**(4): 621-8.

Brown, J., D. Buckley, A. Coulthard, A. K. Dixon, J. M. Dixon, D. F. Easton, R. A. Eeles, D. G. R. Evans, F. G. Gilbert, M. Graves, C. Hayes, J. P. R. Jenkins, A. P. Jones, S. F. Keevil, M. O. Leach, G. P. Liney, S. M. Moss, A. R. Padhani, G. J. M. Parker, L. J. Pointon, B. A. J. Ponder, T. W. Redpath, J. P. Sloane, L. W. Turnbull, L. G. Walker and R. M. L. Warren (2000). "Magnetic resonance imaging screening in women at genetic risk of breast cancer: imaging and analysis protocol for the UK multicentre study." Magnetic Resonance Imaging **18**(7): 765-776.

Brubaker, L. M., E. Bullitt, C. Yin, T. Van Dyke and W. Lin (2005). "Magnetic resonance angiography visualization of abnormal tumor vasculature in genetically engineered mice." Cancer Res **65**(18): 8218-23.

Bryant, L. H., E. K. Jordan, J. W. M. Bulte, V. Herynek and J. A. Frank (2002). "Pharmacokinetics of a high-generation dendrimer-Gd-DOTA." Academic Radiology **9**: S29-S33.

Buckley, D., L. (2002). "Uncertainty in the analysis of tracer kinetics using dynamic contrast-enhanced T1 weighted MRI TEST." Magnetic Resonance in Medicine **47**(3): 601-606.

Bullitt, E., S. R. Aylward, T. Van Dyke and W. Lin (2007). "Computer-assisted measurement of vessel shape from 3T magnetic resonance angiography of mouse brain." Methods **43**(1): 29-34.

Cacheris, W. P., S. K. Nickle and A. D. Sherry (1987). "Thermodynamic Study of Lanthanide Complexes of 1,4,7-Triazacyclononane-N,N',N"-Triacetic Acid and 1,4,7,10-Tetraazacyclododecane-N,N',N",N"'-Tetraacetic Acid." Inorganic Chemistry **26**(6): 958-960.

Caravan, P., J. J. Ellison, T. J. McMurry and R. B. Lauffer (1999). "Gadolinium(III) Chelates as MRI Contrast Agents: Structure, Dynamics, and Applications." Chem Rev **99**(9): 2293-352.

Cassidy, J. and A. G. Schatzlein (2004). "Tumour-targeted drug and gene delivery: principles and concepts." Expert Rev Mol Med **6**(19): 1-17.

Ceelen, W., P. Smeets, W. Backes, N. Van Damme, T. Boterberg, P. Demetter, I. Bouckenooghe, M. De Visschere, M. Peeters and P. Pattyn (2006). "Noninvasive monitoring of radiotherapy-induced microvascular changes using dynamic contrast enhanced magnetic resonance imaging (DCE-MRI) in a colorectal tumor model." Int J Radiat Oncol Biol Phys **64**(4): 1188-96.

Chescoe, D. and P. Goodhew (1990). The Operation of Transmission and Scanning Electron Microscopes, Oxford University Press.

Chiribiri, A., S. Kelle, S. Gotze, C. Kriatselis, T. Thouet, T. Tangeharoen, I. Paetsch, B. Schnackenburg, E. Fleck and E. Nagel (2008). "Visualization of the cardiac venous system using cardiac magnetic resonance." American Journal of Cardiology **101**(3): 407-412.

Cichy, J. and E. Pure (2003). "The liberation of CD44." J Cell Biol **161**(5): 839-43.

Coles, A., J. and A. Compston (2004). "Multiple sclerosis." **32**(11): 87-92.

Cook, M. J. (1965). The Anatomy of the Laboratory Mouse, Academic Press.

Corbin, I. R., H. Li, J. Chen, S. Lund-Katz, R. Zhou, J. D. Glickson and G. Zheng (2006). "Low-density lipoprotein nanoparticles as magnetic resonance imaging contrast agents." Neoplasia **8**(6): 488-498.

Corrie, P., G. (2008). "Cytotoxic chemotherapy: clinical aspects." **36**(1): 24-28.

D'Arceuil, H. E., A. J. de Crespigny, L. Pelc, D. Howard, M. Alley, S. Seric, Y. Hashiguchi, A. Nakatani and M. E. Moseley (2004). "An MRA study of vascular stenosis in a pig model using CH3-DTPA-Gd (NMS60) and Gd-DTPA." Magnetic Resonance Imaging **22**(9): 1243-1248.

D'Arceuil, H. E., A. J. de Crespigny, L. Pelc, D. Howard, S. Seri, Y. Hashiguchi, A. Nakatani and M. E. Moseley (2005). "A comparison of CH3-DTPA-GD (NMS60) and GD-DTPA for evaluation of acute myocardial ischemia." International Journal of Cardiovascular Imaging **21**(5): 539-547.

Daldrup-Link, H. E. and R. C. Brasch (2003). "Macromolecular contrast agents for MR mammography: current status." Eur Radiol **13**(2): 354-65.

Daldrup-Link, H. E., Y. Okuhata, A. Wolfe, S. Srivastav, S. Oie, N. Ferrara, R. L. Cohen, D. M. Shames and R. C. Brasch (2004). "Decrease in tumor apparent permeability-surface area product to a MRI macromolecular contrast medium following angiogenesis inhibition with correlations to cytotoxic drug accumulation." Microcirculation **11**(5): 387-96.

Daldrup, H., D. M. Shames, M. Wendland, Y. Okuhata, T. M. Link, W. Rosenau, Y. Lu and R. C. Brasch (1998). "Correlation of dynamic contrast-enhanced MR imaging with histologic tumor grade: comparison of macromolecular and small-molecular contrast media." AJR Am J Roentgenol **171**(4): 941-9.

de Crespigny, A. J., D. Howard, H. D'Arceuil, H. Muller, A. T. Agoston, S. Seri, Y. Hashiguchi, C. Fujimoto, A. Nakatani and M. E. Moseley (1999). "Dynamic contrast-enhanced MRI of implanted VX2 tumors in rabbit muscle: Comparison of Gd-DTPA and NMS60." Magnetic Resonance Imaging **17**(9): 1297-1305.

Dean, J. A. (1995). Analytical Chemistry Handbook, McGraw Hill.

DeArmond, S. J., M. F. Fusco and M. M. Dewer (1989). Structure of the Human Brain, Oxford University Press.

Degani, H., V. Gusis, D. Weinstein, S. Fields and S. Strano (1997). "Mapping pathophysiological features of breast tumors by MRI at high spatial resolution." Nat Med **3**(7): 780-2.

Dickerson, B. C. (2007). "Advances in Functional Magnetic Resonance Imaging: Technology and Clinical Applications." Neurotherapeutics **4**(3): 360-370.

Dirksen, M. S., H. J. Lamb, P. Kunz, P. Robert, C. Corot and A. de Roos (2003). "Improved MR coronary angiography with use of a new rapid clearance blood pool contrast agent in pigs." Radiology **227**(3): 802-8.

Dorr, A., J. G. Sled and N. Kabani (2007). "Three-dimensional cerebral vasculature of the CBA mouse brain: a magnetic resonance imaging and micro computed tomography study." Neuroimage **35**(4): 1409-23.

Dufes, C., W. N. Keith, A. Bilsland, I. Proutski, J. F. Uchegbu and A. G. Schatzlein (2005). "Synthetic anticancer gene medicine exploits intrinsic antitumor activity of cationic vector to cure established tumors." Cancer Research **65**(18): 8079-8084.

Dufes, C., I. F. Uchegbu and A. G. Schatzlein (2005). "Dendrimers in gene delivery." Adv Drug Deliv Rev **57**(15): 2177-202.

el-Kareh, A. W. and T. W. Secomb (1997). "Theoretical models for drug delivery to solid tumors." Crit Rev Biomed Eng **25**(6): 503-71.

Evelhoch (1999). "Key factors in the acquisition of contrast kinetic data for oncology." Journal of Magnetic Resonance Imaging **10**(3): 254-259.

Farkas, P. and S. Bystricky (2007). "Efficient activation of carboxyl polysaccharides for the preparation of conjugates." Carbohydrate Polymers **68**(1): 187-190.

Fink, C., F. Kiessling, M. Bock, M. P. Lichy, B. Misselwitz, P. Peschke, N. E. Fusenig, R. Grobholz and S. Delorme (2003). "High-resolution three-dimensional MR angiography of rodent tumors: morphologic characterization of intratumoral vasculature." J Magn Reson Imaging **18**(1): 59-65.

Finn, O. J. (2008). "Cancer immunology." N Engl J Med **358**(25): 2704-15.

Fjeldstad, K. and S. O. Kolset (2005). "Decreasing the metastatic potential in cancers--targeting the heparan sulfate proteoglycans." Curr Drug Targets **6**(6): 665-82.

Fukumura, D. and R. K. Jain (2007). "Tumor microvasculature and microenvironment: targets for anti-angiogenesis and normalization." Microvasc Res **74**(2-3): 72-84.

Gaillard, S., C. Kubiak, C. Stolz, B. Bonnemain and D. Chassard (2002). "Safety and pharmacokinetics of p792, a new blood-pool agent: results of clinical testing in nonpatient volunteers." Invest Radiol **37**(4): 161-6.

Gandhi, S. N., M. A. Brown, J. G. Wong, D. A. Aguirre and C. B. Sirlin (2006). "MR contrast agents for liver imaging: what, when, how." Radiographics **26**(6): 1621-36.

Gillies, R. J., Z. M. Bhujwalla, J. Evelhoch, M. Garwood, M. Neeman, S. P. Robinson, C. H. Sotak and B. Van Der Sanden (2000). "Applications of magnetic resonance in model systems: tumor biology and physiology." Neoplasia **2**(1-2): 139-51.

Gossmann, A., Y. Okuhata, D. M. Shames, T. H. Helbich, T. P. Roberts, M. F. Wendland, S. Huber and R. C. Brasch (1999). "Prostate cancer tumor grade differentiation with dynamic contrast-enhanced MR imaging in the rat: comparison of macromolecular and small-molecular contrast media--preliminary experience." Radiology **213**(1): 265-72.

Gotte, M. and G. W. Yip (2006). "Heparanase, hyaluronan, and CD44 in cancers: a breast carcinoma perspective." Cancer Res **66**(21): 10233-7.

Gouin, S. and F. M. Winnik (2001). "Quantitative assays of the amount of diethylenetriaminepentaacetic acid conjugated to water-soluble polymers

using isothermal titration calorimetry and colorimetry." Bioconjug Chem **12**(3): 372-7.

Gouin, S. and F. M. Winnik (2001). "Quantitative assays of the amount of diethylenetriaminepentaacetic acid conjugated to water-soluble polymers using isothermal titration calorimetry and colorimetry." Bioconjugate Chemistry **12**(3): 372-377.

Goyen, M., M. Edelman, P. Perreault, E. O'Riordan, H. Bertoni, J. Taylor, D. Siragusa, M. Sharafuddin, E. R. Mohler, R. Breger, E. K. Yucel, K. Shamsi and R. M. Weisskoff (2005). "MR angiography of aortoiliac occlusive disease: A phase III study of the safety and effectiveness of the blood-pool contrast agent MS-325." Radiology **236**(3): 825-833.

Grist, T. M., F. R. Korosec, D. C. Peters, S. Witte, R. C. Walovitch, R. P. Dolan, W. E. Bridson, E. K. Yucel and C. A. Mistretta (1998). "Steady-state and dynamic MR angiography with MS-325: Initial experience in humans." Radiology **207**(2): 539-544.

Hafez, S. A., T. Caceci, L. E. Freeman and K. E. Panter (2007). "Angiogenesis in the caprine caruncles in non-pregnant and pregnant normal and swainsonine-treated does." Anat Rec (Hoboken) **290**(7): 761-9.

Hanaway, J., T. A. Woolsey, M. H. Gado and M. P. Roberts (1998). The Brain Atlas, FSP.

Harrington, K., J. (2008). "Biology of cancer." **36**(1): 1-4.

Hashizume, H., P. Baluk, S. Morikawa, J. W. McLean, G. Thurston, S. Roberge, R. K. Jain and D. M. McDonald (2000). "Openings between defective endothelial cells explain tumor vessel leakiness." Am J Pathol **156**(4): 1363-80.

Hassid, Y., E. Furman-Haran, R. Margalit, R. Eilam and H. Degani (2006). "Noninvasive magnetic resonance imaging of transport and interstitial fluid pressure in ectopic human lung tumors." Cancer Res **66**(8): 4159-66.

Heinzer, S., G. Kuhn, T. Krucker, E. Meyer, A. Ulmann-Schuler, M. Stampanoni, M. Gassmann, H. H. Marti, R. Muller and J. Vogel (2008). "Novel three-dimensional analysis tool for vascular trees indicates complete micro-networks, not single capillaries, as the angiogenic endpoint in mice overexpressing human VEGF(165) in the brain." Neuroimage **39**(4): 1549-58.

Henderson, E., J. Sykes, D. Drost, H. J. Weinmann, B. K. Rutt and T. Y. Lee (2000). "Simultaneous MRI measurement of blood flow, blood volume, and capillary permeability in mammary tumors using two different contrast agents." Journal of Magnetic Resonance Imaging **12**(6): 991-1003.

Herneth, A. M., S. Guccione and M. Bednarski (2003). "Apparent diffusion coefficient: a quantitative parameter for in vivo tumor characterization." Eur J Radiol **45**(3): 208-13.

Holmes, W. M., S. Maclellan, B. Condon, C. Dufes, T. R. Evans, I. F. Uchegbu and A. G. Schatzlein (2008). "High-resolution 3D isotropic MR imaging of mouse flank tumours obtained in vivo with solenoid RF micro-coil." Phys Med Biol **53**(2): 505-13.

Hwang, H. Y., I. S. Kim, I. C. Kwon and Y. H. Kim (2008). "Tumor targetability and antitumor effect of docetaxel-loaded hydrophobically modified glycol chitosan nanoparticles." J Control Release **128**(1): 23-31.

Hyung Park, J., S. Kwon, M. Lee, H. Chung, J. H. Kim, Y. S. Kim, R. W. Park, I. S. Kim, S. Bong Seo, I. C. Kwon and S. Young Jeong (2006). "Self-assembled nanoparticles based on glycol chitosan bearing hydrophobic moieties as

carriers for doxorubicin: in vivo biodistribution and anti-tumor activity." Biomaterials **27**(1): 119-26.

Invitrogen. "Molecular Probes Literature." from http://probes.invitrogen.com/handbook/figures/0830.html.

Ito, M., H. Ogino, H. Oshima, N. Shiraki, Y. Shibamoto, H. Kasai, M. Mase, Y. Kawamura and T. Miyati (2006). "Evaluation of CH3-DTPA-Gd (NMS60) as a new MR contrast agent: early phase II study in brain tumors and dual dynamic contrast-enhanced imaging." Magnetic Resonance Imaging **24**(5): 625-630.

Jacobsen, N. (2007). NMR Spectroscopy Explained, Wiley.

Jain, R. K. (1987). "Transport of molecules in the tumor interstitium: a review." Cancer Res **47**(12): 3039-51.

Jain, R. K. (2001). "Delivery of molecular medicine to solid tumors: lessons from in vivo imaging of gene expression and function." J Control Release **74**(1-3): 7-25.

Jain, R. K. (2005). "Normalization of tumor vasculature: an emerging concept in antiangiogenic therapy." Science **307**(5706): 58-62.

Jain, R. K. and L. T. Baxter (1988). "Mechanisms of heterogeneous distribution of monoclonal antibodies and other macromolecules in tumors: significance of elevated interstitial pressure." Cancer Res **48**(24 Pt 1): 7022-32.

Jaracz, S., J. Chen, L. V. Kuznetsova and I. Ojima (2005). "Recent advances in tumor-targeting anticancer drug conjugates." Bioorg Med Chem **13**(17): 5043-54.

Jordan, B. F., M. Runquist, N. Raghunand, A. Baker, R. Williams, L. Kirkpatrick, G. Powis and R. J. Gillies (2005). "Dynamic contrast-enhanced and diffusion MRI show rapid and dramatic changes in tumor microenvironment in response to inhibition of HIF-1alpha using PX-478." Neoplasia **7**(5): 475-85.

Kabalka, G., E. Buonocore, K. Hubner, T. Moss, N. Norley and L. Huang (1987). "Gadolinium-Labeled Liposomes - Targeted Mr Contrast Agents for the Liver and Spleen." Radiology **163**(1): 255-258.

Ke, T. Y., Y. Feng, J. Y. Guo, D. L. Parker and Z. R. Lu (2006). "Biodegradable cystamine spacer facilitates the clearance of Gd(III) chelates in poly(glutamic acid) Gd-DO3A conjugates for contrast-enhanced MR imaging." Magnetic Resonance Imaging **24**(7): 931-940.

Kety, S. S. (1951). "The theory and applications of the exchange of inert gas at the lungs and tissues." Pharmacol Rev **3**(1): 1-41.

Kety, S. S. (1960). Methods in Medical Research **8**: 228-236.

Khor, E. and L. Y. Lim (2003). "Implantable applications of chitin and chitosan." Biomaterials **24**(13): 2339-49.

Kim, J. H., Y. S. Kim, K. Park, S. Lee, H. Y. Nam, K. H. Min, H. G. Jo, J. H. Park, K. Choi, S. Y. Jeong, R. W. Park, I. S. Kim, K. Kim and I. C. Kwon (2008). "Antitumor efficacy of cisplatin-loaded glycol chitosan nanoparticles in tumor-bearing mice." J Control Release **127**(1): 41-9.

Kim, K. Y. (2007). "Nanotechnology platforms and physiological challenges for cancer therapeutics." Nanomedicine: Nanotechnology, Biology and Medicine **3**(2): 103-110.

Kim, Y. R., A. Yudina, J. Figueiredo, W. Reichardt, D. Hu-Lowe, A. Petrovsky, H. W. Kang, D. Torres, U. Mahmood, R. Weissleder and A. A. Bogdanov, Jr. (2005). "Detection of early antiangiogenic effects in human colon adenocarcinoma xenografts: in vivo changes of tumor blood volume in

response to experimental VEGFR tyrosine kinase inhibitor." Cancer Res **65**(20): 9253-60.

Klajnert, B. and M. Bryszewska (2001). "Dendrimers: properties and applications." Acta Biochim Pol **48**(1): 199-208.

Kobayashi, H. and M. W. Brechbiel (2005). "Nano-sized MRI contrast agents with dendrimer cores." Adv Drug Deliv Rev **57**(15): 2271-86.

Kobayashi, H., S. K. Jo, S. Kawamoto, H. Yasuda, X. Hu, M. V. Knopp, M. W. Brechbiel, P. L. Choyke and R. A. Star (2004). "Polyamine dendrimer-based MRI contrast agents for functional kidney imaging to diagnose acute renal failure." J Magn Reson Imaging **20**(3): 512-8.

Kobayashi, H., S. Kawamoto, S. K. Jo, H. L. Bryant, Jr., M. W. Brechbiel and R. A. Star (2003). "Macromolecular MRI contrast agents with small dendrimers: pharmacokinetic differences between sizes and cores." Bioconjug Chem **14**(2): 388-94.

Kobayashi, H., S. Kawamoto, S. K. Jo, N. Sato, T. Saga, A. Hiraga, J. Konishi, S. Hu, K. Togashi, M. W. Brechbiel and R. A. Star (2002). "Renal tubular damage detected by dynamic micro-MRI with a dendrimer-based magnetic resonance contrast agent." Kidney Int **61**(6): 1980-5.

Kobayashi, H., S. Kawamoto, T. Saga, N. Sato, A. Hiraga, J. Konishi, K. Togashi and M. W. Brechbiel (2001). "Micro-MR angiography of normal and intratumoral vessels in mice using dedicated intravascular MR contrast agents with high generation of polyamidoamine dendrimer core: reference to pharmacokinetic properties of dendrimer-based MR contrast agents." J Magn Reson Imaging **14**(6): 705-13.

Kobayashi, H., K. Reijnders, S. English, A. T. Yordanov, D. E. Milenic, A. L. Sowers, D. Citrin, M. C. Krishna, T. A. Waldmann, J. B. Mitchell and M. W. Brechbiel (2004). "Application of a macromolecular contrast agent for detection of alterations of tumor vessel permeability induced by radiation." Clin Cancer Res **10**(22): 7712-20.

Kobayashi, H., N. Sato, A. Hiraga, T. Saga, Y. Nakamoto, H. Ueda, J. Konishi, K. Togashi and M. W. Brechbiel (2001). "3D-micro-MR angiography of mice using macromolecular MR contrast agents with polyamidoamine dendrimer core with reference to their pharmacokinetic properties." Magn Reson Med **45**(3): 454-60.

Kobayashi, H., N. Sato, S. Kawamoto, T. Saga, A. Hiraga, T. Ishimori, J. Konishi, K. Togashi and M. W. Brechbiel (2001). "3D MR angiography of intratumoral vasculature using a novel macromolecular MR contrast agent." Magn Reson Med **46**(3): 579-85.

Kobayashi, H., K. Shirakawa, S. Kawamoto, T. Saga, N. Sato, A. Hiraga, I. Watanabe, Y. Heike, K. Togashi, J. Konishi, M. W. Brechbiel and H. Wakasugi (2002). "Rapid accumulation and internalization of radiolabeled herceptin in an inflammatory breast cancer xenograft with vasculogenic mimicry predicted by the contrast-enhanced dynamic MRI with the macromolecular contrast agent G6-(1B4M-Gd)(256)." Cancer Res **62**(3): 860-6.

Kogan, G., L. Soltes, R. Stern and P. Gemeiner (2007). "Hyaluronic acid: a natural biopolymer with a broad range of biomedical and industrial applications." Biotechnol Lett **29**(1): 17-25.

Konety, B. R. (2006). "Molecular markers in bladder cancer: a critical appraisal." Urol Oncol **24**(4): 326-37.

Krucker, T., A. Lang and E. P. Meyer (2006). "New polyurethane-based material for vascular corrosion casting with improved physical and imaging characteristics." Microsc Res Tech **69**(2): 138-47.

Kumar, P. J. and M. L. Clark (1998). Clinical Medicine: A textbook for medical sutdents and doctors, W.B. Saunders.

Kunishima, M., C. Kawachi, K. Hioki, R. Terao and S. Tani (2001). "Formation of carboxamides by direct condensation of carboxylic acids and amines in alcohols using a new alcohol- and water-soluble condensing agent: DMT-MM." Tetrahedron **57**(8): 1551-1558.

Kunishima, M., C. Kawachi, J. Morita, K. Terao, F. Iwasaki and S. Tani (1999). "4-(4,6-dimethoxy-1,3,5-triazin-2-yl)-4-methyl-morpholinium chloride: An efficient condensing agent leading to the formation of amides and esters." Tetrahedron **55**(46): 13159-13170.

Kuruppu, D., C. Christophi, H. Maeda and P. E. O'Brien (2002). "Changes in the microvascular architecture of colorectal liver metastases following the administration of SMANCS/lipiodol." J Surg Res **103**(1): 47-54.

Larsson, H. B. W., M. Stubgaard, J. L. Frederiksen, M. Jensen, O. Henriksen and O. B. Paulson (1990). "Quantitation of blood-brain barrier defect by magnetic resonance imaging and gadolinium-DTPA in patients with multiple sclerosis and brain tumors." Magnetic Resonance in Medicine **16**(1): 117-131.

Li, D. B., J. Zheng and H. J. Weinmann (2001). "Contrast-enhanced MR imaging of coronary arteries: Comparison of intra- and extravascular contrast agents in swine." Radiology **218**(3): 670-678.

Li, K., X. P. Zhu, J. Waterton and A. Jackson (2000). "Improved 3D quantitative mapping of blood volume and endothelial permeability in brain tumors." Journal of Magnetic Resonance Imaging **12**(2): 347-357.

Li, K. L., L. J. Wilmes, R. G. Henry, M. G. Pallavicini, J. W. Park, D. D. Hu-Lowe, T. M. McShane, D. R. Shalinsky, Y. J. Fu, R. C. Brasch and N. M. Hylton (2005). "Heterogeneity in the angiogenic response of a BT474 human breast cancer to a novel vascular endothelial growth factor-receptor tyrosine kinase inhibitor: Assessment by voxel analysis of dynamic contrast-enhanced MRI." Journal of Magnetic Resonance Imaging **22**(4): 511-519.

Li, K. L., L. J. Wilmes, R. G. Henry, M. G. Pallavicini, J. W. Park, D. D. Hu-Lowe, T. M. McShane, D. R. Shalinsky, Y. J. Fu, R. C. Brasch and N. M. Hylton (2005). "Heterogeneity in the angiogenic response of a BT474 human breast cancer to a novel vascular endothelial growth factor-receptor tyrosine kinase inhibitor: assessment by voxel analysis of dynamic contrast-enhanced MRI." J Magn Reson Imaging **22**(4): 511-9.

Li, K. L., X. P. Zhu, D. R. Checkley, J. J. Tessier, V. F. Hillier, J. C. Waterton and A. Jackson (2003). "Simultaneous mapping of blood volume and endothelial permeability surface area product in gliomas using iterative analysis of first-pass dynamic contrast enhanced MRI data." Br J Radiol **76**(901): 39-50.

Li, W. S., Z. F. Li, F. Y. Jing, Y. F. Deng, L. Wei, P. Liao, X. G. Yang, X. J. Li, F. K. Pei, X. X. Wang and H. Lei (2008). "Synthesis and evaluation of Gd-DTPA-labeled arabinogalactans as potential MRI contrast agents." Carbohydrate Research **343**(4): 685-694.

Li, Z. F., W. S. Li, X. J. Li, F. K. Pei, Y. X. Li and H. Lei (2007). "The gadolinium complexes with polyoxometalates as potential MRI contrast agents." Magnetic Resonance Imaging **25**(3): 412-417.

Lind, M. J. (2008). "Principles of cytotoxic chemotherapy." **36**(1): 19-23.

Liney, G. P., P. Gibbs, C. Hayes, M. O. Leach and L. W. Turnbull (1999). "Dynamic contrast-enhanced MRI in the differentiation of breast tumors: User-defined versus semi-automated region-of-interest analysis." Journal of Magnetic Resonance Imaging **10**(6): 945-949.

Liu, Y. T., H. D'Arceuil, J. L. He, M. Duggan, S. Seri, Y. Hashiguchi, A. Nakatani, R. G. Gonzalez, J. Pryor and A. de Crespigny (2005). "Dynamic susceptibility contrast perfusion imaging of cerebral ischemia in nonhuman primates: Comparison of Gd-DTPA and NMS60." Journal of Magnetic Resonance Imaging **22**(4): 461-466.

Lopata, R. G. P., W. H. Backes, P. J. P. van den Bosch and N. A. W. van Riel (2007). "On the identifiability of pharmacokinetic parameters in dynamic contrast-enhanced imaging." Magnetic Resonance in Medicine **58**(2): 425-429.

Lu, Z. R., F. R. Ye and A. Vaidya (2007). "Polymer platforms for drug delivery and biomedical imaging." Journal of Controlled Release **122**(3): 269-277.

Lucas, R. L., M. Benjamin and T. M. Reineke (2008). "Comparison of a tartaric acid derived polymeric MRI contrast agent to a small molecule model chelate." Bioconjugate Chemistry **19**(1): 24-27.

Luciani, A., J. C. Olivier, O. Clement, N. Siauve, P. Y. Brillet, B. Bessoud, F. Gazeau, I. F. Uchegbu, E. Kahn, G. Frija and C. A. Cuenod (2004). "Glucose-receptor MR imaging of tumors: Study in mice with pegylated paramagnetic niosomes." Radiology **231**(1): 135-142.

Mackenzie, P. J. and G. A. Cioffi (2008). "Vascular anatomy of the optic nerve head." Can J Ophthalmol **43**(3): 308-12.

Malcontenti-Wilson, C., V. Muralidharan, S. Skinner, C. Christophi, D. Sherris and P. E. O'Brien (2001). "Combretastatin A4 prodrug study of effect on the growth and the microvasculature of colorectal liver metastases in a murine model." Clin Cancer Res **7**(4): 1052-60.

Manning, T. J. and W. R. Grow (1997). "Inductively Coupled Plasma Atomic Emission Spectrometry." The Chemical Educator **2**(1): 1-19.

Mansfield, P. and A. A. Maudsley (1977). "Medical imaging by NMR." Br J Radiol **50**(591): 188-94.

Marcus, C. D., V. Ladam-Marcus, C. Cucu, O. Bouche, L. Lucas and C. Hoeffel (2008). "Imaging techniques to evaluate the response to treatment in oncology: Current standards and perspectives." Crit Rev Oncol Hematol.

Margerum, L. D., B. K. Campion, M. Koo, N. Shargill, J. J. Lai, A. Marumoto and P. C. Sontum (1997). "Gadolinium(III) DO3A macrocycles and polyethylene glycol coupled to dendrimers - Effect of molecular weight on physical and biological properties of macromolecular magnetic resonance imaging contrast agents." Journal of Alloys and Compounds **249**(1-2): 185-190.

Martin, D. R. (2008). "Nephrogenic system fibrosis: a radiologist's practical perspective." Eur J Radiol **66**(2): 220-4.

Martin, L., C. G. Wilson, F. Koosha, L. Tetley, A. I. Gray, S. Senel and I. F. Uchegbu (2002). "The release of model macromolecules may be controlled by the hydrophobicity of palmitoyl glycol chitosan hydrogels." Journal of Controlled Release **80**(1-3): 87-100.

Martini, F. H. (1998). Fundamentals of Anatomy and Physiology, Pearson.

McKie, S. and J. Brittenden (2005). "Basic science: magnetic resonance imaging." Current Orthopaedics **19**(1): 13-19.

McRobbie, D. W. (2002). MRI: From Picture to Proton, Cambridge.

Merbach, A. E. and E. Toth (2001). The Chemistry of Contrast Agents in Medical Magnetic Resonance Imaging, Wiley.

Meyer, E. P., A. Ulmann-Schuler, M. Staufenbiel and T. Krucker (2008). "Altered morphology and 3D architecture of brain vasculature in a mouse model for Alzheimer's disease." Proc Natl Acad Sci U S A **105**(9): 3587-92.

Meyer, K. and J. W. Palmer (1934). "The Polysaccharide of the Vitreous Humour." The Journal of Biological Chemistry **107**(3): 629-634.

Min, K. H., K. Park, Y. S. Kim, S. M. Bae, S. Lee, H. G. Jo, R. W. Park, I. S. Kim, S. Y. Jeong, K. Kim and I. C. Kwon (2008). "Hydrophobically modified glycol chitosan nanoparticles-encapsulated camptothecin enhance the drug stability and tumor targeting in cancer therapy." J Control Release **127**(3): 208-18.

Misselwitz, B., H. Schmitt-Willich, W. Ebert, T. Frenzel and H. J. Weinmann (2001). "Pharmacokinetics of Gadomer-17, a new dendritic magnetic resonance contrast agent." Magnetic Resonance Materials in Physics Biology and Medicine **12**(2-3): 128-134.

Mohs, A. M., T. Nguyen, E. K. Jeong, Y. Feng, L. Emerson, Y. D. Zong, D. L. Parker and Z. R. Lu (2007). "Modification of Gd-DTPA cystine copolymers with PEG-1000 optimizes pharmacokinetics and tissue retention for magnetic resonance angiography." Magnetic Resonance in Medicine **58**(1): 110-118.

Mokrasch, L. C. (1970). "Determination of small amounts of protein in total lipid extracts by the use of trinitrobenzenesulfonic acid." Anal Biochem **36**(2): 273-7.

Moratal, D., A. Valles-Luch, L. Marti-Bonmati and M. E. Brummer (2008). "k-Space tutorial: an MRI educational tool for a better understanding of k-space." Biomedical Imaging and Intervention Journal **4**(1): 1-15.

Morcos, S. K. (2008). "Extracellular gadolinium contrast agents: differences in stability." Eur J Radiol **66**(2): 175-9.

Muhs, B. E., H. J. Verhagen, M. G. Huddle, V. M. Pai, E. M. Hecht and A. Dardik (2007). "Theory, technique, and practice of magnetic resonance angiography." Vascular **15**(6): 376-83.

Muruganandham, M., M. Lupu, J. P. Dyke, C. Matei, M. Linn, K. Packman, K. Kolinsky, B. Higgins and J. A. Koutcher (2006). "Preclinical evaluation of tumor microvascular response to a novel antiangiogenic/antitumor agent RO0281501 by dynamic contrast-enhanced MRI at 1.5 T." Mol Cancer Ther **5**(8): 1950-7.

Nakajima, N. and Y. Ikada (1995). "Mechanism of amide formation by carbodiimide for bioconjugation in aqueous media." Bioconjug Chem **6**(1): 123-30.

Nakamura, E., K. Makino, T. Okano, T. Yamamoto and M. Yokoyama (2006). "A polymeric micelle MRI contrast agent with changeable relaxivity." Journal of Controlled Release **114**(3): 325-333.

Nastiuk, K. L., H. Liu, M. Hamamura, L. T. Muftuler, O. Nalcioglu and J. J. Krolewski (2007). "In vivo MRI volumetric measurement of prostate regression and growth in mice." BMC Urol **7**: 12.

Navon, G., R. Panigel and G. Valensin (1986). "Liposomes Containing Paramagnetic Macromolecules as Mri Contrast Agents." Magnetic Resonance in Medicine **3**(6): 876-880.

Nobel-Foundation. (2008). from www.nobelprize.org.

O'Connor, J. P., A. Jackson, M. C. Asselin, D. L. Buckley, G. J. Parker and G. C. Jayson (2008). "Quantitative imaging biomarkers in the clinical development

of targeted therapeutics: current and future perspectives." Lancet Oncol **9**(8): 766-76.

Ogan, M. D., U. Schmiedl, M. E. Moseley, W. Grodd, H. Paajanen and R. C. Brasch (1987). "Albumin labeled with Gd-DTPA. An intravascular contrast-enhancing agent for magnetic resonance blood pool imaging: preparation and characterization." Invest Radiol **22**(8): 665-71.

Orth, R. C., J. Bankson, R. Price and E. F. Jackson (2007). "Comparison of single- and dual-tracer pharmacokinetic modeling of dynamic contrast-enhanced MRI data using low, medium, and high molecular weight contrast agents." Magnetic Resonance in Medicine **58**(4): 705-716.

Osuga, T. and S. Han (2004). "Proton magnetic resonance imaging of diffusion of high- and low-molecular-weight contrast agents in opaque porous media saturated with water." Magn Reson Imaging **22**(7): 1039-42.

Padhani, A. R. (2002). "Dynamic contrast-enhanced MRI in clinical oncology: current status and future directions." J Magn Reson Imaging **16**(4): 407-22.

Padhani, A. R. and J. E. Husband (2001). "Dynamic contrast-enhanced MRI studies in oncology with an emphasis on quantification, validation and human studies." Clin Radiol **56**(8): 607-20.

Pannarale, L., P. Onori, F. Borghese, D. Conte and E. Gaudio (2007). "Three-dimensional organization of the hepatic artery terminal branches: a scanning electron microscopic study of vascular corrosion casts of rat liver." Ital J Anat Embryol **112**(1): 1-12.

Parmar, M., K. B. (2008). "Adjuvant therapy." **36**(1): 38-40.

Parmelee, D. J., R. C. Walovitch, H. S. Ouellet and R. B. Lauffer (1997). "Preclinical evaluation of the pharmacokinetics, biodistribution, and elimination of MS-325, a blood pool agent for magnetic resonance imaging." Investigative Radiology **32**(12): 741-747.

Pathak, A. P., D. Artemov and Z. M. Bhujwalla (2004). "Novel system for determining contrast agent concentration in mouse blood in vivo." Magnetic Resonance in Medicine **51**(3): 612-615.

Pathak, A. P., D. Artemov, B. D. Ward, D. G. Jackson, M. Meeman and Z. M. Bhujwalla (2005). "Characterizing extravascular fluid transport of macromolecules in the tumor interstitium by magnetic resonance imaging." Cancer Research **65**(4): 1425-1432.

Pathak, A. P., D. Artemov, B. D. Ward, D. G. Jackson, M. Neeman and Z. M. Bhujwalla (2005). "Characterizing Extravascular Fluid Transport of Macromolecules in the Tumor Interstitium by Magnetic Resonance Imaging." Cancer Res **65**(4): 1425-1432.

Patil, S. D., D. G. Rhodes and D. J. Burgess (2005). "DNA-based therapeutics and DNA delivery systems: a comprehensive review." Aaps J **7**(1): E61-77.

Pauliah, M., V. Saxena, M. Haris, N. Husain, R. K. S. Rathore and R. K. Gupta (2007). "Improved T1-weighted dynamic contrast-enhanced MRI to probe microvascularity and heterogeneity of human glioma." Magnetic Resonance Imaging **25**(9): 1292-1299.

Peake, M., D. (2008). "Lung cancer and its management." **36**(3): 162-167.

Peker, T., S. Omeroglu, S. Hamdemir, H. Celik, I. Tatar, N. Aksakal and H. B. Turgut (2006). "Three-dimensional assessment of the morphology of the umbilical artery in normal and pre-eclamptic placentas." J Obstet Gynaecol Res **32**(5): 468-74.

Pellerin, M., T. E. Yankeelov and M. Lepage (2007). "Incorporating contrast agent diffusion into the analysis of DCE-MRI data." Magnetic Resonance in Medicine **58**(6): 1124-1134.

Pickup, S., R. Zhou and J. Glickson (2003). "MRI estimation of the arterial input function in mice." Acad Radiol **10**(9): 963-8.

Port, M., C. Corot, O. Rousseaux, I. Raynal, L. Devoldere, J. M. Idee, A. Dencausse, S. Le Greneur, C. Simonot and D. Meyer (2001). "P792: a rapid clearance blood pool agent for magnetic resonance imaging: preliminary results." Magnetic Resonance Materials in Physics Biology and Medicine **12**(2-3): 121-127.

Qu, X. Z., V. V. Khutoryanskiy, A. Stewart, S. Rahman, B. Papahadjopoulos-Sternberg, C. Dufes, D. McCarthy, C. G. Wilson, R. Lyons, K. C. Carter, A. Schatzlein and I. F. Uchegbu (2006). "Carbohydrate-based micelle clusters which enhance hydrophobic drug bioavailability by up to 1 order of magnitude." Biomacromolecules **7**(12): 3452-3459.

Raman, V., D. Artemov, A. P. Pathak, P. T. Winnard, Jr., S. McNutt, A. Yudina, A. Bogdanov, Jr. and Z. M. Bhujwalla (2006). "Characterizing vascular parameters in hypoxic regions: a combined magnetic resonance and optical imaging study of a human prostate cancer model." Cancer Res **66**(20): 9929-36.

Rang HP and D. MM (2003). Pharmacology, Churchill Livingstone.

Raymond, K. N. and V. C. Pierre (2005). "Next generation, high relaxivity gadolinium MRI agents." Bioconjug Chem **16**(1): 3-8.

Rescigno, M., F. Avogadri and G. Curigliano (2007). "Challenges and prospects of immunotherapy as cancer treatment." Biochim Biophys Acta **1776**(1): 108-23.

Robinson, M. H. (2008). "Radiotherapy: technical aspects." **36**(1): 9-14.

Rongved, P., T. H. Fritzell, P. Strande and J. Klaveness (1996). "Polysaccharides as carriers for magnetic resonance imaging contrast agents: Synthesis and stability of a new amino acid linker derivative." Carbohydrate Research **287**: 77-89.

Rooney, P., S. Kumar, J. Ponting and M. Wang (1995). "The role of hyaluronan in tumour neovascularization (review)." Int J Cancer **60**(5): 632-6.

Rosen, Y. and R. E. Lenkinski (2007). "Recent advances in magnetic resonance neurospectroscopy." Neurotherapeutics **4**(3): 330-45.

Satake, K., T. Okuyama, M. Ohashi and T. Shinoda (1960). "The Spectrophotometric Determination of Amine, Amino Acid and Peptide with 2,4,6-Trintrobenzene 1-Sulfonic Acid." The journal of Biochemistry **47**: 654-660.

Schmiedl, U., M. D. Ogan, M. E. Moseley and R. C. Brasch (1986). "Comparison of the Contrast-Enhancing Properties of Albumin-(Gd-Dtpa) and Gd-Dtpa at 2.0-T - an Experimental-Study in Rats." American Journal of Roentgenology **147**(6): 1263-1270.

Seierstad, T., S. Folkvord, K. Roe, K. Flatmark, A. Skretting and D. R. Olsen (2007). "Early changes in apparent diffusion coefficient predict the quantitative antitumoral activity of capecitabine, oxaliplatin, and irradiation in HT29 xenografts in athymic nude mice." Neoplasia **9**(5): 392-400.

Seshadri, M., J. A. Spernyak, P. G. Maiery, R. T. Cheney, R. Mazurchuk and D. A. Bellnier (2007). "Visualizing the acute effects of vascular-targeted therapy in vivo using intravital microscopy and magnetic resonance imaging: correlation with endothelial apoptosis, cytokine induction, and treatment outcome." Neoplasia **9**(2): 128-35.

Sherman, L., J. Sleeman, P. Herrlich and H. Ponta (1994). "Hyaluronate receptors: key players in growth, differentiation, migration and tumor progression." Curr Opin Cell Biol **6**(5): 726-33.

Shiftan, L., T. Israely, M. Cohen, V. Frydman, H. Dafni, R. Stern and M. Neeman (2005). "Magnetic resonance imaging visualization of hyaluronidase in ovarian carcinoma." Cancer Res **65**(22): 10316-23.

Shively, M. J. and J. E. Stump (1975). "The systemic arterial pattern of the guinea pig: the abdomen." Anat Rec **182**(3): 355-66.

Slevin, M., J. Krupinski, J. Gaffney, S. Matou, D. West, H. Delisser, R. C. Savani and S. Kumar (2007). "Hyaluronan-mediated angiogenesis in vascular disease: uncovering RHAMM and CD44 receptor signaling pathways." Matrix Biol **26**(1): 58-68.

Snyder, S. L. and P. Z. Sobocinski (1975). "An improved 2,4,6-trinitrobenzenesulfonic acid method for the determination of amines." Anal Biochem **64**(1): 284-8.

Spinazzi, A., V. Lorusso, G. Pirovano and M. Kirchin (1999). "Safety, tolerance, biodistribution, and MR imaging enhancement of the liver with gadobenate dimeglumine: results of clinical pharmacologic and pilot imaging studies in nonpatient and patient volunteers." Acad Radiol **6**(5): 282-91.

Stern, R., A. A. Asari and K. N. Sugahara (2006). "Hyaluronan fragments: an information-rich system." Eur J Cell Biol **85**(8): 699-715.

Stern, R., G. Kogan, M. J. Jedrzejas and L. Soltes (2007). "The many ways to cleave hyaluronan." Biotechnol Adv **25**(6): 537-57.

Su, M.-Y. (1994). "Measurement of vascular volume fraction and blood-tissue permeability constants with a pharmacokinetic model: Studies in rat muscle tumors with dynamic Gd-DTPA enhanced MRI." Magnetic Resonance in Medicine **32**(6): 714-724.

Sun, G. Y., J. H. Feng, F. Y. Jing, F. K. Pei and M. L. Liu (2003). "Synthesis and evaluation of novel polysaccharide-Gd-DTPA compounds as contrast agent for MRI." Journal of Magnetism and Magnetic Materials **265**(2): 123-129.

Swanson, S. D., J. F. Kukowska-Latallo, A. K. Patri, C. Chen, S. Ge, Z. Cao, A. Kotlyar, A. T. East and J. R. Baker (2008). "Targeted gadolinium-loaded dendrimer nanoparticles for tumor-specific magnetic resonance contrast enhancement." Int J Nanomedicine **3**(2): 201-10.

Tee, L. B., M. A. Penrose, J. E. O'Shea, C. M. Lai, E. P. Rakoczy and S. A. Dunlop (2008). "VEGF-induced choroidal damage in a murine model of retinal neovascularisation." Br J Ophthalmol **92**(6): 832-8.

Thompson, K. and S. Michielsen (2006). "Novel synthesis of N-substituted polyacrylamides: Derivatization of poly(acrylic acid) with amines using a triazine-based condensing reagent." Journal of Polymer Science Part a-Polymer Chemistry **44**(1): 126-136.

Thomsen, H. S. and P. Marckmann (2008). "MRI contrast media are used to improve visualization of abnormal structures or lesions in various parts of the body. Introduction." Eur J Radiol **66**(2): 153-9.

Thomsen, H. S., P. Marckmann and V. B. Logager (2008). "Update on nephrogenic systemic fibrosis." Magn Reson Imaging Clin N Am **16**(4): 551-60.

Tofts, P. S. (2003). Quantitative MRI of the brain: measuring changes caused by disease.

Tofts, P. S., G. Brix, D. L. Buckley, J. L. Evelhoch, E. Henderson, M. V. Knopp, H. B. W. Larsson, T.-Y. Lee, N. A. Mayr, G. J. M. Parker, R. E. Port, J. Taylor

and R. M. Weisskoff (1999). "Estimating kinetic parameters from dynamic contrast-enhanced t1-weighted MRI of a diffusable tracer: Standardized quantities and symbols." Journal of Magnetic Resonance Imaging **10**(3): 223-232.

Tofts, P. S. and A. G. Kermode (1991). "Measurement of the blood-brain barrier permeability and leakage space using dynamic MR imaging. 1. Fundamental concepts." Magn Reson Med **17**(2): 357-67.

Turetschek, K., E. Floyd, T. Helbich, T. P. Roberts, D. M. Shames, M. F. Wendland, W. O. Carter and R. C. Brasch (2001). "MRI assessment of microvascular characteristics in experimental breast tumors using a new blood pool contrast agent (MS-325) with correlations to histopathology." J Magn Reson Imaging **14**(3): 237-42.

Turetschek, K., S. Huber, E. Floyd, T. Helbich, T. P. Roberts, D. M. Shames, K. S. Tarlo, M. F. Wendland and R. C. Brasch (2001). "MR imaging characterization of microvessels in experimental breast tumors by using a particulate contrast agent with histopathologic correlation." Radiology **218**(2): 562-9.

Turetschek, K., A. Preda, V. Novikov, R. C. Brasch, H. J. Weinmann, P. Wunderbaldinger and T. P. Roberts (2004). "Tumor microvascular changes in antiangiogenic treatment: assessment by magnetic resonance contrast media of different molecular weights." J Magn Reson Imaging **20**(1): 138-44.

Uchegbu, I. F., L. Sadiq, M. Arastoo, A. I. Gray, W. Wang, R. D. Waigh and A. G. Schatzleina (2001). "Quaternary ammonium palmitoyl glycol chitosan - a new polysoap for drug delivery." International Journal of Pharmaceutics **224**(1-2): 185-199.

von Ludinghausen, M. and N. Ohmachi (2001). "Right superior septal artery with "normal" right coronary and ectopic "early" aortic origin: a contribution to the vascular supply of the interventricular septum of the human heart." Clin Anat **14**(5): 312-9.

Wagner, R. C., K. Czymmek and F. E. Hossler (2006). "Confocal microscopy, computer modeling, and quantification of glomerular vascular corrosion casts." Microsc Microanal **12**(3): 262-8.

Wang, S. C., M. G. Wikstrom, D. L. White, J. Klaveness, E. Holtz, P. Rongved, M. E. Moseley and R. C. Brasch (1990). "Evaluation of Gd-Dtpa Labeled Dextran as an Intravascular Mr Contrast Agent - Imaging Characteristics in Normal Rat-Tissues." Radiology **175**(2): 483-488.

Wang, W., A. M. McConaghy, L. Tetley and I. F. Uchegbu (2001). "Controls on polymer molecular weight may be used to control the size of palmitoyl glycol chitosan polymeric vesicles." Langmuir **17**(3): 631-636.

Wang, Z., M. Y. Su, A. Najafi and O. Nalcioglu (2001). "Effect of vasodilator hydralazine on tumor microvascular random flow and blood volume as measured by intravoxel incoherent motion (IVIM) weighted MRI in conjunction with Gd-DTPA-Albumin enhanced MRI." Magn Reson Imaging **19**(8): 1063-72.

Warde, P. (2008). "Radiotherapy: practical applications and clinical aspects." **36**(1): 15-18.

Wei, W., V. Popov, J. A. Walocha, J. Wen and E. Bello-Reuss (2006). "Evidence of angiogenesis and microvascular regression in autosomal-dominant polycystic kidney disease kidneys: a corrosion cast study." Kidney Int **70**(7): 1261-8.

Weidensteiner, C., M. Rausch, P. M. J. McSheehy and P. R. Allegrini (2006). "Quantitative dynamic contrast-enhanced MRI in tumor-bearing rats and mice with inversion recovery TrueFISP and two contrast agents at 4.7 T." Journal of Magnetic Resonance Imaging **24**(3): 646-656.

Weissig, V., J. Babich and V. Torchilin (2000). "Long-circulating gadolinium-loaded liposomes: potential use for magnetic resonance imaging of the blood pool." Colloids and Surfaces B-Biointerfaces **18**(3-4): 293-299.

Williams, D. H. and I. Fleming (1995). Spectroscopic Methods in Organic Chemistry, McGraw Hill.

Wilmes, L. J., M. G. Pallavicini, L. M. Fleming, J. Gibbs, D. H. Wang, K. L. Li, S. C. Partridge, R. G. Henry, D. R. Shalinsky, D. Hu-Lowe, J. W. Park, T. M. McShane, Y. Lu, R. C. Brasch and N. M. Hylton (2007). "AG-013736, a novel inhibitor of VEGF receptor tyrosine kinases, inhibits breast cancer growth and decreases vascular permeability as detected by dynamic contrast-enhanced magnetic resonance imaging." Magnetic Resonance Imaging **25**(3): 319-327.

Winnik, F. M. (1999). Hyaluronan-Based Imaging Agents W. I. P. Organization.

Work, T. E. and E. Work (1976). Laboratory Techniques in Biochemistry and Molecular Biology in Biochemistry and Molecular Biology, North Holland Publishing.

www.wyatt.com. from www.wyatt.com.

Wyatt, P. J. (1993). "Light-Scattering and the Absolute Characterization of Macromolecules." Analytica Chimica Acta **272**(1): 1-40.

Yamada, T. and T. Kawasaki (2005). "Microbial synthesis of hyaluronan and chitin: New approaches." J Biosci Bioeng **99**(6): 521-8.

Yan, G.-P., L. Robinson and P. Hogg (2007). "Magnetic resonance imaging contrast agents: Overview and perspectives." Radiography **13**(Supplement 1): e5-e19.

Yoshida (1989). "Assessment of T1 Time Course Chnages and Tissue Blood Ratios After Gd-DTPA Administration in Brain Tumours." Magnetic Resonance Imaging **7**(9): 9-15.

Zamboni, W. C. (2008). "Concept and clinical evaluation of carrier-mediated anticancer agents." Oncologist **13**(3): 248-60.

Zeng, C., B. P. Toole, S. D. Kinney, J. W. Kuo and I. Stamenkovic (1998). "Inhibition of tumor growth in vivo by hyaluronan oligomers." Int J Cancer **77**(3): 396-401.

Zhang, Z. D., S. A. Nair and T. J. McMurry (2005). "Gadolinium meets medicinal chemistry: MRI contrast agent development." Current Medicinal Chemistry **12**(7): 751-778.

Appendix Publications